

A Thesis Submitted for the Degree of PhD at the University of Warwick

Permanent WRAP URL:

<http://wrap.warwick.ac.uk/108288>

Copyright and reuse:

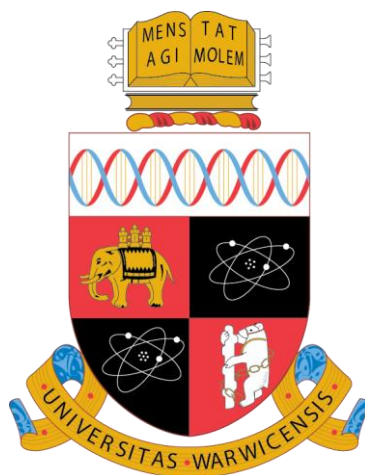
This thesis is made available online and is protected by original copyright.

Please scroll down to view the document itself.

Please refer to the repository record for this item for information to help you to cite it.

Our policy information is available from the repository home page.

For more information, please contact the WRAP Team at: wrap@warwick.ac.uk



^{17}O Solid State NMR Study of Ceria Systems

By

Maria Christine Vlachou

Thesis

Submitted to the University of Warwick

for the degree of

Doctor of Philosophy

Supervised by Dr John Hanna & Dr David Thompsett

Department of Physics

September 2017



Contents

Chapter 1 An Introduction to Ceria	1
1.1 Structure of Ceria	2
1.1.1. Defects	3
1.2 Ceria in Autocatalysis	5
1.3 Ceria Supported Precious Metal Catalysts	7
1.4 Nanoscale Effects	8
1.5 Morphologies of Ceria	10
1.6 Ceria zirconia	11
1.7 O ₂ -Ceria Interactions	13
1.7.1 O ₂ Adsorption	13
Chapter 2 Theory and Methods	15
2.1 NMR Theory	15
2.1.1 Classical Description	16
2.2 Quantum Mechanical Definitions	16
2.2.1 Introduction	16
2.2.2 Angular Momentum Operators	17
2.2.3 The Zeeman Effect	18
2.3 Spin Excitation in the Rotating Frame	20
2.4 NMR Interactions	21
Overview	21
2.4.1 The Internal Nuclear Spin Hamiltonian	22
2.4.2 Frames and Rotations of the Hamiltonian	23
2.4.3 Chemical Shielding and Shift	24
2.4.4 The Dipolar Interaction	26
2.4.5 The Quadrupolar Interaction	26
2.4.6 Paramagnetic Interactions	30
2.5 NMR Methods Used in Chapters 5 and 6	31
2.5.1 Pulsed FT NMR and the NMR Signal	31
2.5.2 Magic Angle Spinning	33
2.5.3 The Quadrupolar Interaction under MAS	34

2.5.4 Single Pulse Sequence.....	36
2.5.5 Hahn-Echo Sequence	37
2.6 Raman Spectroscopy.....	39
Chapter 3 Literature Reviews	41
3.1 Frenkel Type Point Defects	41
3.2 ^{17}O Solid-State NMR of Ceria Systems	46
3.3 A Unique Case: ^{17}O MAS NMR and Frenkel Type Defects.....	60
3.3 Conclusions	62
3.1.1 Frenkel Defects	62
3.1.2 Solid-State ^{17}O MAS NMR	62
Chapter 4 Experimental Details	64
4.1 Sample Syntheses	65
4.1.1 H_2^{17}O Synthesised Ceria: H_2^{17}O Ceria and H_2^{17}O Ceria 500 °C.....	65
4.1.2 Materials for $^{17}\text{O}_2$ Enrichment Methods.....	65
4.1.3 $^{17}\text{O}_2$ Exchange and $^{17}\text{O}_2$ Redox Experiments	66
4.1.4 Peroxide Ceria and H_2O_2 synthesis from $^{17}\text{O}_2$	67
4.1.5 ^{17}O and ^1H NMR Experimental Details	68
4.2 Powder X-ray Diffraction.....	69
4.3 Raman Spectroscopy.....	69
4.4 Magnetisation Measurements (SQUID)	69
4.5 H_2 TPR Measurements	70
4.6 Computation Details	70
Chapter 5 An Investigation of Ceria	72
5.1 H_2^{17}O Ceria and H_2^{17}O Ceria 500 °C.....	73
5.1.1 PXRD and SAXS.....	73
5.1.2 Raman Spectroscopy.....	74
5.1.3 ^{17}O MAS NMR.....	78
5.2 HSA20 Ceria- As Prepared	80
5.2.1 PXRD, XPS, and TEM of HSA20 Ceria.....	81
5.2.2 Raman Spectroscopy.....	82
5.3 $^{17}\text{O}_2$ Direct Exchange of HSA20 at 600 °C.....	83
5.3.1 Raman Spectroscopy.....	84
5.3.2 ^{17}O Solid-State MAS NMR	85
5.4 Reduction and $^{17}\text{O}_2$ Reoxidation of HSA20 Ceria	86

5.4.1 TPR-H ₂ of HSA20.....	86
5.4.2 In Situ Raman Spectroscopy.....	87
5.4.3 PXRD and SAXS.....	88
5.4.4 Raman Spectroscopy.....	89
5.4.5 ¹⁷ O Solid-State MAS NMR	91
5.5 Varying Oxidation Temperature of HSA20.....	95
5.5.1 Raman Spectroscopy.....	96
5.5.2 ¹⁷ O Solid-State MAS NMR	97
5.5.3 Comparison of HSA20-700/300-Redox from Sections 5.3 and 5.4	101
5.5.4 T ₁ Measurement of HSA20-700/300-Redox.....	102
5.5.5 Evolution of HSA20-700/300-Redox	102
5.5.6 Exposure to Air.....	104
5.5.7 Comparison of HSA20-700/300-Redox across Three Fields	105
5.6 Size Comparison: Sigma Aldrich <25 nm Ceria.....	106
5.6.1 Raman Spectroscopy.....	106
5.6.2 ¹⁷ O Solid-State MAS NMR	108
5.6.3 Heating of SA-700/300-Redox in Air	111
5.7 Morphology Comparison: Cubes and Rods.....	112
5.7.1 Raman Spectroscopy.....	113
5.7.2 ¹⁷ O Solid-State MAS NMR.....	114
5.7.3 T ₁ Relaxation of Cubes-700/300-Redox and Rods-700/300-Redox	116
5.8 Peroxides on Ceria	118
5.9 A DFT Investigation of the Frenkel Pair Defect	122
5.10 An Investigation of Ce ³⁺ in Ceria.....	129
5.10.1 Magnetic Measurements of HSA20	129
5.10.2 VT Experiments of HSA20	131
Chapter 6 An Investigation of Loaded and/or Mixed Ceria.....	136
6.1 Investigation of Pd Loaded Ceria	137
6.1.1 TPR	137
6.1.2 Raman Spectroscopy.....	138
6.1.3 ¹⁷ O Solid-State MAS NMR	143
6.2 CeZr Oxides (As-Prepared)	149
6.2.1 TPR	150
6.2.2 Raman Spectroscopy.....	151

6.3 $^{17}\text{O}_2$ Direct Exchange of CeZr Oxides at 600 °C	152
6.3.1 Raman Spectroscopy.....	152
6.3.2 ^{17}O Solid-State MAS NMR	154
6.4 $^{17}\text{O}_2$ Redox Experiments of CeZr Oxides.....	156
6.4.1 Raman Spectroscopy.....	158
6.4.2 ^{17}O Solid-State MAS NMR.....	159
6.5 Investigation of Palladium Loaded $\text{Ce}_{0.5}\text{Zr}_{0.5}\text{O}_2$	161
6.5.1 Raman Spectroscopy.....	161
6.5.2 ^{17}O Solid-State MAS NMR	164
Chapter 7 Conclusions	167
References	175
Appendices.....	185

List of Figures

Figure 1.1: The Unit cell of ceria CeO_2 and CeO_{2-x}	2
Figure 1.2: The Frenkel Interstitial.	4
Figure 1.3: The maximum-efficiency window of the TWC.	6
Figure 1.4: Ceria morphologies.....	10
Figure 1.5: H_2 reduction of ceria	13
Figure 2.1: Vectorial diagram of the Effective Field	21
Figure 2.2: The Euler angles	23
Figure 2.3: Energy level diagram for $I=3/2$ nucleus	28
Figure 2.4 The loss of transverse and longitudinal magnetisation	32
Figure 2.5: Magic angle spinning (MAS)..	33
Figure 2.6: The Legendre polynomials.....	36
Figure 2.7: A single-pulse sequence.....	37
Figure 2.8: A solid echo pulse sequence.....	37
Figure 3.1: ^{17}O MAS NMR spectra of ceria and lanthana doped ceria	46
Figure 3.2: ^{89}Y and ^{17}O MAS NMR spectra of YDC	48
Figure 3.3: ^{17}O MAS NMR spectra of YDC	49
Figure 3.4: ^{17}O MAS NMR spectra of LDC.	51
Figure 3.5: ^{17}O MAS NMR spectrum of CeO_2/NaX	52
Figure 3.6: ^{17}O solid-state MAS NMR spectra of nanoceria	53
Figure 3.7: EM and ^{17}O MAS NMR spectra of ceria nanorods.....	55
Figure 3.8: ^{17}O MAS NMR spectra of bulk and nano ceria, before and after reduction and oxidation.....	56
Figure 3.9: ^{17}O MAS NMR spectra of doped and pure CeO_2	57
Figure 3.10: ^{17}O MAS DNP NMR of ^{17}O enriched CeO_2 nanoparticles	58
Figure 3.11: ^{17}O MAS NMR spectra of ^{17}O enriched CeO_2 nanorods.....	60
Figure 3.12: ^{17}O MAS NMR spectra of ^{17}O enriched LDCs.	61
Figure 4.1: ^{17}O enrichment methods using $^{17}\text{O}_2$	67
Figure 5.1: XRD Patterns of (a) H_2^{17}O Ceria and (b) H_2^{17}O Ceria 500 °C.	74
Figure 5.2: Raman spectra of H_2^{17}O Ceria and H_2^{17}O Ceria 500 °C.....	75

Figure 5.3: Raman spectra of the O-H region of H_2^{17}O Ceria & H_2^{17}O Ceria 500 °C..	77
Figure 5.4: ^{17}O MAS NMR SP spectra of H_2^{17}O Ceria and H_2^{17}O Ceria 500 °C..	79
Figure 5.5: Raman spectrum of HSA20 (as-prepared).	82
Figure 5.6: Raman and ^{17}O MAS NMR spectra of HSA20-600Ex	84
Figure 5.7: TPR- H_2 of HSA20 to 975°C.	86
Figure 5.8: In situ Raman spectra HSA20	87
Figure 5.9: Raman spectra HSA20 (between 50 and 1600 cm^{-1})	89
Figure 5.10: Raman spectra of HSA20 (between 2800 and 3900 cm^{-1})	90
Figure 5.11: ^{17}O MAS rotor synchronised Hahn echo NMR spectra of HSA20	92
Figure 5.12: T_1 editing of HSA20-700/300-Redox:	94
Figure 5.13: Deconvolutions of HSA20 ^{17}O NMR Spectra	95
Figure 5.14: Raman spectra between 50 and 1600 cm^{-1} of HSA20.	97
Figure 5.15: ^{17}O MAS single pulse spectra of HSA20.	98
Figure 5.16: A diagrammatic description of surface reorganisation.	100
Figure 5.17: ^{17}O spectra of HSA20-700/300-Redox from Sections 5.3 and 5.4.	101
Figure 5.18: Deconvolution of HSA20-700/300-Redox.	102
Figure 5.19: Hahn-echo spectra of HSA20: Sample Evolution	103
Figure 5.20: ^{17}O MAS NMR spectral changes of HSA20 after air exposure	104
Figure 5.21: Spectra of HSA20_700-300_Redox at 14.1, 11.7 and 9.4 T	105
Figure 5.22: Raman spectra between 50 and 1600 cm^{-1} of 25 nm ceria	107
Figure 5.23: ^{17}O MAS spectra of 25 nm ceria	109
Figure 5.24: ^{17}O MAS NMR spectra of 25 nm ceria after heating in air	110
Figure 5.25: Deconvolutions of 25 nm ceria after heating in air	112
Figure 5.26: Raman spectra between 50 and 1600 cm^{-1} of cubes and rods.	113
Figure 5.28: ^{17}O single pulse spectra of cubes and rods.	115
Figure 5.29: T_1 fits of cubes and rods	117
Figure 5.30: ^{17}O MAS NMR and Raman spectra of ^{17}O peroxo-ceria	120
Figure 5.31: Frenkel defect in a 3x3x3 cell and $\delta_{\text{iso}} = -(\sigma_{\text{iso}} - \sigma_{\text{ref}})$ calibration curve for ^{17}O calculated shifts	124
Figure 5.32: Simpson simulations of the DFT-calculated ^{17}O parameters of the Frenkel defect	126
Figure 5.33: DFT calculated ^{17}O NMR spectrum of $\text{Ce}_{108}\text{O}_{216}$ compared to	

experimental data.....	128
Figure 5.34: Magnetic (M vs H) measurement of HSA20-700/300-Redox.....	130
Figure 5.35: VT ^{17}O MAS NMR data of HSA20-500/300-Redox.....	132
Figure 5.36: Theoretical ^{17}O chemical shifts calculated from ceria unit cells having undergone lattice expansion due to increases in temperature.....	133
Figure 6.1: TPR- H_2 of HSA20-1%Pd to 900°C.....	137
Figure 6.2: Raman spectra of HSA20-1%Pd, Cubes-1%Pd and Rods-1%Pd.....	139
Figure 6.3: ^{17}O MAS single pulse spectra HSA20-1%Pd.....	144
Figure 6.4: ^{17}O MAS single pulse spectra of Cubes-1%Pd.....	145
Figure 6.5: ^{17}O MAS single pulse spectra of Rods-1%Pd.....	147
Figure 6.6: ^{17}O MAS NMR spectra of the bare ceria supports and Pd loaded systems.....	148
Figure 6.7: TPR- H_2 of $\text{Ce}_{0.75}\text{O}_{0.25}\text{O}_2$, $\text{Ce}_{0.5}\text{O}_{0.2}\text{O}_2$ and $\text{Ce}_{0.25}\text{O}_{0.75}\text{O}_2$ to 975°C.....	150
Figure 6.8: Raman spectra of as-prepared $\text{Ce}_{0.75}\text{Zr}_{0.25}\text{O}_2$, $\text{Ce}_{0.5}\text{Zr}_{0.5}\text{O}_2$ and $\text{Ce}_{0.25}\text{Zr}_{0.75}\text{O}_2$	151
Figure 6.9: Raman spectra of $\text{Ce}_{0.75}\text{Zr}_{0.25}\text{O}_2$ -600Ex and $\text{Ce}_{0.5}\text{Zr}_{0.5}\text{O}_2$ -600Ex.....	153
Figure 6.10: ^{17}O MAS Hahn-echo spectra $\text{Ce}_{0.75}\text{Zr}_{0.25}\text{O}_2$ -600Ex and $\text{Ce}_{0.5}\text{Zr}_{0.5}\text{O}_2$ -600Ex.....	155
Figure 6.11: Raman spectra of $\text{Ce}_{0.75}\text{Zr}_{0.25}\text{O}_2$ -700/300-Redox, $\text{Ce}_{0.5}\text{Zr}_{0.5}\text{O}_2$ -700/300-Redox, $\text{Ce}_{0.25}\text{Zr}_{0.75}\text{O}_2$ -700/300-Redox and $\text{Ce}_{0.75}\text{Zr}_{0.25}\text{O}_2$ -700/150-Redox.....	157
Figure 6.12: Difference spectra of $\text{Ce}_{0.75}\text{Zr}_{0.25}\text{O}_2$ -700/300-Redox, $\text{Ce}_{0.75}\text{Zr}_{0.25}\text{O}_2$ -700/150-Redox and $\text{Ce}_{0.75}\text{Zr}_{0.25}\text{O}_2$ -600Ex.....	159
Figure 6.13: ^{17}O MAS NMR of $\text{Ce}_{0.75}\text{Zr}_{0.25}\text{O}_2$ -700/300-Redox, $\text{Ce}_{0.5}\text{Zr}_{0.5}\text{O}_2$ -700/300-Redox and $\text{Ce}_{0.25}\text{Zr}_{0.75}\text{O}_2$ -700/300-Redox.....	160
Figure 6.14: Raman spectra of $\text{Ce}_{0.5}\text{Zr}_{0.5}\text{O}_2$ -1%Pd, $\text{Ce}_{0.5}\text{Zr}_{0.5}\text{O}_2$ -1%Pd-600Ex, $\text{Ce}_{0.5}\text{Zr}_{0.5}\text{O}_2$ -1%Pd -700/300-Redox.....	162
Figure 6.15: ^{17}O MAS NMR spectra of $\text{Ce}_{0.5}\text{Zr}_{0.5}\text{O}_2$ -1%Pd-600Ex and the unloaded material: $\text{Ce}_{0.5}\text{Zr}_{0.5}\text{O}_2$ -600E.....	163
Figure 6.16: ^{17}O MAS NMR of $\text{Ce}_{0.5}\text{Zr}_{0.5}\text{O}_2$ 1%Pd-700/300-Redox.....	165

List of Tables

Table 5.1: Parameters extracted from Raman data presented in Figure 5.2.	76
Table 5.2: Summary of previously acquired characterisations of HSA20.	81
Table 5.3: Parameters extracted from Raman data presented in Figure 5.29.	121

Acknowledgements

I would like to thank my academic supervisor Dr John Hanna of the University of Warwick, and my industrial supervisor, Dr David Thompsett at Johnson Matthey, for giving me the opportunity of embarking on this work, just 4 years ago. I am grateful to Johnson Matthey and to the iMR CDT for both the funding and the facilities/ materials that were so necessary to get me to this point in my career.

This work would not have been possible without three key persons: Janet Fisher who expertly prepared in-house synthesized samples, Loredana Mantarosie whose ingenuity facilitated the key $^{17}\text{O}_2$ experiments, and Stephen Day, whose DFT handy-work contributed to the key conclusions presented, all deserve a special thank you, so thank you! Many other JM employees helped me along the way, including Chris Brown, Markus Knaebbeler-Buss, the NMR guys who were so generous with their spectrometer time, and Amy Kolpin for her enthusiasm when discussing my results. I would like to acknowledge all members of the NMR group at Warwick who I now consider my lifelong friends, many of whom assisted me at some point, especially Sam Page for his assistance in acquiring (very last minute) magnetic measurements. Thanks to Steven Hubbard for offering and providing the SAXS measurements and to Edman Tsang for providing the essential rods and cubes specimens.

I am very grateful to my sister Denise Vlachou for her patience in proof reading most of this thesis, my parents for always providing a welcome reprieve from the slog, and to Helen Vlachou (who would sulk if she didn't get a mention) for providing comedy when needed.

Finally and not the least, an exceptional, second acknowledgement to Stephen Day for his meticulous care of my work as well as my emotional state in the writing of this thesis, and ultimately his guidance at the end. Without him, this work and thesis would not have reached its full potential.

Declarations

The experimental work contained in this thesis is original research carried out by myself at the University of Warwick between October 2013 and September 2017 in support of my application for the degree of Doctor of Philosophy. It has not been submitted in any previous application for any other degree. Janet Fisher (of JMTC) acquired the TPR measurements, and sample preparations (where detailed) were conducted by her. SAXS measurements were attained by Steven Hubbard at the University of Warwick. DFT calculations were conducted by Stephen Day.

Results from other authors have been referenced in the text in the usual manner.

Abstract

Ceria is a highly commercial, valuable material. Its diverse set of real-world applications demonstrates its far-reaching influence on modern society. Indeed, one only has to consider its extensive employment as an essential component of automotive, three-way catalysis (TWC) for reducing pollutants in vehicular exhaust gases; a technology that is used on a daily basis by millions of people, to appreciate its importance.

Its popularity is partially due to its extraordinary oxygen storage capacity, i.e. its ability to release and store oxygen through redox reactions mediated by the two oxidation states of cerium ($\text{Ce}^{3+}/\text{Ce}^{4+}$). This unique ability can be heavily influenced by ceria's particle size and shape, dopant concentration and surface chemistry, and is still a very active area of research today. Whilst there have been over 26,000 scientific publications on ceria since the 1950s, and although the bulk-ceria oxygen chemical shift (877 ppm) was first observed with ^{17}O solid-state NMR in 1989, it is only within the past decade that solid-state NMR has been employed as a probe for ceria's structure-function relationships.

This study presents an extensive ^{17}O solid-state NMR investigation into various ceria systems, in conjunction with complementary Raman spectroscopy (for which the literature is abundant). An alternative spectral assignment for the ^{17}O NMR spectrum of nanoceria based on experimental deductions and DFT quantum mechanical calculations is proposed. The current working assignment for nanoceria is based on the work of Wang *et al.*, where DFT calculations of a core-shell model are used to deconvolute the NMR data. In contrast to this model, it is suggested that the most upfield peak at $\delta_{\text{CG}} = 822$ ppm (that is actually part of a multicomponent region centred at ~ 830 ppm), corresponds to oxygen species displaced from their standard sublattice positions, to occupy a Frenkel type defect site. The resonance regions observed at ~ 830 and 920 ppm are proposed to be bulk oxygen environments feeling the effects of the Frenkel defect and concomitant oxygen vacancy. For reduced ceria systems, a broad component is detected that spans > 1000 ppm, and is assigned to oxygen directly bonded to Ce^{3+} , in agreement with the current working model. Finally, it is observed that the most deshielded peak at ~ 1030 ppm is multi-component and (one of these components)

possesses an extensive spinning sideband manifold in comparison to the other ^{17}O resonances. Variable temperature investigations show a small inverse temperature dependence of the peak positions, suggesting weak pseudocontact paramagnetic shifts are influencing the spectrum. In light of this, the peak at ~ 1030 ppm is assigned to oxygen in closer proximity to (but not directly bonded) to Ce^{3+} , as is reported by current ^{27}Al solid-state NMR studies of Ce^{3+} doped systems and as is reflected by the extensive sideband manifold.

The novel ^{17}O preparation treatments implemented in this work were engineered to probe oxygen environments near defects. Ceria's defects are manipulated by exposure to certain temperature/atmospheric conditions, and when these replicate those of possible catalyst operating temperatures with ^{17}O enriched gas, ^{17}O is able to probe the distribution of oxygen in distinct sites that are important to the OSC process. A prereduction of ceria was therefore implemented, following $^{17}\text{O}_2$ reoxidation to target these sites. This process was also able to identify a surface reorganization mechanism in which a low reoxidation temperature/pressure of $^{17}\text{O}_2$ is insufficient to reverse the onset of bulk oxygen diffusion induced by the reduction, an effect which is seen to be enhanced with the loading of Pd. Furthermore, the storage of these treated systems dictates the evolution of the ^{17}O species, with an almost closed-system (to air) detecting the pathway of reoxidised oxygen species to more stable sites over time.

Ceria zirconia systems are also investigated in this work. The ^{17}O solid-state NMR spectra show an even greater sensitivity to the $^{17}\text{O}_2$ enrichment conditions. The pre-reduction of the systems induces a greater oxygen removal compared to pure ceria, and thus an increase in Ce^{3+} paramagnetic centres, i.e. the broad component (> 1000 ppm) characterising the oxygen- Ce^{3+} bond reveals a greater relative intensity. The complication of increasing Ce^{3+} paramagnetic centres near the ^{17}O adsorption sites is evidenced by the significant loss in ^{17}O spectral resolution. These effects are exacerbated when ceria zirconia is supported with Pd, known to (stably) reduce the state of the system even further. A straight exchange of the ^{17}O isotope in ceria zirconia helps to inhibit these effects, allowing observation of (1) the chemical shift of the bulk-ceria oxygen move to a more shielded position compared to the pure ceria material at 877 ppm (caused by the inherent contraction of the ceria zirconia lattice), and (2) a broad resonance at ~ 730 ppm, attributed to oxygen species bridging cerium and zirconium.

Abbreviations

BMS	Bulk Magnetic Susceptibility
CASTEP	Cambridge Serial Total Energy Package
CN	Coordination Number
CSA	Chemical Shift Anisotropy
CT	Central Transition
DFT	Density Functional Theory
DNP	Dynamic Nuclear Polarisation
DOF	Degrees of Freedom
DOR	Double Rotation
EFG	Electric Field Gradient
EM	Electromagnetic
EPR	Electron Paramagnetic Resonance
FC	Fermi Contact
FID	Free Induction Decay
FT	Fourier Transform
GIPAW	Gauge Including Projector Augmented Waves
IR	Infrared
LDC	Lanthanum Doped Ceria
MAS	Magic Angle Spinning
NMR	Nuclear Magnetic Resonance
NP	Nanoparticle
OSC	Oxygen Storage Capacity
PAS	Principle Axis System
PDF	Pair Distribution Function
PGM	Platinum Group Metal
ppm	Parts Per Million
PCS	Pseudo Contact Shift
PXRD	Powder X-ray Diffraction
QM	Quantum Mechanics value

RF	Radio Frequency
RTFM	Room Temperature Ferromagnetism
SAXS	Small Angle X-ray Scattering
SMSI	Strong Metal Support Interaction
ST	Satellite Transition
SQUID	Superconducting Quantum Interference Device
TEM	Transmission Electron Microscopy
TPD	Temperature Programmed Desorption
TPR	Temperature Programmed Reduction
TWC	Three Way Catalyst
VASP	Vienna AB Initio Simulation Package
WGS	Water-Gas Shift
XPS	X-ray photoelectron spectroscopy
XRD	X-ray Diffraction
YDC	Yttrium Doped Ceria

Chapter 1

An Introduction to Ceria

From the era in which it became clear that the treatment of vehicular exhaust gases was of paramount importance to the environment and public health, ceria has been regarded as an industrially critical material. On a truly worldwide scale, ceria's use is in automotive or three way catalysis, and has been since the 1970s.¹ It has a long-standing reputation of possessing remarkable, unique oxygen storage and release properties that brand it as invaluable for countless industrially-relevant applications. Ceria has been heavily investigated for other uses, including hydrogen production,² solid oxide fuel cells,³ solar cells,⁴ and gas sensors.⁵ Nevertheless, there still exists voids in the understanding of ceria's function, from both physical and chemical standpoints, in addition to many contradictory studies concerning its properties. This is somewhat evidenced by the vast number of ceria publications (26,000), released between 1950 and 2015,⁶ the number of which rises year on year. However, these figures can also be credited with an ever-increasing realisation of novel medical applications, some of which include a form of non-toxic, synergistic anti-cancer drug delivery,⁷ an antibacterial coating mixed with silver nanoparticles for implant devices intended to prevent associated infections,⁷ and the detection of breast cancer cells via a peroxidase-like activity⁸. Ceria's potential and efficacy are boundless and, as a result it appears to be perpetually in the research limelight.

Regardless of the vast wealth of analytical and physical characterisation data collected on ceria, there exists very limited literature on the use of solid-state Nuclear Magnetic Resonance (NMR) as a characterisation probe, the reasons for which are elaborated in Chapter 4. Accordingly, a literature review of the existing studies is

presented in Chapter 3, in order to afford the reader a platform to the experimental data presented in Chapters 5 and 6. *Catalysis by Ceria and Related Materials Edn. 1* was published in 2002, whilst the 2nd edition was published in 2013. Arguably, these books have consolidated some of the most prominent ceria findings from spectroscopy and microscopy in recent years. However, NMR studies do not really feature - they are a product of this decade and are therefore an active and exciting investigative area of ceria research. Chapters 5 and 6 of this thesis are largely dedicated to using ^{17}O NMR to probe ceria systems. Whilst Raman spectroscopy was initially implemented as a control technique (for its strong presence in the ceria literature as a characterisation technique), the data transpired to elucidate significant insight into the investigated systems and contribute unique observations to this spectroscopic area also.

1.1 Structure of Ceria

Ceria's use in these applications stems from cerium's position in the periodic table; it is the first of the lanthanides to acquire 4f electrons (electron shell configuration of $[\text{Xe}] 4f^1 5d^1 6s^2$), with the redox capability to adopt both the Ce^{4+} and Ce^{3+} oxidation states. Under oxidative conditions, cerium forms a range of possible oxides between the extremes of CeO_2 ; where cerium is in its Ce^{4+} oxidation state only, and Ce_2O_3 ; cerium is in its Ce^{3+} oxidation state only. Stoichiometric cerium dioxide (CeO_2), annealed at high temperature and high oxygen partial pressure, adopts the open cubic fluorite structure with space group $Fm3m$ (analogous to its namesake CaF_2) as shown in Figure 1.1. The cerium cations in a +4 oxidation state form a face-centred cubic (fcc) network, the oxygen anions occupy the resulting tetrahedral holes, and the larger octahedral sites (the centre of the unit cell) are empty. Each oxygen is

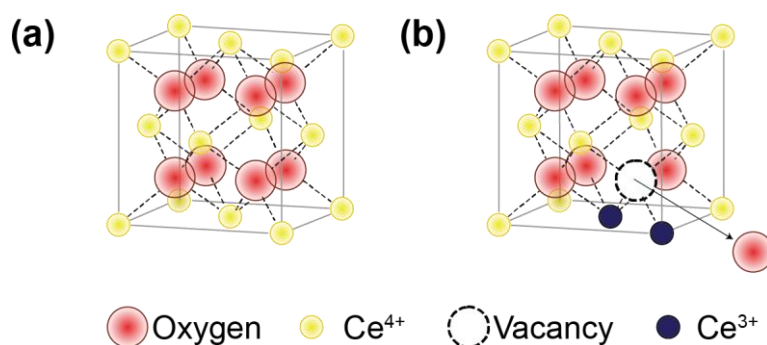
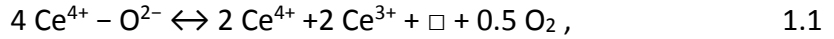


Figure 1.1: Unit cell of ceria (a) CeO_2 and (b) CeO_{2-x}

coordinated to four cerium and each cerium coordinated to eight oxygen. The lattice parameter at room temperature, a , is 5.411 Å in this case. Ceria's extraordinary attributes reveal themselves under reducing conditions, i.e. oxygen deficient/increased temperature. As a result of cerium's ability to change its oxidation state from Ce^{4+} to Ce^{3+} , oxygen can be released from the structure, seen in Figure 1.1 (b). Indeed, this reversible ability to store and release oxygen defines ceria's most powerful property of oxygen storage capacity (OSC). Incredibly, the ceria lattice can release oxygen; becoming highly disordered, whilst maintaining its open $Fm3m$ structure (essential to the reversibility of the process), up to a maximum deficiency of $\text{CeO}_{1.714}$.⁹ The release of an O^{2-} anion creates a vacancy (\square) in the lattice via:



where the two electrons from the oxygen anion are transferred to two of the cerium cations nearest the vacant site, reducing them to the +3 state. As the ionic radius of Ce^{3+} (1.14 Å) is larger than that of Ce^{4+} (0.97 Å), there is an associated lattice parameter increase with the reduction. A full conversion of Ce^{4+} to Ce^{3+} results in the sesquioxide Ce_2O_3 and a change in structure to the hexagonal $P\bar{3}m1$ structure, but this takes place under extreme reduction conditions (≈ 1273 K). In the intermediate region between $\text{CeO}_{1.714}$ and Ce_2O_3 , the lattice retains a close-to-fcc structure, with Ce deviating slightly from the fcc-like sites.⁹

1.1.1. Defects

It is the defects in ceria that give rise to its impressive properties. Defects are defined by anything that perturbs the perfect, stoichiometric, $Fm3m$ arrangement, which includes Ce^{3+} cations, vacancies and point defects. Many synthesis routes of ceria focus on engineering defects into its structure. *Extrinsic* defects can be promoted through doping of the ceria structure with cations such as Zr^{4+} (a case which shall be discussed in Section 1.6), where the goal of the dopant is to stabilise the presence of Ce^{3+} cations, and/or introduce more vacancies. In addition to the removal of oxygen under reducing conditions (charge balanced by the creation of vacancies and Ce^{3+} cations) as described by Equation 1.1, *intrinsic* defects can be induced via tailoring

the preparation conditions of ceria. Many studies show a defect concentration dependence on crystallite size^{10,11} and the last decade has seen strong evidence for the existence of Frenkel-type point defects in ceria.¹²⁻¹⁷

There are innumerable studies that show how effective two of these three defect types are to enhancing ceria's properties. For example, Ce^{3+} cations on a 5 nm ceria surface have been shown to bond with molecular O_2 , forming $\text{Ce}^{4+}\text{-O}_2^-$ superoxide species, greatly enhancing the amount of oxygen that can be stored on the surface.¹⁸ In the case of vacancies, it has been shown that their nature and formation control ceria's reducibility as they define the rate controlling step of oxygen diffusion.¹⁹ Microscopy studies reveal that surface vacancies exist as three different structures: single vacancies, linear clusters and tri-clusters.^{19,20} It is important to note that oxygen vacancies and Ce^{3+} centres are found to be more stable at ceria's surface/subsurface.^{21,22}

Unlike the presence of vacancies and Ce^{3+} cations, investigations and evidence of Frenkel-type point defects in ceria are relatively unexplored and so Chapter 3, in addition to reviewing current ^{17}O NMR studies of ceria, is dedicated to a review of the existing literature. Frenkel defects are interstitial oxygen ions that are located in the ordinarily vacant octahedral sites, balanced by a vacancy in the usual tetrahedral position of the sublattice, shown in Figure 1.2. They are thought to significantly contribute to ceria's OSC, a consequence of enhanced mobility as compared to the oxygen in the tetrahedral sites, and/or by maintaining vacancies in the sublattice. High temperature treatments are thought to irreversibly deactivate

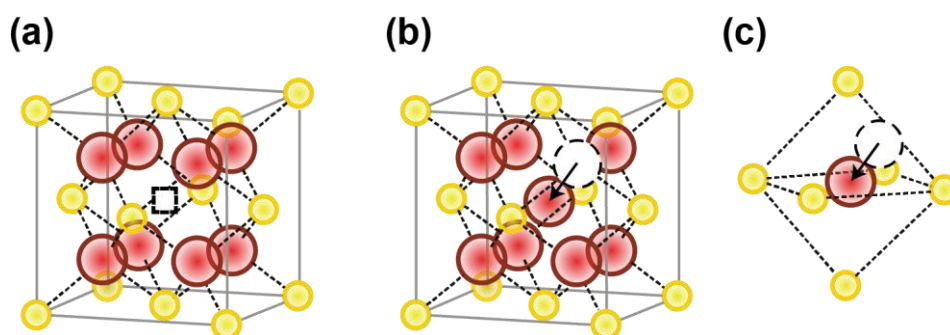
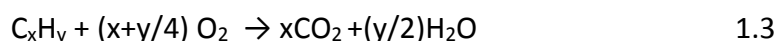


Figure 1.2: The Frenkel interstitial. (a) Unit cell of ceria depicting the vacant octahedral site. (b) The octahedral site is occupied, balanced by a vacancy in the sub lattice. (c) The Frenkel defect is coordinated by 6 cerium cations.

these defects by providing sufficient energy to escape the potential of the octahedral site, annihilating the tetrahedral vacancy in the sublattice. As the structure becomes less disordered, i.e. the cubic structure becomes more rigid, the lattice oxygen are effectively locked into place. Therefore when ceria is exposed to elevated temperatures, in addition to a loss of surface area, the deactivation of Frenkel-type defects is also considered to be a causative factor in the loss of ceria's OSC. Further to this, defects are known to be more stable towards the surface of the ceria particle,²¹ and so a loss in surface area (caused by sintering) decreases the defect concentration.

1.2 Ceria in Autocatalysis

Autocatalysis is a form of heterogeneous catalysis in which a solid catalyst, in contact with the gas phase exhaust, removes undesirable combustion products. More specifically, a petrol engine relies on a three way catalyst (TWC) to simultaneously convert the harmful emissions of carbon monoxide (CO), hydrocarbons (HCs) and nitrous oxides (NO_x) into carbon dioxide (CO₂), water (H₂O) and nitrogen gas (N₂), via:



A small-particulate ceria formulation in the form of a washcoat, also typically composed of high surface area γ -Al₂O₃, is coated onto a ceramic, honeycomb, cordierite monolith, which has long parallel channels for the exhaust gas to travel through, with nanoparticles of platinum group metal (PGM), e.g. Pt, Rh, and Pd, dispersed throughout. γ -alumina has also been an instrumental component of TWCs and has a history that runs parallel to that of ceria in this application. In fact, one could say that it shows a synergistic relationship with ceria in this case, where ceria inhibits a phase change of γ -alumina at high catalyst operating temperatures created by the engine exhaust gases, whilst the high surface area of γ -alumina enhances ceria's dispersion. Ceria's purpose is several fold: it increases the surface area (thus promoting the precious metal dispersion), it increases the thermal stability of the

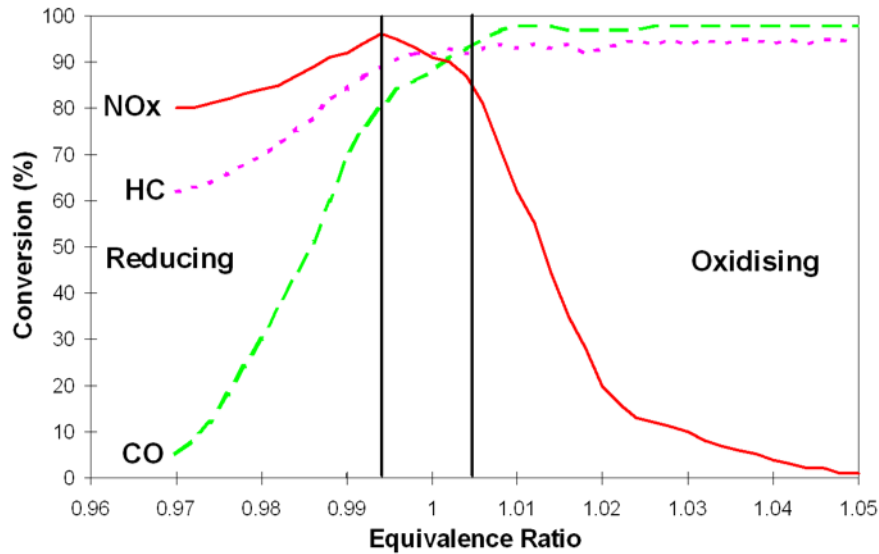


Figure 1.3: The maximum-efficiency window of the TWC. Image provided by Amy Kolpin, Johnson Matthey.

catalyst (by inhibiting PGM sintering and a phase change of $\gamma\text{-Al}_2\text{O}_3$ to the lower surface area polymorph $\alpha\text{-Al}_2\text{O}_3$), it acts as a direct platform for the water-gas shift (WGS) reaction: $\text{CO} + \text{H}_2\text{O} \rightarrow \text{CO}_2 + \text{H}_2$, and most importantly, ceria's primary objective is to control the amount of oxygen in the exhaust via the reaction:



The reason for this can be deduced by evaluating Equations 1.2 - 1.4. The CO and HC conversions require oxidation reactions whilst the NO_x conversion requires reduction, i.e. these are contrary tasks. However, provided that the oxygen partial pressure is kept within a specific window as shown in Figure 1.3, via Equation 1.5, then the quantities of reducing gases (CO and HCs) and oxidising gases (O_2 and NO_x) are equal and conversions maintain maximum efficiency. Ceria does this by releasing oxygen in oxygen-lean conditions (creating vacancies) and adsorbs excess oxygen in oxygen-rich conditions (filling vacancies), and it does so whilst retaining the fluorite structure.

Temperature programmed reduction (TPR) studies conducted over the years have ascertained a reducibility-dependence on ceria's surface area.²³⁻²⁵ Due to the ease with which pure ceria thermally ages, and given that the exhaust gas temperatures are capable of exceeding 1100°C ,²⁶ the ceria support formulation has

had to evolve to prevent ceria from sintering under functioning conditions. Sintering of ceria nanoparticles results in the significant decrease of pollutant gas conversions and an increase in the light-off temperature (conversion initiation temperatures). In 1987, a ceria support was shown to become thermally stable at TWC operating temperatures by doping zirconium into ceria's $Fm3m$ structure, forming a so-called ceria zirconia solid solution.²⁷ Interestingly, the support also revealed an enhanced reduction, and thus a greater OSC. At the time of writing, there has been no alternative doped ceria material with comparative complementary properties at an industrially reasonable cost, and therefore ceria zirconia supports are still implemented in all current TWCs.

1.3 Ceria Supported Precious Metal Catalysts

When a PGM is supported onto the ceria surface, it can promote the reduction of ceria's surface oxygen species (but not the bulk oxygen species), as evidenced by an immense amount of TPR-based studies.^{1,23,24,28-31} For example, Kaspar *et al.* revealed a decrease in the temperature required to remove surface oxygen of CeO_2 (from 497 °C to 227 °C) when supported with rhodium, which is the same temperature at which rhodium oxide itself is reduced.³⁰ Originally, this behaviour was rationalised by the H_2 spillover model, which postulates that under H_2 reducing conditions, the PGM adsorbs H_2 and the molecule disassociates into H. Highly mobile H then spills over to the ceria surface, reducing it by removing an O from the surface in the form of H_2O . More recently however, Collier *et al.*³² have rationalised this behaviour as an electronic interaction between the metal and ceria surface; a form of the so-called strong metal support interaction (SMSI). The SMSI was first observed by Tauster *et al.* on TiO_2 in 1977,^{33,34} and whereas TiO_2 is seen to (reversibly) completely deactivate a PGM catalyst at high temperatures, the ceria-PGM interaction shows the reverse effect of enhancing the PGM catalyst activity. An electronic perturbation in which charge is transferred from the PGM particle through the interface to the ceria surface is considered responsible.

The SMSI mechanism is well described by Bruix *et al.* via spin polarised density functional theory (DFT) calculations of an eight atom Pt nanoparticle (Pt_8) on CeO_2 , in which they conclude that the Pt_8 particle spontaneously reduces the CeO_2

substrate. They deduce that oxygen spillage can occur from the ceria surface to the Pt_8 particle, oxidising it. The resulting vacancy on the ceria surface is concomitantly charge balanced by two localised electrons (polarons) on the cerium cations, reducing them to Ce^{3+} . They additionally investigate how the Pt_8 particle influences the vacancy formation energy on the ceria surface compared to a clean ceria surface. They predict that the reverse spillover of oxygen from the ceria surface to the Pt particle expends 1.25 eV less energy than oxygen removal straight from the clean ceria surface, which further oxidises the Pt particle.³⁵ This form of prereduction of ceria by Pt is strongly evidenced by experimental observations by Thompsett & Tsang,³⁶ in which a catalyst with Pt particles totally encapsulated by a ceria substrate, i.e. there is no surface Pt available for surface catalysis, is tested via the WGS reaction against conventional ceria-supported Pt catalysts. In fact, better activity was observed for the encapsulated Pt catalysts, suggesting that the prereduction of ceria is more effective than exposed Pt sites in this case of catalysis.³⁶

As palladium is widely used in autocatalysis, experimental work in Chapter 6 shall investigate Pd on ceria and ceria/zirconia systems. Depending on preparation of Pd-ceria systems, the nature of this Pd-ceria interaction can lead to the formation of solid solutions, i.e. Pd^{2+} cations are substituted for Ce^{4+} cations in the ceria lattice, but in a square planar formation,³⁷ or a surface ionic Ce-O-Pd layer is established. Whilst the formation of Ce-O-Pd bonding has revealed high dispersion of Pd oxide, it is highly unstable at elevated temperatures as Pd is prone to sintering, forming larger Pd metal particles. Pd metal is oxidised at 300 °C³⁸ and after which, it demonstrates a relative decrease in activity.³⁹

1.4 Nanoscale Effects

Synthesizing ceria nanoparticles is highly desirable because increased surface area allows both an increase in the contact area between a support and a PGM catalyst (as discussed in Sections 1.2 and 1.3), and an increase in the amount of reactive, exposed edges/corners/steps. However, its benefits are not solely related to surface area, in fact an electronic effect exists. Consequently, as the particle size decreases, ceria becomes easier to reduce at lower temperatures. In other words, a greater percent of oxygen than just those on the surface can contribute to ceria's OSC for

smaller nanoparticles than it can for larger particles because the bulk oxygen becomes more active.³⁰ These observations are generally accepted in the ceria research community, but there are contradictions in the literature as to the structural, chemical and electronic modifications responsible.

As a structural example, it is well observed that the unit cell volume of ceria increases with decreasing particle size. Whilst some studies claim that the amount of Ce^{3+} increases as the particle size decreases (with the increase in the unit cell volume due to the accommodation of the larger Ce^{3+} cation and associated vacancies)⁴⁰⁻⁴⁴, more recent studies now attribute the unit cell expansion to surface strain effects compensating for the higher-energy nanoparticle surface,^{18,45,46} Furthermore, whilst some studies suggest that ceria nanoparticles are more reactive/have an increased OSC due to this relative increase in Ce^{3+} cations present on the surface, other investigations conclude that Ce^{3+} is not the origin of this increased reactivity. A study by Sun and Xue in which they use chemical bonding theory to calculate the thermodynamics of crystal growth, concludes that smaller ceria particles have an increased Ce/O ratio with cerium is in a +4 oxidation state (not +3) as the origin of the increased activity.⁴⁷

Experimentally, it has been observed that as the size of ceria nanoparticles decreases, the more non-stoichiometric or oxygen deficient they become; attributed to the increased stability of the vacancy at the surface.^{43,44,48} Moreover, DFT studies have established that there is a decrease in the vacancy formation energy^{49,50} with a decrease in particle size. Whilst the advantages of defective ceria were previously discussed in Section 1.1.1, it is also worthwhile noting the enhanced dispersion of the PGM metal whilst in contact with defective ceria.⁵¹

Certainly in the bulk, Ce^{3+} is considered as a Ce^{4+} cation with an electron localised on its usually empty 4f state. However at the surface, the electrons appear to behave differently. Firstly, there is both computational and experimental evidence that indicates that these electrons on the cerium ion can localise near the vacancy.²² Furthermore, electrons can become trapped in the otherwise 2+ vacancy, defined as an F centre. If the F centre has a +1 charge, then a local magnetic moment is generated in neighbouring atoms which order ferromagnetically,^{52,53} resulting in the observed room temperature ferromagnetism (RTFM) phenomenon.

1.5 Morphologies of Ceria

The previous discussions have outlined how varying the level of surface exposure, mainly in the case of heterogeneous catalysis, can critically alter ceria's chemistry. On the nanoscale, ceria adopts the three major low-index $\{111\}$, $\{110\}$, and $\{100\}$ surface planes, which due to their different atomic coordinations, impart different properties that can be desirable and selective to catalysis applications. According to the Wulff Construction Theorem that minimises the Gibbs free energy at the surface, these surfaces can be selectively made dominant by directing the growth of ceria crystals via the manipulation of the synthesis conditions, i.e. the morphology of ceria can be engineered to preferentially expose these facets. There are many different shapes that ceria has been shown capable of adopting, but of interest to this thesis are octahedrons which expose the $\{111\}$ plane, rods which terminate via the $\{110\}$, and $\{100\}$ planes, and cubes exposing the $\{100\}$ plane, as illustrated in Figure 1.4.

$\{100\}$, $\{110\}$, and $\{111\}$ facets can be classified according to Tasker's ionic model of three types of surfaces.⁵⁴ Type I contains stoichiometric planes of Ce and O; the $\{110\}$ adopts this charge neutral system. Type II alternates planes of Ce and O planes that are perpendicular to the surface, with the resulting charge counterbalanced by a O-Ce-O surface layer; the $\{111\}$ assumes this type. Type III consists of alternating planes of Ce and O that run parallel to the surface which is not charge neutral, and consequently generates a dipole moment. The $\{100\}$ is of this surface type, making it inherently unstable.⁵⁵ Oxygen and cerium form different bonding coordinations in the three surfaces; with CeO_7 and OCe_3 for the $\{111\}$, CeO_6 and OCe_3 for the $\{110\}$, and CeO_6 and OCe_2 for the $\{100\}$, defining their stability.

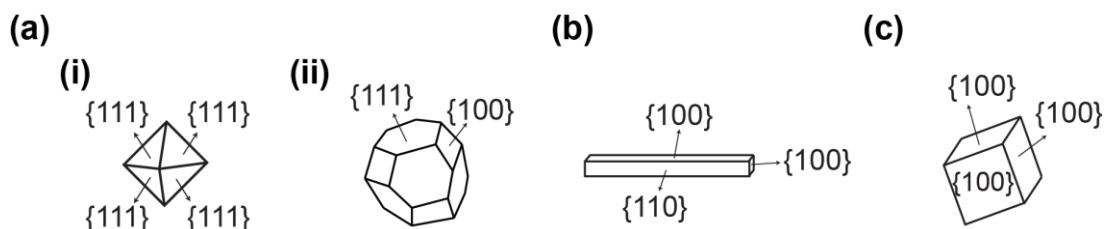


Figure 1.4: Different ceria morphologies. (a) (i) An octahedron exposing $\{111\}$, (ii) a truncated octahedron exposing $\{111\}$ and $\{100\}$, (b) rod exposing $\{110\}$ and $\{100\}$, and (c) cube exposing $\{100\}$.

Whilst the order of increased stability is firmly established as $\{111\} > \{110\} > \{100\}$, evident by experimental and computer simulation studies employing energy minimisation codes,^{21,56} there exists some incongruities in the literature as to the order of reactivity of these planes. For example, in 2005, Mai *et al.* hydrothermally prepared ceria nanopolyhedra (truncated octahedrons), nanorods and nanocubes, and tested the OSC of each morphology by catalysis of the CO oxidation reaction.⁵⁷ From their results of OSC per unit surface area, they surmised the order of reactivity as nanocubes > nanorods >> nanopolyhedra, and hence the reactivity of the planes as $\{100\} > \{110\} >> \{111\}$. They additionally concluded that the nanocubes and nanorods contributed bulk oxygen as well as surface oxygen to the OSC, whilst the nanopolyhedra only released surface oxygen. On the other hand, Lopez *et al.* reveal a greater catalytic activity for nanorods over nanocubes for the total oxidation of toluene,⁵⁸ which the author postulates is due to the increased concentration of defects that are more likely to form in the rod morphologies.⁵⁹ These studies emphasise that the catalytic reactivity is not simply determined by stability considerations of the oxygen atoms within the exposed facets; it is further complicated by its dependence on the desired catalytic process.

1.6 Ceria zirconia

The significance of ceria zirconia systems to three-way catalysis was discussed at the end of Section 1.2. In addition to improving thermal stability, the addition of zirconia was also seen to enhance the OSC in comparison to pure ceria, as has been thoroughly quantified by H₂-TPR and oxygen uptake experiments. Murota *et al.* were the first to publish such results, confirming that an enhanced bulk reducibility takes place at lower temperatures.⁴⁸ This was later suggested to be caused by an enhanced mobility in the bulk of ceria zirconia,^{60,61} allowing greater access and release of these species.

Undoped ZrO₂ adopts the monoclinic tetragonal *t* phase, which is a distorted fluorite-like *P2₁/c* structure with a Zr⁴⁺ coordination number (CN) of 7,⁶² whereas as already stated, CeO₂ has a cubic fluorite (*c*) arrangement (CN=8). When zirconia is mixed with ceria, a mixed phase system results, the form of which is dependent on the preparation conditions. A ceria zirconia solid solution is formed if Zr⁴⁺ cations

replace Ce^{4+} cations in the ceria cubic lattice, with phase separation into separate domains of ceria and zirconia taking place at high temperatures²⁶ ($>1000\text{ }^{\circ}\text{C}$). The ceria-zirconia phase diagram is highly complex, and so discussed here are descriptions relevant to this thesis. For a dopant level of $x < 15\%$ for $\text{Ce}_{1-x}\text{Zr}_x\text{O}_{2-y}$ (where y indicates the number of defects), the cubic fluorite phase is retained. For $15\% < x < 90\%$, two different temperature-dependent, tetragonal (space group $P4_2/nmc$) t'' and t' phases can result, with the t'' phase having the same cation lattice positions as the cubic phase and a thermal barrier existing between the two.⁶³ As the change in unit cell is only a displacement of oxygen anions along the c -axis, this phase is difficult to distinguish from XRD patterns, and is therefore considered pseudo-cubic and is grouped together with c , to form the c' phase.

To characterise such systems fully, a range of physical techniques are necessary. For example, due to the smaller tetravalent cation size (0.84 \AA for Zr^{4+} compared to 0.97 \AA for Ce^{4+}), the introduction of zirconium into the ceria lattice causes a decrease in lattice expansion to the cubic phase, which is observed by PXRD. Raman spectroscopy however allows phase distinction due to its sensitivity to oxygen displacement and medium range order.⁶⁴

Interestingly for nano ceria zirconia systems, this phase transformation picture is (preferably) different, with a dependence of the phase boundaries on particle size. For example, in a study by Zhang *et al.* in 2006 in which XRD and Raman spectroscopy characterised a range of ceria zirconia samples annealed at increasing temperatures, they reveal that the cubic phase can be maintained at higher zirconium content for lower annealing temperatures which consequently resulted in smaller particle sizes.⁶³ They furthermore show that the ideal zirconia composition that inhibits particle sintering is between 40% and 50% ZrO_2 on the nanoscale also reveals phase changes; below 30 nm, it begins to adopt the tetragonal $P4_2/nmc$ phase.

1.7 O₂-Ceria Interactions

As can be elucidated from previous discussions, probing oxygen-surface interactions and surface-bulk diffusion within ceria is key to understanding the OSC mechanism. In applications of heterogeneous catalysis, the exposed atoms of the ceria surface

promote the adsorption of gas molecules to reduce surface free energy. One such example is CO in a TWC where, after adsorption, oxygen from the ceria surface interacts with the CO molecule to form CO_2 , followed by the breaking of the surface bond, i.e. desorption of CO_2 to the gas phase.

The O_2 molecule is different; it has a lower bond strength of 500 kJ mol^{-1} (compared to CO at 1076 kJ mol^{-1}), which results in disassociation after adsorption. Under oxidative conditions following a reductive pretreatment (as seen in a TWC), disassociated oxygen atoms diffuse to vacancies present on the ceria surface, which is followed by diffusion to vacancies in the bulk.

1.7.1 O_2 Adsorption

Ceria surface-adsorption of O_2 however is not a simple process, in fact it is a highly complex area of research in its own right. When an O_2 molecule adsorbs to a vacancy for instance, it heals the vacancy, with the vacancy giving up its $2+$ charge to the O_2 molecule, forming peroxide (O_2^{2-}). Similarly, and as briefly mentioned in Section 1.1.1, O_2 can attach directly to a Ce^{3+} cation, which gives up its electron, thus changing its oxidation state to Ce^{4+} and forming superoxide (O_2^-). These species are shown in Figure 1.5 and are considered the intermediates of the reoxidation process, with their contributions to the process dependent on many factors such as treatment conditions, cation doping, PGM loading, and morphology.⁶⁵⁻⁶⁷ The reoxidation

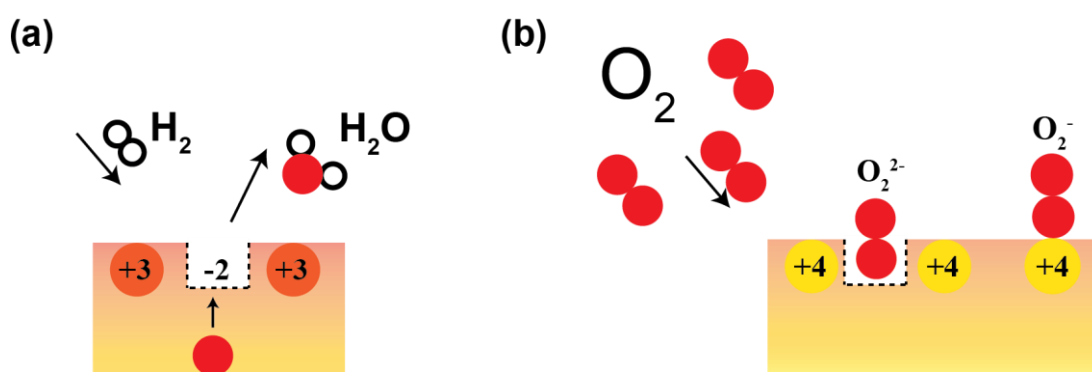
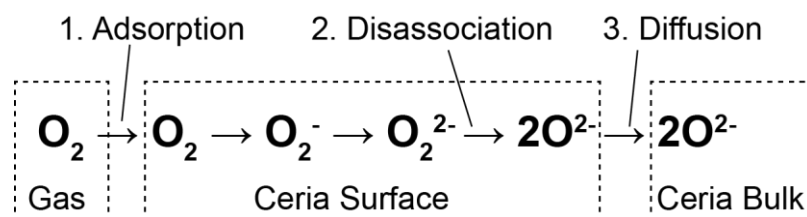


Figure 1.5: (a) The creation of vacancies by H_2 reduction, producing H_2O . (b) The reoxidation of the surface with O_2 via the formation of O_2^{2-} and O_2^- species.

process of ceria in general can be regarded as a transfer of electrons from the reduced ceria to the O_2 molecule, expressed as:



and can be simplified into the three steps of 1. O_2 adsorption, 2. O_2^{2-} disassociation and 3. O^{2-} diffusion.

Chapter 2

Theory and Methods

2.1 NMR Theory

Nuclear Magnetic Resonance (NMR) is a spectroscopic technique in which electromagnetic (EM) radiation is used to manipulate the intrinsic magnetic properties of matter to provide detailed structural information. More specifically, a static magnetic field is able to generate nuclear energy states that will interact with incident radio-frequency (RF) photons. If the RF waves are a commensurate frequency to these energy splittings, then there will be an absorption followed by an induced emission of an RF wave that can be used to generate an NMR spectrum.

2.1.1 Classical Description

NMR exploits the intrinsic, angular momentum property, nuclear spin $\|I\| = \sqrt{I(I+1)}\hbar$, where I is the spin quantum number that is quantised into half integer or integer values dependent on the nucleus. I determines the properties of the nuclear magnetic moment, μ , in addition to an intrinsic nuclear property known as the gyromagnetic ratio or γ ($\text{rad s}^{-1}\text{T}^{-1}$). An isolated nuclear spin, I_i is related to, μ_i , through the relation:

$$\mu_i = \gamma I_i . \quad 2.1$$

When placed inside a strong homogenous magnetic field B_0 , the random orientation of μ_i is altered such that they align with or against the field's directional axis. A bulk

magnetisation is generated along the field direction (as this has a slightly lower energy state) and so for an assembly of spins:

$$\mathbf{M} = \sum_i \boldsymbol{\mu}_i = \gamma \mathbf{I} . \quad 2.2$$

Placing a magnetic moment within a magnetic field induces a torque $\boldsymbol{\tau}$:

$$\boldsymbol{\tau} = \mathbf{M} \wedge \mathbf{B}_0 , \quad 2.3$$

which attempts to align \mathbf{M} with the field, resulting in a precessional motion at a characteristic frequency about the applied field. From Newton's 2nd law:

$$\boldsymbol{\tau} = \frac{d}{dt} \mathbf{I} . \quad 2.4$$

It can be seen from equating Equations 2.3 and 2.4, followed by the substitution of $\mathbf{I} = \mathbf{M}/\gamma$ from Equation 2.2, that the equation of motion for \mathbf{M} is:

$$\frac{d}{dt} \mathbf{M}(t) = \gamma \mathbf{M}(t) \wedge \mathbf{B}_0(t) . \quad 2.5$$

2.2 Quantum Mechanical Definitions

The vector model described so far is useful in comprehending the theory of a simple spin system, but NMR involves understanding how a complicated spin ensemble behaves. Quantum mechanics (QM) is the tool that allows the determination of physical observables on the scale of atomic systems.

2.2.1 Introduction

To define the state of a system at a particular time and position, QM uses the wavefunction:

$$\Psi = \sum_n c_n \psi_n , \quad 2.6$$

which is the sum of all eigenfunctions, ψ_n , with corresponding coefficients, c_n , and they form a complete basis set. As well as being orthogonal to one another, these basis states must be normalisable, or in other words it has to be possible to integrate the square modulus of the wavefunction, as this is equal to the probability density of finding the particle somewhere in space, i.e. unity. Combining these definitions is known as orthonormality and is expressed as:

$$\int \psi_n^* \psi_m d\tau = \delta_{nm}, \quad 2.7$$

where δ_{nm} is the Kronecker delta function, where for two variables n and m , if $n \neq m$, $\delta_{nm} = 0$ and if $n = m$, $\delta_{nm} = 1$. To calculate the value of a physical observable of a system, the wavefunction is acted upon by a linear operator corresponding to the observable. The operator of a system's total energy is called the Hamiltonian operator, \hat{H} . For a time-independent system, it acts upon an eigenfunction ψ to produce the time-independent Schrödinger equation:

$$\hat{H}\psi = E\psi, \quad 2.8$$

where E is the eigenvalue of the system and corresponds to the energy. If the couplings of the system vary with time, it is necessary to solve the time-dependent Schrödinger equation:

$$\hat{H}(t) \psi(t) = i\hbar \frac{\partial \psi(t)}{\partial t}. \quad 2.9$$

Dirac notation is frequently employed to simplify complex mathematical expressions in quantum mechanics. In the Dirac formalism the state of the system $|\psi\rangle$ is depicted in a way that easily enables the recovery of both wave and matrix representation, where $\langle\psi|$ is its complex conjugate, and they are known as ket and bra, respectively. The wavefunction described in Equation 2.6 is now represented as:

$$|\Psi\rangle = \sum_i c_i |\psi_i\rangle. \quad 2.10$$

The expectation value of an operator in this notation is expressed as:

$$\langle\hat{A}\rangle = \langle\psi|\hat{A}|\psi\rangle. \quad 2.11$$

2.2.2 Angular Momentum Operators

NMR is concerned with describing and manipulating nuclear spin states. In the mathematical formulation of QM, spin operators that act upon spin eigenfunctions to obtain spin eigenvalues define the NMR experiment. Before exploring these spin operators, it is important to define the commutation relation. Two physical observables are compatibly measured if they share the same set of eigenfunctions and for this to be the case, their corresponding operators must commute. In the case of spin angular momentum, the square of the magnitude of the total spin angular

momentum \hat{I}^2 and any one directional component, \hat{I}_z (by convention), commute. That is:

$$[\hat{I}^2, \hat{I}_z] = \hat{I}^2 \hat{I}_z - \hat{I}_z \hat{I}^2 = 0, \quad 2.12$$

and therefore they share eigenfunctions ψ_{lm} with eigenvalue equations of:

$$\hat{I}^2 |\psi_{lm}\rangle = I(I+1) |\psi_{lm}\rangle \quad \text{and} \quad \hat{I}_z |\psi_{lm}\rangle = m |\psi_{lm}\rangle, \quad 2.13$$

where m is the spin quantum number that takes values of $-l$ to $+l$ in integer steps, for a total of $2l+1$ states. Thus, for each nuclear spin there will $2l+1$ eigenfunctions for any of the angular momentum operators, demonstrating the quantisation of the total spin angular moment and its z-component. As convention dictates that the static, external magnetic field is usually applied along z-axis the eigenfunctions and eigenvalues of \hat{I}_z have a special significance that is elaborated on in the following section.

2.2.3 The Zeeman Effect

In analogy to Equation 2.1, the magnetic moment operator is given by:

$$\hat{\mu} = \gamma \hbar \hat{I}. \quad 2.14$$

The energy of a magnetic moment within a magnetic field is orientation dependent and can be represented by the Hamiltonian:

$$\hat{H} = -\hat{\mu} \cdot \mathbf{B}_0. \quad 2.15$$

For a magnetic field fixed along the z-axis, this simplifies to the Zeeman energy:

$$\hat{H}_Z = -\mu_z B_0 = -\gamma \hbar \hat{I}_z B_0, \quad 2.16$$

where the magnetic field lifts the degeneracy of the $2l+1$ spin states, splitting their energies. The energies of the possible spin states $E_{l,m}$ are identified by operating on ψ_{lm} with \hat{H}_Z :

$$\hat{H}_Z |\psi_{lm}\rangle = E_{l,m} |\psi_{lm}\rangle. \quad 2.17$$

Substituting in \hat{H}_Z , (derived in Equation 2.16) and $\hat{I}_z |\psi_{lm}\rangle$, (given in Equation 2.13), gives:

$$\hat{H}_Z |\psi_{lm}\rangle = -\gamma \hbar B_0 m |\psi_{lm}\rangle, \quad 2.18$$

and therefore a measurement of this interaction will return the energy:

$$E = -\gamma \hbar B_0 m. \quad 2.19$$

The splittings of the ground state are called the Zeeman splittings. These energies correspond to the eigenvalues of the free-precession Hamiltonian whilst the energy levels correspond to the eigenfunctions. An RF pulse of frequency ν will be absorbed and induce a spectroscopic transition if it satisfies the condition:

$$\Delta E = E_{upper} - E_{Lower} = h\nu . \quad 2.20$$

QM selection rules require $\Delta m = \pm 1$, therefore a transition is observed only for:

$$-\gamma\hbar B_0 = h\nu_0 . \quad 2.21$$

This characteristic frequency ν_0 is called the Larmor frequency and is formally represented in units of rad s^{-1} by:

$$\omega_0 = -\gamma B_0 . \quad 2.22$$

At equilibrium, the Boltzmann distribution dictates the proportion of spin states that occupy an eigenstate $|\psi\rangle$. For a spin $I = \frac{1}{2}$ nucleus for which there are just two possible states ($\alpha = \frac{1}{2}$ and $\beta = -\frac{1}{2}$), the probability of finding a spin in state α over state β is represented by:

$$p_{|\alpha\rangle} = \frac{e^{-E_\alpha/kT}}{e^{-E_\alpha/kT} + e^{-E_\beta/kT}} . \quad 2.23$$

The probability defines the population of each eigenstate for an ensemble of spin systems in a given sample. Thus, for an ensemble of spins the expectation value of a given operator is calculated from the summation of the eigenstates scaled by the population of each eigenstate and is known as an ensemble average. For the z-magnetisation the ensemble average is defined as:

$$\langle \overline{\mu_z} \rangle = \gamma\hbar \sum_{\psi} p_{\psi} \langle \Psi | \hat{I}_z | \Psi \rangle . \quad 2.24$$

For isolated spin $I = \frac{1}{2}$ nuclei in a static magnetic field, B_0 , the z-magnetisation reduces to:

$$\langle \overline{\mu_z} \rangle = \frac{1}{2} \gamma\hbar (p_\alpha - p_\beta) \quad 2.25$$

It is evident from Equation 2.25 that the population difference between the eigenstates defines the z-magnetisation. As the population of a given eigenstate can be enhanced by manipulation of the external conditions, i.e. an increase of B_0 and a decrease of the temperature T , it follows that changing these external variables can alter the sensitivity of the NMR technique.

2.3 Spin Excitation in the Rotating Frame

As has been alluded to several times, an RF pulse is applied to manipulate the nuclear magnetisation. This RF pulse is applied perpendicular to the z-axis and corresponds to a second linearly oscillating field denoted \mathbf{B}_1 that is several orders of magnitude smaller than \mathbf{B}_0 . This field ($\mathbf{B}_1 = \omega_1/\gamma$) has two counter rotating components with frequencies $\pm\omega_{\text{rf}}$ and amplitudes that superpose, i.e. $B(t) = 2B_1 \cos(\omega_{\text{rf}}t + \phi)$ where ϕ is the phase of the EM wave. For $\pm\gamma$, \mathbf{M} precesses clockwise or anticlockwise respectively. Only the component of the \mathbf{B}_1 field that shares this direction interacts with the magnetization. Under incident RF radiation, a nuclear spin will experience the static magnetic field \mathbf{B}_0 along the z-axis and the oscillating $\mathbf{B}_1(t)$ field. Convention directs the applied pulse along the x-axis and therefore the Hamiltonian (defined in Equation 2.15) becomes:

$$\hat{H} = -\gamma(\hat{I}_z B_0 + \hbar \hat{I}_x (2B_1 \cos(\omega_{\text{rf}}t + \phi))). \quad 2.26$$

Assuming $-\gamma$, if the frame of reference is converted to one that rotates, i.e. $\omega_{\text{rot.f}} = \omega_{\text{rf}}$, the \mathbf{B}_1 field appears stationary; it loses its time dependence. In the rotating frame, precession occurs at the offset frequency Ω , given by the frequency difference:

$$\Omega = \omega_0 - \omega_{\text{rot.f}} = \omega_0 - \omega_{\text{rf}} \quad 2.27$$

Transformation into the rotating frame means the Hamiltonian defined in Equation 2.26 becomes \hat{H}' :

$$\hat{H}' = ((\gamma B_0 - \omega_{\text{rf}})\hat{I}_z + \hbar \hat{I}_x B_1). \quad 2.28$$

When $\omega_{\text{rf}} = \omega_0$, the RF pulse is said to be on-resonance and $\Omega = 0$. For a general case however, the rotating frame reduces the large applied field \mathbf{B}_0 to the residual field:

$$\Delta B = -\frac{\Omega}{\gamma}. \quad 2.29$$

ΔB and \mathbf{B}_1 are now both linear fields directed along the z and x axes respectively, resulting in an overall effective field, depicted in Figure 2.1 of:

$$B_{\text{eff}} = \sqrt{B_1^2 + \Delta B^2}. \quad 2.30$$

In this frame, the magnetization precesses about the effective field at $\omega_{\text{eff}} = |\gamma| B_{\text{eff}}$. Provided the offset is small, or that the radiofrequency is much greater than the offset, this corresponds to the \mathbf{B}_1 field. Therefore, in the rotating frame the RF field,

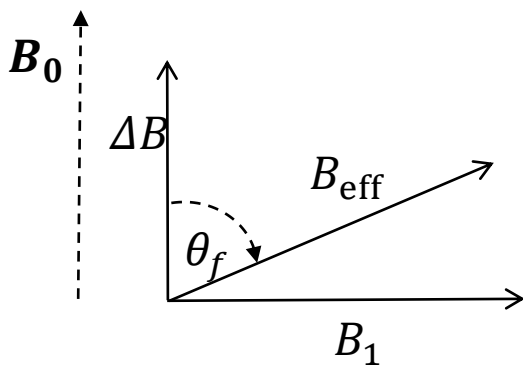


Figure 2.1: Vectorial diagram demonstrating the dominance of the effective field B_{eff} ; seen in Equation 2.30, whilst in a frame that rotates at or near the Larmor frequency.

B_1 , works in an analogous manner to the external magnetic field, B_0 , in the stationary laboratory frame: the magnetization is flipped (fully or partially) into the xy-plane. The extent of the rotation of the net magnetisation upon the application of an RF pulse is defined as the flip angle. For an RF pulse with nutation frequency ω_1 and duration t_p the corresponding flip angle, θ_f , is defined by $\theta_f = \omega_1 t_p$. Maximum signal is obtained with a 90° flip angle, which denotes the rotation of the net magnetisation into the xy-plane.

Given that the magnetization precesses about B_{eff} within the rotating frame, we can re-define the evolution of the magnetisation in analogy to Equation 2.5:

$$\frac{d}{dt} \mathbf{M} = \gamma \mathbf{M} \wedge \mathbf{B}_{\text{eff}} . \quad 2.31$$

The three directional components, $\frac{dM_x}{dt}$, $\frac{dM_y}{dt}$ and $\frac{dM_z}{dt}$ of this equation are called the Bloch equations. These equations can be used to calculate the macroscopic nuclear magnetisation as a function of time and, as such, are referred to as the equations of motion for nuclear magnetisation. These equations are discussed in more detail later in the chapter.

2.4 NMR Interactions

Overview

Assuming a uniform external magnetic field, the evolution of the nuclear magnetisation is completely defined by the internal interaction terms of the nuclear spin Hamiltonian. These internal terms are defined by the structure of the sample under investigation and therefore can be used to investigate structural conformation. Under the secular approximation, the internal NMR interactions can be viewed as perturbations to the Zeeman energy levels and are generally split into

isotropic and anisotropic components. Anisotropic terms are those for which there is a dependence on the orientation of the nuclear spin states with respect to the external magnetic field. In solution state NMR, isotropic tumbling of molecules averages the anisotropic interactions to zero. However, in solid-state NMR the dependence of the NMR frequency on orientation becomes visible. For solid powders, all possible orientations will be sampled in the magnet. The corresponding spectrum will be a sum of individual lines for all possible orientations and is known as a powder pattern.

2.4.1 The Internal Nuclear Spin Hamiltonian

Generally, the Zeeman interaction \hat{H}_Z is at least an order of magnitude larger than the other interactions allowing time-dependent perturbation theory to accurately calculate energies of the perturbed spin states. This is known as the secular approximation. The evolution of the magnetization depends on the total Hamiltonian \hat{H}_T of the system, which can be defined as a sum of all contributing interactions:

$$\hat{H}_T = \hat{H}_Z + \hat{H}_1 = \hat{H}_Z + (\hat{H}_{rf} + \hat{H}_{CS} + \hat{H}_D + \hat{H}_Q \dots), \quad 2.32$$

where \hat{H}_{CS} , \hat{H}_D , and \hat{H}_Q are to be discussed subsequently. The subsequent local field Hamiltonian at the site of the nucleus can be written as $\hat{H}_{loc} = \gamma \hat{\mathbf{I}} \cdot \mathbf{B}_{loc}$. The local field is dependent on molecular orientation and can be represented as $\tilde{\mathbf{A}}_{loc} \cdot \mathbf{B}_{int}$, where $\tilde{\mathbf{A}}_{loc}$ is a second-rank Cartesian tensor that transforms two vectors in different Cartesian frames to the same frame, and describes the strength and orientation dependence of an interaction:

$$\hat{H}_{int} = -\gamma \hat{\mathbf{I}} \cdot \tilde{\mathbf{A}}_{loc} \cdot \mathbf{B}_{int}. \quad 2.33$$

For example, the Zeeman interaction, which is the coupling between a spin and the \mathbf{B}_0 applied field can be represented as:

$$\hat{H}_Z = -\gamma \hat{\mathbf{I}} \cdot \tilde{\mathbf{A}}_{loc} \cdot \mathbf{B}_0 = -\gamma \begin{bmatrix} \hat{I}_x & \hat{I}_y & \hat{I}_z \end{bmatrix} \begin{bmatrix} a_{xx} & a_{xy} & a_{xz} \\ a_{yx} & a_{yy} & a_{yz} \\ a_{zx} & a_{zy} & a_{zz} \end{bmatrix} \begin{bmatrix} 0 \\ 0 \\ B_z \end{bmatrix}. \quad 2.34$$

2.4.2 Frames and Rotations of the Hamiltonian

Interaction tensors are reported in their diagonalised form. This is because the entries of the diagonalised interaction tensor correspond to its eigenvalues and the

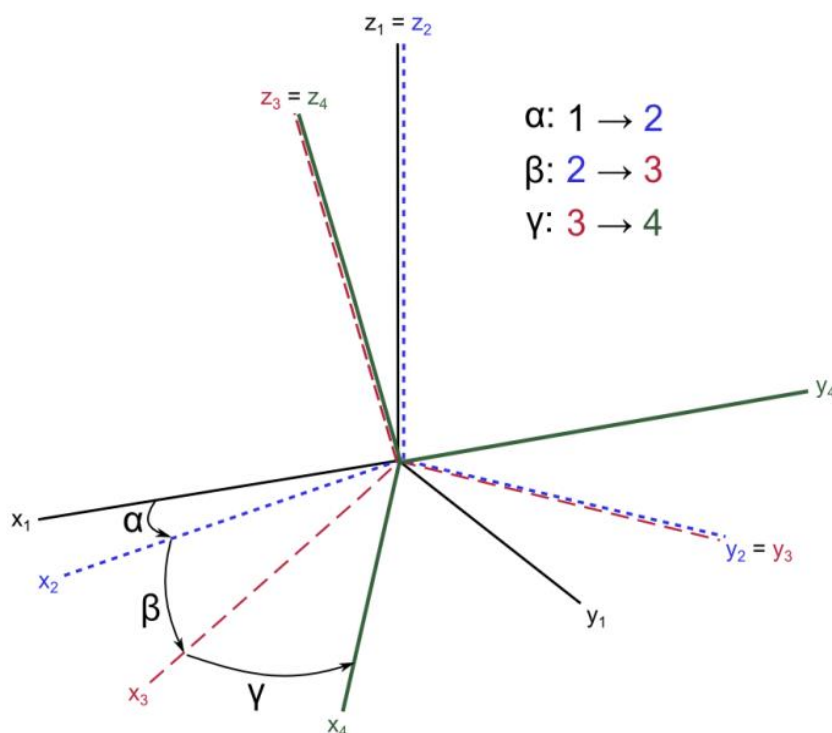


Figure 2.2: Diagram demonstrating the three consecutive axes transformations as governed by the Euler angles α , β , and γ , which facilitate conversion between interaction frames. α rotates about the z axis (black to blue axes), β rotates about the y axis (blue to red axes), and finally γ rotates again about the z axis (red to green axes).

axes of the diagonal matrix are made up of its eigenstates. When the interaction tensor is written in its diagonal form, the frame is said to be in the principal axes system (PAS), which is subject to the localised environment of the nucleus, and its three diagonal components are referred to as the principal values. However, the PAS is not the frame in which the experiment takes place, i.e. the LAB frame, and therefore the interaction tensors must undergo a rotation from the PAS frame to the LAB frame. Euler angles describe this frame rotation and are conventionally labelled by the angles α , β , γ . While there are a number of possible conventions, the Rose convention (ZYZ) is implemented as follows:

1. The system is rotated around the z -axis by the angle α , where α subtends the angle from the z -axis of the PAS to the z -axis of the LAB frame
2. β displaces the new y -axis to the y -axis of the LAB frame, and
3. γ again rotates this new z -axis to the z -axis of the LAB frame.

This is depicted in Figure 2.2 and can be fully described as the product of each transformation:

$$R(\alpha, \beta, \gamma) = \hat{R}_z(\alpha) \hat{R}_y(\beta) \hat{R}_z(\gamma) = e^{-i\alpha \hat{I}_z} e^{-i\beta \hat{I}_y} e^{-i\gamma \hat{I}_z}. \quad 2.35$$

In order to transform Cartesian tensors from one frame to another, the Hamiltonian can be described by a summation of irreducible spherical tensor operators $\hat{T}_{l,-m}$ that describe the spin components, and the spatial tensor $A_{l,m}$, the components of which can be found in the literature:⁶⁸

$$\hat{H} = C \sum_{l=0}^2 \sum_{m=-l}^{+l} (-1)^m A_{l,m} \hat{T}_{l,-m}. \quad 2.36$$

C includes any constants of the particular interaction, and m the order where $m = l - 1 \dots -l$. Only the spatial part is affected by a rotation and this is described by the Wigner D matrix:

$$\hat{R}(A_{l,m'}) = \sum_{m=-l}^{+l} A_{l,m} D_{m'm}^l, \quad 2.37$$

where the D matrix is given by:

$$D_{m'm}^l(\alpha, \beta, \gamma) = e^{-i\alpha} d_{m'm}^l(\beta) e^{-i\gamma} \quad 2.38$$

in which $d_{m'm}^l$ is the reduced rotation matrix and its value is determined by the angle β . For the case $m-m'=0$, i.e. symmetric transitions,

$$D_{00}^l(\alpha, \beta, \gamma) = P_l \cos(\beta), \quad 2.39$$

where P_l are the Legendre polynomials.

2.4.3 Chemical Shielding and Shift

A bare nucleus, with a nuclear spin will precess at the Larmor frequency in the magnetic field used in the NMR experiment. However, in reality electrons will surround the nucleus. The electrons react to the presence of the static magnetic field to generate localised magnetic fields that augment or oppose the applied field experienced by that nucleus. Therefore the nucleus is said to be shielded or deshielded and the result is a localized field of:

$$\mathbf{B}_{\text{loc}} = \mathbf{B}_0 (1 - \sigma), \quad 2.40$$

where σ is a second-rank tensor called the magnetic shielding tensor. The perturbation of the Zeeman interaction due to the electronic response of a nucleus in a static magnetic field, \mathbf{B}_0 , can be written as:

$$\hat{H}_{CS} = \gamma \hat{\mathbf{I}} \cdot \tilde{\sigma} \cdot \mathbf{B}_0 = -\gamma \begin{bmatrix} \hat{I}_x & \hat{I}_y & \hat{I}_z \end{bmatrix} \begin{bmatrix} \sigma_{xx} & \sigma_{xy} & \sigma_{xz} \\ \sigma_{yx} & \sigma_{yy} & \sigma_{yz} \\ \sigma_{zx} & \sigma_{zy} & \sigma_{zz} \end{bmatrix} \begin{bmatrix} 0 \\ 0 \\ B_z \end{bmatrix}. \quad 2.41$$

It is clear from Equation 2.41 that the strength of the chemical shift is directly proportional to the applied magnetic field. This complicates direct comparison of chemical shifts (in Hz) across different fields. Therefore, chemical shielding is converted to a universal field-independent chemical shift parameter, δ , by quoting the observed chemical shift against a given standard response, ν_{ref} . The definition of a field-independent peak position relative to this reference compound is shown below:

$$\delta_{\text{iso}} = \frac{\nu_0 - \nu_{\text{ref}}}{\nu_{\text{ref}}} \times 10^6. \quad 2.42$$

where δ_{iso} is the isotropic chemical shift and is quoted in the dimensionless quantity, parts per million (ppm). For $\delta_{\text{iso}} > 0$, a resonance is said to be less shielded than the reference, or located downfield. For $\delta_{\text{iso}} < 0$, a resonance experiences more shielding or is located upfield.

In the PAS the diagonalised chemical shielding tensor has the form:

$$\delta_{\text{PAS}} = \begin{bmatrix} \delta_{xx} & 0 & 0 \\ 0 & \delta_{yy} & 0 \\ 0 & 0 & \delta_{zz} \end{bmatrix}. \quad 2.43$$

The trace of the diagonalised chemical shielding tensor defines the isotropic chemical shift, δ_{iso}

$$\delta_{\text{iso}} = \frac{\delta_{xx} + \delta_{yy} + \delta_{zz}}{3}. \quad 2.44$$

The diagonal components are assigned by the Haeberlen convention⁶⁹ so that $|\delta_{zz} - \delta_{\text{iso}}| \geq |\delta_{xx} - \delta_{\text{iso}}| \geq |\delta_{yy} - \delta_{\text{iso}}|$. Thus, the anisotropy $\Delta\delta$ is defined as the largest frequency difference from δ_{iso} , and the asymmetry parameter η_δ indicates how close the environment is to axial symmetry:

$$\Delta\delta = \delta_{zz} - \delta_{\text{iso}} \quad \text{and} \quad \eta_\delta = \frac{\delta_{yy} - \delta_{xx}}{\Delta\delta}. \quad 2.45$$

Practically, the chemical shift lineshape can be completely parametrised by the isotropic (δ_{iso}) and anisotropic ($\Delta\delta, \eta_\delta$) components of the chemical shielding interaction.

2.4.4 The Dipolar Interaction

The magnetic dipole interaction is the direct interaction between any two magnetic dipole moments. Between two nuclei that are arbitrarily labelled as nuclei 1 and nuclei 2, the magnitude of this interaction is dependent on the strengths of the magnetic moments, the distance between them and their relative orientation to each other. It's Hamiltonian takes the form:

$$\hat{H}_D = -\frac{\mu_0}{4\pi} \frac{\hbar^2 \gamma_1 \gamma_2}{r^3} \left[\hat{\mathbf{I}}_1 \cdot \hat{\mathbf{I}}_2 - \frac{3(\hat{\mathbf{I}}_1 \cdot \mathbf{r})(\hat{\mathbf{I}}_2 \cdot \mathbf{r})}{r^2} \right], \quad 2.46$$

where $\hat{\mathbf{I}}_1$ and $\hat{\mathbf{I}}_2$ refer to the spins of the two nuclear isotopes. Expressing this in polar coordinates and only using terms that commute with \hat{I}_z (secular terms), results in

$$\hat{H}_D = -\frac{\mu_0}{8\pi} \frac{\hbar^2 \gamma_1 \gamma_2}{r^3} \left[2\hat{I}_{1z}\hat{I}_{2z} - \frac{1}{2}(\hat{I}_{1+}\hat{I}_{2-} + \hat{I}_{1-}\hat{I}_{2+}) \right] (3\cos^2\theta - 1), \quad 2.47$$

where θ is the angle subtended from the magnetic field to the internuclear vector. Dipolar couplings are small in this work, and are completely suppressed by magic angle spinning (discussed below). It can be seen that an average internuclear vector angle of 54.74° with respect to the external magnetic field reduces the $3\cos^2\theta - 1$ term to zero.

2.4.5 The Quadrupolar Interaction

Nearly 75% of NMR-active nuclei have a spin $I > 1/2$ and consequently, in addition to a magnetic dipole moment, exhibit a non-spherically symmetric distribution of charge, implying the property of an electric quadrupole moment \mathbf{Q} , a constant specific to each nuclear isotope. A quadrupolar nucleus exhibits a three-dimensional ellipsoid structure that cannot be modelled as a classical point source of charge. The charges surrounding the quadrupolar nucleus establish an electric field gradient (EFG) that couples to the quadrupole moment to produce the quadrupolar interaction. The energy E of a charge density distribution $\rho(\mathbf{r})$ of a nucleus inside an electrostatic potential $V(\mathbf{r})$ at a distance r across a volume element $d\tau$, is given by:

$$E = \int \rho(\mathbf{r}) \cdot V(\mathbf{r}) d\tau. \quad 2.48$$

This can be expanded as a Taylor polynomial with three terms, the zeroth term of which refers to the isotropic electrostatic energy, the 1st order term refers to the dipole moment which (due to its symmetry) has a zero contribution and the 2nd order term corresponds to the anisotropic quadrupole moment and takes the form:

$$\frac{1}{2} \sum_{\alpha, \beta=x,y,z} \left(\frac{\partial^2 V}{\partial r_\alpha \partial r_\beta} \right) \int \rho(\mathbf{r}) r_\alpha r_\beta d\tau, \quad 2.49$$

where α and β refer to the Cartesian co-ordinate frames of the spin and EFG tensors, respectively. The classical definition of the electric quadrupole moment tensor is:

$$Q_{\alpha\beta} = \int \rho(\mathbf{r}) (3 r_\alpha r_\beta - \delta_{\alpha\beta} r^2) d\tau. \quad 2.50$$

The potential or EFG centred about the nucleus is a second-rank tensor, defined by the components V_{xx} , V_{yy} , and V_{zz} when in the PAS:

$$V_{PAS} = \begin{bmatrix} V_{xx} & 0 & 0 \\ 0 & V_{yy} & 0 \\ 0 & 0 & V_{zz} \end{bmatrix} \quad 2.51$$

with $|V_{zz}| \geq |V_{yy}| \geq |V_{xx}|$. When a quadrupolar nucleus is positioned at a site which doesn't have point symmetry, the electric quadrupole moment interacts with the EFG, creating further shifts in the nuclear spin energy levels. In free space, Laplace's equation states that an electrostatic potential must equal zero, therefore these principal components of the EFG sum to zero and instead are simplified by two parameters:

$$C_Q = \frac{eQV_{zz}}{h} \quad \text{and} \quad \eta_Q = \frac{V_{xx} - V_{yy}}{V_{zz}}, \quad 2.52$$

where $V_{zz} = eq$ and $0 \leq \eta_Q \leq 1$. The shape of the powder pattern is largely determined by the asymmetry parameter η_Q , which describes the axial symmetry of the EFG whilst the quadrupolar coupling constant, C_Q , indicates the magnitude of the interaction. In general, a low C_Q specifies a site that has high spherical symmetry whilst a high C_Q indicates that more charge is concentrated within a plane.

The quadrupolar coupling is related to the quadrupolar frequency by:

$$v_Q^{PAS} = \frac{3C_Q}{2I(2I-1)}. \quad 2.53$$

The subsequent descriptions follow closely the work of Mackenzie & Smith⁷⁰ (note that for simplicity, η shall replace η_Q). The full quadrupole Hamiltonian takes the form:

$$\hat{H}_Q = \frac{eQ}{2I(2I-1)\hbar} \hat{\mathbf{I}} \cdot \tilde{\mathbf{V}} \cdot \hat{\mathbf{I}}, \quad 2.54$$

where $\tilde{\mathbf{V}}$ is the field gradient represented as a second-rank tensor. This is expanded into Cartesian coordinates using the Wigner-Eckhart Theorem, and positioned into its PAS by incorporating the EFG components V_i defined as $V_0 = v(\frac{3}{2})eq$, $V_{\pm 1} = 0$ and $V_{\pm 2} = \frac{1}{2}eq\eta$:

$$\hat{H}_Q^P = \frac{eQh}{4I(2I-1)\hbar} \left[\sqrt{\frac{3}{2}} (3\hat{I}_z^2 - \hat{I}^2) V_0 + [\hat{I}_z \hat{I}_+ + \hat{I}_+ \hat{I}_z] V_{-1} - [\hat{I}_z \hat{I}_- + \hat{I}_- \hat{I}_z] V_1 + \hat{I}_+^2 V_{-2} + \hat{I}_-^2 V_2 \right], \quad 2.55$$

where $\hat{I}_{\pm} = \hat{I}_x \pm i\hat{I}_y$ (the ladder operators). The effect of the quadrupolar interaction on the spin states subjected to the Zeeman interaction can be calculated, using time-dependent perturbation theory upon \hat{H}_T , under the secular approximation. For half integer quadrupolar nuclei, the perturbed energy to first order, i.e. $E_m^{(1)} = \langle m | \hat{H}_Q | m \rangle$, retains the Zeeman energy spacing for the transition between $m = +\frac{1}{2}$ and $m = -\frac{1}{2}$, or the central transition (CT), as depicted in Figure 2.3. The other transitions known as satellite transitions (STs), experience a shift in frequency, the degree of which is

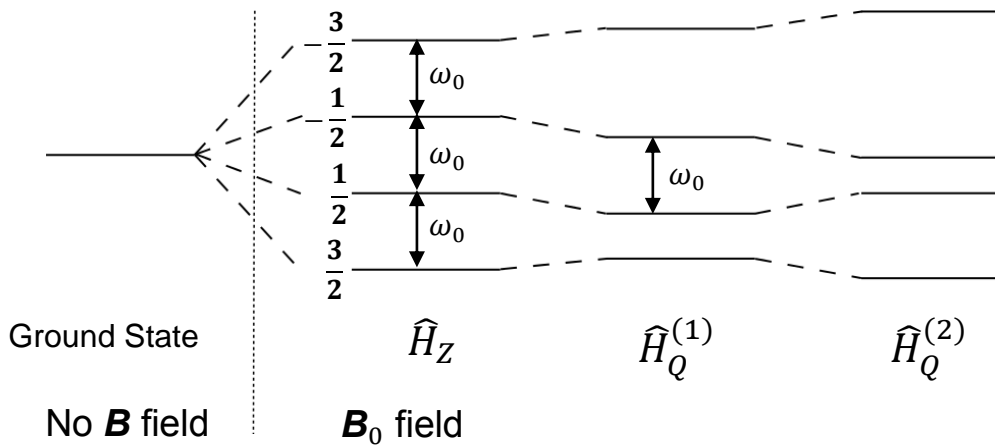


Figure 2.3: Energy level diagram for $I=3/2$ nucleus, which depicts the energy shifts resulting from the perturbation by the quadrupolar interaction. The first-order term, $\hat{H}_Q^{(1)}$, shifts the satellite transitions only, and the second-order term $\hat{H}_Q^{(2)}$, shifts all transitions.

dependent on ν_Q , and between 0 and several hundred MHz. Due to the difficulty in observing these transitions, the CT is usually the focus of studies investigating quadrupolar nuclei. In the case that the quadrupolar interaction is strong relative to the Zeeman interaction, i.e. 5% or more, then the second-order perturbation contributes a significant energy correction, given by:

$$E_m^{(2)} = \sum_{m \neq n} \left(\frac{\langle n | \hat{H}_Q | m \rangle \langle m | \hat{H}_Q | n \rangle}{E_n^{(0)} - E_m^{(0)}} \right). \quad 2.56$$

The second-order perturbation of the quadrupolar interaction broadens and shifts the energy of the CT. Substituting \hat{H}_Q^P from Equation 2.55, this correction is:

$$E^{(2)} = -\frac{2}{\nu_0} \left[\frac{eQ}{4I(2I-1)\hbar} \right]^2 \left[V_{-1}V_1(24m(m-1) - 4I(I+1) + 9) + \frac{V_{-2}V_2}{2}(12m(m-1) - 4I(I+1) + 6) \right]. \quad 2.57$$

The 2nd order perturbation of the CT is typically 100-1000 times smaller than ν_Q (Figure 2.3 greatly exaggerates the shifts). The V_i elements can be transformed into the LAB frame (by the aforementioned Wigner rotation matrices of Equation 2.37), which is given by:

$$V_i^{\text{LAB}} = \sum_{j=-2}^2 D_{ji}^{(2)}(\alpha, \beta, \gamma) V_j^{\text{PAS}}, \quad 2.58$$

and results in components:

$$V_{-1}V_1 = -\frac{3}{4}e^2q^2 \left[\begin{aligned} &\left(-\frac{1}{3}\eta^2\cos^2 2\alpha + 2\eta\cos 2\alpha - 3\right)\cos^4\beta \\ &+ \left(\frac{3}{2}\eta^2\cos^2 2\alpha - 2\eta\cos 2\alpha - \frac{1}{3}\eta^2 + 3\right)\cos^2\beta \\ &+ \frac{1}{3}\eta^2(1 - \cos^2 2\alpha) \end{aligned} \right] \quad 2.59$$

and

$$V_2V_{-2} = -\frac{3}{2}e^2q^2 \left[\begin{aligned} &\left(-\frac{1}{24}\eta^2\cos^2 2\alpha - \frac{1}{4}\eta\cos 2\alpha - \frac{3}{8}\right)\cos^4\beta \\ &+ \left(-\frac{1}{12}\eta^2\cos^2 2\alpha - \frac{1}{6}\eta^2 - \frac{3}{4}\right)\cos^2\beta \\ &+ \frac{1}{3}\eta^2\cos^2 2\alpha + \frac{1}{4}\eta\cos 2\alpha + \frac{3}{8} \end{aligned} \right]. \quad 2.60$$

Substitution of Equations 2.59 and 2.60 into Equation 2.57 allows calculation of the energy shift for the second order perturbation. The quadrupolar frequency for the CT ($m=\frac{1}{2}$) is therefore be given by:

$$\nu_{CT}^{(2)} = -\frac{1}{6\nu_0} \left[\frac{3C_Q}{2I(2I-1)} \right]^2 \left[I(I+1) - \frac{3}{4} \right] (A(\alpha, \eta) \cos^4 \beta + B(\alpha, \eta) \cos^2 \beta + C(\alpha, \eta)), \quad 2.61$$

where

$$\begin{aligned} A(\alpha, \eta) &= -\frac{27}{8} + \frac{9}{4} \eta \cos 2\alpha - \frac{3}{8} \eta^2 \cos^2 2\alpha \\ B(\alpha, \eta) &= \frac{30}{8} - 2\eta \cos 2\alpha + \frac{3}{4} \eta^2 \cos^2 2\alpha \\ C(\alpha, \eta) &= -\frac{3}{8} + \frac{\eta^2}{3} - \frac{1}{4} \eta \cos 2\alpha - \frac{3}{8} \eta^2 \cos^2 2\alpha. \end{aligned} \quad 2.62$$

2.4.6 Paramagnetic Interactions

The magnetic moment of an electron μ_e , is 662 times larger than the proton, therefore the unpaired electrons in paramagnetic centres that interact with NMR observed nuclei can induce strong, local fields (B_{eff}) around them:

$$B_{\text{eff}} = \frac{2\pi A \mu_B g B_0 I(I+1)}{3\gamma_N kT} + \frac{\mu_0 \mu_B^2 g^2 B_0 I(I+1)(3\cos^2 \theta - 1)}{3kT r^3 + B_{BMS}} + BMS, \quad 2.63$$

where A is the isotropic electron-nucleus hyperfine coupling constant, μ_B is the Bohr magneton, r is the electron-nucleus distance, θ the angle between electron-nucleus vector and B_0 and g the electron g -factor. The BMS field refers to the demagnetisation field that is induced by the bulk magnetic susceptibility of the sample (and is often ignored). The magnitude of these local fields can be significantly stronger than the couplings previously mentioned (Sections 2.4.3 to 2.4.5), and can effectively mask the other interactions. However, beneficial effects such as enhanced relaxation mechanisms are demonstrated,⁷¹ with paramagnetic doping studies even promoting structural interpretation.⁷²

Two mechanisms govern the effects of the interaction: the Fermi contact (FC) shift and the pseudocontact shift (PCS), which are through-bond and through-space interactions, respectively. The FC shift is given by the first term in Equation 2.63; for

a bond between a paramagnetic centre and the observed nucleus, this can be on the order of <3000 ppm in magnitude and have anisotropies of 3500-4000 ppm.⁷³ The second term of Equation 2.63, with a $3\cos^2\theta-1$ dependence is the dipolar interaction generated between the electron and the nucleus. Provided the spinning rate ν_r under MAS is less than the magnitude of the interaction, this term manifests as an intense spinning sideband manifold in the NMR spectrum. The PCS is given by:

$$\delta_{PCS} = \frac{1}{12\pi} r^{-3} + \{\Delta\chi_{AX}(3\cos^2\theta - 1) + \Delta\chi_{RH}\sin^2\theta\cos 2\phi\}, \quad 2.64$$

where r is the paramagnetic centre-nucleus distance and θ and ϕ orientate the nucleus relative to the PAS of magnetic susceptibility tensor χ of its axial (AX) and rhombic (RH) elements, respectively (where the paramagnetic centre is at the origin).⁷³

To summarise, in addition to significant peak broadening, the strength of the paramagnetic interaction also controls the degree to which a resonance is shifted away from its δ_{iso} position in the diamagnetic state. Both the PCS and FC shifts have been observed to affect δ_{iso} up to five bond lengths away.^{74,75} Furthermore, paramagnetic shifts increase almost linearly with increasing paramagnetic coordination of the observed nucleus i.e. two paramagnetically coordinated centres result in double the observed shift as compared to one coordinated centre.

2.5 NMR Methods Used in Chapters 5 and 6

2.5.1 Pulsed FT NMR and the NMR Signal

In pulsed Fourier Transform (FT) NMR, magnetization \mathbf{M} that lies along the large homogenous field fixed along the z-axis ($\mathbf{B}_0 = B_0\hat{\mathbf{z}}$) is perturbed into the transverse plane by the application of a secondary field \mathbf{B}_1 in the form of a short intense pulse. As \mathbf{M} returns to its' equilibrium, the precessing magnetization cuts through the coil that surrounds the sample and by Faraday's Law of Induction, generates a voltage. As a function of time, this signal is defined as the free induction decay (FID), which when added coherently, proportionally increases in amplitude with the number of acquisitions, N . At the same time however, it has to compete with the signal of background/internal electrical noise, which increases as \sqrt{N} . As has been discussed, NMR is a highly insensitive technique and it is necessary to increase the size of the

signal (by inducing a larger magnetization \mathbf{M}), in addition to obtaining adequate acquisitions N .

In order to completely restore \mathbf{M} after an acquisition, so that it can be fully delivered to the next perturbation, it has to return to the equilibrium magnetization M_0 from the transverse plane. This duration is system dependent, and is governed by T_1 , the spin-lattice relaxation constant. The time between acquisitions that allows for this is known as the recycle delay and a pulse sequence followed by the recycle delay is defined as a transient.

System relaxation causes time-dependent magnetic field components of the magnetization in both the longitudinal (z-axis) and transverse planes (xy-plane), with

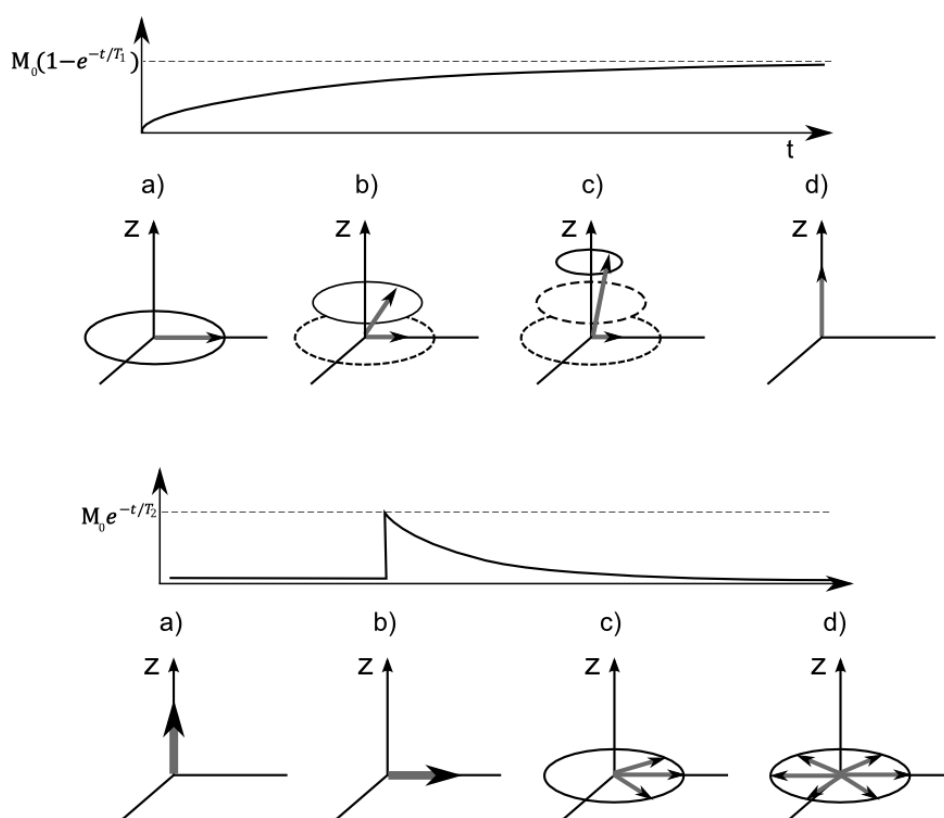


Figure 2.4

Top: The recovery of longitudinal magnetization as a function of time. (a) Bulk magnetization lies in the transverse plane after a $\pi/2$ pulse, (b) some spins begin to return to equilibrium, (c) most of the transverse magnetization is lost and (d) bulk magnetization is completely restored along the z -axis.

Bottom: The loss of transverse magnetization as a function of time. (a) Zero transverse magnetization, (b) a $\pi/2$ pulse flips \mathbf{M} into the transverse plane, (c) the spins begin to dephase until (d) transverse magnetisation is completely lost.

respective time constants of T_1 and T_2 . The evolution of \mathbf{M} described in Equation 2.5 can be separated into its axial components, known as the Bloch Equations:⁷⁷

$$\begin{aligned}\frac{d}{dt}M_x(t) &= \gamma[B_z(t)M_y(t) - B_y(t)M_z(t)] - \frac{M_x(t)}{T_2} \\ \frac{d}{dt}M_y(t) &= \gamma[B_z(t)M_x(t) - B_x(t)M_z(t)] - \frac{M_y(t)}{T_2} \\ \frac{d}{dt}M_z(t) &= \gamma[B_x(t)M_y(t) - B_y(t)M_x(t)] + \frac{M_0 - M_z(t)}{T_1}\end{aligned}\quad 2.65$$

where the solutions take the form of exponential decays back to equilibrium from $t = 0$ by:

$$\begin{aligned}M_x(t) &= M_x(0)\cos(\omega_0 t)e^{-t/T_2} \\ M_z(t) &= M_z(0) - [M_0 - M(0)]e^{-t/T_1}.\end{aligned}\quad 2.66$$

The behaviour of the two magnetisation components is shown in Figure 2.4.

M_x and M_y manifest as cosine waveforms, oscillating within the envelope of the decaying time signal (the FID). Fourier transformation converts this signal to a frequency domain display (a spectrum), which is able to identify frequencies of the nuclear environments within the sample.

2.5.2 Magic Angle Spinning

The dipolar interaction, the quadrupolar interaction and the chemical shift coupling, are time-dependent interactions and all share the trigonometric dependence $3\cos^2\theta - 1$. If a powder sample is rotated at $\theta = 54.74^\circ$ with respect to the direction of the applied field and rotated about this axis with frequency ν_r , then the average

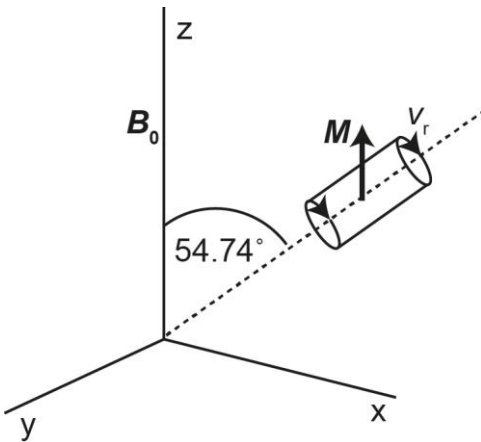


Figure 2.5: Experimental set-up of magic angle spinning (MAS). The rotor is at $\theta = 54.74^\circ$ to the z axis, and rotated at ν_r , averaging interactions with a $3\cos^2\theta - 1$ dependence.

orientation of the internuclear vector falls along this $\theta = 54.74^\circ$ axis, averaging the dipole-dipole interaction to zero as demonstrated by Equation 2.47, the chemical shift anisotropy is averaged to the isotropic value, the STs of the quadrupolar interaction to first-order are reduced to zero and to second-order lineshapes are significantly narrowed as indicated by Equation 2.68. This technique is called magic angle spinning (MAS) and its purpose is to increase spectral resolution by narrowing resonances. If the rotor spinning rate does not satisfy the fast condition, i.e. the rotor spinning rate is not greater than the linewidth (strength of the interaction),⁷⁸ then the spectrum will disperse the anisotropy within a range of spinning sidebands, separated by the spinning frequency.

2.5.3 The Quadrupolar Interaction under MAS

As briefly mentioned in Section 2.4.3, MAS acts to remove or diminish the anisotropic contributions to the NMR spectrum. The sample, orientated at $\theta = 54.74^\circ$ from the z-axis, is fixed within the rotor frame (ROT). Using Equation 2.58, the elements $V_{-1}V_1$ and V_2V_{-2} must first be rotated to this ROT frame (before the LAB frame), again using the Wigner-Eckhart Theorem. The result of this is:

$$E^{(2)} = \frac{1}{v_0} \left[\frac{3C_Q}{2I(2I-1)\hbar} \right]^2 \begin{bmatrix} C_0(I, m)F_0(\eta) \\ +C_2(I, m)P_2(\cos \theta)F_2(\beta, \gamma, \eta) \\ +C_4(I, m)P_4(\cos \theta)F_4(\beta, \gamma, \eta) \end{bmatrix}, \quad 2.67$$

where $P_2(\cos \theta) = \frac{1}{2}(3\cos^2\theta - 1)$ and $P_4(\cos \theta) = \frac{1}{8}(35\cos^4\theta - 30\cos^2\theta + 3)$ are the second- and fourth rank terms of the Legendre polynomials, seen from Equation 2.39. Coefficients C_0 , C_2 , and C_4 can be found in the literature⁷⁰ and

$$\begin{aligned} F_0(\eta) &= 1 + \frac{\eta^2}{3}, \\ F_2(\beta, \gamma, \eta) &= \left(1 - \frac{\eta^2}{3}\right) P_2(\cos \beta) \eta \sin^2 \beta \cos 2\gamma \\ F_4(\beta, \gamma, \eta) &= \left(1 + \frac{\eta^2}{3}\right) P_4(\cos \beta) \\ &\quad + \frac{5\eta}{96} (7\cos 4\beta - 4\cos 2\beta - 3) \cos 2\gamma \end{aligned} \quad 2.68$$

$$+ \frac{35\eta^2}{1152} (\cos 4\beta - 4\cos 2\beta + 3)\cos 4\gamma.$$

The second-order perturbation of the quadrupole interaction has terms that are proportional to $P_2(\cos\theta)$ and $P_4(\cos\theta)$, which cannot be reduced to zero with a single angle. At $\theta = 54.74^\circ$ (as well as removing 1st order quadrupolar effects), P_2 is reduced to zero, but P_4 has two roots of 30.6° and 70.1° . Effectively, spinning at two angles as illustrated by Figure 2.6, would average both P_2 and P_4 to zero, (implemented by the double rotation (DOR) technique), thus fully averaging the interaction.

Under MAS conditions ($\theta = 54.7^\circ$ only) and in the fast spinning limit (larger than the magnitude of the interaction), the second-order quadrupolar line for the CT is given by

$$\begin{aligned} \nu_{CT}^{(2)MAS} = & -\frac{1}{6\nu_0} \left[\frac{3C_Q}{2I(2I-1)} \right]^2 \left[I(I+1) - \frac{3}{4} \right] (F_0(\alpha, \eta)\cos^4\beta \\ & + F_2(\alpha, \eta)\cos^2\beta + F_4(\alpha, \eta)), \end{aligned} \quad 2.69$$

where

$$\begin{aligned} F_0(\alpha, \eta) &= \frac{21}{16} - \frac{7}{8} \eta \cos 2\alpha + \frac{7}{48} \eta^2 \cos^2 2\alpha \\ F_2(\alpha, \eta) &= -\frac{9}{8} + \frac{\eta^2}{12} + 2\eta \cos 2\alpha - \frac{7}{24} \eta^2 \cos^2 2\alpha \\ F_4(\alpha, \eta) &= \frac{5}{16} - \frac{1}{8} \eta \cos 2\alpha + \frac{7}{48} \eta^2 \cos^2 2\alpha. \end{aligned} \quad 2.70$$

The CT is narrowed under MAS conditions but retains a width defined by:

$$\Delta\nu_Q^{(2)MAS} = \frac{(6 + \eta^2)}{504} \frac{\nu_Q^2}{\nu_0} \left[I(I+1) - \frac{3}{4} \right]. \quad 2.71$$

Resonant frequencies are also shifted away from the isotropic chemical shift by the residual second order perturbation by:

$$\nu_{Q,iso}^{(2)MAS} = -\frac{3C_Q^2}{40\nu_0 I^2 (2I-1)^2} [I(I+1) - 9m(m-1) - 3] \left(1 + \frac{\eta^2}{3} \right). \quad 2.72$$

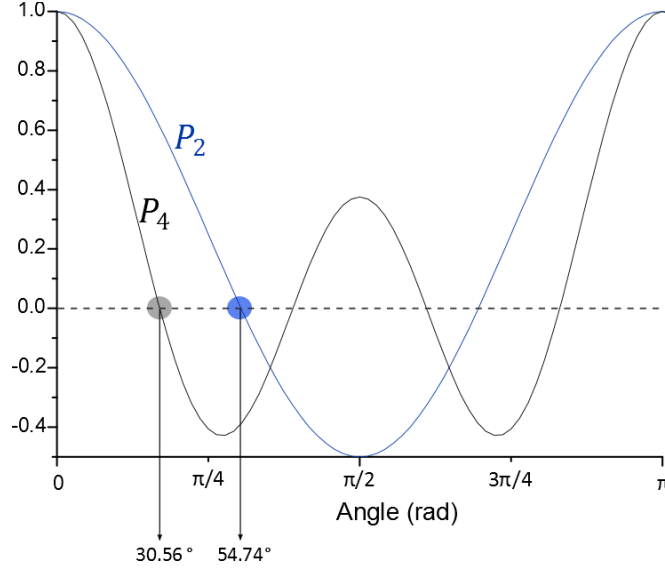


Figure 2.6: Diagram showing the roots for P_2 and P_4 , the second and fourth rank terms of the Legendre polynomials.

This frequency shift is inversely dependent on the Larmor frequency, and therefore it follows that the frequency shift is also inversely proportional to the magnetic field. The centre of gravity of the observed line δ_{cg} is the sum of the isotropic chemical shift δ_{iso} , and second-order quadrupolar shift $\delta_Q^{(2)}(I, m)$ contributions:

$$\delta_{cg} = \delta_{iso} + \delta_Q^{(2)}(I, m). \quad 2.73$$

For the CT, this can be written as:

$$\delta_{cg} = \delta_{iso} - \frac{3}{40} \left[\frac{I(I+1) - \frac{3}{4}}{I^2(2I-1)^2} \right] \frac{P_Q^2}{\nu_0^2}, \quad 2.74$$

where P_Q is defined as the quadrupolar product and given by:

$$P_Q = C_Q \sqrt{1 + \frac{\eta^2}{3}}. \quad 2.75$$

2.5.4 Single Pulse Sequence

A pulse sequence comprises RF pulses followed by delays in which free precession of the magnetization takes place. A single pulse experiment is the simplest case and creates single-quantum coherence, rotating the bulk magnetization (aligned along the z-axis) into the transverse plane. The experimental conditions (B_0 and B_1) and the observed system determine the optimal angle θ_f (defined in Section 2.3) for the magnetisation to be perturbed by.

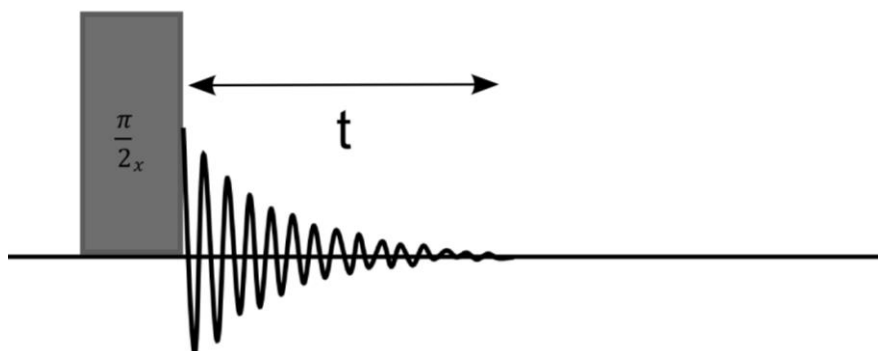


Figure 2.7: A single pulse sequence, here using a 90° flip angle about the x-axis. For quadrupolar nuclei, a $30\text{--}45^\circ$ angle usually ensures equal excitation of all CT resonances.

For quadrupolar nuclei, different nutation profiles of the nuclear environments are determined by the magnitude of the interaction (C_Q) and the strength of the RF pulse, in addition to the offset of the resonant frequency (defined in Equation 2.27). For large C_Q compared to the RF pulse, the RF pulse is selective to the CT, whereas for smaller C_Q environments, more of the STs will be excited due to the non-selectivity of the RF pulse. Therefore, in order to ensure equal excitation of all resonances (and therefore quantitative data), a $30\text{--}45^\circ$ angle is typically used. The magnetization is then allowed to precess under the evolution period t as shown in Figure 2.7.

2.5.5 Hahn-Echo Sequence

The components in the RF circuit e.g. the coil around the sample, have the dual task of delivering the RF pulse and recording the FID. Therefore, immediately following

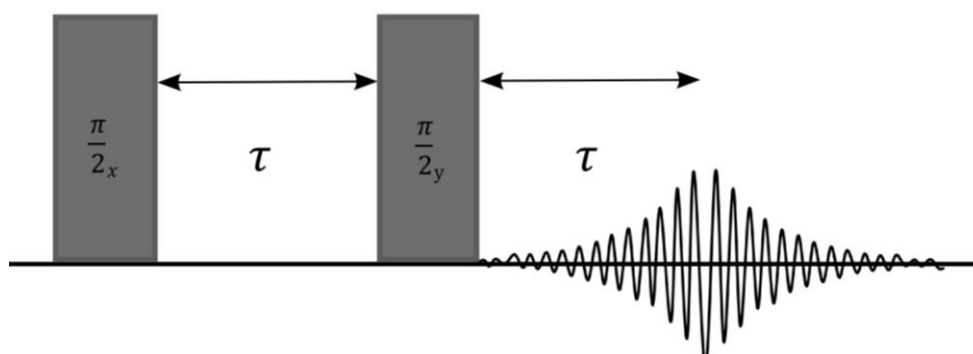


Figure 2.8: A solid echo pulse sequence diagram.

the application of an RF pulse, there are delays between pulse delivery and FID acquisition that are associated with electronic switches, acoustic vibrations induced in the circuitry (ringing), etc. A dead time is therefore implemented immediately after the pulse and before the receiver is turned on to record the FID.

However, for broad spectral lines such as those seen in quadrupolar or paramagnetically influenced resonances with fast-decaying FIDs, most of the data containing the definition of the lineshape is contained within the beginning of the FID.⁷⁹ If the dead time is too long, then the broad components are not recorded and if the dead time is too short, ringing is recorded in the FID, manifesting as artefacts in the spectrum (usually in the form of a rolling baseline).

The solution to this is the spin echo sequence that takes the form:

$$\frac{\pi}{2}_x - \tau - \pi_x - \tau .$$

After the $\pi/2$ pulse, the longitudinal magnetization is flipped into the transverse plane and during the time τ , the spin vectors diverge away from one (within the transverse plane) another as was depicted in Figure 2.4. The second pulse perturbs the magnetization by π from this position, as if the coherence has been reflected in a mirror plane.⁸⁰ The diverging spins converge back on themselves within time τ . This sequence is independent of the offset and the duration of the RF pulse (which controls the flip angle). For nuclei affected by large quadrupolar coupling, the first order quadrupolar interaction significantly destroys the formation of the full spin echo. Instead the solid echo (shown in Figure 2.8), which takes the form: 2.55

$$\frac{\pi}{2}_x - \tau - \frac{\pi}{2}_y - \tau ,$$

is commonly used to ensure equal excitation of all sites (for systems where sites adopt a range of C_Q sizes)

This refocusing pulse however is not 100% efficient and some coherence will be lost, the extent of which is dependent on T_2 . For experiments that require maximum magnetisation to acquire sufficient signal to noise, e.g. where the number of nuclear spins is low, this effect is apparent.

2.6 Raman Spectroscopy

Raman spectroscopy is a technique that observes the inelastic scattering of EM radiation with molecular vibrations, which are quantised. Unlike infrared spectroscopy (IR), it is a scattering technique, i.e. the energy of the incident photons do not have to be equal to two energy levels that comprise a transition. The scattered light is collected, and energy lost or gained from the incident light represents the energies of the transitions present in the molecule. The change in the frequency between the scattered (ν_s) and incident (ν_I) frequencies is known as the Raman shift:

$$\Delta\nu = |\nu_s - \nu_I|. \quad 2.76$$

As most molecules are in their vibrational ground state at room temperature, the transitions in which energy is lost are observed (known as the Stokes lines) due to their greater sensitivity (Anti Stokes lines define transitions for an energy gain compared to the incident wave). The incident wave, when considered as the propagation of a linearly oscillating dipole with field \mathbf{E} , causes the electrons and nuclei to respond, a result of the Coulombic interaction, generating an induced dipole moment in the molecule:⁷⁶

$$\boldsymbol{\mu}_{ind} = \alpha \mathbf{E}. \quad 2.77$$

The polarizability α is an intrinsic, tensorial property of the molecule, represented as:

$$\begin{bmatrix} \mu_x \\ \mu_y \\ \mu_z \end{bmatrix} = \begin{bmatrix} a_{xx} & a_{xy} & a_{xz} \\ a_{yx} & a_{yy} & a_{yz} \\ a_{zx} & a_{zy} & a_{zz} \end{bmatrix} \begin{bmatrix} E_x \\ E_y \\ E_z \end{bmatrix}. \quad 2.78$$

An atom has three degrees of freedom (DOF) for each movement type: vibrational, rotational, and translational. For a molecule of N atoms therefore, $3N-6$ vibrational DOF occur, except for a linear molecule, which has just two rotational DOF and so $3N-5$ vibrational DOF. Often called normal modes, symmetry relations determine whether they are detectable by Raman spectroscopy (Raman active modes), IR, both, or neither. A normal mode is only Raman active however for vibrations which cause a change in the polarizability of the electron distribution around the molecule, and is typically the case for symmetric vibrations.

There are some complications in the Raman spectrum that are necessary to discuss. Usually, one quanta causes the excitation of the 1st excited vibrational state,

however for special cases, >1 quanta are absorbed, inducing higher excited states. The short-lived photons from these states are called overtones and, in the Raman spectrum, occur with constant frequency intervals, enabling their identification. Furthermore, vibrational levels pertaining to distinct vibrations can overlap and cause combination bands.

Chapter 3

Literature Reviews

This chapter summarises existing literature relevant to two principal contributing themes in Chapters 5 and 6: Frenkel-type point defects and solid-state ^{17}O NMR of ceria systems. Frenkel-type defects are a (more) recently accepted element of ceria's unique ability to store and release O, hence publications date from the last two decades. Whilst the first solid-state ^{17}O NMR study of CeO_2 dates back to 1989/1990,^{81,82} this was a natural abundance study that looked at micrometre sized particles; the study of nanoceria systems has only been instigated within the last decade.

3.1 Frenkel Type Point Defects

Interstitial defects in fluorite structures were first observed in UO_2 ⁸³ in 1963 and the possibility of the presence of interstitial O in ceria were suggested by an X-ray diffraction study via electron density distribution maps.¹⁷ Frenkel-type defects for ceria, where the interstitial anion is charge compensated by a vacancy in the regular lattice, were first hypothesized by E. Mamontov and T. Egami in 1999¹³ following a pulsed neutron diffraction study. They introduced the idea of Frenkel-type defects in ceria by discussing some observations in previous literature,⁸⁴⁻⁸⁶ in which the deterioration of ceria's OSC after high-temperature treatments is seen to not exclusively stem from the sintering of the particles as believed at the time. They compile the conclusions of these papers to the following details:

- Desorption of O from CeO₂ films during temperature programmed desorption (TPD) experiments in which CO was oxidised, revealed a low temperature peak at ~727 °C and a high temperature peak ~ 1027 °C.
- Only a small amount of oxygen contributed towards the low temperature peak, and was sourced from the lattice.
- This oxygen was not seen to exchange with other oxygen in the film.
- A high-temperature treatment of the film to 1447 °C resulted in the loss of the OSC and this could not be correlated with sintering of the sample.
- Whilst there was an observed growth of crystallite size with increasing temperature, there was no significant particle growth in the temperature range for which the OSC was deactivated.

The interpretation of these observations was the presence of weakly bound oxygen in ceria, in addition to the regular oxygen from the sublattice. These additional oxygen sites are known to be part of the bulk (not the surface), they only make up a small amount of the total oxygen, and are deactivated at high temperatures. Mamontov and Egami suggest that these weakly bound O are vital to the OSC in ceria and have eluded observation in previous neutron diffraction studies due to insensitivity of the technique to defects/deviations from crystallinity and/or initial sample preparations influencing their presence.

They implemented Rietveld refinement and the atomic pair distribution function (PDF) analyses following neutron diffraction to compare two ceria samples, one as-prepared, and the other heated at 800 °C. For the as-prepared sample, the PDF obtained from the structure function was accurate and in order to match this experimental result to a likely model, they depict four potential structural models of ceria.

- Model 1: stoichiometric ceria with oxygen occupying the tetrahedral position,
- Model 2: ceria distributed with randomly generated vacancies,
- Model 3: ceria with displaced O from the tetrahedral sites to the neighbouring octahedral position in the [110] direction (the Frenkel type defect) and,
- Model 4: similar to Model 3, but with additional O ions displaced from their initial positions along the [111] direction.

PDF difference curves show that Model 1 is the least compatible result, with only minor improvements observed for Model 2, which incorporates the inherent vacancies. Dramatic improvements however are apparent for Model 3 and marginally more so for Model 4. After thermal treatment at 800 °C, increased atomic order is the primary observation and the difference plot between treated ceria and Model 1 is shown to have excellent agreement.

For the untreated ceria sample, Rietveld refinement indicates that an interstitial concentration C of 12-16%, using Model 4 with stoichiometry, provides the most accurate description of the system, pertaining to ceria with frenkel-type defects and associated vacancies. Furthermore, a maximum 2-4% overall oxygen deficiency was found possible. The heat-treated sample could be fitted against all models to a satisfactory standard, however it showed a lower interstitial concentration (4%) when it was fitted to Model 4.

The interstitial O are suggested to form during sample synthesis. In Mamontov and Egami's discussion, they propose that preparations of ceria do not always undergo high temperature treatments and in these cases, when CeO_{2-x} is initially oxidised, O can enter the roomier vacant octahedral site, leaving the smaller, adjacent, tetrahedral site vacant. Only if a high annealing temperature is implemented does this overcome the potential barrier of the tetrahedral site in the regular sublattice, and remove the associated vacancy.

One year after this study on Frenkel defects in ceria, Mamontov and Egami published a similar work on a ceria-zirconia solid solution (≈ 67 mol% ceria, 30 mol% zirconia) to compare to pure ceria, again using pulsed neutron diffraction, and in addition to TPR and EPR measurements. They investigate samples as-prepared and after intervals of heat treatment up to 850 °C. Structural refinement of the pre-heated ceria zirconia systems reveal vacancy and interstitial concentrations to be 17% and 9% respectively, implying a highly oxygen deficient system (unsurprising for ceria-zirconia systems). These values remain more or less unchanged throughout the heat treatment. In comparison, the concentrations of vacancies and interstitials of pure ceria are initially 8% and 7%, respectively (close to stoichiometry) and both decrease substantially at 760 °C, indicating that the frenkel type defects recombine with vacancies at this temperature.

EPR results of the ceria sample obtained at 77 K show no evidence of the octahedral interstitial O, which suggests (1) they adopt the O^{2-} oxidation state and (2) there are no trapped electrons in the corresponding vacancy site. The ceria zirconia sample however reveals an intense peak that is assigned to Ce^{3+} (observable only at low temperature) and associated O vacancies which, as described in Chapter 1, may be in an oxidation state that gives a paramagnetic signal.

The TPR profiles of thermally aged ceria reveals two reduction peaks; one located at 400 °C (this is the readily released O), and another at around 900 °C. The low temperature reduction peak is consistent in intensity until ceria is thermally aged at 800 °C, after which only a small amount of the readily releasable O is preserved. In comparison, the ceria zirconia exhibits a single peak at 460 °C and remains at near-constant intensity up to the maximum aging temperature of 850 °C (these results are in-keeping with other TPR studies). Furthermore, the approximate crystallite growth estimated by neutron diffraction does not correlate with the TPR results, implying that a loss in surface area is not solely responsible for the loss in OSC.

Ultimately, all three characterisation methods suggest that the Frenkel-type defects in ceria zirconia are retained under their study conditions. It is suggested that the smaller ionic radius of zirconium results in a smaller lattice constant, and therefore a smaller tetrahedral site with greater compressive stress, i.e. more energy would be required to escape the potential than the equivalent site in ceria. This would explain the ability of ceria-zirconia to retain Frenkel-type defects at higher temperatures. Furthermore, it is proposed that the Frenkel-type defect may either play a direct role in the OSC process and/or enhance OSC by maintaining O vacancies in the regular sublattice.

In 2010, Wu *et al.* published their work on Raman spectroscopy probing the defect sites on ceria nanorods, nanocubes, and nano-octahedra. The Raman spectra of the three morphologies reveal a definite difference in their defect concentrations via the relative intensities of the defect mode I_D to the F_{2G} mode $I_{F_{2G}}$, with the rods as the most defective system. In their discussion, they propose that a previously assigned Raman band at 592 cm^{-1} as the vibrational mode of Ce^{3+} in the MO_8 unit, is implausible and assign it to the Frenkel type defect instead; this is due to three pieces of evidence.

1. They observe the thermal stability of the band up to 400 °C, which is in-keeping with Mamontov & Egami's observations of the deactivation of Frenkel-type defects at higher temperatures than this.
2. An attempt to adsorb O₂ to these defect sites failed, evident by the unaltered state of the band associated with vacancies at $\sim 560\text{ cm}^{-1}$. This can be rationalised if there is already a charge balance of this defect site by an interstitial O residing in the neighbouring, octahedral site.
3. Finally, they use X-ray photoelectron spectroscopy (XPS) to examine the Ce 3d state on the three ceria morphologies. They observe very similar spectra which resemble that of pure stoichiometric ceria, suggesting that very little Ce³⁺ is present.

These interpretations, along with the significant differences in the defect ratio I_D/I_{F2G} across the three morphologies, indicate that this 592 cm^{-1} band is not associated with Ce³⁺.

In 2014, Agarwal *et. al* published a paper that investigates ceria rods via Raman and FTIR techniques.¹⁴ They looked at ceria nanorods at room temperature, 200 °C and 350 °C via in situ Raman spectroscopy. At room temperature, they observe a band at 589 cm^{-1} , assigning this to the Frenkel-type defect, and observe slight shifts to higher wavenumber upon heating, increasing to 597 cm^{-1} at 350 °C. Furthermore, when different gases (CO, He, and H₂O) were flowed over the sample at 200 °C and 350 °C, minimal changes in this Frenkel band were observed relative to the fluorite bands and vacancy modes. However, this study also observes other bands in the defect region (between 525 and 570 cm^{-1}), which appear as shoulders on the vacancy band at 550 cm^{-1} . They suggest this could be either evidence of additional defects (Ce or O interstitials and Schottky defects) or clustering of vacancies into dimers and trimers. Shoulder bands are also observed at 404 and 487 cm^{-1} , either side of the F_{2G} band at 455 cm^{-1} and are suggested to be caused by lattice distortion induced by vacancies, i.e. Ce-O_x units with $x = 5-7$.

Agarwal *et. al* published again the following year (2015) and compared ceria rods (111 terminated), cubes (100 terminated), and octahedra (111 terminated), again via in situ Raman and FTIR spectroscopy.¹⁵ (Chapter 1 depicts rods as terminating via the {110} and {100} surfaces, but there are some discrepancies in the

literature indicating a {111} termination is possible).⁸⁷ The purpose of the study is to probe the dependency of defects on the surface terminated plane. Raman spectra of the octahedrons and cubes, as-prepared and reduced under H₂ conditions at 350 °C, are shown to have very similar features. Firstly in the F_{2G} region, there are again distinct shoulders at 404 and 487 cm⁻¹, either side of the F_{2G} band at 455 cm⁻¹ (as the rods revealed in their previous study). These shoulder bands are more intense for the ceria cubes (in addition to the reduced octahedral), indicating greater lattice distortion, which is in agreement with XRD data acquired for a study they published in 2013.⁸⁸ Furthermore, they identify three bands in the defect region at 540, 563 and 594 cm⁻¹, again with intensities greater for the cubes compared to the octahedra. As expected, the I_D/I_{F2G} ratio is higher for the reduced samples than the non-reduced, and this is more apparent in the cubes, suggesting the cubes are more readily reduced.

3.2 ¹⁷O Solid-state NMR of Ceria Systems

Oldfield *et al.* were the first to publish the ¹⁷O chemical shift of the single, distinct, crystallographic site OCe₄ of bulk CeO₂ at 877 ppm in 1989,⁸¹ with Bastow & Stuart⁸²

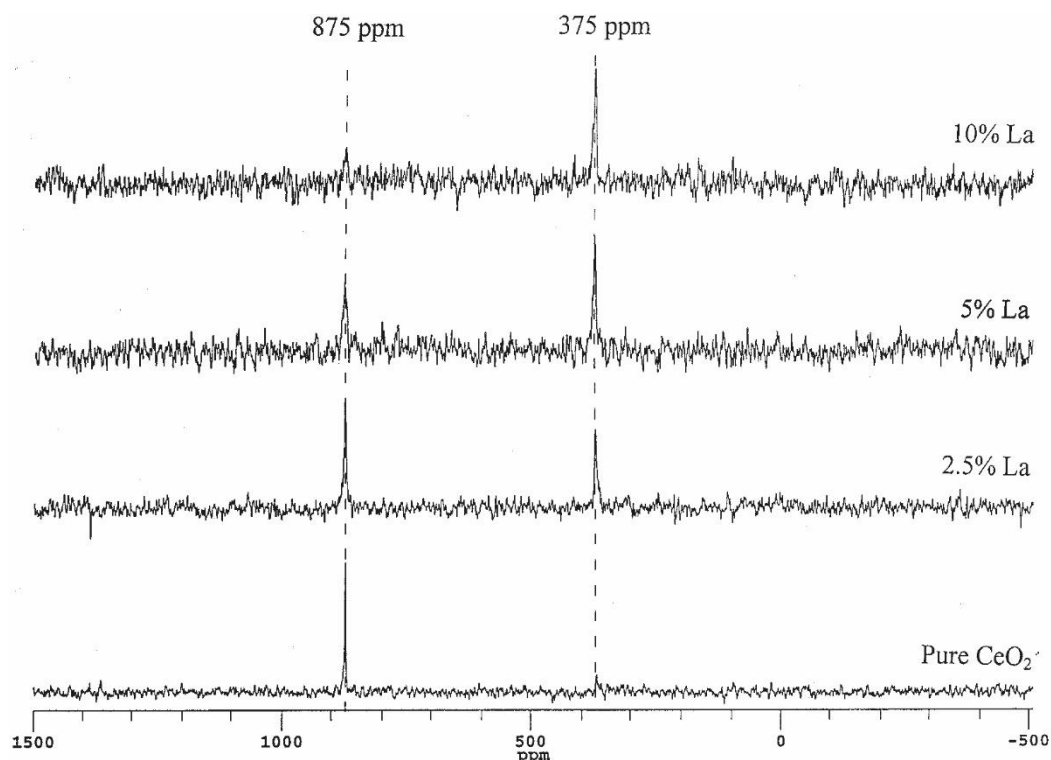


Figure 3.1: ¹⁷O MAS NMR spectra of ceria and lanthana doped ceria, aged at 1000 °C. Reproduced with permission from Reference [89].

(878 ppm) a year behind. Ten years on, O'Neil & Morris⁸⁹ investigated a range of mixed lanthana–ceria cubic solid solutions on the micrometre scale. Samples were ^{17}O enriched via heating in H_2^{17}O . The solid-state ^{17}O MAS NMR spectra shown in Figure 3.1 reveal a narrow peak at $\delta_{\text{iso}} = 875$ ppm, assigned to OCe_4 ; with a decrease in intensity seen for an increase in La concentration, and a narrow peak at $\delta_{\text{iso}} = 375$ ppm, which reveals the reverse behaviour of an increasing intensity with an increase in La loading. They assign $\delta_{\text{iso}} = 375$ ppm to originate from an oxygen coordinated to both Ce^{3+} and La^{3+} cations for its deshielded position. This is relatively unlikely given the paramagnetic nature of Ce^{3+} and the comparative sharpness of the corresponding resonance (direct bonding with Ce^{3+} results in very broad lines, as shall be discussed subsequently). In fact it is more probable that this is the signal from tetragonal zirconia from the rotor⁹⁰ (which is supported by the incremental increase in signal to noise with increased La concentration). Their data suggests that an increase in La loading decreases the exchange of ^{17}O during the labelling technique. Aliovalent doping of La^{3+} for Ce^{4+} should promote oxygen vacancy formation in the lattice. It appears that in this case, the La stabilises the vacancies thereby inhibiting oxygen mobility, and ultimately the exchange of ^{17}O into the bulk.

Kim & Stebbins conducted a ^{89}Y and ^{17}O MAS NMR study on yttria-doped ceria (YDC) cubic solid solutions in 2007,⁹¹ with the Y^{3+} cation balanced by inherent vacancies. Samples prepared via solid-state reactions at 1500 °C for 2-3 days were then heated in $^{17}\text{O}_2$ at 600 °C for 12 hours. Single pulse MAS NMR spectra were acquired at room temperature at 14.1 T for both nuclei. A recycle delay of 1 s is implemented (solid $\pi/6$ flip angle), which is unusually short for O species in crystalline environments (T_1 not measured). The ^{89}Y results on the left hand side of Figure 3.2 show that as Y doping is increased, the amount of YO_6 units increase, whilst the more coordinated YO_8 units decrease, i.e. there is an increase in vacancies. It is calculated that vacancies are more likely to be located next to Y cations over Ce cations.

The ^{17}O MAS NMR results on the right hand side of Figure 3.2 depict pure ceria (bottom), with a chemical shift of 877 ppm for OCe_4 (labelled peak A); in-

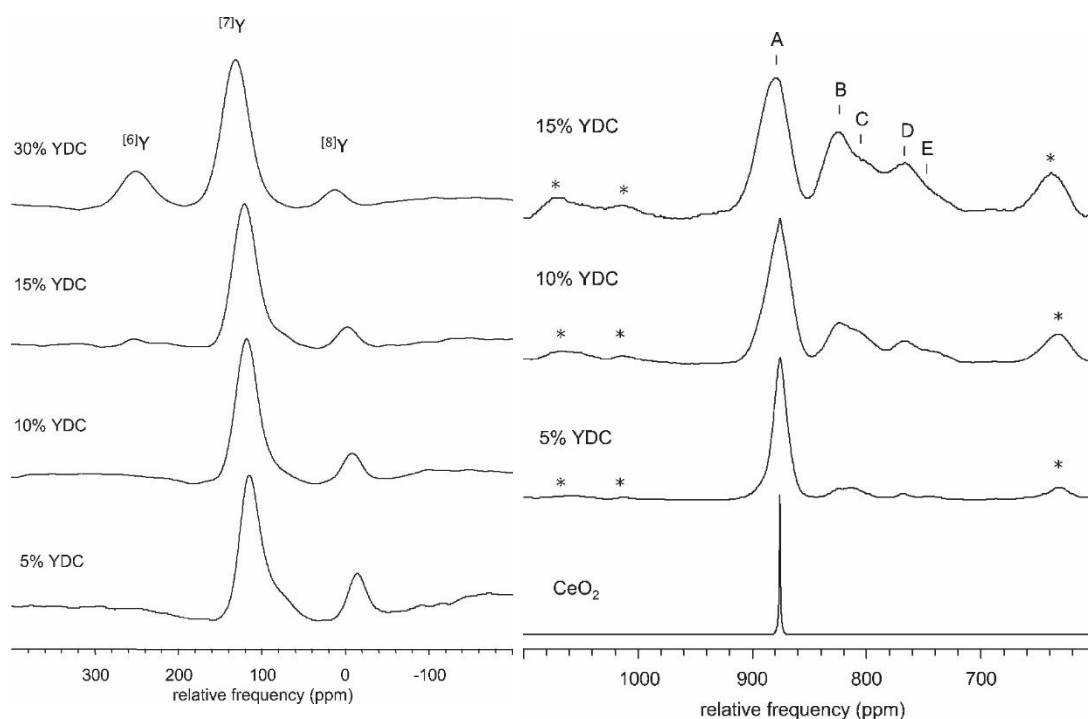


Figure 3.2: The left hand side shows ^{89}Y MAS NMR data and the right hand side shows ^{17}O MAS NMR of Y_2O_3 -doped CeO_2 at 14.1 T. $\nu_r = 20$ kHz and sidebands marked by asterisks. Peak A is assigned to OCe_4 , peaks B and C to OCe_3Y , and peaks D and E to OCe_2Y_2 . Reprinted with permission from Reference [91].

keeping with the previous three studies. The YDCs reveal five resonances in total, with increasing contributions from the four additional peaks (located at 826, 812, 768 and 743 ppm) as Y doping increases. The four other resonances are assigned to the other two 1st coordination sphere environments that occur: OCe_3Y as peaks B and C, and OCe_2Y_2 as peaks D and E. The dual nature of these coordinations is attributed to the presence/absence of a vacancy in the second coordination sphere on the Y^{3+} cation (indicated by the ^{89}Y MAS NMR results).

No significant differences in line widths are observed at $B_0 = 18.8$ T, thus linewidths are caused by chemical shift distributions, not 2nd order quadrupolar effects. The considerable linewidth of peak A indicates greater disorder from an increase in random distributed vacancies. However, by comparing the chemical shift of peak A between 0% and 15% Y doping, a slight shift to higher ppm is apparent. The authors note that this is somewhat incongruous as a vacancy in a second coordination sphere should result in a shorter bond between the direct bond of the oxygen and Ce cation, and this increase in electron density would result in a shift to lower ppm. The shift in peak position is likely an indication of the expanding lattice,

due to the increased incorporation of the larger Y^{3+} cation (1.019 Å), vacancies and/or the larger Ce^{3+} cation.

The authors suggest that a comparison of a random model of vacancy distributions with (the integration of) the ^{17}O results implies that an O vacancy is more likely to pair with two Y cations. However, it is not clear whether these results are quantitative (1 s recycle delay used) and furthermore, the possibility that the ^{17}O exchange with some sites is more preferable than others is not considered.

Finally, a YDC with 5% dopant concentration is investigated at temperatures up to 500 °C. At 400 °C, a single peak located at the centre of gravity of all resonances (that were observed at room temperature) is apparent, indicating total structural O exchange. Peaks B to D (those associated with one or two Y) however, begin to exchange from just 110 °C around their centre of gravity point, indicating that O bonded to Y cations are more mobile. However, the authors note that this may only happen on a local scale, i.e. their tendency to pair with vacancies may bind them to short range mobility, and not contribute to the long range migration.

Ando *et al.* published a similar ^{17}O MAS NMR study in 2011⁹² of YDCs up to a 30% dopant concentration, at 21.8 T. Preparations of the YDCs included sintering at 1600 °C for 10-20 hours and ^{17}O enrichment under 2.6 kPa of $H_2^{17}O$ at 500 °C for 12 hours. For the NMR acquisition, T_1 was not measured but a longer delay of 5 s was used for a solution $\pi/18$ flip angle. As can be deduced from Figure 3.3, the ^{17}O MAS

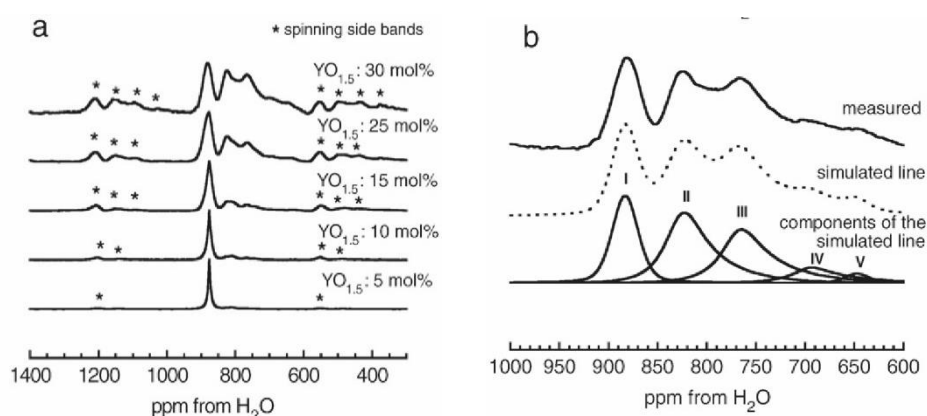


Figure 3.3: Left hand side: (a) ^{17}O MAS NMR spectra of YDC with 5, 10, 15, 25 and 30% Y_2O_3 -doping at 21.8 T and $\nu_r = 22$ kHz. 12,000- 52,000 scans were accumulated with a 5 s recycle delay. (b) Deconvolution of the YDC sample with 30% Y_2O_3 -doping. Asterisks denoted spinning side bands. Reprinted with permissions from Reference [92].

NMR spectral profiles look similar to those of Kim & Stebbins. However, it is clear that the bulk OCe_4 signal is significantly more intense relative to the other peaks, in contrast to Kim and Stebbins study (compare the ^{17}O spectra of 15% YDC in Figure 3.3Figure 3.12 with Figure 3.2(a)). This could indicate that the data presented by Kim and Stebbins was not quantitative. However, a faster relaxing system due to greater structural disorder/paramagnetic Ce^{3+} concentration as determined by the treatment conditions, cannot be disregarded, e.g. different ^{17}O labelling procedures were used (H_2^{17}O vs $^{17}\text{O}_2$).

The higher-dopant samples reveal δ_{CG} positions of 883, 826, 768, 696 and 647 ppm assigned to OCe_4 , OCe_3Y , OCe_2Y_2 , OCeY_3 , and OY_4 respectively. They refer to previous literature which has observed OCe_4 at 877 ppm⁸² (Bastow) and OY_4 between 346 and 383 ppm in Y_2O_3 ,⁹³ although they do not comment on a >250 ppm deviation for the OY_4 species. Moreover, they state that the dual-peak nature attributed to vacancies in the second shell is not observed. As has been already stated, the lineshapes acquired by both studies on the YDC are very similar except for the intensity of the bulk. The differences in the two pieces of work respectively arise due to the contrasting deconvolution styles for both studies, therefore the absence of the dual-peaks is due to interpretation of the data as opposed to being absent from it. Data acquired at lower magnetic field of 11.7 T revealed no apparent difference in lineshapes, implying insignificant 2nd order quadrupolar effects, consistent with the work of Kim & Stebbins.

In the following year, Ando *et al.* conducted a further ceria study of $\text{LnO}_{1.5}\text{-CeO}_2$, $\text{Ln} = \text{La, Nd}$ (LDCs and NdDCs) by ^{17}O MAS NMR.⁹⁴ Compositions of $x\text{LnO}_{1.5}(1-x)\text{CeO}_2$ for $x = 0.1\text{-}0.4$ were prepared and calcined at 1650 °C for 10-23 hours, with enrichment and NMR acquisition parameters the same as their previous study. The spectra of LDC systems are seen on the left hand side of Figure 3.4(a) and reveal four peaks (I to IV), evident from the deconvolution of $(\text{CeO}_2)_{0.86}(\text{LaO}_{1.5})_{0.14}$, shown in Figure 3.4(b) with I as OCe_4 , II and III as OCe_3La and IV as OCe_2La_2 . They propose that the splitting of the OCe_3La species in the LDC structure is due to the presence and absence of vacancies in the second coordination sphere, causing two distinct chemical shifts. They furthermore validate this description with referencing Kim & Stebbins' study of YDCs (as previously reviewed), however, incongruously they go on

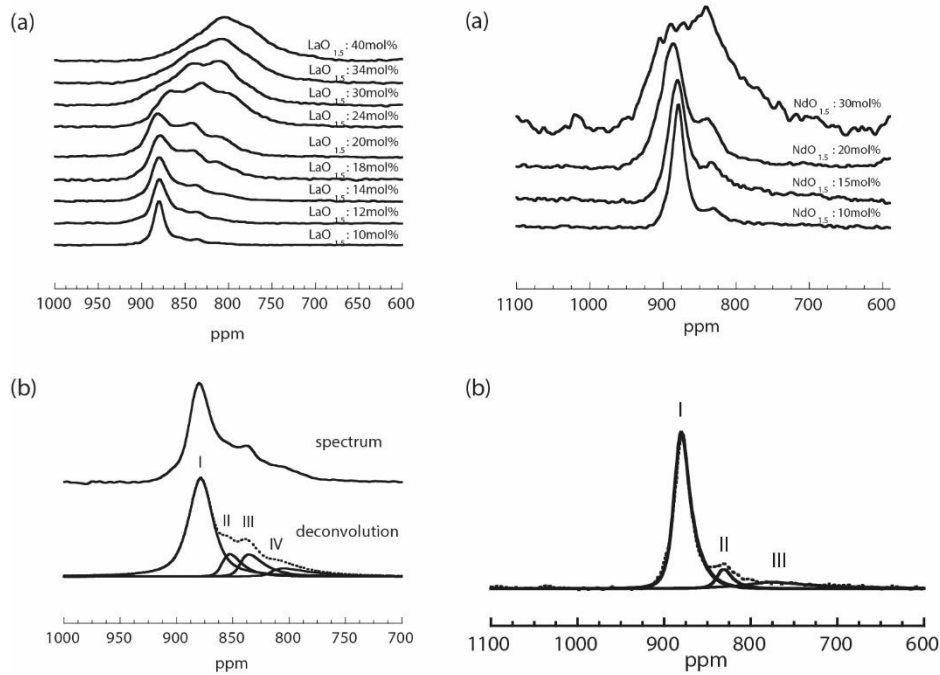


Figure 3.4: (a) ^{17}O MAS NMR spectra of $x\text{LnO}_{1.5} - (1-x)\text{CeO}_2$ at 11.7 T under 22 kHz MAS spinning. 7,000 - 24,000 scans were accumulated with a 5 s recycle delay, where the left hand side shows $\text{Ln} = \text{La}$ with 10, 12, 14, 18, 20, 24, 30, 34 and 40% doping and the right hand side shows $\text{Ln} = \text{Nd}$ with 10, 15, 20 and 30% doping. (b) Deconvolutions of $(\text{CeO}_2)_{0.86}(\text{LaO}_{1.5})_{0.14}$ on the left hand side and $(\text{CeO}_2)_{0.9}(\text{NdO}_{1.5})_{0.1}$ on the right hand side. Reproduced with permission from Reference [94].

to suggest that they do not observe these vacancy effects in their own previous study of YDCs because of the difference between cation sizes of La^{3+} (1.16 Å) and Y^{3+} (1.019 Å). This is a very contradictory conclusion.

To clarify, the differences between the two YDC studies could arise from several other factors. Firstly, Kim & Stebbins may have saturated bulk resonances with no vacancies in the second shell by using a shorter, 1 s recycle delay; the experimental conditions acted like a T_1 filter, preferentially selecting faster relaxing species, i.e. those resonances with a vacancy. The reported differences in the number of unique oxygen environments looks to, at least partially, be caused by the style of deconvolution of the ^{17}O data. Alternatively, the preparation and ^{17}O enrichment techniques of the samples in these studies may be responsible for introducing more/less vacancies and other defects.

The ^{17}O MAS NMR spectra of the NdDCs are shown on the right hand side of Figure 3.4, with a deconvolution shown beneath in (b), where they assign peaks I, II

and III as OCe_4 , OCe_3Nd , and OCe_2Nd_2 , respectively. At 30% $\text{NdO}_{1.5}$ concentration, broadening due to the interaction of ^{17}O with paramagnetic Nd^{3+} is significant.

In 2013, Maupin *et al.* studied the interaction between gaseous dioxygen and lattice oxygen of 13 nm ceria dispersed onto the zeolite NaX with a Si/Al ratio of 1.2 (Faujasite).⁹⁶ $^{17}\text{O}_2$ was heated with this system at 600 °C and the ^{17}O MAS NMR spectrum is shown in Figure 3.5. Two clear peaks are identified at 28 and 875 ppm, assigned to Si-O-Si/Si-O-Al and Ce-O-Ce respectively. They propose that the CeO_2 clusters act as portholes for O_2 , which then spills over to the zeolite, with exchange taking place near the NaX- CeO_2 interface, thus allowing exchange of the zeolite to occur at lower temperatures than normal.

Of the most significance to this thesis is the paper of Wang *et al.* published in 2015,⁹⁷ on the identification of different O species in nanoceria via ^{17}O NMR techniques. Nanoceria is prepared by hydrothermal methods and ^{17}O enrichment is achieved by heating samples in a $^{17}\text{O}_2$ atmosphere at a range of temperatures between 523 and 1073 K. PXRD confirms nanoparticle sizes between 4 and 42 nm (dependent on heating temperature). As a comparison, they provide data on micrometre sized bulk ceria enriched in $^{17}\text{O}_2$, for which the ^{17}O MAS NMR data indeed shows the expected single narrow peak at 877 ppm corresponding to OCe_4 , as shown in Figure 3.6 (A). For the nanoparticles however, OCe_4 at 877 ppm is much broader

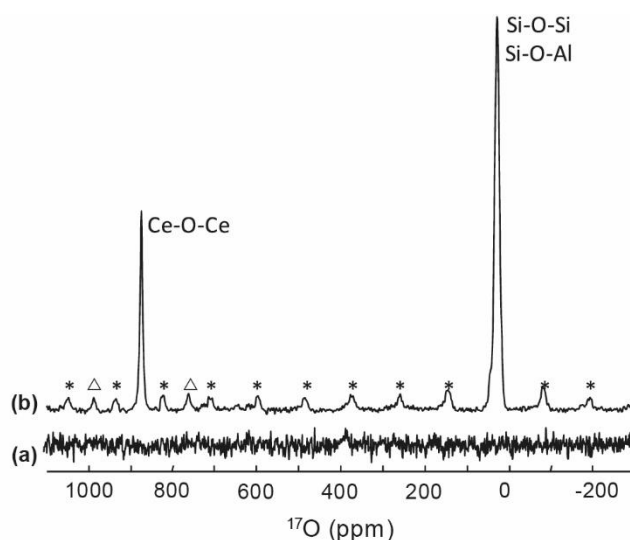


Figure 3.5: ^{17}O MAS NMR spectrum of CeO_2/NaX samples acquired at 19.9 T, using a Bruker 4 mm probe spinning at 13 kHz and a recycle delay of 60 s. (a) Before $^{17}\text{O}_2$ exchange and (b) post-exchange. Asterisks and triangles represent spinning sidebands of the peaks located at 28 and 875 ppm respectively. Reprinted with permission from Reference [96].

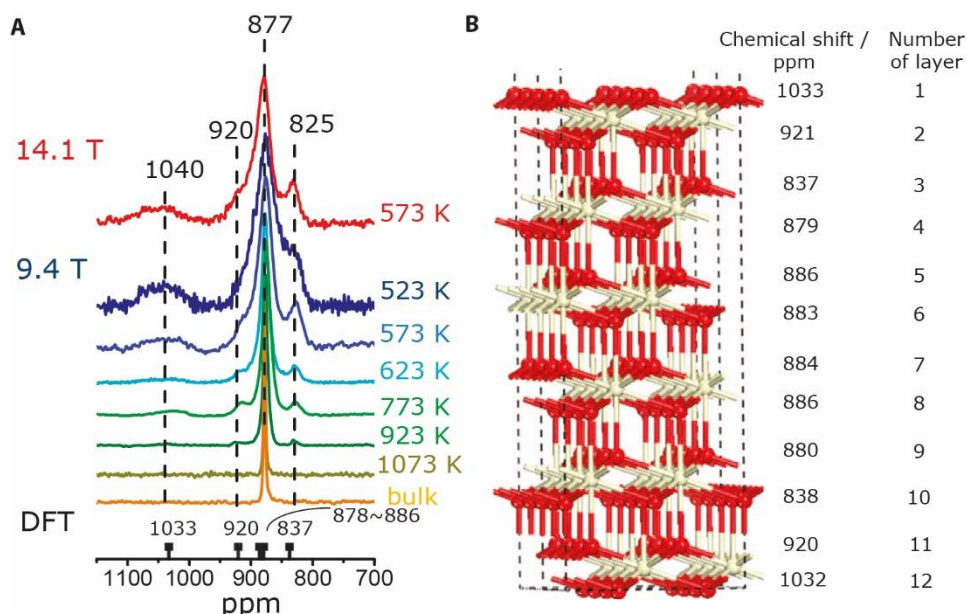


Figure 3.6: (A) ^{17}O solid-state MAS NMR spectra of nanosized ceria enriched at different temperatures compared with bulk ceria (yellow), acquired at 14.1 and 9.4 T, with respective spinning speeds of 55 and 20 kHz. $\pi/72$ to $\pi/18$ pulses for H_2O^{17} were used alongside optimised pulse delays from 1 to 100 s to ensure quantitative observations. (B) The structural model used in the DFT calculations, with red and white spheres representing oxygen and cerium ions respectively. The exposed surface is {111}, and the calculated chemical shift of ^{17}O in each layer is shown on the right. Figure from Reference [97]. Reprinted with permission from AAAS.

and additional peaks at 1040, 920, and 825 ppm are observed, with the intensities of these additional peaks decreasing with increasing particle size and thus decreasing surface area. It is proposed therefore that they are associated with the surface or defect sites, which are reinforced with shorter T_1 times (0.013, 0.038, 0.032 s for 140, 920, and 825 ppm peaks, respectively) compared to that of OCe_4 at 877 ppm (0.090 s). However, it should be noted that these values are not indicative of formal T_1 values as the experimental parameters suggest a solution $\pi/18$ pulse was used to obtain these values. The confusing nature of these relaxation measurements is further emphasised by the use of 1 to 100 s recycle delays for the experiments reported.

No shifts or broadenings of resonances are observed between 14.1 and 9.4 T, indicating small C_Q values. To aid assignments of these additional peaks, DFT calculations using the VASP platform were carried out on a slab model composed of 6 layers of Ce, 12 of O and terminated by the {111} plane, as shown in Figure 3.6 (B). Similar chemical shifts are calculated for layers 4 to 9 of ~ 880 ppm, close to the bulk

value of 877 ppm. For the three surface layers (layers 1, 2, 3, 10, 11, and 12) of the slab however, values of 1033, 921, and 837 ppm were calculated (all with C_Q values smaller than 0.14 MHz), which are remarkably close to the unassigned experimental values. The lines at 1040, 921, and 837 ppm are therefore assigned to the 1st, 2nd, and 3rd surface O species, respectively. Based on chemical shielding, the authors propose that as the peak located at 1040 ppm is less shielded than the others, this is attributed to an O species with a coordination of OCe_3 . On the other hand, they do not comment on the position of the more shielded position of their assigned 3rd layer at 837 ppm, which is 40 ppm more shielded than the bulk.

Calculations for the {110} and {100} terminated surfaces are also provided (in their SI). For the 1st, 2nd, and 3rd layers in the slab model, the calculated chemical shifts were 1061, 809, and 906 ppm, respectively for the {110} termination and 1129, 716, and 915 ppm, respectively for the {100}. The more deshielded values of their assigned 1st layer O are in-keeping with the chemical shielding trend of a less coordinated O. Furthermore, the surface O of the {100} plane is coordinated to just two cerium (as opposed to three for {111} and {100}), which complements the more deshielded value of 1129 ppm. However, no comment is made on the significant fluctuations of the values for the 2nd and 3rd layers.

To aid spectral assignments, natural abundance H_2O is adsorbed to the ^{17}O enriched nanoparticles and, following the ^{17}O MAS NMR result, observe the disappearance of the 1040, 920, and 825 ppm lines. Instead, a new signal at 850 ppm (again defined by a small C_Q) and a peak at 32 ppm appear; the latter disappears when the sample is dried under vacuum at room temperature. They therefore assign this peak at 32 ppm to H_2O adsorbed to the surface. When they heat the sample to 573 K, the peak at 850 ppm is lost and the peaks at 1040, 920 and 825 ppm return. They assign the peak at 850 ppm as the third layer in contact with H_2O (further to DFT calculations of ceria in contact with H_2O) and suggest that they don't observe layer 1 and 2 because of fast O exchange between these layers and H_2O . Reversely, they adsorb H_2^{17}O to non-enriched ceria nanoparticles at room temperature and observe a ^{17}O NMR spectrum strongly dominated by a peak at 32 ppm. Upon drying under vacuum at 373 K, this peak disappears and peaks at 1040, 877, and 270 ppm emerge from the signal. They assign this peak at 270 ppm (which is broader than the

others) to hydroxyl groups, i.e. OCe^{4+}H , based on the low chemical shift. To confirm this, they use cross polarisation (CP) and rotational echo double resonance (REDOR) NMR techniques, using the ^{17}O - ^1H dipolar coupling to ascertain a bond between the two nuclei. Both spectra reveal a resonance at 270 ppm and experimental δ_{iso} and P_Q values of 325 ppm and 5.1 MHz are approximated via the shift difference observed between 14.1 and 9.4 T. It is important to note that the drying conditions used by the authors for these set of experiments (vacuum at elevated temperatures) easily reduces ceria nanoparticles, and thus defects such as vacancies and Ce^{3+} cations are likely to be introduced during these treatments.

In order to confirm that the peaks at 1040 and 920 ppm are those of the surface and subsurface O species, prepared nanorods characterised by the {111} face are enriched via the two methods of H_2^{17}O adsorption at room temperature and heating in $^{17}\text{O}_2$. The ^{17}O MAS NMR results (SI) of these enriched rods reveals, for the $^{17}\text{O}_2$ heated sample, essentially the same peak positions as the nanoparticles, i.e. 1027, 920, 877, and 825 ppm, as seen in Figure 3.7. A comparison between Figure 3.7 (B) and (C) shows that the H_2^{17}O water dissociation selectively labels the 1027 and 920 ppm species. Based on calculations of vacancy formation energies (SI) which reveal the lowest formation energies for the 1st and 2nd layers, the authors support these two assignments. It is worth noting that a comparison between morphologies

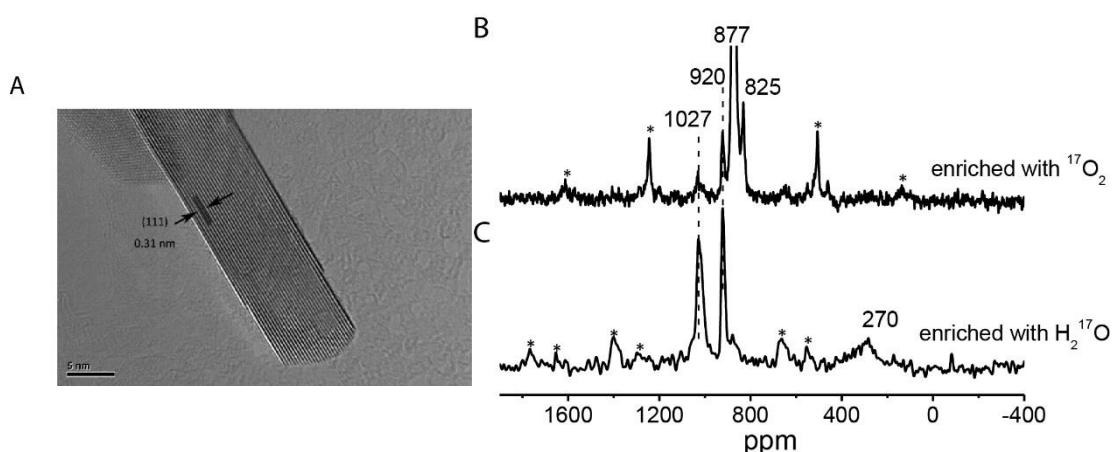


Figure 3.7: (A) Electron microscopy of ceria nanorods and ^{17}O MAS NMR spectra acquired at 9.4 T of (B) ceria nanorods enriched in $^{17}\text{O}_2$ atmosphere at 923 K and (C) ceria nanorods enriched by H_2^{17}O adsorption at room temperature followed by heating in vacuum at 373 K. Spinning speed of 20 kHz, asterisks denote spinning sidebands. Figure from (SI of) Reference [97]. Reprinted with permission from AAAS.

terminating via different planes would have been more useful here as there is no validation of the calculations for {110} and {100} surfaces.

The evolution of the peaks from the spectra of the ceria nanoparticles are furthermore observed with increasing temperature. At 773 K, most of the signal at 1040 ppm has been lost, with an intensity gain for the bulk O at 877 ppm, implying O exchange with the bulk from the surface.

Finally, they consider the presence of Ce^{3+} cations and vacancies by implementing H_2 TPR on both the ^{17}O enriched micrometre ceria and ceria nanoparticles. The ^{17}O MAS NMR spectrum of bulk ceria, reduced at 1073 K, can be seen in Figure 3.8 A. In addition to the single narrow peak observed at 877 ppm, a low intensity peak at 845 ppm was revealed. This was tentatively assigned to O ions near vacancies or oxygen ions in the second coordination sphere from Ce^{3+} . The $^{17}\text{O}_2$ enriched nanoparticles which were formerly heated to 773 K (seen in Figure 3.6 (A)), were reduced at 773 K. The narrow bulk component in Figure 3.8 B is seen to shift to 870 ppm (from 877 ppm) with a distribution towards lower frequencies. They provide DFT calculated chemical shift values in their SI for oxygen environments near

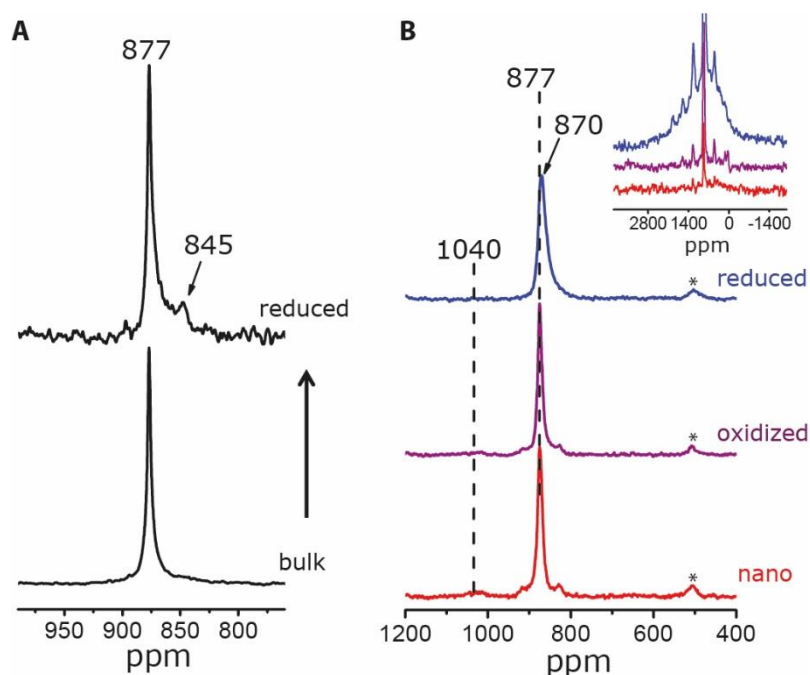


Figure 3.8: ^{17}O MAS NMR spectra acquired at 9.4 T of (A) bulk ceria enriched in $^{17}\text{O}_2$ at 1073 K (bottom) and reduced in H_2 at 1073 K (top) and (B) ceria nanoparticles enriched in $^{17}\text{O}_2$ at 773 K (bottom), reduced in H_2 atmosphere at 773 K (top) and reoxidised in air (middle). Inset shows the full sweep width. Spinning speeds were 20 kHz, asterisks denote sidebands. A rotor synchronised Hahn echo sequence was used. Figure from Reference [97]. Reprinted with permission from AAAS.

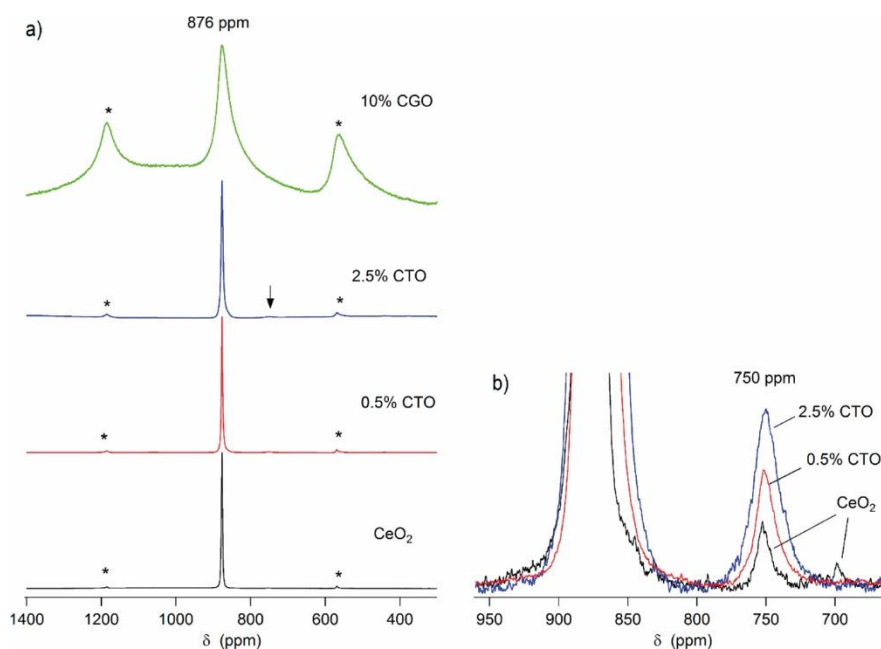


Figure 3.9: ^{17}O MAS NMR spectra of doped and pure CeO_2 . (a) full sweep width, (b) region between 650 and 950 ppm. Spinning speed of 25 kHz, sidebands denoted by asterisks. The arrow in (a) marks the smaller peaks shown in (b). Reprinted with permissions from Reference [98].

vacancies in the surface, subsurface and bulk. Across these three models, they compute an average value of 845 ppm and therefore assign the experimentally observed peak at 845 ppm as O near vacancies. The full sweep width can be seen in the inset of Figure 3.8 and it reveals a very broad component that they ascribe to O directly bonded to the paramagnetic cation Ce^{3+} , with the large distribution of chemical shifts arising from the interaction with ^{17}O and the unpaired electron via the FC interaction.

A study of pure ceria, ceria doped Ta (0.5% and 2.5%) labelled 0.5% CTO and 2.5% CTO and ceria doped Gd (10%) labelled 10% CGO was conducted in 2016 by Heinzmann *et al.*⁹⁸ which employed the ^{17}O MAS NMR technique. They achieved ^{17}O enrichment by heating the samples in a $^{17}\text{O}_2$ atmosphere for 96 hours. ^{17}O NMR data was acquired at 14.1 T using a recycle delay of 10 s. As seen in Figure 3.9, the results for CeO_2 , 0.5% CTO and 2.5% CTO show a sharp signal at 877 ppm, attributed to the bulk oxygen environment for ceria, with the peak width increasing with Ta doping. The Ta doped ceria samples reveal a further signal at 750 ppm, with a correlation of increasing intensity with an increase in dopant concentration, and assign it to O-Ta bonds. Pure CeO_2 reveals two additional low intensity peaks at 750 and 699 ppm. The

authors attribute the latter to vacancies, with the former implying that the pure CeO_2 sample has a small amount of Ta impurities.

The Gd doped ceria exhibits a much broader signal (top of Figure 3.9) due to the Fermi contact interaction between the paramagnetic Gd^{3+} cation and ^{17}O , with a broader component underlying the OCe_4 peak and sidebands.

In January of this year (2017), Hope *et al.* released a study investigating ceria nanoparticles via direct ^{17}O Dynamic Nuclear Polarisation (DNP) NMR⁹⁹ at 14.1 T. In this case DNP is used to preferentially select surface oxygen of ceria nanoparticles: spin polarisation is transferred from the unpaired electrons of radicals (impregnated into ceria) to ^{17}O , thereby achieving signal enhancements of oxygen species on the surface of the nanoparticle. 11 nm ceria particles with octahedral morphology ($\{111\}$ terminated) were enriched in $^{17}\text{O}_2$ at 623 K for 24 hours and handled in an inert atmosphere. TEM analysis after thermal treatment reveals particle sintering to 15 nm.

The impressive result obtained at 95 K, using a 60 s recycle delay is presented in Figure 3.10 and shows three peaks (in addition to the bulk at 875 ppm) at 1055, 893 and 843 ppm. They identify them as resonances associated with the 1st, 2nd, and 3rd O layers respectively, based on the work of Wang *et al.* The shift differences are acknowledged from those of Wang *et al.* (1040, 920, and 825 ppm), and are attributed to minor differences between samples.

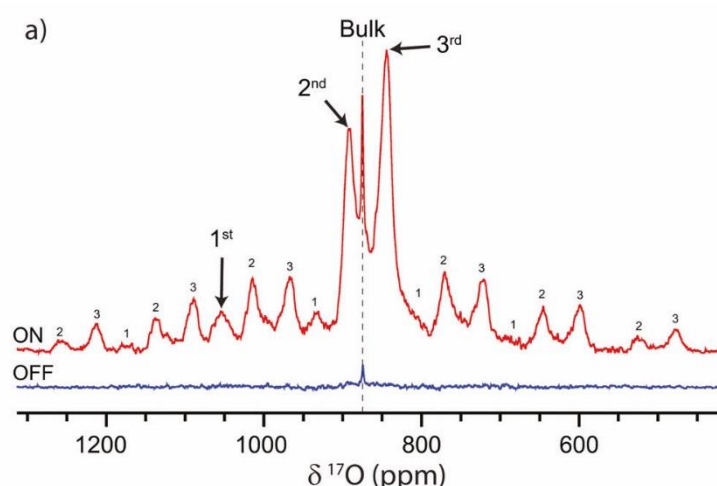


Figure 3.10: ^{17}O MAS NMR (acquired at 14.1 T and 95 K) spectra of ^{17}O enriched CeO_2 nanoparticles mixed with the TEKPol radical in TCE, with and without microwave irradiation using a presaturated Hahn echo experiment. Spinning at 10 kHz with sidebands labelled by the assigned layer that the signal originates from. Figure reproduced from Reference [99]- Published by The Royal Society of Chemistry.

For comparison, conventional ^{17}O MAS NMR is demonstrated (of a sample without radicals) for a quantitative result, which reveals that the intensities of these three peaks are in fact similar. The DNP data intensity differences are caused by quenching of the ^{17}O DNP NMR signals of the 1055 and 893 ppm oxygen environments of Figure 3.10, due to closer proximity to the radicals. The DNP build up constant T_{DNP} is measured, which is dependent on the distance between the oxygen species and radical, with polarisation transfer falling off as $(1/r^6)$. The bulk at 875 ppm has a long T_{DNP} of 1600 s as expected (bulk sites must await excess polarisation to reach them via spin diffusion), with the other three sites having much shorter T_{DNP} times of 67 ± 6 , 62 ± 2 , and 85 ± 3 s for the peaks at 1055, 893, and 843 ppm respectively. From these extracted values however, it is evident that the T_{DNP} times for the reported 1st and 2nd layers are essentially identical.

The influence of enriching the 11 nm particles under a greater $^{17}\text{O}_2$ pressure and handling in air is then explored. The ^{17}O DNP MAS NMR spectrum shows that the resonance at 1055 ppm is now absent. This is ascribed to O exchange of the assigned 1st layer with ^{16}O in the air, confirmed by exposing the ^{17}O enriched ceria nanoparticles (prepared for the conventional ^{17}O NMR analysis) to air, which indeed shows a loss of intensity over time. Furthermore, a much greater bulk intensity is observed, a result of the greater $^{17}\text{O}_2$ pressure used in the enrichment process, driving surface to bulk diffusion. Due to the greater overall enrichment level, the 893 and 843 ppm peaks are discernible via conventional ^{17}O MAS NMR after an overnight acquisition.

Indirect ($^1\text{H} \rightarrow ^{17}\text{O}$) DNP at 14.1 T reveals resonances located at 225 and -20 ppm, confirmed to be caused by direct O-H bonding and are assigned as Ce-OH and H_2O adsorbed to the ceria surface, respectively. These assignments are compared with Wang *et al.*, however as has been reviewed, these values were $\delta_{\text{iso}}=325$ ppm (300 ppm at 14.1 T) and 32 ppm for Ce-OH species and adsorbed H_2O , respectively (75 ppm and >52 ppm shift differences).

Finally, ceria nanorods enriched at 350 °C in $^{17}\text{O}_2$, with a TEM-characterised 9.1 nm thickness (terminated via the {111} surfaces) are investigated via direct ^{17}O DNP NMR (figure in the SI) as seen in Figure 3.11. The most intense and narrow signal is the bulk oxygen environment, and further signals at 1049, 873, and 850 ppm

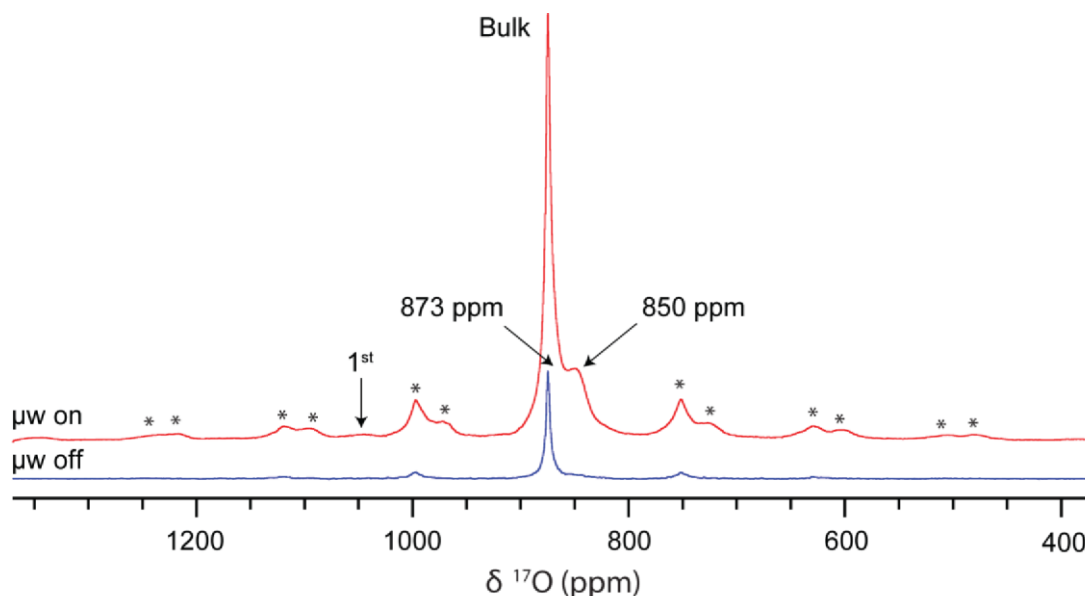


Figure 3.11: ^{17}O MAS NMR (14.1 T and 95 K) spectra of ^{17}O enriched CeO_2 nanorods mixed with the TEKPol radical in TCE, with and without microwave irradiation using a presaturated Hahn echo experiment. Spinning at 10 kHz, asterisks denote sidebands. Figure reproduced from (the SI of) Reference [99]- Published by The Royal Society of Chemistry.

assigned to 1st, 2nd, and 3rd layers, respectively, are observed. This result is not in agreement with their model. The nanorods, having more surface area than the nanoparticles, should exhibit greater intensity from the assigned surface resonances, as compared to the nanoparticles seen in Figure 3.10. This observation however is not made by the authors. Additionally, it should be noted that these values are quite different from the ^{17}O experimental measurements of Wang *et al.* for ceria nanorods (1027, 920, 877, and 825 ppm).

3.3 A Unique Case: ^{17}O MAS NMR and Frenkel Type Defects

As the single study (as far as I am aware) that combines both themes of this chapter, it warrants special attention. Heinmaa *et al.* investigated La doped ceria (LDC) by ^{17}O MAS NMR in 2010¹⁰⁰ with the data acquired via single pulse sequences (solid $\pi/2$ pulse), as shown in Figure 3.12. ^{17}O enrichment was achieved by heating samples with $^{17}\text{O}_2$ at 800 °C for 10 hours. For low dopant concentrations (0.2% and 0.5%), small peaks within 2 ppm either side of the bulk OCe_4 signal are observed and are assigned as O with La three bond lengths away, i.e. O-Ce-O-La. However, no further interpretation/validation is given. For the higher doped LDCs on the right hand side of Figure 3.12, more intense and shifted (to lower ppm) features are observed.

Gaussian fits were used on the basis that peak positions/relative intensities remained unchanged at a lower magnetic field. Following the work of Kim and Stebbins, they assign peak A as OCe_4 , B and C as OCe_3La with and without a vacancy on the La^{3+} cation, respectively, and D to OCe_2La_2 . The authors note however, that the probabilities of these sites (for a random distribution of La model) do not fit with the integrated intensities. Whilst this could be caused by the use of a solid $\pi/2$ flip angle (resulting in varying nutation rates and thus non-quantitative spectra), the relatively hard pulse used here may also be exciting the satellite transitions of peak A (possible for small C_Q environments), resulting in two of the smaller peaks either side of these spectra. Furthermore, it is also likely that discrepancies would exist regardless, due to a non-random distribution of La within the ceria lattice, i.e. that there is short range ordering/La surface enrichment, or ^{17}O exchange under the conditions of the ^{17}O labelling could be selective.

T_1 was measured for the bulk peak at a range of temperatures. The relaxation curves are characterised with two maxima at 327 and 727 °C, assigned to relaxation paths A and B, respectively. They assign the high temperature process to O hopping through vacancies. Interestingly, the low temperature process is ascribed to O

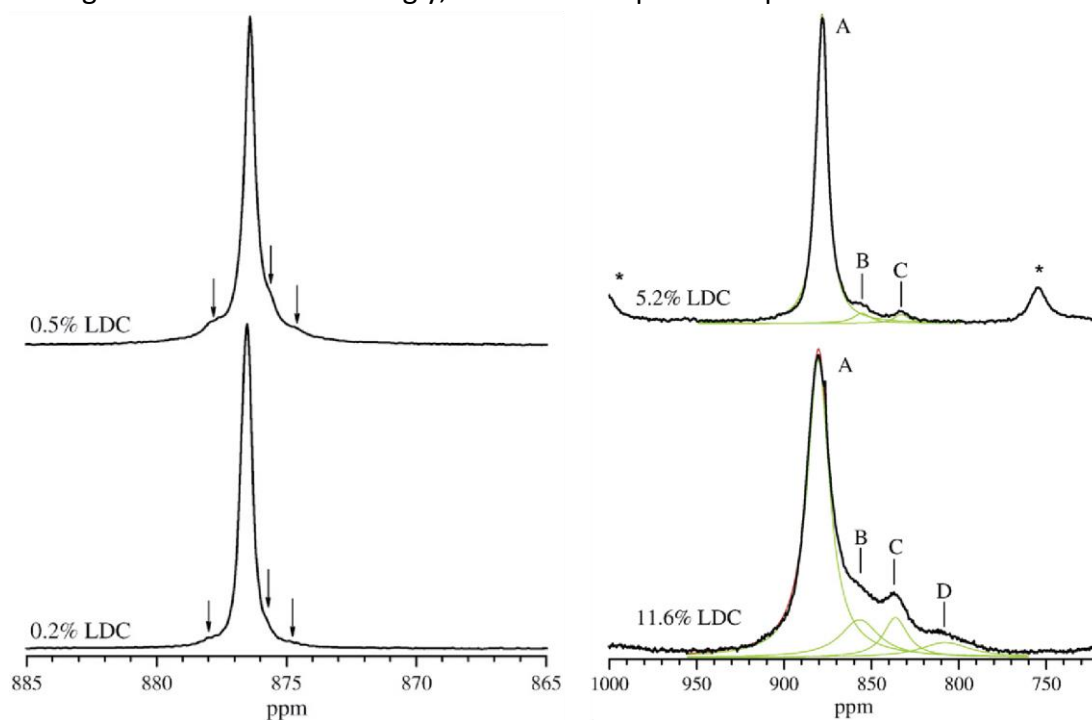


Figure 3.12: ^{17}O MAS NMR spectra of ^{17}O enriched LDCs. Arrows point out small peaks and A, B, C, and D refer to OCe_4 , OCe_3La with a vacancy (on the La^{3+}), OCe_3La without a vacancy, and OCe_2La_2 , respectively. $\nu_r = 10$ kHz. Reprinted with permission from Reference [100].

hopping between the regular lattice site and a second lattice site. Their conclusions are based on neutron diffraction studies by Yashima⁹⁵, in which it was seen that, for pure ceria, 5% of the total O were not in their lattice sites. Whilst not explicitly stated, the literature evidence presented in Section 3.1 suggests that Heinmaa *et al.* are describing the Frenkel-type defect. If this is the case, then the resonance of the Frenkel oxygen environment may be present in Figure 3.12.

3.4 Conclusions

3.4.1 Frenkel Defects

Frenkel defects in ceria were formally proposed by Mamontov and Egami due to observations made from several previous studies. Their own investigations using neutron diffraction of ceria and ceria zirconia conclusively revealed the presence of Frenkel defects in both systems, with greater amounts shown for ceria zirconia. In light of their research, Raman spectroscopy has dominated the ceria- Frenkel-defect field, ascribing its Raman band wavenumber to $\sim 590\text{-}600\text{ cm}^{-1}$, and that of ceria zirconia to $> 600\text{ cm}^{-1}$. It seems that the significance of Frenkel defects to ceria's OSC relates to its ability to promote access to bulk oxygen. However, it is not yet known whether they:

- (1) contribute to the active oxygen species that move through the structure, and/or
- (2) allow a more open structure/less rigid lattice for oxygen to move through.

3.4.2 Solid-state ^{17}O MAS NMR

The ^{17}O NMR studies reviewed in this chapter are (as far as I am aware) the complete literature on ceria. Whilst exhaustive in the experimental details divulged, the significance of the summarised data reveals the following key points:

- Spectra are (probably) not always quantitative due to long pulses and/or short recycle delays. Due to the difficulty in obtaining T_1 data, this is not usually investigated, but should be considered in quantitative analysis.
- With the exception of Ce-OH species, no shifts with field are observed, regardless of dopant (C_Q values are small).
- Whilst Chapter 1 emphasized the importance of sample preparation and treatment, it is apparent that ceria's unique OSC process is not always

considered in the interpretation of ^{17}O NMR results. For example, ^{17}O exchange can be selective depending on the preparation conditions, and so the modelling of random distributions to correlate with ^{17}O peak intensities may be erroneous.

- ^{17}O NMR is extremely sensitive to ceria's seemingly simple structure and/or its sample preparation. Even between studies of pure ceria, with the same surface terminations and similar particle sizes, the spectral profiles can vary drastically, in both peak positions and intensities.
- The current models describing/assigning ^{17}O NMR spectra reveal significant inconsistencies.

Chapter 4

Experimental Details

Chapter 3 demonstrates that limited ^{17}O solid-state NMR data exists for ceria, with most literature published from recent studies. There are a few reasons for this; firstly, of the five isotopes (three oxygen and two cerium) that compose the ceria system, only ^{17}O is NMR active. Furthermore, ^{17}O comprises just 0.037% of the oxygen total which, unless an oxygen environment is highly symmetrical (causing an almost negligible C_Q and therefore narrow resonance), will not result in an NMR signal that rises above the noise level of the spectrometer. Bulk-like, micrometre-size ceria is however one such case due to the point symmetry of the single, magnetically-equivalent oxygen of the cubic fluorite structure, as first illustrated by Bastow & Stuart.⁸² Even for this perfect case, acquisition times are on the scale of days. For oxygen environments that don't fulfil these criteria therefore (rendering ^{17}O NMR measurements unfeasible on a practical timescale), ^{17}O isotopic enrichment of samples, typically via labelled water (H_2^{17}O) or labelled oxygen gas ($^{17}\text{O}_2$), is necessary. Due to their great expense, enrichment levels are typically dependent on the user requirements, i.e. the intended experiments (10% for 1D and 35% for 2D spectroscopy)⁷⁰ as well as any limiting factors of oxygen exchange via the enrichment process, e.g. dilution from precursors, necessary heating of the sample after preparation which causes ^{17}O losses, etc.

Ceria and ceria systems have been ^{17}O labelled via both processes in the past, also detailed in Chapter 3. Chapter 5 investigates the influences of preparing ceria by both of these means. Furthermore, due to ceria's OSC process, it is possible to ^{17}O enrich reduced ceria systems in order to observe the O environments that represent the releasable oxygen, and their subsequent reoxidation pathway.

The following section describes the preparation of ceria from a H_2^{17}O precursor, followed by a novel $^{17}\text{O}_2$ enrichment method used on samples obtained from several sources, including Johnson Matthey in-house ceria systems.

4.1 Sample Syntheses

4.1.1 H_2^{17}O Synthesised Ceria: H_2^{17}O Ceria and H_2^{17}O Ceria 500 °C

$(\text{NH}_4)_2\text{Ce}(\text{NO}_3)_6$ (1.654g, 3 mmol) was dissolved in water (1 ml) and H_2^{17}O (1 ml). A 10 ml beaker was charged with water (1 ml) and H_2^{17}O (1 ml). N_2 gas was bubbled carefully through a Dreschel bottle freshly charged with concentrated NH_3 and then into the water for 5 mins at pH ca. 12. A small stirrer bar was placed in the ammonia/water and the ammonium ceric nitrate solution was added dropwise. A precipitate formed immediately with pH 10. The precipitate slurry was stirred for circa 10-15 mins and then collected by filtration. Anhydrous ethanol (10 ml) was used to aid the transfer of the precipitate to filter paper/to wash precipitate (water was not used in order to prevent ^{16}O exchange with the surface). The sample, from now on labelled H_2^{17}O Ceria, was left drying on the filter bed for 1 h and then transferred to a covered evaporating dish and left to dry at ambient temperature for 4 days.

After characterisation data was acquired on H_2^{17}O Ceria, the sample was heated at 500 °C for an hour and is defined as H_2^{17}O Ceria 500 °C.

4.1.2 Materials for $^{17}\text{O}_2$ Enrichment Methods

The principal sample investigated in Chapter 5 is defined as a high surface area ceria (HSA20) and is bought in from Rhodia (of the Solvay Group) by Johnson Matthey, along with HSA20 with a 1% Pd loading (HSA20-1%Pd), zirconia doped ceria materials: $\text{Ce}_{0.75}\text{Zr}_{0.25}\text{O}_2$, $\text{Ce}_{0.5}\text{Zr}_{0.5}\text{O}_2$, $\text{Ce}_{0.25}\text{Zr}_{0.75}\text{O}_2$, and $\text{Ce}_{0.5}\text{Zr}_{0.5}\text{O}_2$ -1%Pd. Synthesis details of these systems are unknown. Ceria rods and cubes, with and without a 1% Pd loading were obtained from Professor Edman Tsang's group from the University

of Oxford, prepared by Abdul Hanif Mahadi¹⁰¹ and 25 nm CeO₂ was bought in from Sigma Aldrich.

Four 1 L O₂ gas canisters with a 99.9% purity and isotope composition ¹⁷O (71%), ¹⁶O(25.6%), and ¹⁸O (3.3%) were bought in from Cortecnet (France) and is defined as ¹⁷O₂ in this work. Impurities: CO, CO₂, H₂, and N₂ made up the remaining 0.1%.

4.1.3 ¹⁷O₂ Exchange and ¹⁷O₂ Redox Experiments

The ¹⁷O₂ labelling procedures developed for this work were established within the confines of three factors: ceria's OSC mechanism, the form of ¹⁷O label (70% ¹⁷O gas) that is readily available/affordable, and the restrictions imposed by the instrument that facilitated the exchange processes.

0.3 g of the above mentioned materials (Section 4.1.2) was placed in a quartz three-port U-tube reactor supported between quartz wool (ultra-fine grade) and connected in a through flow fashion to a Quantachrome Autosorb-iQ-C Analyzer. The third port, as demonstrated by Figure 4.1, is positioned on the side of the reactor and sealed by a rubber septum. Two different sample treatments were used, one where the ¹⁷O₂ was directly exchanged with the samples (defined as ¹⁷O₂ exchange) and the other where the samples were prereduced and reoxidised with ¹⁷O₂ (defined as ¹⁷O₂ Redox).

The ¹⁷O₂ exchange protocol (designed into a macro) and simply shown in Figure 4.1(a) was as follows. The system was purged with He, and a short evacuation down to to ~ 0.1 mmHg was achieved. The temperature was increased to 40 °C, 30 mL ¹⁷O₂ was injected into the system to an average pressure of 600 mmHg (~ 0.8 atm) and a temperature ramp of 20 °C /min increased the temperature to 600 °C. This temperature was held overnight (~ 20-22 hours).

The ¹⁷O₂ redox protocol (also designed into a macro) as shown in Figure 4.1(b) was as follows. The system was purged with He, and a temperature ramp of 20 °C /min increased the temperature to 700 °C. H₂/N₂ (5%/95%) was flowed in eight incremental injections from 0 to 760 mmHg over the course of ~ 2 hours. The H₂/N₂ flow was removed and the system was evacuated for 20 mins to remove residual H₂ and the system was cooled back to room temperature. The characteristic yellow of

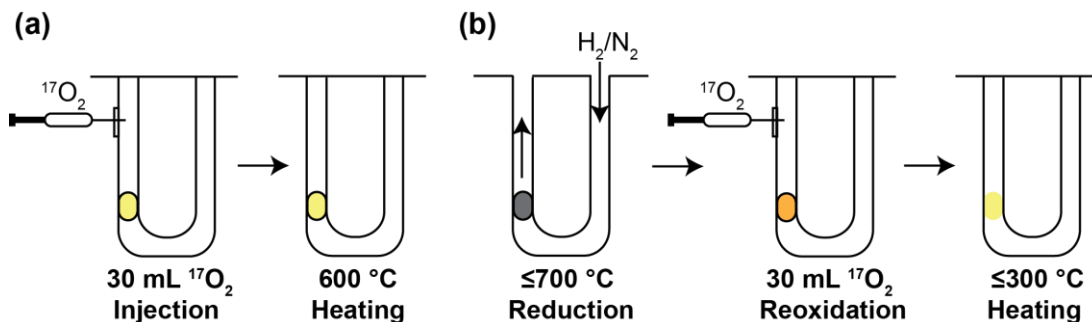


Figure 4.1: Diagrams depicting the ^{17}O enrichment methods using $^{17}\text{O}_2$ (70%/30% $^{17}\text{O}/^{16}\text{O}$ oxygen gas) in this work. (a) Direct $^{17}\text{O}_2$ injection followed by heating at 600 °C, and (b) prereduction via (5%/95%) H_2/N_2 followed by $^{17}\text{O}_2$ reoxidation and heating at temperatures up to 300 °C. The $^{17}\text{O}_2$ is injected through the third port on the reactor, through a rubber septum.

oxidised ceria changed to dark grey/ black after this reduction process for ceria/ceria mix systems. 30 mL of $^{17}\text{O}_2$ was injected into the reactor to an average pressure of 600 mmHg, and either left at room temperature, or heated to 150 or 300 °C for an overnight (~ 18-20 hour) soak.

After both treatments ($^{17}\text{O}_2$ exchange and $^{17}\text{O}_2$ redox), the reactors were briefly evacuated to remove the oxygen atmosphere, and backfilled with Ar. All samples were then packed into NMR rotors in a glovebox under Ar conditions.

Some restrictions of the systems included a maximum reoxidation temperature of 300 °C for the $^{17}\text{O}_2$ redox process and the inability to read the cell pressures when systems were put under temperature. ~ 0.8 atm pressures were used as this allowed for pressure increases whilst heating ‘blind’.

One further point is pertinent concerning the experimental procedures used here. Mass-dependent isotope fractionation effects that influence isotope exchange mechanisms and kinetic processes will most likely be influencing isotope loss/uptake here, as described by Hayles and Bao,¹⁰² but this examination is beyond the scope of this work.

4.1.4 Peroxide Ceria and H_2O_2 synthesis from $^{17}\text{O}_2$

Based on the study by Damatov & Mayer¹⁰³ in 2016, ^{17}O labelled (0.16%) hydrogen peroxide was added to a solution of CeO_{2-x} to stabilise peroxide-like species on to the surface of ceria nanoparticles.

^{17}O labelled H_2O_2 was synthesised via a direct combination technique of H_2 and O_2 in a stirred autoclave. The total vessel pressure was 32.4 bar, with 0.9 bar of 70% labelled O_2 gas and 31.5 bar H_2 (2.22%) N_2 (58.18%) and O_2 (39.6%). The reaction was catalysed over 27.1 mg Pd catalyst with a 20 ml acidic reagent solution of 0.5 M HNO_3 + 0.0006 M NaBr used to decrease decomposition of H_2O_2 . The reaction temperature was at 23 °C (room temperature), stirred at 1000 rpm and held under these conditions for four hours. The concentration of H_2O_2 in H_2O was measured by titration to be 0.16%. Due to the cost of $^{17}\text{O}_2$ and the difficulty in its removal from the gas cylinder, only 5% of the oxygen in the system was calculated to be ^{17}O .

4.1.5 ^{17}O and ^1H NMR Experimental Details

^{17}O MAS NMR spectra were obtained from two different locations: Johnson Matthey Technology Centre (Reading) on a Bruker Avance III 400 MHz spectrometer (9.4 T), and the University of Warwick facility using instruments: 400 MHz Bruker Avance III HD (9.4 T), 500 MHz Bruker Avance III (11.7 T), 600 MHz Bruker Avance II+ (14.1 T) and 600 MHz Sweepable Varian spectrometer (14.1 T). 4 mm HX/ HXY probes were chiefly used, with ZrO_2 4 mm rotors, with the occasional implementation of 3.2 mm and 2.5 mm probes where faster spinning was necessary. Data acquisition and processing were facilitated by Topspin and VnmrJ software.

^{17}O spectra were referenced to $\text{H}_2\text{O}(=0)$ and not the recommended IUPAC reference of $\text{D}_2\text{O}(=0)^{104}$ so that chemical shifts are in line with the ^{17}O literature (which very rarely uses D_2O). ^{17}O measurements were acquired on all field strengths listed above, with Larmor frequencies of $\omega_0=81.34$ MHz at $B_0=14.1$ T, $\omega_0=67.78$ MHz at $B_0=11.7$ T, and $\omega_0=54.23$ MHz at $B_0=9.4$ T. Pulse lengths were calibrated on H_2O , with 'solid' pulses scaled by $1/(I+1/2)=1/3$.

Single pulse measurements were acquired with solid $\pi/4$ pulses (or $\pi/12$ solution pulses) as a compromise between increasing S/N and obtaining quantitative results; quadrupole interactions are small. For these reasons, 90- τ_1 -180- τ_2 Hahn echo sequences were implemented instead of solid echo sequences (both of which were described in Section 2.5.4). To reach maximal peak intensities, Hahn echo experiments were rotor synchronised by setting τ_1 (the inter-pulse delay) to $1/\nu_r$. The second delay τ_2 (in which time the coherence is refocused) was set to $\tau_2 < \tau_1$ in order

to observe the echo top, ensuring no loss of FID. The FID was left shifted to the echo top before Fourier transformation. Single pulse measurements and Hahn echo experiments were collected with transients between 1024- 155,000, depending on recycle delay used, which took values between 0.25 and 120 s.

Variable temperature measurements were facilitated by a Bruker H12083 4mm HX probe between -20 and +58 °C under MAS at 14.1 T.

4.2 Powder X-ray Diffraction

Powder X-ray Diffraction (PXRD) is used in this thesis to determine phases (where possible) and to estimate crystallite size using the Scherrer Equation. All PXRD measurements were acquired by angle dispersive diffraction (ADD) in which the x-ray source is monochromatic and the detector is incremented by 2 θ steps.

Powder XRD patterns were collected with a Bruker AXS D8 diffractometer operating at 40 kV and 40 mA, over a 2 θ range 10-130°, and sampled at a 0.044° step size.

4.3 Raman Spectroscopy

Raman spectra were recorded on a Renishaw inVia Reflex system with scattered light collected in backscattering geometry. A laser excitation of 532 nm was used, delivering ~50 mW power (at 100% laser power) at the source, focused with a microscope with either a 50x or 20x objective lenses and coupled with a CCD detector. Spectra were acquired with a 1800 g/mm diffraction grating, giving a spectral resolution of 2 cm⁻¹. Wavenumber calibration was achieved using the 520.5 cm⁻¹ signal of silicon. WiRE software was used to collect the data. 1s exposure times resulted in typical spectral acquisitions of 64 s (for static scans). Data (wxd files) were converted to txt for analysis and processing carried out in OriginLab. Unless otherwise stated, all Raman spectra are normalised to the F_{2g} peak of the cubic fluorite structure.

4.4 Magnetisation Measurements (SQUID)

Magnetic measurements were conducted on a Quantum Design MPMS 5S SQUID Magnetometer (5T), which has a 5×10^{-8} emu resolution, at 300 K. The sample was supported in a plastic straw within a gelatine capsule and moved through a

superconducting wire. Magnetisation as a function of field (M vs H) plot was obtained by taking measurements of the change in magnetic flux density of the superconducting wire, induced as the sample passes through it. Measurements were taken every 40 mT from 0 to 120 mT, and every 0.2 T up to 1 T and reversed back down to 0 T. These measurements were repeated with H along the opposite directions, resulting in the full response curve.

4.5 H₂ TPR Measurements

H₂-TPR data for all TPR results were attained using conventional flow apparatus under a 10% H₂/N₂ 30 ml/min flow, the thermal conductivity of which was measured pre and post contact with the sample. The temperature was ramped linearly with time and H₂O, the result of H₂ oxidation, was removed from the gas flow via a cold trap. Typically, H₂ consumption is quantified by integration of the TPR profile, however for the purposes here, these data were not required.

4.6 Computational Details

First-principles quantum-mechanical calculations were carried out using Kohn-Sham density functional theory (DFT) using the CASTEP 16 software.¹⁰⁵ This code can calculate the electronic properties of periodic solids using a plane-wave basis set under the pseudopotential approximation. Unless otherwise stated, all calculations reported in this thesis employed ultrasoft pseudopotentials that were generated on-the-fly (OTF) using the default CASTEP 16 pseudo-atom definitions in conjunction with the Perdew-Burke-Ernzerhof (PBEsol)¹⁷⁶ generalised gradient approximation (GGA) for the exchange-correlation functional.

The basis-set convergence was calibrated with respect to the planewave basis set size and Brillouin zone k-point sampling to a minimum accuracy of 0.25 mH per atom. This level of accuracy was achieved using a plane-wave cut-off energy of 900 eV and k-point Monkhorst-Pack grids of 3x3x3 for Na₂MoO₄ and Na₂WO₄, 5x5x4 for SiO₂, 5x5x3 for ZnO and 5x5x5 for CeO₂, respectively.

Geometry optimisations were converged to the default CASTEP 16 tolerances: a maximum force 0.05eV/Å on any atom and a maximum change in energy of 2x10⁻⁵ eV per optimisation step. The maximum force change for the

electronic structure calculation at each geometry optimisation step was reduced to 10^{-4} eV/Å to guarantee an accurate wavefunction.

The gauge-including projector augmented-wave (GIPAW) DFT method was used to calculate NMR parameters for the relaxed structures. For all NMR calculations the over-converged plane-wave basis set and k-point Monkhorst-Pack grids outlined previously were considered sufficient to produce fully converged NMR parameters. The magnetic shielding parameters calculated for ZnO, SiO₂, Na₂MoO₄, Na₂WO₄ (ICSD entry codes: 157724, 173227, 2133, and 151970), were used to create a linear calibration curve ($\delta_{\text{iso}}(^{17}\text{O}) = -1.0257(\sigma_{\text{cal}} - 250.2876)$) to reference all calculated ^{17}O magnetic shielding parameters for ceria. This curve was additionally used to calibrate a shift for the 4f orbital of the pseudo-atom definition in order to compensate for the hybridisation of the unoccupied 4f state with the O 2p states. The empirical shift was adjusted until the magnetic shielding value for bulk ceria, assuming $\delta_{\text{iso}}(^{17}\text{O}) = 877$ ppm, was consistent with the linear calibration curve. This was achieved using a +0.4135 Ha shift in the Ce 4f orbital.

The supercell approach was employed to model the intrinsic Frenkel defect for ceria. A 3×3×3 supercell was created from the room temperature CeO₂ structure taken from the ICSD (entry code: 9009008). An oxygen atom was displaced from its sublattice position so that it occupied the theorised Frenkel position in the middle of the unit cell (0.5, 0.5, 0.5) and accompanying vacancy. The structure was geometry optimised as outlined above except that the Frenkel oxygen was fully constrained and a random displacement of 0.2 Å was added to all atoms before the structure relaxation.

The calculated ^{17}O NMR parameters were used to simulate ^{17}O NMR spectra for the structure using SIMPSON¹⁷⁷. All calculations were performed on the world-class ARCHER UK National Supercomputing Service as allocated by the Materials Chemistry Consortium.

Chapter 5

An Investigation of Ceria

Chapters 1 and 3 have introduced the reader to some basic ceria background and previous literature that has emphasized a rich and complex chemical and structural nature; ceria's complexities should not be underestimated. This chapter shall introduce some contradictory NMR theories to those currently held. In particular, the final two sections shall present evidence that deviates from the current ^{17}O NMR model, initially put forward by Wang *et al.* Their core-shell model attributes ^{17}O resonances (additional to the bulk species) to the first three layers of oxygen in a nanoparticle, based on DFT calculations of the NMR parameters.⁹⁷ An alternative proposal is presented that assigns these distinct ^{17}O resonances to oxygen sites generated by the concomitant lattice distortion induced by vacancies and Frenkel defects. Furthermore, these oxygen environments show a Curie dependence under varying temperature, implying that some nuclear environments are in varying proximity to Ce^{3+} paramagnetic centres. This phenomenon has been observed in three different solid-state ^{27}Al and ^{89}Y NMR studies of Ce^{3+} doped YAG by McCarty & Stebbins,¹⁰⁶ George *et al.*,⁷⁵ and He *et al.*¹⁰⁷ and is further supported by ^{17}O NMR studies of paramagnetically doped cubic oxides, also by McCarty and Stebbins.⁷⁴

Firstly, this chapter studies pure ceria systems that have been prepared (for ^{17}O NMR observation) by different routes, that range through the nanoscale, and finally that adopt different morphologies. They are characterised via solid-state ^{17}O MAS NMR techniques, alongside Raman spectroscopy, which plays the role of a

scientific control technique on account of its heavy presence in the ceria literature. Raman spectroscopy can reveal the presence of distinct oxygen environments, surface adsorbates, lattice defects, and phase distinctions and therefore is used here to map correlations with the ^{17}O NMR data. PXRD, SAXS, TPR, DFT calculations, and to a lesser extent, TEM, XPS, and SQUID measurements are also used to provide complementary data. Attempts (including both failures and triumphs) at assigning and interpreting the acquired data are then reported. To avoid confusion, I refer to 'ceria' as opposed to CeO_2 when referring to the real systems reported here (as they are certainly not 100% stoichiometric).

5.1 H_2^{17}O Ceria and H_2^{17}O Ceria 500 °C

As described in Chapter 4, ceria was synthesized via a H_2^{17}O route (^{17}O at 40%) in which, importantly, ^{17}O is free to occupy all oxygen sites equally and is here defined as H_2^{17}O Ceria. This sample was then heated at 500 °C and labelled H_2^{17}O Ceria 500 °C, in order to alter intrinsic defects and sinter particle size. These systems were synthesized and handled in air. Here follows a PXRD, Raman spectroscopy, and solid-state ^{17}O NMR analysis.

5.1.1 PXRD and SAXS

The diffractograms obtained from the PXRD of H_2^{17}O Ceria and H_2^{17}O Ceria 500 °C are shown in Figure 5.1. Rietveld refinement was used to fit the scattering patterns against a full structural model for a cubic CeO_2 phase (no other phases were present) with Pawley analysis used to extract lattice parameters a of 5.424(2) and 5.4102(3) Å and crystallite sizes of <2 nm and 11 nm for H_2^{17}O Ceria and H_2^{17}O Ceria 500 °C, respectively. The nano-particulate nature of H_2^{17}O Ceria is clear from the exceptionally broad lines of Figure 5.1(a) and the larger a value of 5.424 Å indicates a 2.4% lattice expansion as compared to bulk ceria (5.411 Å)⁶². The 2.4% lattice expansion seen here is consistent with that found for a 2 nm ceria particle via a TEM study (2.6%) by Hailstone *et al.*¹⁰⁸ The expansion was attributed to the strain caused by significant amounts of Ce^{3+} cations (larger than Ce^{4+}) and vacancies. They

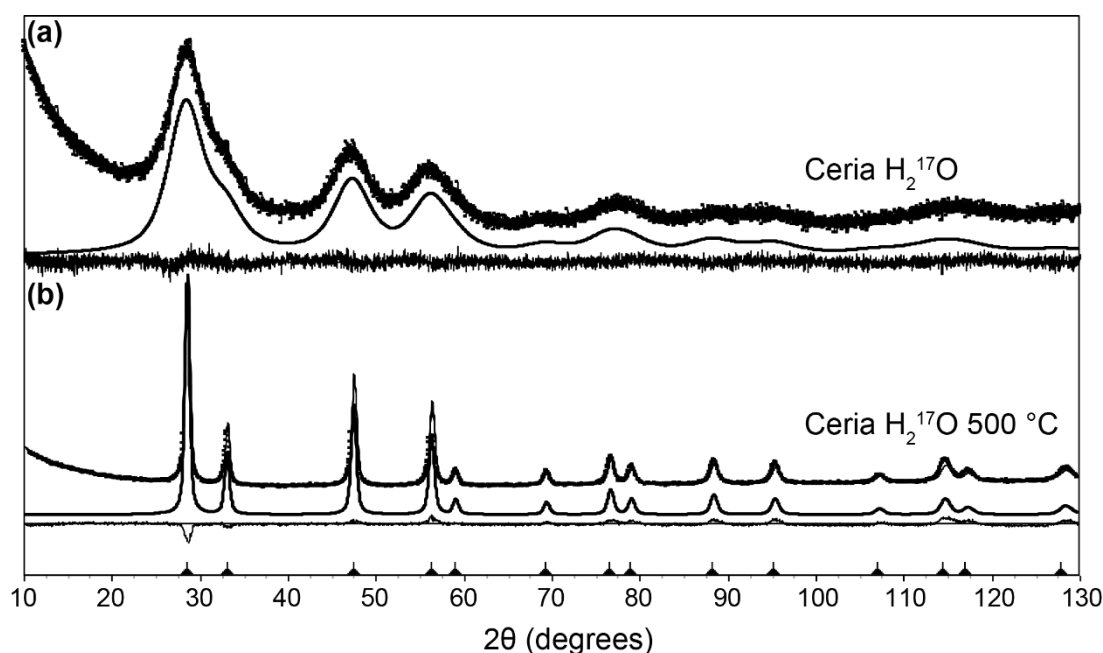


Figure 5.1: XRD patterns of (a) H_2^{17}O Ceria and (b) H_2^{17}O Ceria 500 °C.

ascertained that for particles down to 1 nm (80% surface), the fluorite lattice is still retained.

Small angle x-ray scattering (SAXS) provides a more accurate measure of particle size, in addition to elucidation of particle size distribution. SAXS measurements of these systems (found in Appendix B) reveal particle sizes of 1.5 and 4.7 nm, and particle size distributions of 0.8 and 7.2 nm for H_2^{17}O Ceria and H_2^{17}O Ceria 500 °C, respectively. It is evident that the Scherrer equation overestimates the particle size for samples with a large particle size distribution.

5.1.2 Raman Spectroscopy

Figure 5.2 (a) shows four Raman spectra acquired for H_2^{17}O Ceria, with the sample showing an irreversible structural change as a function of laser power. Laser powers were increased from 0.86 to 7.8 mW and cycled back down again. Starting with the top spectrum collected at low power (which is below the sample modification threshold), several dominant peaks are present, in addition to the single and strong F_{2g} mode of the CeO_2 fluorite phase (symmetrical stretching of the CeO_8 cube), normally observed at 464 cm^{-1} . The F_{2g} band in Figure 5.2 (a) is instead considerably softened and shifted to lower energy at 450 cm^{-1} , indicating an increase of lattice constant due to the small particle size/increase in Ce^{3+} present, and is considerably

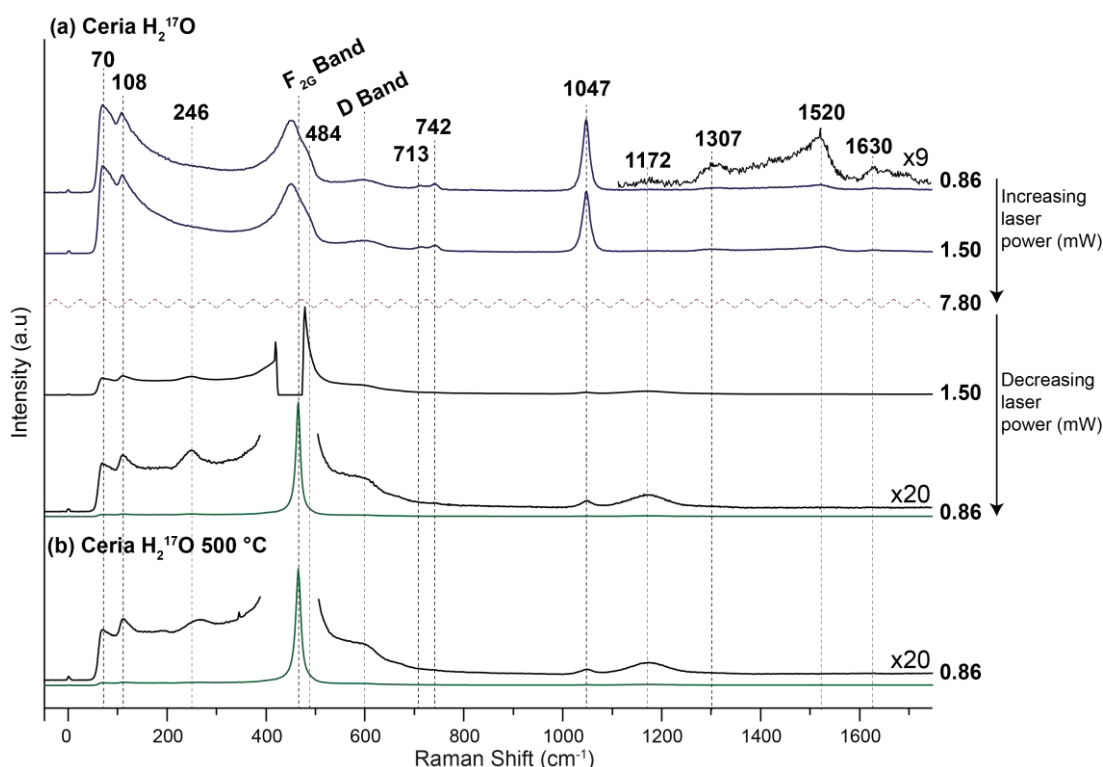


Figure 5.2: Raman spectra acquired with $\lambda_{\text{ex}}=532$ nm for (a) H_2^{17}O Ceria and (b) H_2^{17}O Ceria 500 °C. All Raman spectra are normalised to the $\text{F}_{2\text{G}}$ peak.

broadened with an asymmetrical tailing towards lower energies, alluding to an inhomogeneous strain broadening caused by a dispersion in particle size and phonon confinement.¹⁰ The broad peak at 600 cm^{-1} is attributed to Frenkel defects, with an additional band between 540 and 560 cm^{-1} , due to cation-vacancy vibrations,¹⁵ which is typically observed but can be obscured by the bands either side when particle size is small, i.e. the Frenkel defect band at 600 cm^{-1} becomes comparable in intensity and the $\text{F}_{2\text{G}}$ band is broad, as is the case here. It is conventional to call this overall Raman region the defect (D) band (between 540-600 cm^{-1}) and is often relied upon to indicate sample defect concentration.

The bands at 713 and 742 cm^{-1} are those of bonded nitrates whilst the intense signal at 1047 cm^{-1} is that of free nitrate¹⁷⁴, indicating an incomplete decomposition of the ammonium ceric nitrate during sample synthesis.¹⁰⁹ Other features of the spectrum are the very intense low energy bands found at 70 and 108 cm^{-1} , with a broad distribution extending to higher energies. These are characteristic modes of nanoceria and have been assigned to confined acoustic vibrations of spherical nanoparticles,¹¹⁰ with the band positions dependent on particle size.¹¹¹ The spectra

Table 5.1: Parameters extracted from Raman data presented in Figure 5.2.

	F_{2G} (cm^{-1})	D (cm^{-1})	$I_D / I_{F_{2G}}$	Γ of F_{2G} (cm^{-1})	Ce-OH (cm^{-1})
H_2^{17}O Ceria	450.0 ± 0.4	600	0.174	77 ± 2	246
H_2^{17}O Ceria 500 °C	463.8 ± 0.1	600	0.016	12 ± 0.3	252

shown in Figure 5.2 are quite unique to the literature. Such a large (14 cm^{-1}) Raman shift of the F_{2G} mode is usually observed for highly defective ceria, when reduced at high temperatures,¹¹⁰ or ceria synthesized under controlled (oxygen deficient) conditions to expose the more catalytically-active surfaces.¹⁵

An increase of the laser power leads to irreversible spectral changes. The bottom spectrum of Figure 5.2 (a) is drastically altered, now dominated by a narrow F_{2G} band positioned at 463.8 cm^{-1} , more typical of crystalline ceria. Heating from the laser has structurally sintered the sample (as well as removed most of the nitrates), behaviour that is documented in the literature. In fact, localised temperatures between 400 and 2000 K have been measured for powers between 0.6 and 4.2 mW, respectively for a $\text{MnO}_x\text{-CeO}_x$ composite (an extreme case however as manganese oxides have strong light-absorption properties).¹¹² Moreover, additional signals at 246 cm^{-1} , 670 cm^{-1} and 1174 cm^{-1} are also now apparent, the former of which has previously been assigned as a second-order transverse acoustic mode (2TA) vibration of the lattice,^{16,66} to a cation-vacancy vibration,¹¹³ and more recently as a Ce-OH vibration,¹⁰⁹ and the latter two are attributed to second-order longitudinal optical (2LO) modes of the F_{2G} band⁵⁹ (overtone and combination band- recall Section 2.5).

The Raman spectrum acquired for H_2^{17}O Ceria 500 °C is shown in Figure 5.2 (b) and is identical to the (high power) laser-heated H_2^{17}O Ceria spectrum. This compatible result further confirms the crystallisation of H_2^{17}O Ceria by heating from the Raman laser. The intensities of the two modes $I_{F_{2G}}$ and I_D are frequently used to infer relative oxygen vacancy concentration^{16,58} based on the assumption that total defect concentration is approximately quantitative with relative Raman intensities.¹⁵ Relative intensities of both samples are shown in Table 5.1 and reveal that there is an order of magnitude loss in defects after heating at 500 °C in air.

Many studies use the half width (Γ) of the F_{2G} band to calculate particle size^{10,114-116} however, a study conducted by Hess *et al.* in 2016¹⁰⁹ reveals that this can be erroneous as, in addition to size effects, Γ is also dependent on the presence of bulk defects and therefore preparation methods.¹⁰ Alternatively, they suggest that for a given crystallite size, the defect density of ceria nanoparticles can be inferred from Γ .

Finally, it should be noted that isotope effects from ^{17}O incorporation into the ceria network may cause some additional broadening and band shifts (more severely for O-O bands) as compared to Raman band values of natural abundance oxygen (^{16}O) in the literature. In an $^{18}\text{O}/^{16}\text{O}$ exchange Raman study of ceria (81 nm particle size), the F_{2G} band shifted 17 cm^{-1} to lower frequency, from 463 cm^{-1} to 446 cm^{-1} for a 65% ^{18}O enriched sample.¹¹⁷ ^{17}O enrichment methods of samples in this study however achieve considerably lower isotopic levels, (and from here on, most of this will be concentrated in the surface) and therefore isotopic effects will mainly manifest as additional broadening to lower frequency, (i.e. ^{16}O is always the most dominant isotope).

Raman spectra acquired in the $2800\text{--}4000\text{ cm}^{-1}$ range of H_2^{17}O Ceria and H_2^{17}O Ceria $500\text{ }^\circ\text{C}$ are shown in Figure 5.3. This region typically reveals surface adsorbate species and therefore probes (such as CO and methanol that can attach to the ceria surface), have been thoroughly utilised to investigate surface architectures (these species shall be discussed later on in the chapter). Figure 5.3 reveals an dominating concentration of O-H stretching vibrations belonging to physisorbed water between

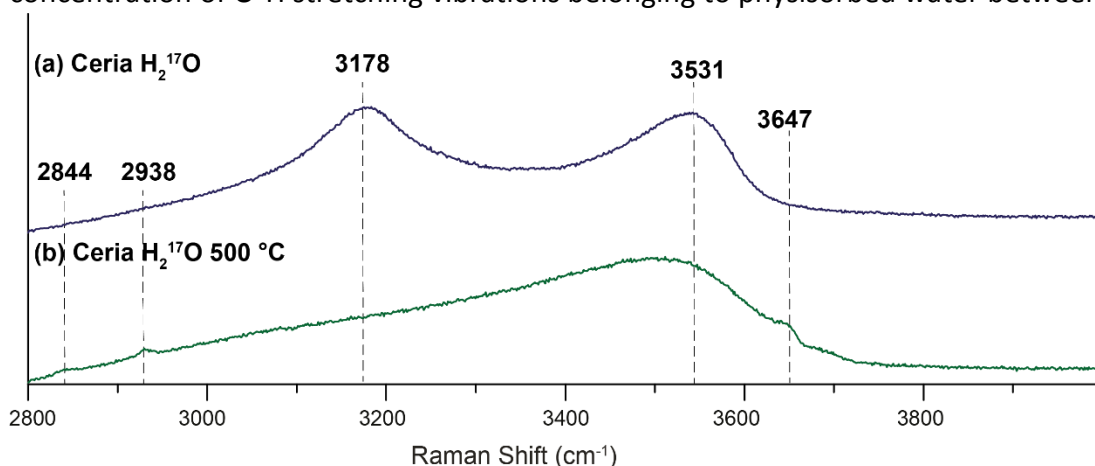


Figure 5.3: Raman spectra between 2800 and 4200 cm^{-1} of (a) H_2^{17}O Ceria and (b) H_2^{17}O Ceria $500\text{ }^\circ\text{C}$.

3000 and 3600 cm^{-1} . After heating at 500 °C, distinct bands are exposed at 2844, 2938, and 3647 cm^{-1} , with the first two attributed to formate (C-H) vibrations and the latter to a doubly bridging hydroxyl coordinated near a Ce^{3+} cation,¹¹⁸ confirming the presence of Ce^{3+} on the surface.

5.1.3 ^{17}O MAS NMR

Figure 5.4 shows the ^{17}O MAS NMR results of H_2^{17}O Ceria and H_2^{17}O Ceria 500 °C, acquired at three different magnetic fields with a 10 s recycle delay (with the exception of the inset). It is immediately clear that peak positions in (a) and (b) appear independent of magnetic field, i.e. there are no significant 2nd order quadrupolar effects, consistent with current ^{17}O NMR studies of ceria.^{91,92,97} This phenomenon has been observed before for alkali-earth titanates and zirconates by Schramm & Oldfield¹¹⁹ in 1984, and again for MgO by Chadwick *et al.*¹²⁰ in 1997, in which the latter determined that the ionicity of the bonding is first and foremost the overriding effect on the EFG at the site of the oxygen, not the site symmetry. Section 2.4.5 describes the EFG as having a $1/r^3$ dependence and therefore is governed by charge close to the nucleus. For a purely ionic bond, electrons are not shared between the bonded oxygen and metal, and so the electrons of the oxygen (which are always nearly spherical) will mainly contribute to the EFG. These are quite exceptional cases in which narrow, Gaussian lines are observed regardless of the lattice distortion, and any information on the local bonding symmetry that C_Q usually divulges, is inaccessible. To clarify, the small C_Q values observed here may not be representative of site symmetry, but of ionic bonding. The broadening associated with the 2 nm H_2^{17}O Ceria is dominated by chemical shift dispersion, evident by the negligible shift with field and the absence of sidebands in spectrum in (a), acquired at 7.05 T. At 11.7 and 14.1 T, there is a very marked increase in spinning sideband intensity, becoming both broader and more extensive. This field dependence of the sideband manifold intensity, the magnitude of the interaction, and the observed peak broadening are indicative of a paramagnetic shift anisotropy, which was defined in the second term of Equation 2.63.

The expanded region shows a deconvoluted spectrum of H_2^{17}O Ceria at 14.1 T, acquired via a Hahn echo, spinning at $\nu_r = 30$ kHz, and with a longer T_1 of 30 s. Firstly, it is evident by the change in lineshape that relaxation is long and data acquired at 10 s is not quantitative. However, as the spectrum acquired here required a 4 day acquisition, a T_1 measurement is unfeasible. Three dominant chemical shift regions are apparent at 873, 858, and 846 ppm, with a tentative, smaller intensity resonance possibly observed at 830 ppm. Part of this deconvolution is again consistent with the ^{17}O solid-state NMR study of nanophase magnesium oxide (MgO) conducted by Chadwick *et al.*,¹²⁰ of crystallite sizes ranging between 1.8 and 35 nm.

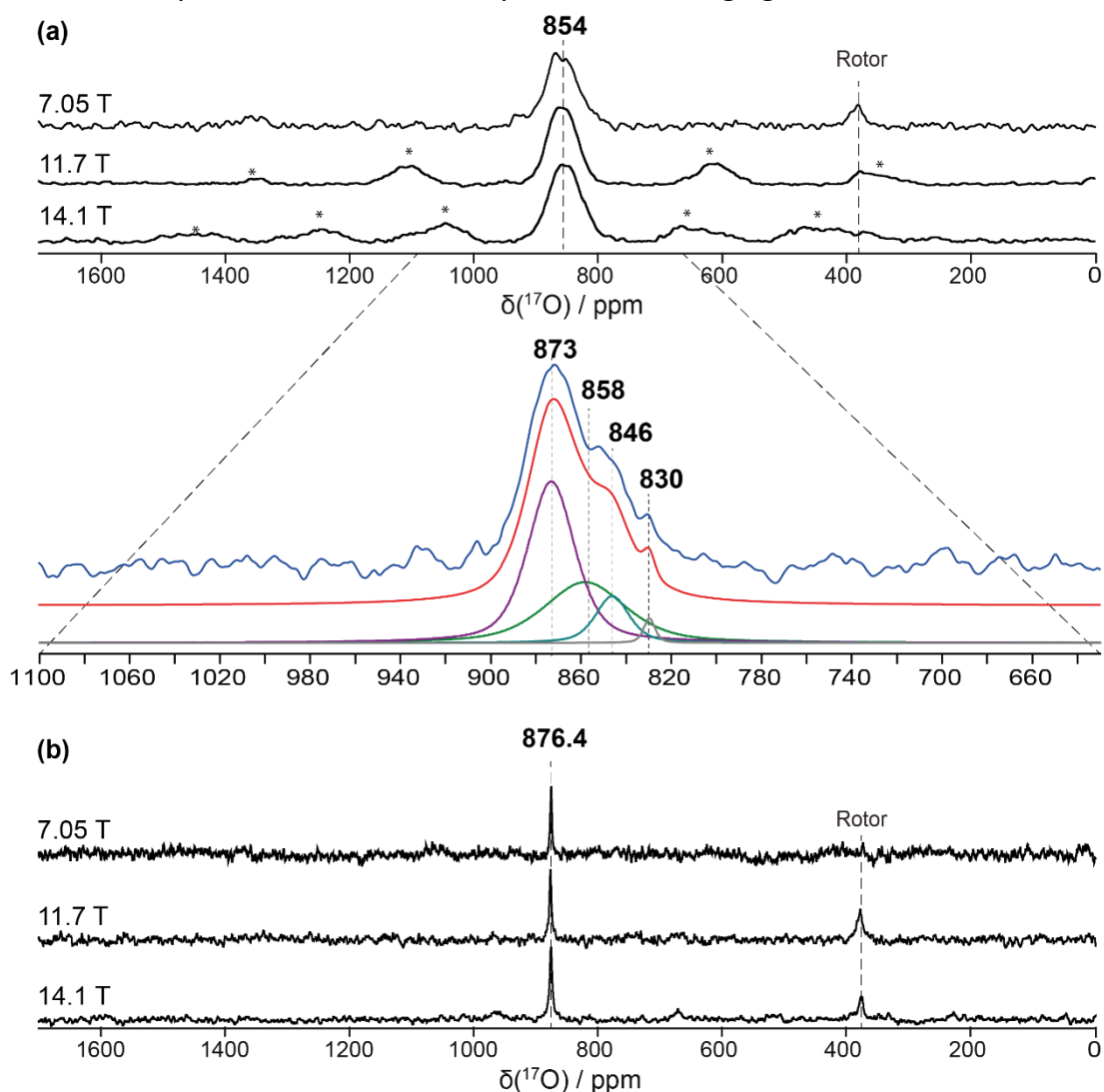


Figure 5.4: ^{17}O MAS NMR spectra acquired at 7.05, 9.4 and 14.1 T via a single pulse sequence using a $\pi/12$ (solution pulse) with a recycle delay of 10 s of (a) H_2^{17}O Ceria and (b) H_2^{17}O Ceria 500 °C. $\nu_r = 14$ kHz. The expanded region of (a) shows a deconvolution of a spectrum obtained at 14.1 T via a Hahn-echo sequence with a recycle delay of 30 s (accounting for the profile difference between the single pulse experiment) and spinning at 30 kHz. Asterisks denote spinning sidebands.

The ^{17}O MAS NMR spectrum of bulk MgO depicts a rock-salt, highly ionic structure, with a single narrow ^{17}O peak positioned at 47 ppm. Deconvolution of the ^{17}O spectra of the nanophase MgO systems at 13.5 nm and smaller revealed three lines however; two narrow and one broad underlying the other two. The most deshielded of the narrow signals was attributed to that of bulk Mg-O bonds at 47 ppm, i.e. an oxygen coordinated to six magnesium, with each magnesium having five other oxygen bonds. An increase in linewidth as the particle decreases in size was also observed for this peak. The underlying broad peak, with a more shielded chemical shift position than bulk MgO, which becomes more shielded with a decrease in particle size, was assigned to surface MgO. (The final oxygen species, more shielded than the other two but with a similar linewidth to that of the bulk signal, was characterised as bulk MgO with H or CH_3 in the third coordination sphere). Furthermore, Scolan *et al.* investigated ^{17}O solid-state NMR of anatase titanium oxide (TiO_2) nanoparticles.¹²¹ The bulk ^{17}O signal of anatase TiO_2 appears at the (field-dependent) position of 561 ppm, which they observed on top of a broad, underlying peak in a more-shielded position and ascribed to the oxygen species at the surface.

In general, it can be seen that, as compared to H_2^{17}O Ceria 500 °C, which was characterised as a particle with a mean size of 4.7 nm (but with a 7 nm particle size distribution), there is a very distinct broadening and an upfield shift of the 2 nm H_2^{17}O Ceria. H_2^{17}O Ceria 500 °C has most likely lost the ^{17}O label (heated in air) and the signal is that of natural abundance ^{17}O in the bulk of the particle.

This behaviour of chemical shifts becoming more shielded and increasing in distribution for smaller particle size has also been observed for ZnSe ¹²² and CdSe ¹²³ nanoparticle systems, in which surface layers contribute their own chemical shifts. Based on these studies, it is appropriate to assign the peaks at 873 and 858 ppm from the deconvolution in Figure 5.4, to bulk and surface peaks, respectively.

5.2 HSA20 Ceria- As Prepared

HSA20 is a high surface area ceria powder supplied to Johnson Matthey Technology Centre for research purposes, and is the principal system investigated in this chapter. As a commercial standard, it has been characterised by some material analysis methods at Johnson Matthey, the results for which are summarised in the following

Table 5.2: Summary of previously acquired characterisations of HSA20.

XRD	Cubic fluorite structure of CeO ₂ , crystallite size = 5.8 nm, $a = 5.411 \text{ \AA}$.
XPS	Adventitious carbon is present.
TEM	5-10 nm grain size, $d = 0.262/0.265 \text{ nm}$, (200) terminations.

subsection, with the TEM data presented in Appendix D. From this data, inferences on the morphology and synthesis conditions are made.

5.2.1 PXRD, XPS, and TEM of HSA20 Ceria

PXRD verified the phase of HSA20 as the cubic fluorite structure, with all of the diffraction peaks in the diffractogram closely matching the powder diffraction file No.04-013-4361 from the ICSD database. Pawley fitting approximated the average crystallite size as 5.8 nm and a lattice parameter of 5.411 Å.

X-ray photoelectron spectroscopy (XPS) is a semi-quantitative technique capable of revealing elements and their oxidative states within a fixed penetrative depth of the surface. In addition to cerium and oxygen, the XPS spectrum of HSA20 reveals some carbon contamination (adventitious carbon), accounting for 36.4% of total atomic mass detected (although as hydrogen is not quantified in this total and there is peak overlap between the C 1s and Ce 4s signals, this is most likely an overestimate). Analysis of the XPS data indicates that the surface contains just 6.6% Ce, in the Ce⁴⁺ state, and after 2 hours of x-ray bombardment, Ce³⁺ increases from 0% to 16% of the cerium total.

Transmission electron microscopy (TEM) is able to observe fine structure down to the atomic level. A limited number of TEM images in bright field imaging mode of HSA20 confirms an approximate 5-10 nm particle size, consistent with the Pawley analysis of the XRD diffractogram, and reveals interplanar spacing values (or d-spacings) of 0.262/0.265 nm corresponding to the (200) facet belonging to the {100} plane.¹²⁴ The (200) facet is indexed to a d spacing of 0.27;¹²⁵ the smaller d spacings here indicate a compressive stress on the crystallites, typically caused by structural defects, e.g. vacancies, interstitials. The (200) face is dominant when ceria nanocrystals are grown non-stoichiometrically.¹²⁶ This would suggest that HSA20 consists of some nanocube-like structures with capped edges, as illustrated by the images in Appendix D, (they almost appear spherical), and so more stable facets with

a higher Miller index are likely to be present. According to the literature, this capping or smoothing suggests that the sample has undergone an ageing treatment of $> 500\text{ }^{\circ}\text{C}$, with nearly rounded particles observed after aging at $750\text{ }^{\circ}\text{C}$.¹²⁷ The morphology resembles that seen by Mai *et al.*⁵⁷, who defined their particles as polyhedral, i.e. a truncated octahedral shape defined by both the $\{111\}$ and $\{100\}$ plane series, which is typical of a 3-10 nm particle size-range.¹²⁸

Furthermore, a thin film is apparent on the surface of HSA20 and is suggested to be evidence of adventitious hydrocarbons from the atmosphere, consistent with the XPS detection of carbon. The main conclusions and parameters extracted from the XRD, XPS, and TEM results are summarised in Table 5.2.

5.2.2 Raman Spectroscopy

The $0\text{--}1800\text{ cm}^{-1}$ region of the Raman spectrum of HSA20 is shown in Figure 5.5. The $\text{F}_{2\text{G}}$ band of CeO_2 dominates the spectrum at 461.9 cm^{-1} , with $\Gamma = 23.0\text{ cm}^{-1}$, a position and width that suggest an intermediate defect concentration of this 5.8 nm particle, as compared to the measurements collected for the 2 nm H_2^{17}O Ceria and the 11 nm H_2^{17}O Ceria $500\text{ }^{\circ}\text{C}$ samples (XRD characterised crystallite sizes). The Frenkel defect band is easily distinguished as a sharp shoulder at 600 cm^{-1} , and returns an overall $I_{\text{D}}/I_{\text{F}_{2\text{G}}}$ ratio of 0.032, which correlates well with the aforementioned $\text{F}_{2\text{G}}$ band trend.

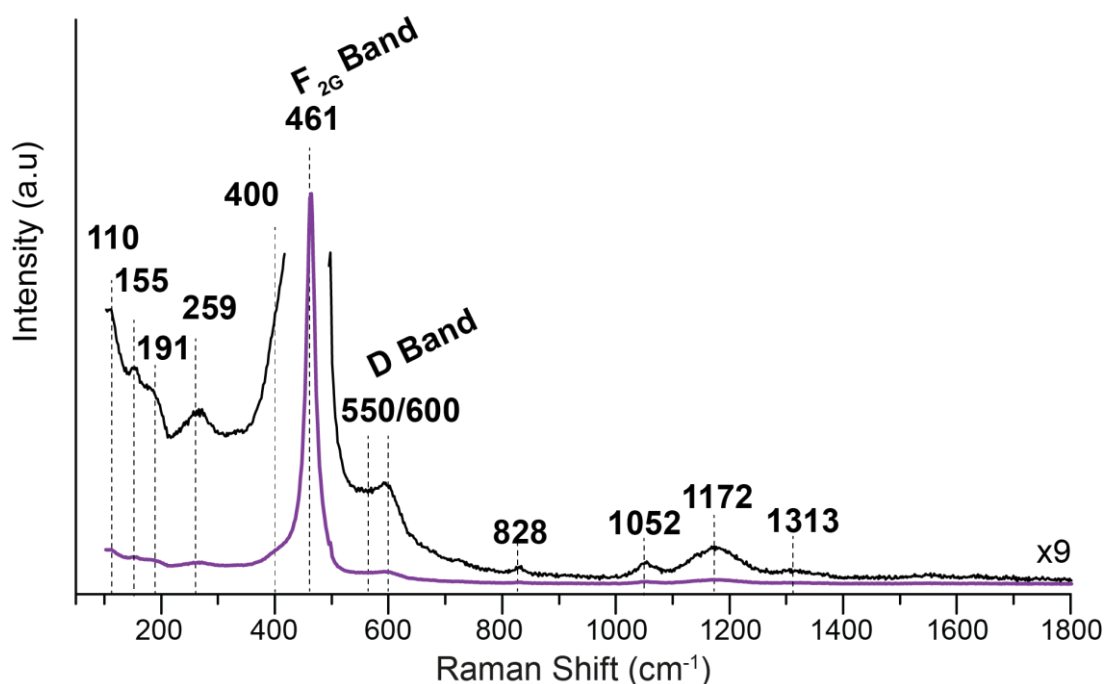


Figure 5.5: Raman spectrum of HSA20 (as-prepared) for $\lambda_{\text{ex}}=532\text{ nm}$.

The unresolved signal at 400 cm^{-1} is less frequently observed in Raman spectra of ceria and will be discussed in Section 5.4.2. The weak bands at 1052 and 1313 cm^{-1} have not yet been observed and are simply those of residual phosphate¹⁶ and bridging nitrite,¹²⁹ most likely leftover from the synthesis method. These, along with Raman bands in the low energy region ($>200\text{ cm}^{-1}$), a result of lattice vibrations of the particles and other species previously assigned in Section 5.1.2 are unimportant to this work, and will no longer be discussed.

5.3 $^{17}\text{O}_2$ Direct Exchange of HSA20 at $600\text{ }^\circ\text{C}$

As explored by the literature review in Section 3.2, previous ^{17}O NMR studies have typically enriched ceria by a $^{17}\text{O}_2$ direct-exchange method, and therefore this subsection can be compared to the results therein. Here, an exchange temperature of $600\text{ }^\circ\text{C}$ is implemented at a $\sim 0.8\text{ atm}$ pressure. The sample is labelled HSA20-600Ex. PXRD estimates the crystallite sizes as 8.4 nm (see Appendix B).

5.3.1 Raman Spectroscopy

Raman spectroscopy is particularly useful in the comparison of ceria before and after a temperature/gas treatment and therefore where it is deemed beneficial, the untreated sample is presented on the sample plot, as is the case in Figure 5.6 (a) for HSA20-600Ex. The inset reveals a broadening and shift to lower energy of the $\text{F}_{2\text{G}}$ peak to 460.6 cm^{-1} from 461.6 cm^{-1} . As discussed in Section 5.1.2, there are three factors that will contribute to the changes in the $\text{F}_{2\text{G}}$ band after treatment: primarily that of particle growth and defect concentration changes (^{17}O incorporation to a small extent only).

From observations of the D band, there is an increase in the $I_{\text{D}}/I_{\text{F}_{2\text{G}}}$ ratio of 0.032 to 0.037 . This can be rationalised by an increase in cation-vacancy vibrations caused by a reduction via the oxygen deficient conditions in which HSA20 was heated during the $600\text{ }^\circ\text{C}$ treatment. This would cause the observed broadening of the $\text{F}_{2\text{G}}$ band, on account of a greater defect density, and shift the $\text{F}_{2\text{G}}$ peak to lower wavenumber due to a lattice expansion, caused by the presence of the larger Ce^{3+} cation. Indeed, ceria reduction is observed in a low-pressure O_2 atmosphere at

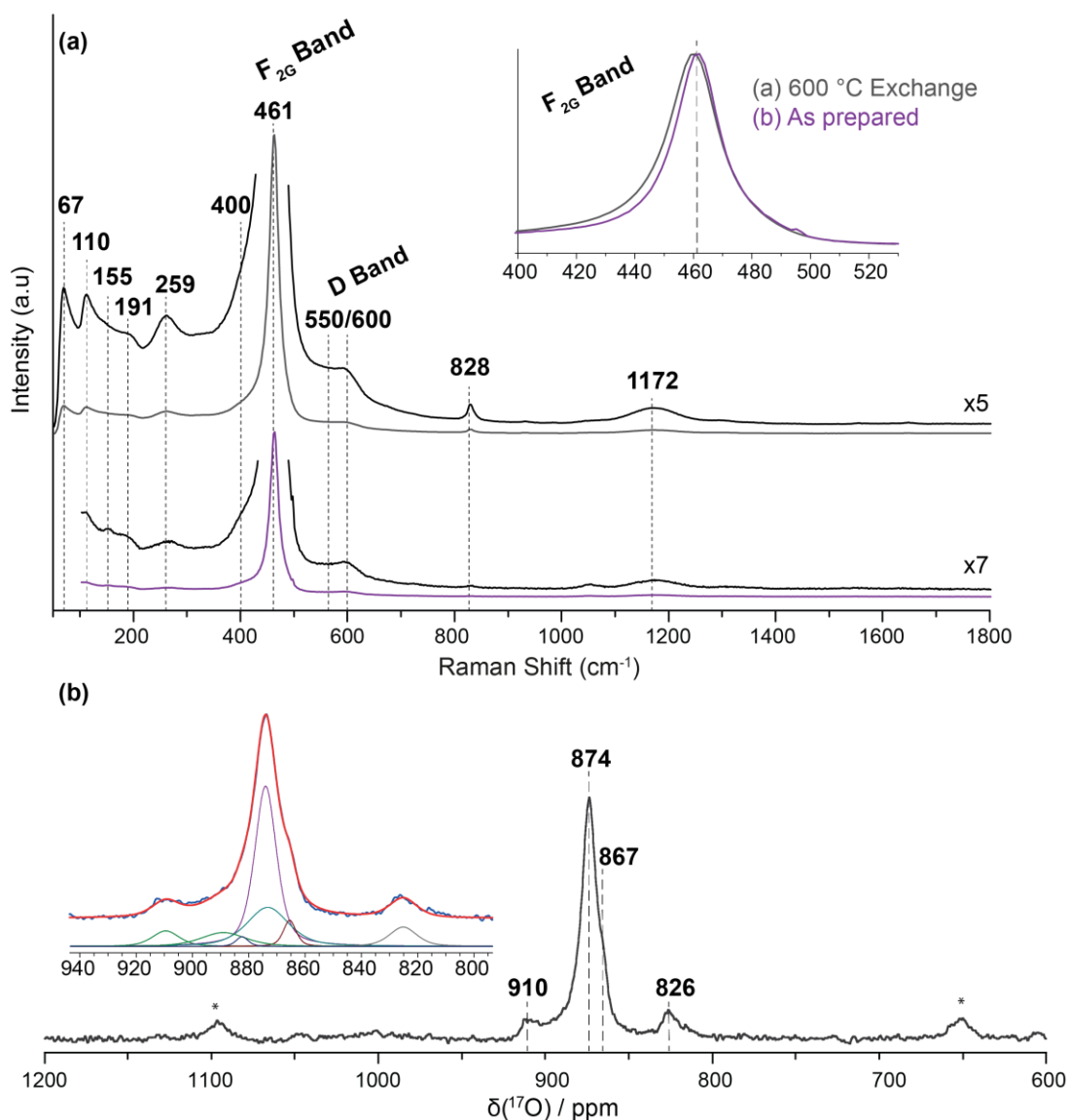


Figure 5.6: (a) Raman spectrum of HSA20-600Ex with the un-prepared sample shown beneath for comparison for $\lambda_{\text{ex}}=532$ nm. (b) ^{17}O MAS NMR spectrum acquired at 9.4 T with a rotor synchronised Hahn echo sequence and a 45 s recycle delay. The inset shows a rudimentary deconvolution, used to highlight the complexity of the fit. $\nu_r = 12$ kHz.

elevated temperatures.¹⁰² However, ^{17}O incorporation may contribute as a factor in the shift to lower wavenumber, in addition to the peak broadening. Furthermore, it should be noted that a band at 259 cm^{-1} increases after the treatment, an observation made by Filtschew *et al.* after a $400\text{ }^{\circ}\text{C}$ treatment in air,¹⁰⁹ in addition to a feature at 828 cm^{-1} assigned to peroxide (both to be discussed below).

5.3.2 ^{17}O Solid-state MAS NMR

Figure 5.6 (b) presents the ^{17}O MAS NMR spectrum of HSA20-600Ex which was acquired at 9.4 T using a 90-180 Hahn echo sequence and a recycle delay of 45 s. The dominant peak at 874 ppm with a peak breadth δ_{FWHM} of 550 Hz can be ascribed to bulk-like OCe_4 , and small and almost-equal low intensity peaks situated either side of the bulk at 826 and 910 ppm are apparent. This result is similar to that found by Wang *et al.*⁹⁷ (see Figure 3.6) for the similar exchange temperature of 573 °C, with the exception of the presence of the broader peak at 1040 ppm. According to the assignments of Wang's study, these ^{17}O NMR chemical shift positions can be ascribed to a core and surface-shell model, with the first, second, and third oxygen layers assigned to positions at 1040, 920, and 835 ppm respectively. As already mentioned in Chapter 4, unless stated, all samples have been handled under argon conditions until sealed in the rotor (which is airtight on the timescale of the experiment), and so the absence of this peak at 1040 ppm cannot be ascribed to exchange with oxygen in air. Moreover, the enhanced S/N of this spectrum reveals a more-complex bulk peak nature, as portrayed by the deconvolution in the inset. A broader component underneath the bulk with a slightly more shielded position of 867 ppm is apparent, attributed to surface Ce-O bonds, in line with the surface assignment of H_2^{17}O Ceria in Section 5.1.3. At least two other environments are present (three additional peaks were used to obtain a better fit). From the Raman spectrum in Figure 5.6(a), an increase in Ce^{3+} was evidenced, and these additional peaks are speculated to be caused by the subsequent structural perturbations induced by the reduction.

With the absence of the assigned surface peak, the result in Figure 5.6 (b) does not fit with the model proposed by Wang *et al.* Furthermore, the model fails to account for the presence of anticipated oxygen or defect environments (that are mostly responsible for ceria's redox properties), e.g. vacancies, Ce^{3+} cations, intermediate reoxidation species such as peroxides and superoxides, Frenkel defects, and oxygen near points of defect clustering. These are observed in other characterisation techniques, and even at ambient pressure and temperature, such species are anticipated in nanoceria.

Through the probing of ceria with different physical properties and the control of ^{17}O preparation conditions which influence the chemical structure, the following subsections examine ceria for the existence of these species, via solid-state ^{17}O NMR, alongside complementary techniques.

5.4 Reduction and $^{17}\text{O}_2$ Reoxidation of HSA20 Ceria

As discussed in Chapter 1, when ceria is exposed to a reducing atmosphere (e.g. elevated temperatures under H_2 gas), oxygen desorbs from the surface leaving behind vacancies and corresponding Ce^{3+} cations, and provided the temperature is great enough, bulk diffusion takes place to the surface. This section investigates reduction effects on HSA20.

5.4.1 TPR- H_2 of HSA20

The reduction properties of ceria are typically measured by temperature programmed reduction (TPR) under H_2 or CO , where gas consumption is measured as a function of temperature. Figure 5.7 reveals a TPR- H_2 trace of HSA20 recorded to 975°C . The two separate broad peak regions, assigned to surface (centred at 425°C) and bulk (centred at 850°C) oxygen reduction respectively, which is an anticipated result⁶². The intense and narrow signal at 380°C is most likely oxygen removal from surfaces with lower vacancy formation energy, i.e. from the (200) facets or from steps/other low-coordinated oxygen species. The low intensity signal observed at 160°C is possibly the loss of lowly coordinated hydroxy groups.¹¹⁸

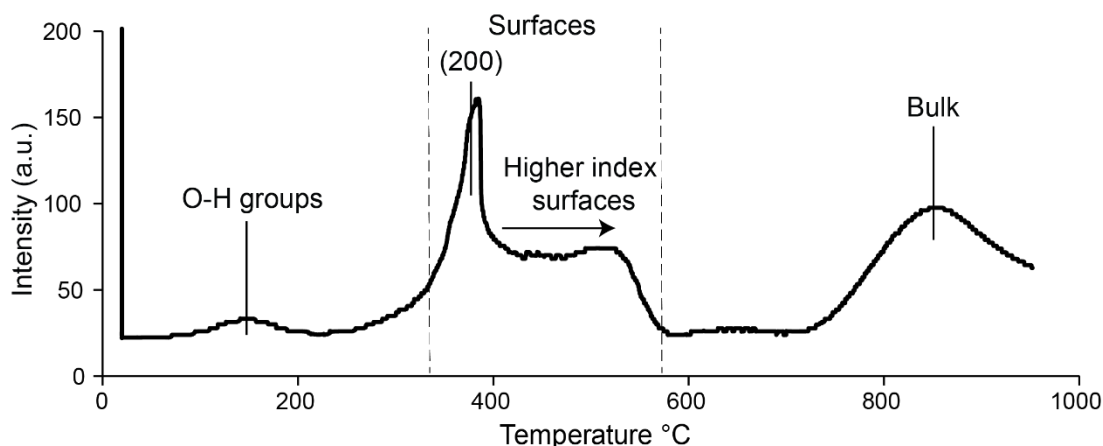


Figure 5.7: TPR- H_2 of HSA20 to 975°C .

5.4.2 In Situ Raman Spectroscopy

In situ Raman spectroscopy of HSA20 under a H_2 atmosphere with increasing temperature is shown in Figure 5.8. The inset shows the broadening and shift to lower energy of the F_{2G} band (from 462.2 cm^{-1} at 65°C to 444.0 cm^{-1} at 571°C), which is well documented in the literature.^{10,130} This behaviour clearly illustrates that the width and position of the F_{2G} band is dependent on the bulk defects of ceria, i.e. conversion of Ce^{4+} to Ce^{3+} /vacancy generation causes lattice expansion. The presence of a smaller component, distinct at 400 cm^{-1} was observed by Agarwal *et al.*,^{14,15} who attributed it to distortions in the fluorite lattice ($Ce-O_x$ units for $5 < x < 8$). Figure 5.8 clearly shows the evolution of this band, i.e. it broadens considerably as the sample is reduced, becoming unresolvable from the broadening F_{2G} band, and from the characteristic asymmetric tail towards low energies. Agarwal's description is consistent with the removal of oxygen, creating a greater distribution of $Ce-O_x$ units with $x < 8$. The D band appears to shift to lower energies, from 600 to 550 cm^{-1} ,

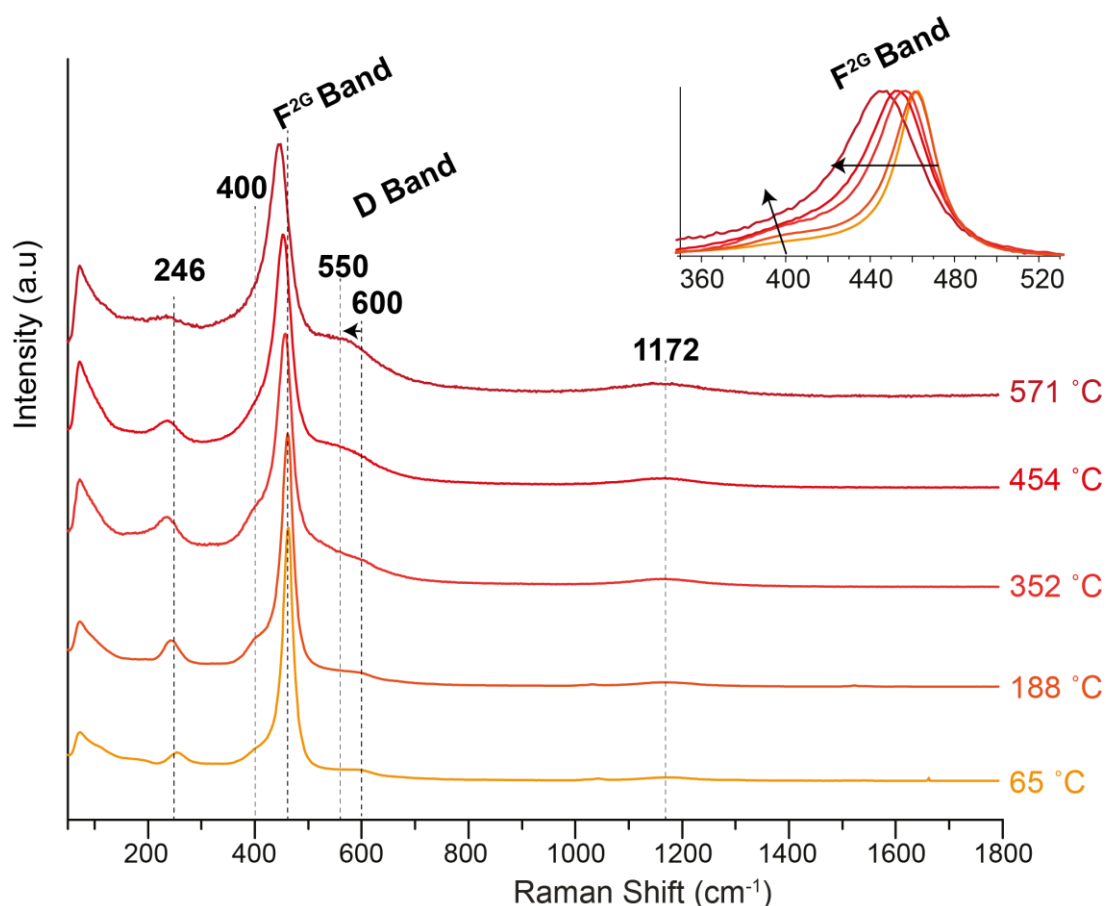


Figure 5.8: In situ Raman spectra showing the evolution and reduction of HSA20 under 10%/90% H_2/N_2 flow with increasing temperature.

suggesting a decrease in the interstitial Frenkel defects relative to the increasing amount of vacancies that correspond to the reduction.¹³¹ Relative intensities of I_D to I_{F2G} (I_D / I_{F2G}) increase from 4.1% at 65 °C to 23.6% at 571 °C.

Furthermore, at 571 °C the band at 246 cm^{-1} is almost undetectable. As stated in Section 5.2.2, Filtschew *et al.* have recently reassigned this feature to a Ce-OH species.¹⁰⁹ Their work observes more than one band in this region for a range of ceria particles and they correlate an increase in intensity of these bands with a decrease in particle size, thus contradicting the former assignment of a lattice vibration. Moreover, upon exposure to air at 400 °C, they witness an intensity increase, which can be rationalised by a disassociation of H_2O and thus the formation of hydroxyl groups. The 246 cm^{-1} band observed in Figure 5.8 appears to initially increase in intensity and almost disappear at 571 °C, behaviour that can be rationalised by the formation of hydroxyl species from the H_2 environment and disassociation of H_2O , up until they desorb from the surface at 571 °C.

The TPR of HSA20 in Figure 5.7 indicates that at 300 °C, surface reduction is activated, and by 600 °C, surface reduction is complete. It should be noted here that, from the in situ Raman data shown in Figure 5.8, the F_{2G} band is significantly altered by reduction of the surface alone. This increase of disorder and the decrease in Frenkel defects, indicates oxygen removal from the surface of the lattice and from the Frenkel defect.

In order to investigate ceria's highly reactive oxygen species, three different reduction temperatures of 700, 500 and 300 °C under H_2 conditions were used to reduce HSA20 to varying oxygen deficient states. To clarify, natural abundance oxygen was removed (99.75% ^{16}O , 0.2% ^{18}O , and 0.04% ^{17}O), leaving behind oxygen vacancies. The three reduced samples were then reoxidised with 30 mL $^{17}\text{O}_2$ (below atmospheric pressure at 300 °C), thus filling these vacancies with ^{17}O probes, and are defined as HSA20-700/300-Redox, HSA20-500/300-Redox, and HSA20-300/300-Redox, respectively.

5.4.3 PXRD and SAXS

PXRD diffractograms of HSA20-700/300-Redox, HSA20-500/300-Redox, and HSA20-300/300-Redox shown in Appendix C all confirmed the presence of the cubic CeO_2

phase only and average crystallite sizes of 12.7, 8.1, and 8.0 nm, respectively (Scherer analysis). SAXS measurements however demonstrated that particle size is overestimated by PXRD when broad size distributions are present (see Appendix B), yielding values of 8.3 ± 5.1 nm, 7.3 ± 4.7 nm and 7.4 ± 4.5 nm for HSA20-700/300-Redox, HSA20-500/300-Redox and HSA20-300/300-Redox, respectively.

5.4.4 Raman Spectroscopy

The Raman spectra of HSA20-700/300-Redox, HSA20-500/300-Redox and HSA20-300/300-Redox are shown in Figure 5.9(a), (b) and (c), respectively. The inset shows the F_{2G} band narrowing and shifting to higher energy with an increase in reduction temperature and thus an increase in particle size and/or oxygen deficiency, ranging from (c) 461.7 cm^{-1} with a peak width of 23 cm^{-1} to (a) 464.4 cm^{-1} with a peak width of 14 cm^{-1} (see Appendix A) as expected. The particle sizes correspond well with the F_{2G} width here, with HSA20-500/300-Redox and HSA20-300/300-Redox having almost identical particle sizes and F_{2G} widths.

The vibration at 400 cm^{-1} , is now apparent once again (post reoxidation) as a shoulder of the F_{2G} band, perhaps indicating that these oxygen species were vacated

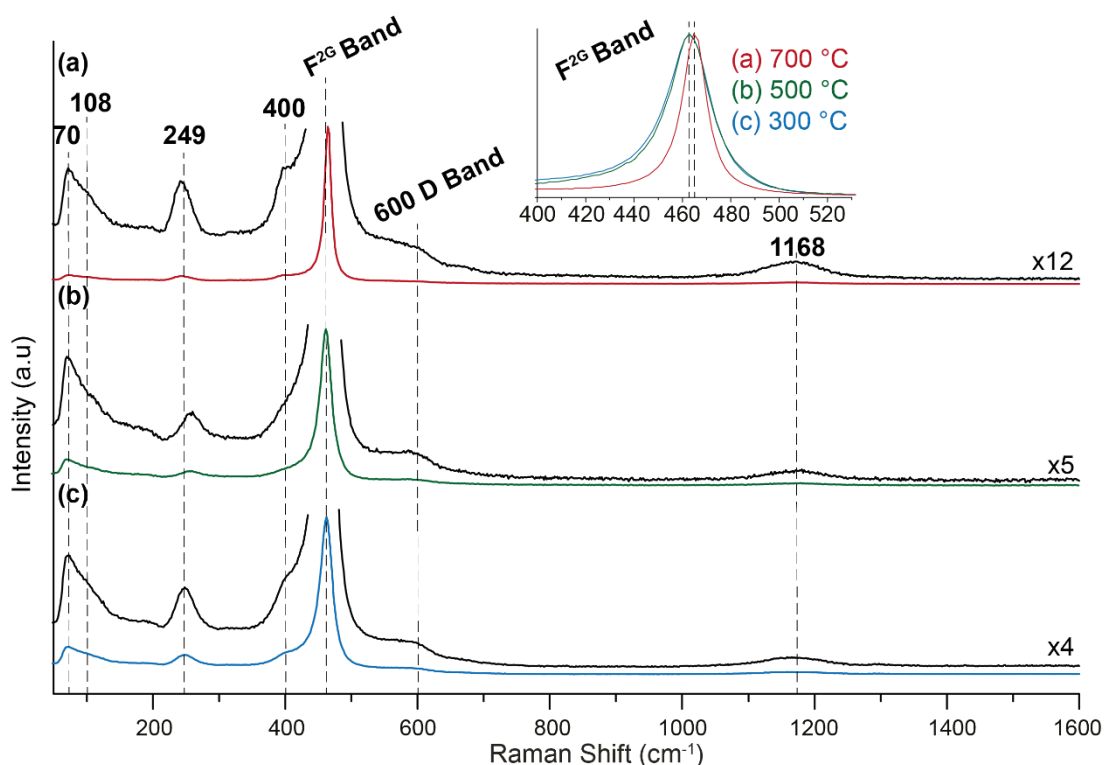


Figure 5.9 Raman spectra between 50 and 1600 cm^{-1} at 532 nm excitation of (a) HSA20-700/300-Redox, (b) HSA20-500/300-Redox and (c) HSA20-300/300-Redox.

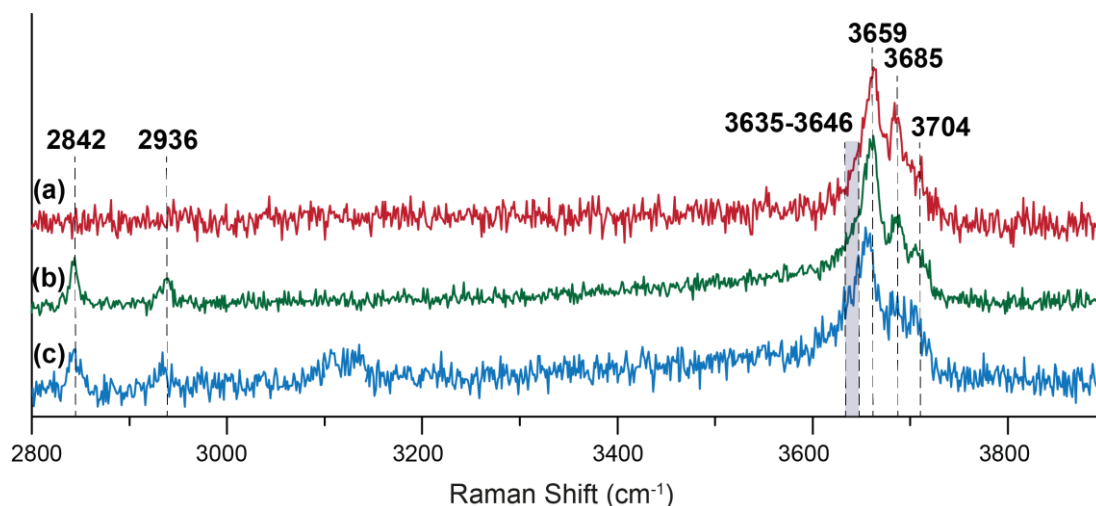


Figure 5.10: Raman spectra between 2800 and 3900 cm^{-1} at 532 nm excitation of (a) HSA20_700-300_Redox, (b) HSA20_500-300_Redox and (c) HSA20_300-300_Redox.

under reduction, and have now recombined during ^{17}O oxidation. Recall that this vibration has been ascribed to the stretching of Ce-O_x (for $5 < x < 8$) units. The intensity of this band appears to correlate with the width of the $\text{F}_{2\text{G}}$ band, i.e. it is more intense in Figure 5.9 (c) at the low reduction temperature (300 $^{\circ}\text{C}$), where the particle size is smaller (7.4 nm). The only reason it appears more distinctive in (a) is due to the narrowing of the $\text{F}_{2\text{G}}$ band (larger particle size of 8.3 nm), along with the band itself appearing to narrow, again indicative of increasing order. For these observations, it is speculated that the band at 400 cm^{-1} is attributed to releaseable oxygen species. Furthermore, as (70%) ^{17}O reoxidises these species, this band will appear to slightly lower wavenumber on account of the increased mass of the ^{17}O isotope, perhaps explaining its more red shifted position, post the $^{17}\text{O}_2$ redox process.

The relative intensity of the band at 245 cm^{-1} decreases as the reduction temperature increases, which as previously discussed, may suggest a decrease in hydroxy groups. A similar observation can be made for the D band at 600 cm^{-1} (extending toward 540 cm^{-1}) encompassing Frenkel defects and O^{2-} vacancies; the $I_{\text{D}}/I_{\text{F}_{2\text{G}}}$ ratios more than half, from 0.042 for HSA20-300/300-Redox to 0.019 for HSA20-700/300-Redox, with increasing reduction temperature (see Appendix A). These ratio changes suggest that defects are lost with increasing reduction temperature (post the redox process).

Figure 5.10 depicts the spectral region between 2800 and 3900 cm^{-1} , with the three distinct high energy bands at 3659, 3685, and 3704 cm^{-1} , attributed to the O-H

stretching vibrations of mono-coordinated OH species, undissociated water and doubly-bridging OH species, respectively, bands formerly observed on a non-reduced ceria surface¹¹⁸. All spectra also appear to have a shoulder (shaded region), unresolved from the band at 3659 cm^{-1} , between the region 3635 and 3646 cm^{-1} . These vibrations have previously been assigned to doubly bridging OH species near vacancies attached to Ce^{4+} and Ce^{3+} , respectively.¹¹⁸

The signals observed at 2842 and 2936 cm^{-1} are those of formate (C-H) vibrations, the fundamental and first overtone modes, respectively.¹³² This is in agreement with the XPS and TEM analyses, which suggested that adventitious carbon is present on the surface. Figure 5.10 suggests that at a high reduction temperature of $700\text{ }^{\circ}\text{C}$, formates are no longer stable and are removed from the ceria surface.

5.4.5 ^{17}O Solid-state MAS NMR

Figure 5.11 (a), (b), and (c) presents ^{17}O MAS NMR Hahn echo spectra of HSA20-700/300-Redox, HSA20-500/300-Redox, and HSA20-300/300-Redox across a ~ 2000 ppm range, acquired at 14.1 T , and spinning at $11,400\text{ Hz}$. Sidebands unfortunately fall on top of the data shown (and therefore data acquired at 9.4 T was obtained, shown below). The inset reveals the full spectral width, expanded upwards to show a vast spinning sideband manifold ($\sim 2000\text{ ppm}$), an exceptionally broad ($>1000\text{ ppm}$), underlying signal centred at $\sim 825\text{ ppm}$, in addition to a typically-broad resonance (5000 Hz) located at 230 ppm , the intensity of which decreases with increasing reduction temperature. The first of these signals has been previously observed in the work of Wang *et al.*, after reducing ceria nanoparticles at $500\text{ }^{\circ}\text{C}$ under H_2 , as discussed in Section 3.2. They attributed the broader signal to an oxygen ion in the first coordination sphere of Ce^{3+} , as direct bonding with a paramagnetic cation would cause significant broadening.⁹⁷

A T_1 edited spectrum attained for HSA20-700/300-Redox is shown in Figure 5.12 (black), using a recycle delay of 0.25 s . Signals from non-protonated or non-paramagnetically influenced species are suppressed. The deconvolution clearly depicts three peaks at 324 , 277 , and 227 ppm , assigned to Ce-OH bonds based on the chemical shift positions observed by Wang *et al.* at 300 ppm (14.1 T),⁹⁷ and Hope *et al.* at 325 ppm (14.1 T),⁹⁹ as discussed in Chapter 3. These assignments are supported

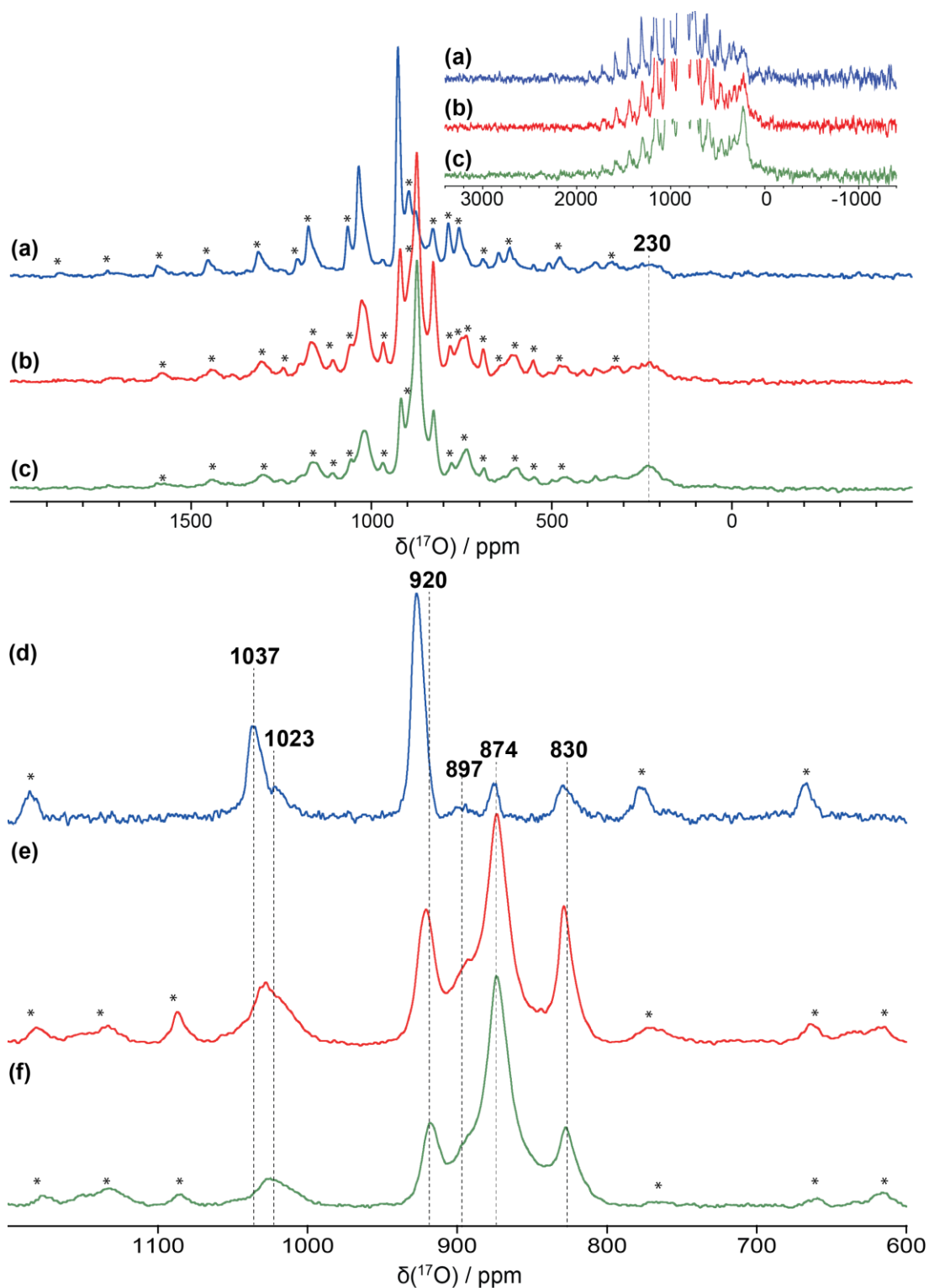


Figure 5.11: ^{17}O MAS rotor synchronised Hahn echo NMR spectra acquired at 14.1 T and ^{17}O MAS single pulse spectra acquired at 9.4 T of (a) and (d) HSA20-700/300-Redox, (b) and (e) HSA20-500/300-Redox and (c) and (f) HSA20-300/300-Redox, respectively. $\nu_r = 14$ kHz, asterisks denote spinning sidebands. (Note that experiment times for Echo experiments are 4-6 days and single pulse experiments ~ 1 day).

by a correlating intensity loss seen in Figure 5.11 (a), (b), and (c), with the intensity loss of the 245 cm^{-1} Raman band in Figure 5.9(a), (b), and (c), as a function of reduction temperature. This is further support for the hydroxyl species spectral identification (and their reduced stability at the higher reduction temperatures).

Figure 5.11 (d), (e), and (f) presents single pulse data between 600 and 1200 ppm of HSA20-700/300-Redox, HSA20-500/300-Redox, and HSA20-300/300-Redox, respectively. It is appropriate to justify here that the single pulse experiment (certainly in the case of these systems) experiences far superior S/N, indicating a loss of coherence between the nutation and refocusing pulses of the Hahn echo experiment; this is a result of fast T_2 . This decrease in S/N is especially noticeable at the lower field of 9.4 T (governed by Equation 2.23), which along with the spinning speed of 14 kHz, are ideal conditions for acquiring ^{17}O spectra of the materials shown in this thesis (as sidebands are free from the centre bands).

The similarities between (e) and (f) are immediately apparent, suggesting similar redox states, and the S/N in (d) is considerably reduced, indicating less ^{17}O incorporation overall. The proposed cause of this latter result shall be discussed in Section 5.5. First impressions of the spectra reveal six peaks in total, with many of them shared between all three spectra. Beginning with the most deshielded shift, a broad signal at 1023 ppm initially dominates at the lowest reduction temperature (f), with an increase seen in (e). However in (d), the broad component is now dominated by a more narrow line at 1037 ppm, which has a significant amount of its intensity in the extensive sideband manifold. The most intense resonances observed in (e) and (f) are those of bulk (OCe^{4+}_4) oxygen at 875 ppm, whilst (d) is dominated by a line at 930 ppm, an environment that (e) and (f) observe at a more shielded position of 920 ppm. Very little bulk oxygen is observed in (d) at its position of 876 ppm. The prominent differences in line widths and the 1 ppm shift differences of the three bulk environments reflect the particle size deviations and disorder in the ^{17}O environments. All three spectra show peaks at positions 897 and 830 ppm, with increased amounts (relative to the bulk) between (e) and (f).

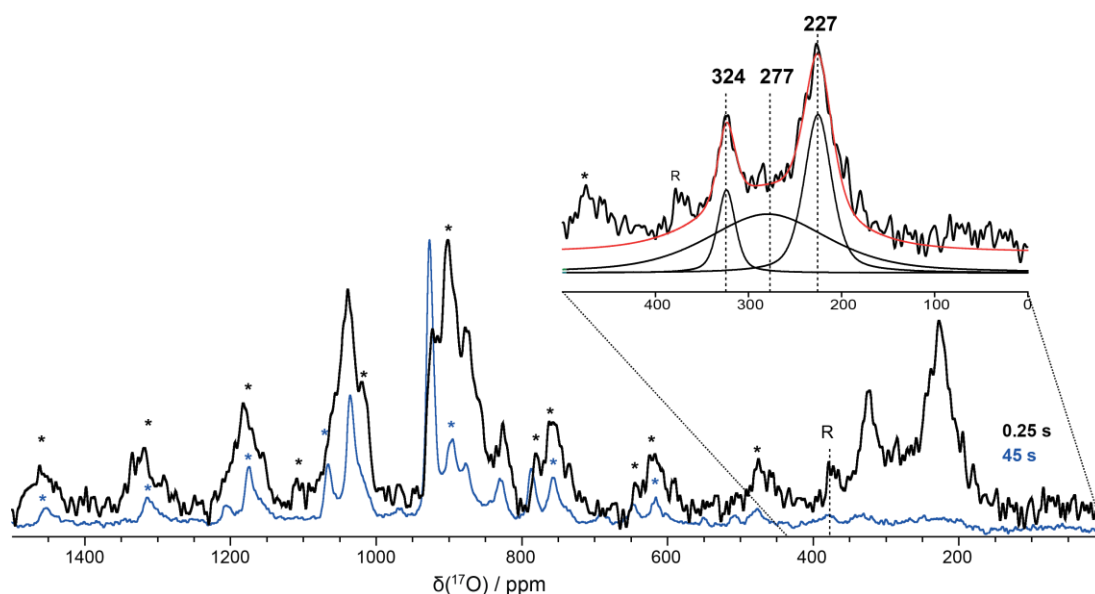


Figure 5.12: T_1 editing of HSA20-700/300-Redox: ^{17}O Hahn echo with recycle delay 0.25 s (black), acquired with 155,000 scans, with the spectrum from Figure 5.11(a) (acquired with a 45 s recycle delay) shown underneath (blue). The expanded region shows a deconvolution resolving three O-H species.

It is interesting that the deshielded chemical shift position at 1035-1020 ppm (assigned by Wang *et al.* as the surface oxygen in ceria), is now observable for HSA20, compared to preparation by exchange (HSA20-600Ex). It suggests that more complex behaviour (based on sample redox properties) governs these oxygen sites. In order to quantify these species, the significant sideband manifolds (of the spectra in Figure 5.11(d)-(f)) were added to their respective centre bands (shown in purple), with the result shown in Figure 5.13. The difference between the MAS spectra (shown in red) emphasize the magnitude of the signal averaged by MAS for this site (1037/1023 ppm). Moreover, a systematic increase in the two shielded positions (1037/1023 ppm and ~ 925 ppm) becomes evident, with the concomitant (relative) loss of the bulk at 874 ppm. This behaviour suggests that the reduction is a limiting factor; bulk oxygen exchange certainly appears to favour a less oxygen-deficient system and/or a smaller particle size. As the reduction temperature increases, ^{17}O appears to dominate environments associated with the active oxygen that are removed during the reduction process rather than take the place of lattice oxygen. The TPR in Figure 5.7 suggests that at 700 °C, surface-oxygen reduction is complete, therefore when

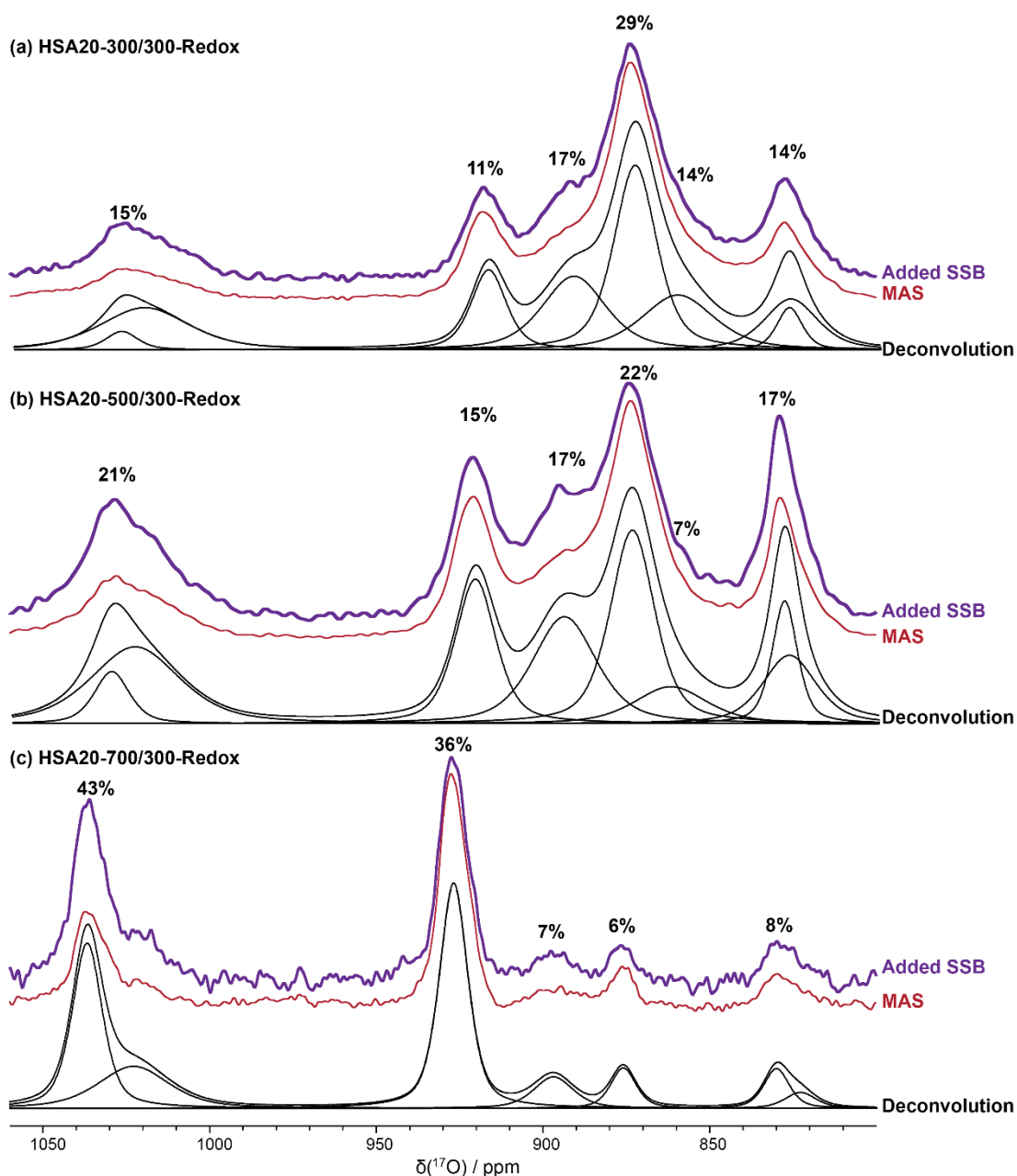


Figure 5.13: Spectra of (a) HSA20-700/300-Redox, (b) HSA20-500/300-Redox, and (c) HSA20-300/300-Redox, where spinning sidebands have been added on to the centre band (purple), and corresponding deconvolution (black). Quantities of species taken from the deconvolution. The MAS profile (Figure 5.11(d), (e), and (f)) is shown in red.

HSA20 is reoxidised, ^{17}O is taken up primarily by these reactive sites, and appear to be stable (i.e. they do not diffuse) in these positions at the reoxidation temperature of 300 °C.

5.5 Varying Oxidation Temperature of HSA20

To explore the effects of Section 5.4 further, in which it was seen that a critical point (complete surface reduction) at the reduction temperature of 700 °C was reached,

reoxidation temperatures were varied whilst maintaining the reduction temperature of 700 °C. Similarly to Section 5.4, samples are defined as HSA20-700/300-Redox, HSA20-700/150-Redox, and HSA20-700/25-Redox for re-oxidation temperatures of 300, 150, and 25 °C respectively. As the control sample, HSA20-700/300-Redox (from fresh) underwent reduction and ($^{17}\text{O}_2$) re-oxidation again in order to ascertain reproducibility. It should be noted that a probable batch change in HSA20 occurred for the following data and therefore some slight changes are present.

5.5.1 Raman Spectroscopy

The position and widths of the $\text{F}_{2\text{G}}$ bands of HSA20-700/300-Redox and HSA20-700/150-Redox presented in Figure 5.14 (a) and (b) respectively, are seen in the inset. (Raman data for HSA20-700/25-Redox is not shown due to air exposure). More subtle differences are apparent between the samples compared to Section 5.4, thus the spectrum for the as-prepared material is also shown. The $\text{F}_{2\text{G}}$ bands of HSA20-700/300-Redox and HSA20-700/150-Redox are almost identical in both position and width. The H_2 -reduction of these systems at 700 °C drives particle sintering, i.e. particle size is anticipated to be the same for both cases. The reoxidation temperature appears to have had similar influences on this mode and it can be determined that they are in a similar state of reduction (similar concentrations of Ce^{3+} present). However, an increase of the $I_{\text{D}}/I_{\text{F}_{2\text{G}}}$ ratio is observed for HSA20-700/300-Redox (0.020) compared to HSA20-700/150-Redox (0.016), which therefore must be attributed to a greater concentration of Frenkel defects at 600 cm^{-1} (recall that the defect band is comprised of two bands: one associated with vacancies and the other with interstitial defects).

In Figure 5.14(c), a band at 832 cm^{-1} is evident, which is well established as an O-O stretch of an adsorbed peroxide (O_2^{2-}) species to an isolated two electron defect on the surface of ceria.^{16,59,66} Under O_2 conditions, these species have been shown to be highly stable, even at elevated temperatures of 350 °C.¹⁵ Appendix F

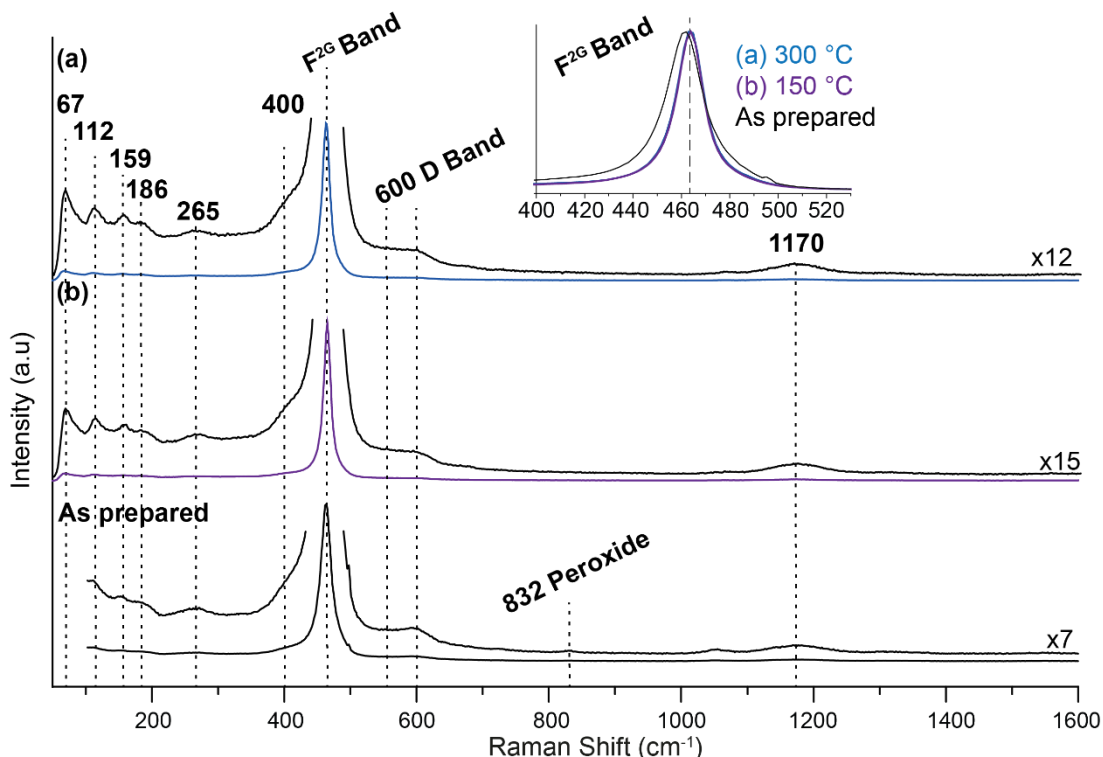


Figure 5.14: Raman spectra for $\lambda_{\text{ex}}=532$ nm between 50 and 1600 cm^{-1} of (a) HSA20-700/300-Redox and (b) HSA20-700/150-Redox. The as prepared sample spectrum is shown below (black).

demonstrates that under O_2 conditions at room temperature, peroxides are easily formed and maintained on the unreduced HSA20 surface.

5.5.2 ^{17}O Solid-state MAS NMR

Figure 5.15 (a), (b), and (c) presents the full observable region, and (d), (e) and (f) the expanded region, of the ^{17}O MAS NMR spectra of HSA20-700/300-Redox, HSA20-700/150-Redox, and HSA20-700/25-Redox, respectively. Time restraints prevented the acquisition of Hahn-echo spectra as the sample preparations resulted in considerably reduced ^{17}O enrichment levels and so only single pulse data is shown. Any broad components are lost in the dead time and due to baseline distortion (ringing), splines have been fitted to the data.

Of immediate notice is the increasing ^{17}O enrichment with increase in reoxidation temperature, i.e. S/N is significantly improved at $300\text{ }^{\circ}\text{C}$ in (d) compared to a room temperature reoxidation in (f), suggesting a greater reoxidation with increase in temperature. The signals at 1035 and 1020 ppm are present in all three

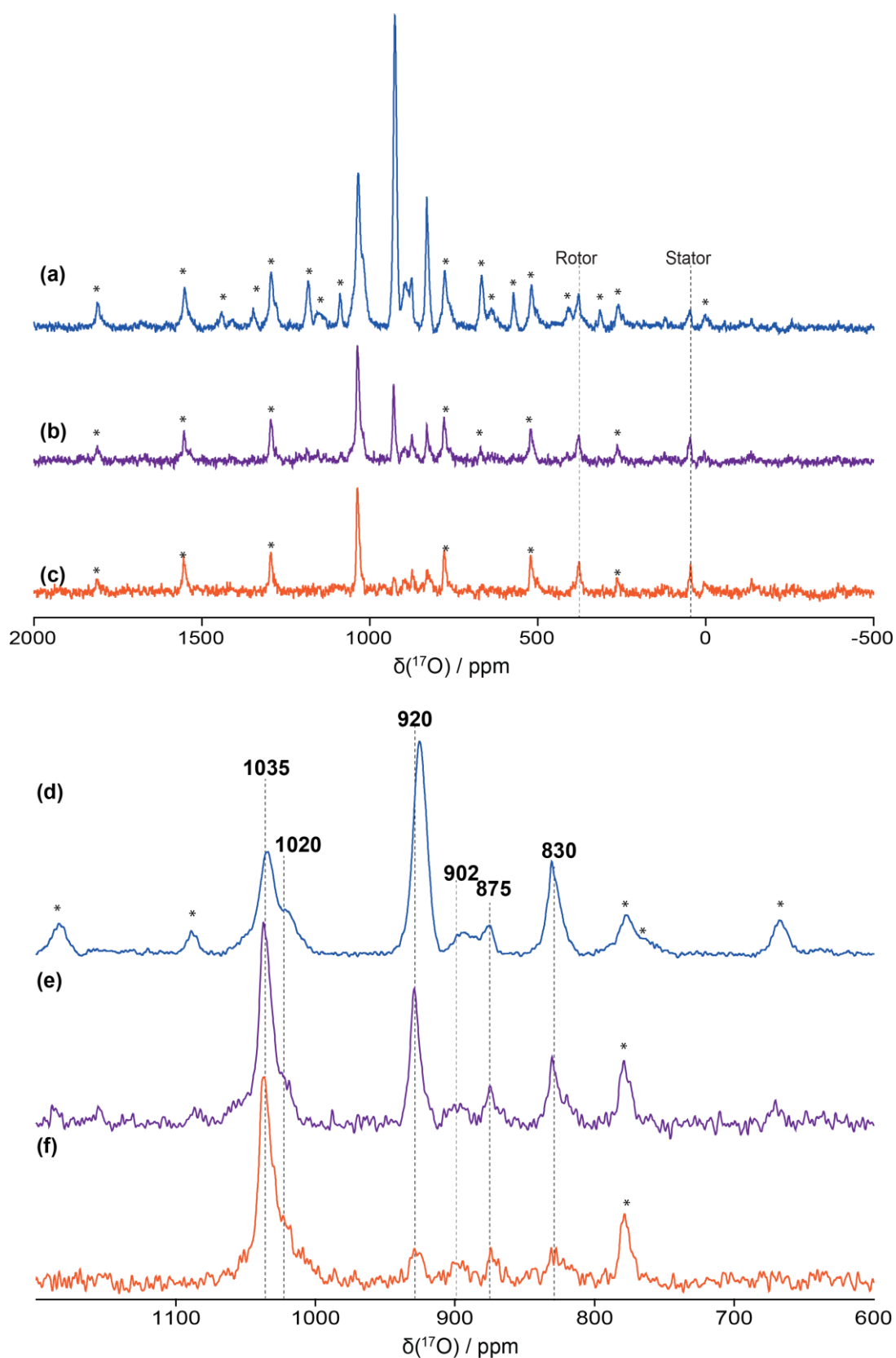


Figure 5.15: ^{17}O MAS single pulse spectra acquired at 9.4 T of (a),(d) HSA20-700/300-Redox, (b),(e) HSA20-700/150-Redox and (c),(f) HSA20-700/25-Redox, respectively. 1024 scans acquired for each spectrum. $\nu_r = 14$ kHz, asterisks denote spinning sidebands and the natural abundance oxygen from the zirconia rotor and macor stator are labelled.

spectra and dominate in (e) and (f), defining these oxygen species as the primary gateway into the structure and therefore the most reactive. In (d), the intensity of the signal just below 930 ppm vastly increases, surpassing that of the primary species, behaviour that could be indicative of the overcoming of a rate limiting step. There is a small 5 ppm shift between this signal in (d) compared to (e) and (f), indicating that at this reoxidation temperature, there is either a change in environment, or the development of a second component. Similar observations can be made for all remaining peaks in that all intensities steadily increase with an increase in reoxidation temperature, relative to the most reactive environments at 1035 and 1020 ppm. Whilst this behaviour may be unexpected (as it is generally accepted that ceria reoxidises at room temperature) studies done below atmospheric pressure under O₂ conditions have seen analogous effects.

In an FTIR study conducted by Badri *et al.* in 1996,¹¹⁸ ceria was reduced under H₂ at 400 °C, and two OH bridging species associated with vacancies were observed. When they reoxidised at room temperature with O₂, they observed only one of these species moving to a band associated with the reoxidised hydroxyl species. The other retained its vacancies until it was heated to 400 °C. They concluded that the reduction at 400 °C initiated a surface-subsurface reorganisation, which is the preliminary step to bulk reduction. To elaborate, once the surface is fully reduced, and under elevated temperatures, an oxygen in the subsurface begins to exchange with the vacancy in the surface; and as the two are associated with the same Ce³⁺ cation, the Ce³⁺ oxidation state is unaltered. When the sample is exposed to reoxidising conditions at ambient temperature, oxygen on the surface (now stabilised by the subsurface vacancy), require an elevated temperature to reverse this surface reorganisation. Badri *et al.* therefore observed that room temperature reoxidation was insufficient to fully reoxidise the sample and only at elevated temperatures (400 °C) did they see the FTIR band associated with the bridging OH species on a reduced ceria surface convert to a bridging OH species on a reoxidised surface.

Binet *et al.* originally observed this phenomenon in ceria under H₂ conditions, through the use of hydroxy and methoxy spectroscopic probes for FTIR detection.¹³³ For example, via the former probe, and for the unreduced sample, bands were observed attributed to OH species on the oxidised surface. As the temperature was

increased, one of these bands systematically shifted to positions associated with OH species on the reduced ceria surface. At 350 °C however, a band emerged in the wavenumber range attributed to OH species on an oxidised surface and continued to increase in intensity at 400 °C. They conclude that a surface reorganisation has occurred through the migration of subsurface oxygen to the surface.

Furthermore, this phenomenon has been observed by Raman spectroscopy by Wu *et al.*, where nanoceria was (CO) reduced at a range of temperatures, followed by reoxidation via O₂ adsorption.¹⁶ They observed a dramatic decrease in adsorbed oxygen in the form of peroxides (O₂²⁻) after a 500 °C reduction compared to 400 °C, and further still at 600 °C. As peroxides are formed when O₂ molecules interact with a two-electron defect, reasoning of this result was originally attributed to a loss in the concentration of defect sites on the surface. However, the authors confirmed through UV Raman that the sample reduced at 600 °C actually had more of these vacancy-associated defects through the increase of the 560 cm⁻¹ band, as compared to the lower temperatures. They attribute this behaviour therefore to surface reorganisation, the first stage of bulk reduction in which oxygen from the subsurface fills the vacancies at the surface, eliminating defect sites available for O₂ adsorption.

Figure 5.15 is easily rationalised via this surface-subsurface reorganisation model, which is simplistically described by Figure 5.16. TPR of HSA20 in Figure 5.7

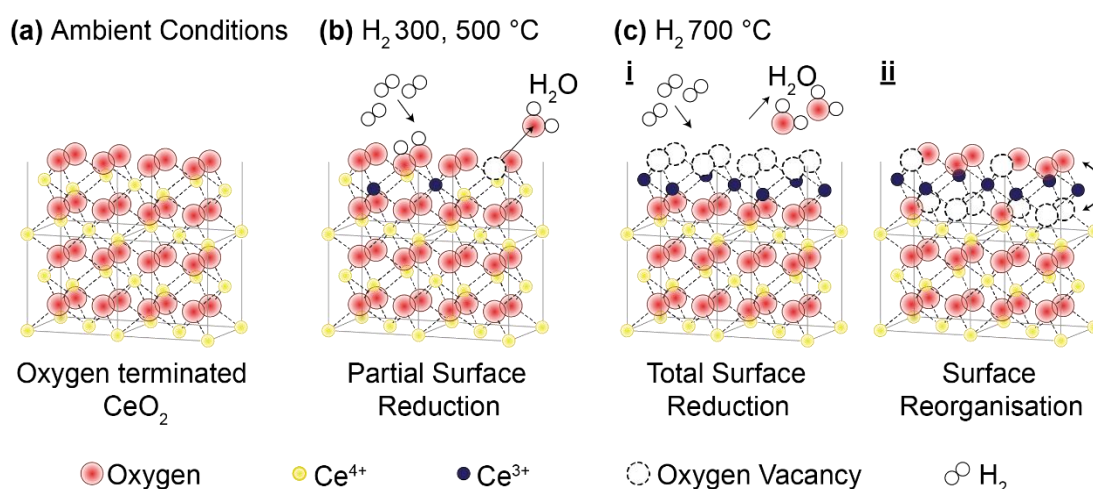


Figure 5.16: A diagrammatic description of surface reorganisation. Note that the surface terminations here are used for simplicity and are not representative of a stable cleavage. (a) Ambient conditions, (b) some oxygen is removed at intermediate temperatures, (c) i) total surface reduction at 700°C, and ii) vacancies at the surface begin to exchange with the subsurface oxygen, initiating the reduction of the bulk.

shows an intermediate stage between surface and bulk reduction at 700 °C, at which point the subsurface oxygen begins to exchange with the vacancies at the surface (before the percolative process of bulk reduction begins), reoxidising the surface and leaving HSA20 in a state that essentially has an oxygen-buffer surface layer. Reduction of the bulk is constrained by oxygen diffusion to the surface, but as ceria's reoxidation process is typically investigated under conditions of high O₂ pressure and temperature, the fact that the reoxidation is constrained to the same mechanism is often overlooked.

5.5.3 Comparison of HSA20-700/300-Redox from Sections 5.3 and 5.4

A change in batch of HSA20 between Sections 5.4 and 5.5 was previously mentioned. For completeness, a comparison of the ¹⁷O MAS NMR data of the sample HSA20-700/300-Redox prepared from the two different HSA20 batches is shown in Figure 5.17, with the data normalised to the signal at 930 ppm. Overall, δ_{CG} positions appear consistent, however a significant reduction in the $\delta_{CG} = 830$ ppm and a smaller intensity loss in $\delta_{CG} = 1035$ ppm could indicate differences in sample properties. As discussed in Section 3.1, the presence and quantity of Frenkel defects is highly dependent on the initial state and preparation of ceria. Factors such as calcination temperature can have a significant effect on these intrinsic defects, which could imply that $\delta_{CG} = 830$ ppm is related to an intrinsic defect.

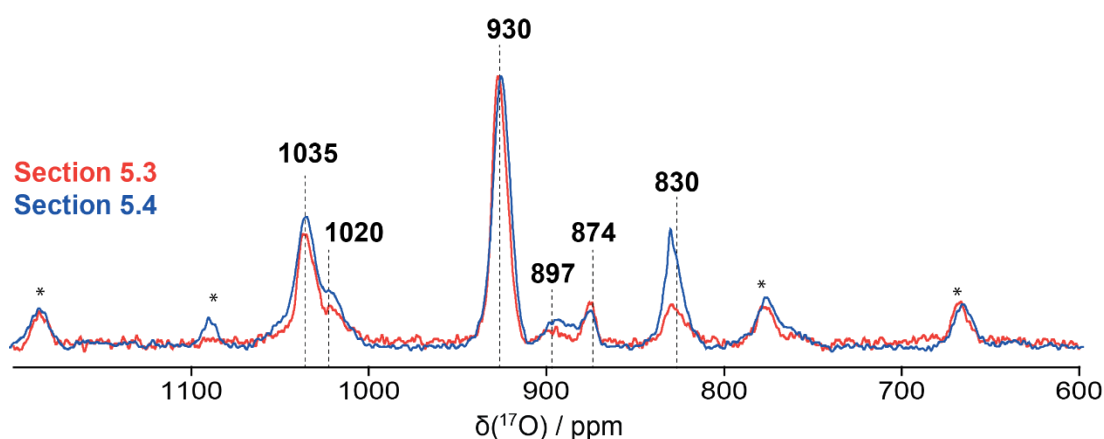


Figure 5.17: Overlaid spectra of HSA20-700/300-Redox from Sections 5.3 and 5.4.

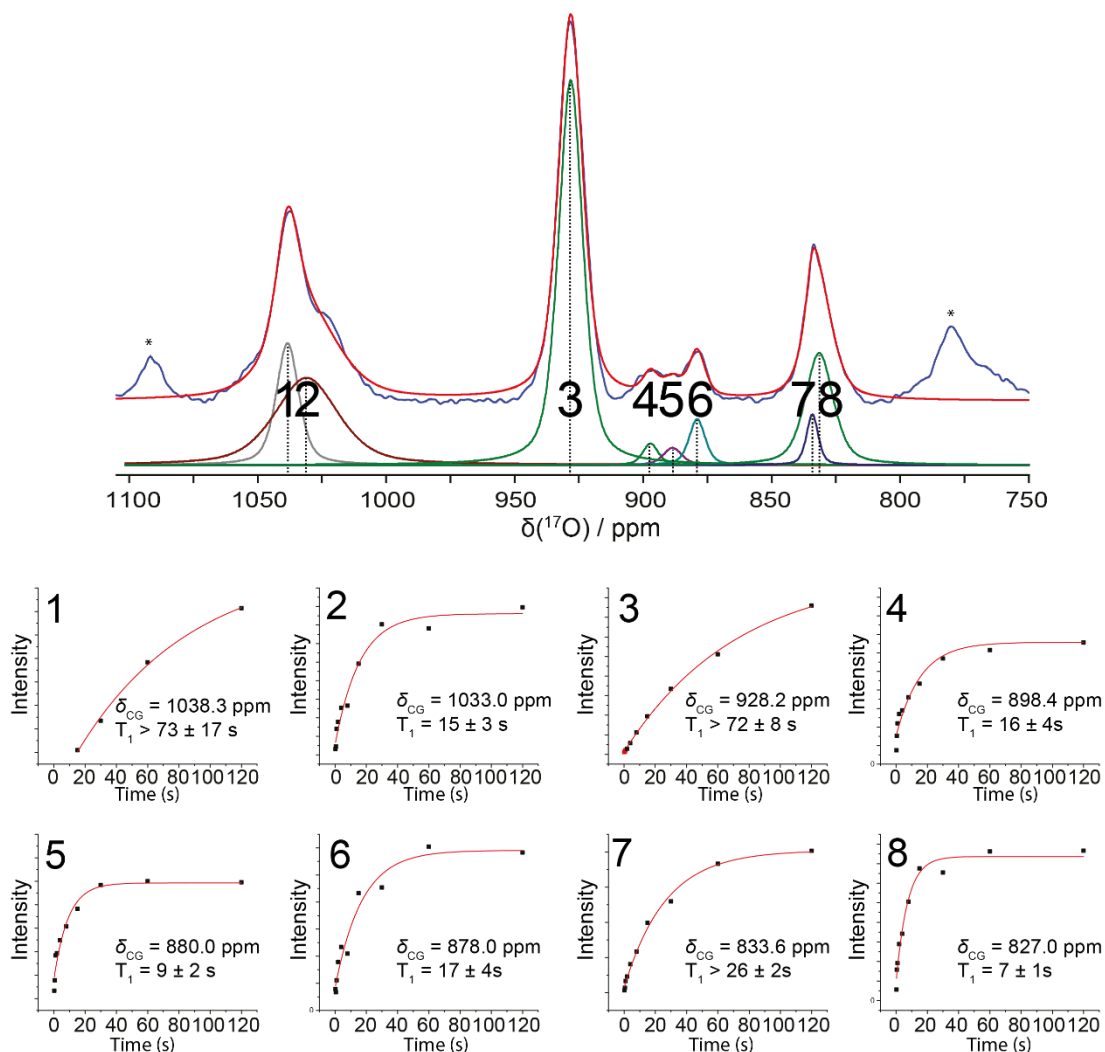


Figure 5.18: Deconvolution of HSA20-700/300-Redox, with T_1 curves acquired via the Saturation Recovery experiment for each site numbered in the spectrum.

5.5.4 T_1 Measurement of HSA20-700/300-Redox

T_1 measurements were acquired for HSA20-700/300-Redox via the Saturation Recovery sequence, with delays of 0.125, 0.25, 0.5, 1, 2, 4, 8, 60 and 120 s. The data, shown in Figure 5.18 reveals a wide range in T_1 values (between 7 and >73 s). For sites labelled 1, 3 and 6, it is evident that a 120 s delay was still insufficient to determine exact values; relaxation is slow for some of these oxygen environments.

5.5.5 Evolution of HSA20-700/300-Redox

On the timescale of a typical solid-state NMR experiment, it appears that the ZrO_2 rotor with Kel-F cap is effectively airtight. However, over the timescale of

weeks/months, this is proven to not be the case, as seen in Figure 5.19, which presents repeat Hahn-echo experiments of HSA20-700/300-Redox (which were kept packed in the rotor between experiments), with 4552 scans accumulated in each case. (Note that these measurements were acquired at 14.1 T and spinning at 14 kHz, resulting in spinning sidebands located on/near centrebands at 900 ppm). A significant loss of ^{17}O can be seen by direct comparison of the spectra acquired after (a) 1 day and (d) 122 days. Simply put, ^{17}O is escaping the system.

Of greater interest however, is the observation of significant sample evolution, i.e. peak movement for those signals at 1035/1020 and 926 ppm overtime, with that at 926 ppm also broadened in (d). As their intensity is lost due to ^{17}O exchange with air, the chemical environments also change, becoming more shielded. This phenomenon is more clearly demonstrated in (e) and (f) for HSA20-700/25-Redox, where ^{17}O is seen to stay within the system and moves to environments that

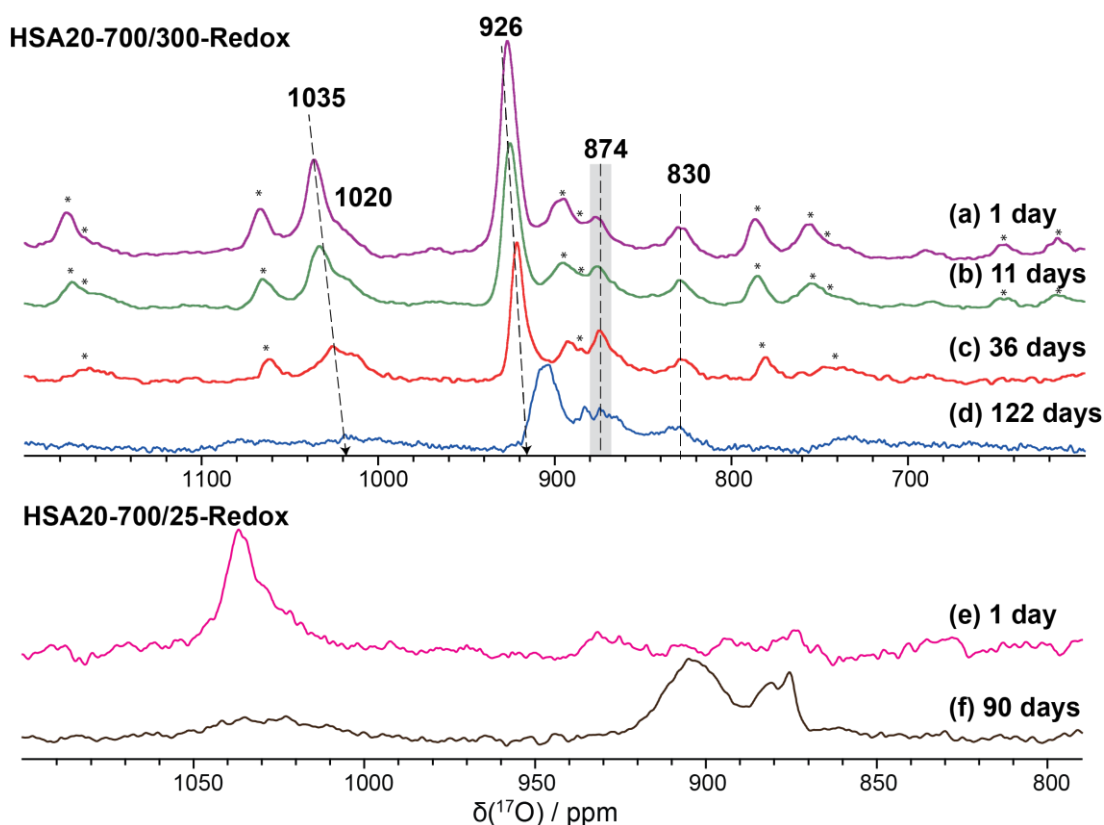


Figure 5.19: Hahn-echo spectra of HSA20-700/300-Redox acquired at 14.1 T after (a) 1 day (b) 11 days, (c) 1 month, and (d) 4 months after the ^{17}O Redox process. 4552 scans were accumulated with a 45 s recycle delay implemented. (e) and (f) depict single pulse spectra of HSA20-700/25-Redox acquired at 9.4 T, 3 months apart. Number of scans are not the same. $\nu_r = 14$ kHz, asterisks denote spinning sidebands.

are closer to the bulk oxygen position over the course of 90 days, resulting in a broad, low intensity resonance at ~900 ppm, similar in profile and position to that seen in (d). This behaviour suggests oxygen migration is active at room temperature in the bulk on these timescales, with ^{17}O tracing the migration pathway. ^{17}O appears to be migrating to a more stable position, potentially the result of a vacancy driven mechanism, for which it is well established (as discussed in Chapter 1) that vacancies are more stable on the surface. Furthermore, if vacancies are diffusing through these systems, perhaps annihilated by oxygen from the air, then Ce^{3+} is reoxidised to Ce^{4+} . These spectral changes are most likely ascribed to both of these defects. Certainly, these oxygen resonances appear to be intermediate to the reoxidation process.

5.5.6 Exposure to Air

In order to exacerbate these changes, HSA20-700/300-Redox was exposed to air (cap of the rotor removed only), for 12 hours, and again for four days with the data presented in Figure 5.20. Firstly, it is evident that there is a diffusion of ^{17}O , determining the more reactive sites as those at 1013, 918 and 827 ppm. Furthermore, after exposure to air for 12 hours, a distinction of four oxygen

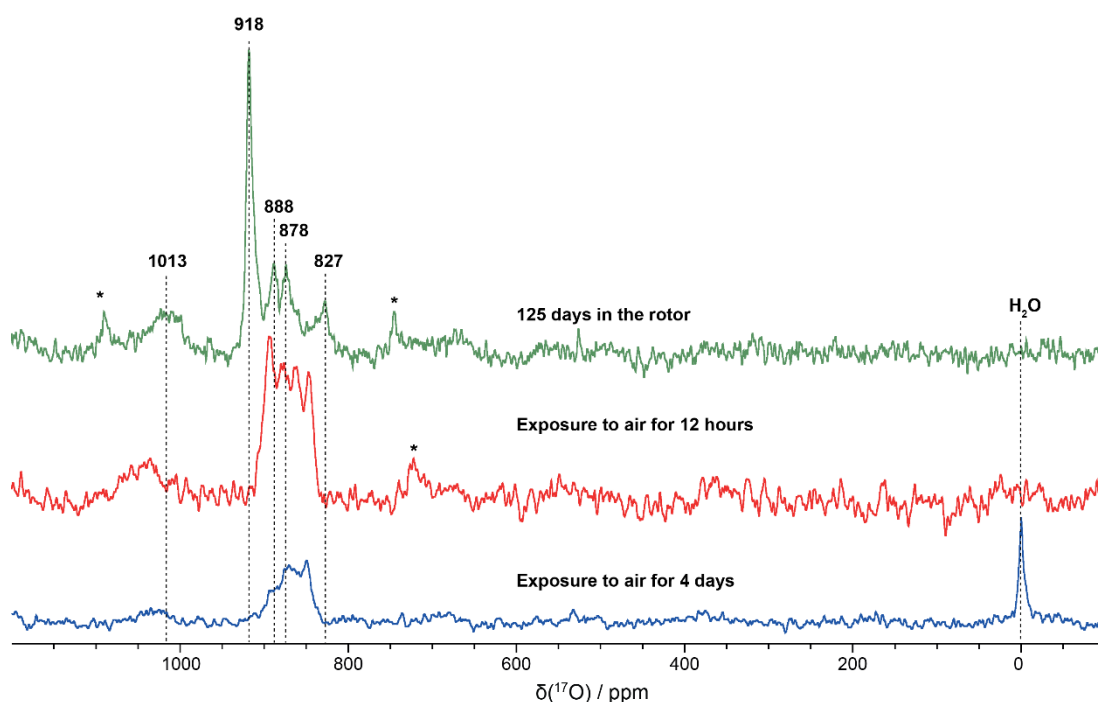


Figure 5.20: ^{17}O MAS NMR spectral changes seen for HSA20-700/300-Redox after exposure in air for 12 hours (middle) and 4 days (bottom), as compared to 125 days packed in the rotor (top). Spectra acquired with Hahn echo sequences, 45 s recycle delays and $\nu_r = 14$ kHz. Asterisks denote spinning sidebands.

environments at 846, 862 878, and 894 ppm (exact 16 ppm shift differences between them) suggests that the ^{17}O probes are in environments with discrete vacancy neighbours in the second coordination sphere. This behaviour was observed by Kim and Stebbins (see Figure 3.2) who reported a shift difference of 14 ppm between two OCe_3Y environments, with and without a vacancy in the second coordination shell.

After four days of air exposure, there is an appearance of free H_2O , and a loss of ^{17}O from ceria sites; the addition of water vapour is known to enhance the surface exchange rate of ceria.¹³⁴ The signal pertaining to the residual O-Ce bonds represents the more stable/least mobile oxygen species.

5.5.7 Comparison of HSA20-700/300-Redox across Three Fields

In order to determine whether any of the oxygen environments observed are affected by quadrupolar interactions, spectra of HSA20-700/300-Redox were acquired at 14.1, 11.7, and 9.4 T, a day after the ^{17}O Redox process and, in light of the spectral evolution seen in Section 5.5.4, they were acquired simultaneously (to the second). As seen in Figure 5.21, across all three fields, peak positions appear

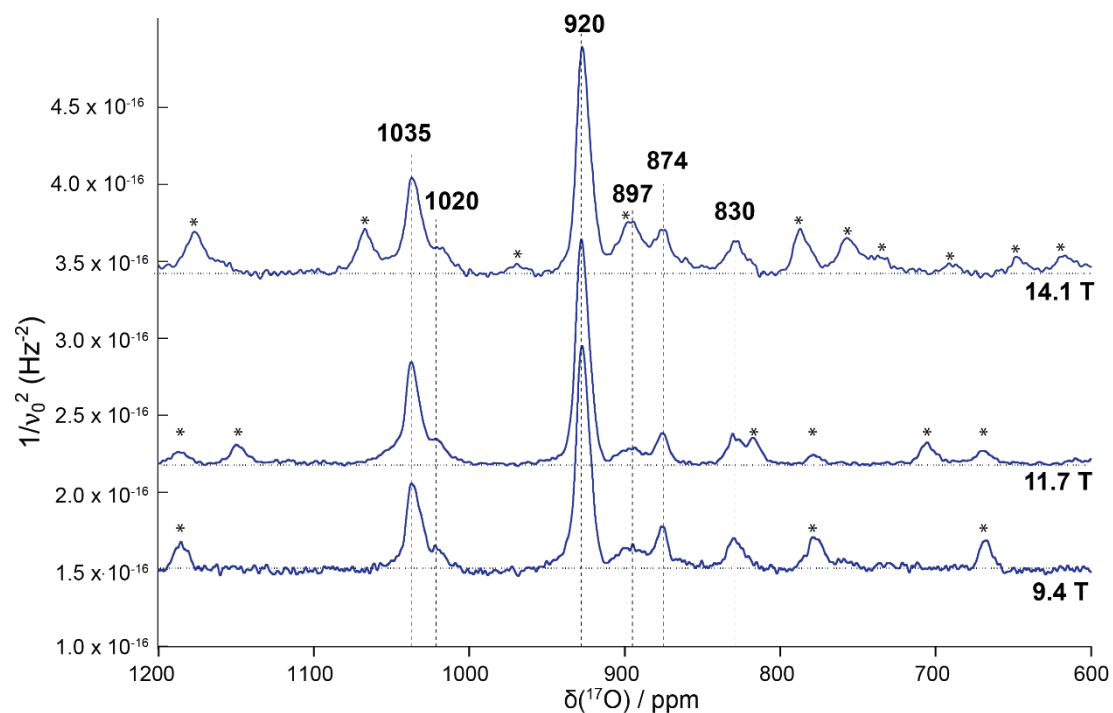


Figure 5.21: Spectra of HSA20-700/300-Redox acquired simultaneously at 14.1, 11.7, and 9.4 T plotted against the inverse of the Larmor frequency squared. The dashed lines clearly establish that negligible shifts are observed with field strength. $\nu_r = 14$ kHz, asterisks denote spinning sidebands.

constant. This is consistent with the result of the multiple field data for H_2^{17}O Ceria seen in Section 5.1.3, and again implies highly ionic bonding environments.

5.6 Size Comparison: Sigma Aldrich <25 nm Ceria

In order to investigate size effects of the preparations of ceria on the solid-state ^{17}O spectral profiles, commercial <25 nm ceria was acquired from Sigma Aldrich (defined as <25 nm SA Ceria). A previous SEM study has characterised this material as highly faceted octahedral particles, exposing the {111} plane, with evidence of truncation by the presence of the {100} plane.¹³⁵

The same preparation conditions for ^{17}O measurements were implemented on <25 nm SA Ceria as that of HSA20 in Sections 5.3 and 5.5, i.e. an exchange with $^{17}\text{O}_2$ at 600 °C for ~ 20hours, defined as SA-600Ex, and $^{17}\text{O}_2$ redox experiments: reduction at 700 °C under H_2 , reoxidation with 30 mL $^{17}\text{O}_2$ at 300 °C, 150 °C and 25 °C, defined as SA-700/300-Redox, SA-700/150-Redox and SA-700/25-Redox, respectively.

5.6.1 Raman Spectroscopy

Figure 5.22 (a) and (b) shows the Raman spectrum of the as-prepared <25 nm SA Ceria and SA-600Ex, respectively. The position of the $\text{F}_{2\text{G}}$ bands (seen in the inset) shifts to lower energy for SA-600Ex, from 463.4 cm^{-1} (for the as prepared sample) to 462.5 cm^{-1} ; analogous to that seen for HSA20 in Figure 5.6. There is no other change in the spectrum (e.g. there is no increase in the defect band, recall Figure 5.8) to suggest that this is caused by reduction of the bulk. It is therefore proposed that ^{17}O has exchanged considerably more with bulk oxygen in this sample, thus causing lower energy bands due to the heavier ^{17}O isotope present. The PXRD and SAXS results reveal that the crystallite have also sintered to 31.7 nm. Whilst these effects should manifest as a narrowing of the $\text{F}_{2\text{G}}$ band, significant ^{17}O incorporation will compensate for this narrowing by the occurrence of overlapping components of the $\text{F}_{2\text{G}}$ band due to a range of $\text{Ce-O}^{16}_x\text{O}^{17}_y$ vibrational units (where $x+y=8$).

Figure 5.22 (c), (d) and (e) depict the Raman spectra of SA-700/300-Redox, SA-700/150-Redox and SA-700/25-Redox, respectively. All three spectra visually appear very similar, however a 0.4 cm^{-1} shift to lower frequency is observed (see Appendix A) for SA-700/300-Redox and negligible change in peak width (as was observed for SA-600Ex), although the crystallite size has increased to 36.9 nm. This is

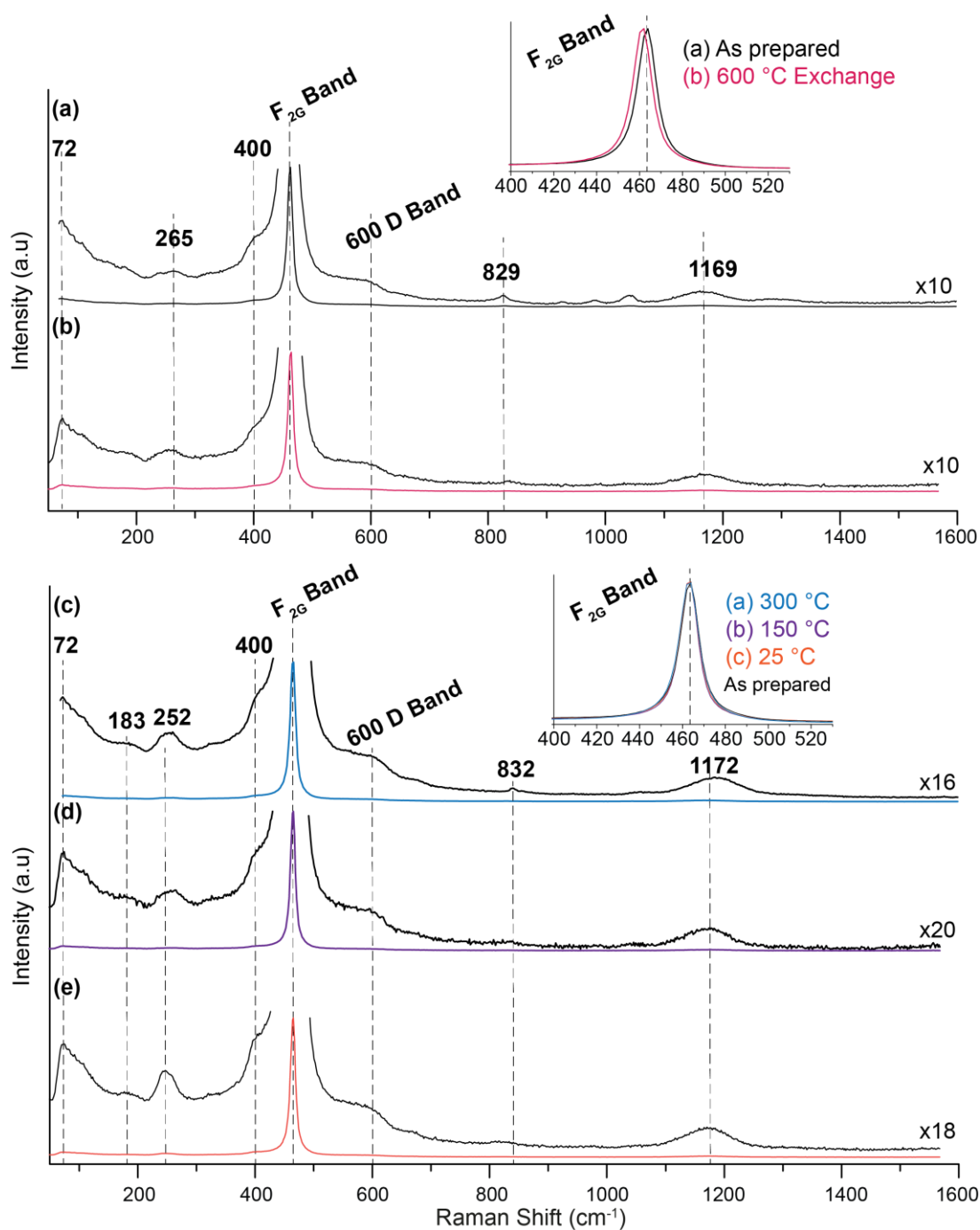


Figure 5.22: Raman spectra between 50 and 1600 cm^{-1} of (a) as- prepared $<25\text{ nm}$ SA Ceria, (b) SA-600Ex (c) SA-700/300-Redox, (d) SA-700/150-Redox and (e) SA-700/25-Redox. $\lambda_{\text{ex}}=532\text{ nm}$.

again indicative of an appreciable ^{17}O concentration. Of course, this alludes to decreased uptake of ^{17}O for the SA-700/150-Redox and SA-700/25-Redox systems.

It is evident that at these sizes (>25 nm), the $\text{F}_{2\text{G}}$ band is less sensitive to relative states of reduction in contrast to HSA20 (<12.7 nm).

5.6.2 ^{17}O Solid-state MAS NMR

Figure 5.23 (a) presents the single pulse ^{17}O MAS NMR spectrum of SA-600Ex which was acquired at 9.4 T. For comparison, the ^{17}O NMR spectrum of HSA20-600Ex from Figure 5.6 is shown directly below in (b). As was implied by the Raman spectrum of HSA20-600Ex in the previous section, significantly greater ^{17}O uptake has been achieved than the equivalent sample preparation of HSA20. It is also apparent that the signal pertaining to bulk oxygen is considerably narrower for <25 nm SA Ceria (110 Hz) compared to HSA20 (590 Hz), an indication that particle size effects (i.e. range in bond lengths) are the prevailing influence on the distribution of chemical shifts. Furthermore, a downfield shift to 875 ppm is observed from HSA20 (874 ppm), which is in-keeping with the observed trend of a larger particle size moving toward a more deshielded position (recall bulk oxygen resonance $\delta_{\text{CG}} = 873$ ppm for the <2 nm H_2^{17}O Ceria). To clarify, the position of the bulk oxygen appears size-dependent, with greater shielding observed for a smaller particle. No other resonances, i.e. those observed at 925, 900, 868, 860, and 831 ppm of SA-600Ex are shared with HSA20-600Ex. However, those signals at 925, 900 and 831 ppm are present in the ^{17}O Redox experiments of HSA20 from Sections 5.4.4 and 5.5.2, implying that these are common oxygen environments and can be irrespective of particle size.

Single pulse ^{17}O MAS NMR spectra of SA-700/300-Redox, SA-700/150-Redox and SA-700/25-Redox are depicted in Figure 5.23 (c), (e) and (g), respectively. Underneath each spectrum in (d), (f) and (h) are the ^{17}O NMR measurements of HSA20 from Section 5.5.2., which have undergone the same preparation conditions. The spectrum in (c) reveals considerable ^{17}O uptake in the bulk species at 876 ppm which, alongside SA-600Ex, was evident in Section 5.6.1 by its corresponding Raman spectrum. The x10 magnification of (c) reveals similar signals (within 2 ppm) as that of HSA20 below: 1030, 1020, 926, 900, 876, and 832 ppm and that of SA-600Ex above:

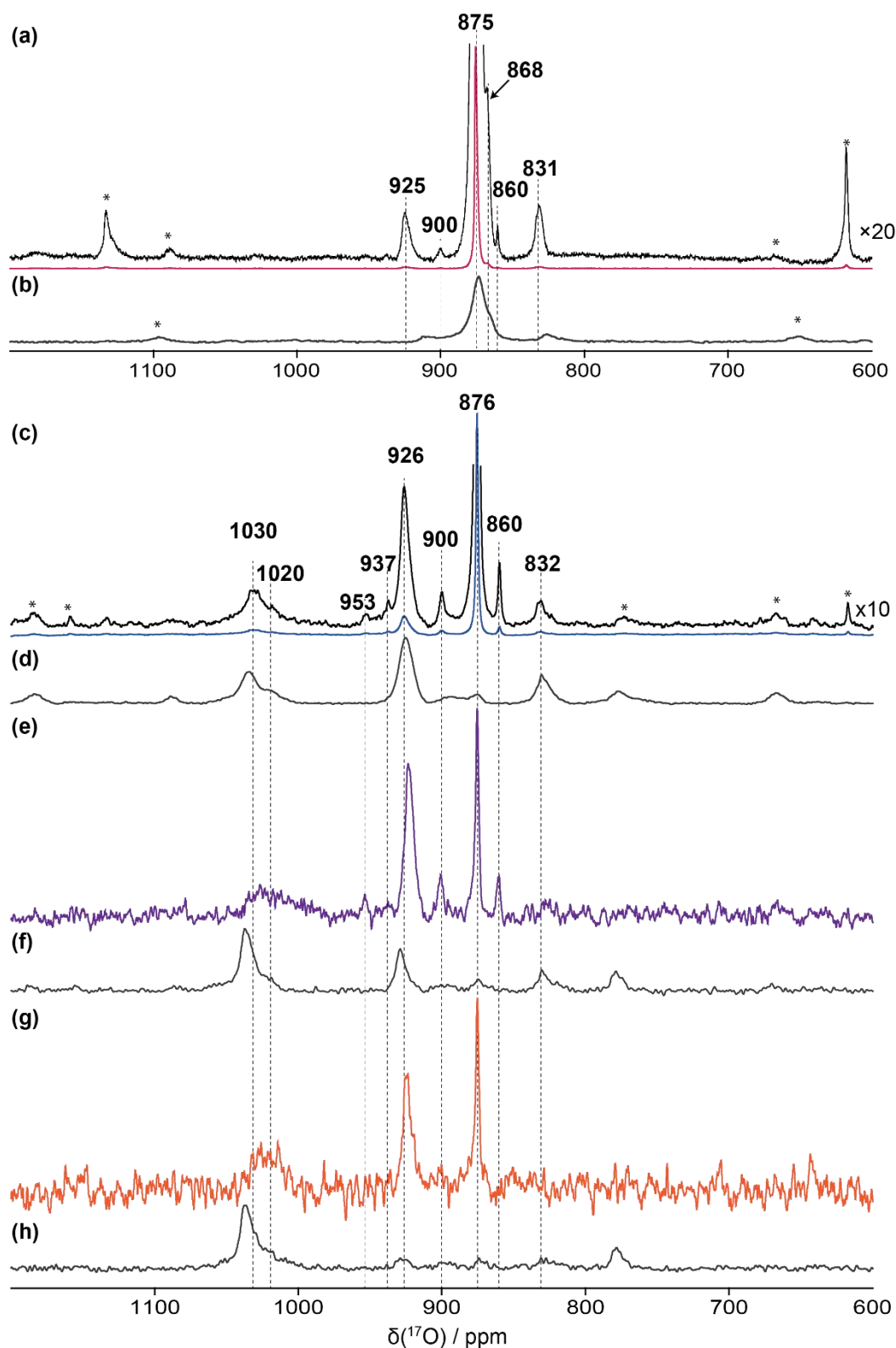


Figure 5.23: ^{17}O MAS single pulse spectra acquired at 9.4 T of (a) SA-600Ex, (c) SA-700/300-Redox, (e) SA-700/150-Redox and (g) SA-700/25-Redox. Comparative spectra (grey) underneath are those of HSA20 having undergone the same preparation (taken from Figure 5.6 and Figure 5.15): (b) HSA20-600Ex, (d) HSA20-700/300-Redox, (f) HSA20-700/150-Redox and (h) HSA20-700/25-Redox. $\nu_r = 14$ kHz, except (b) where $\nu_r = 12$ kHz. Asterisks denote spinning sidebands.

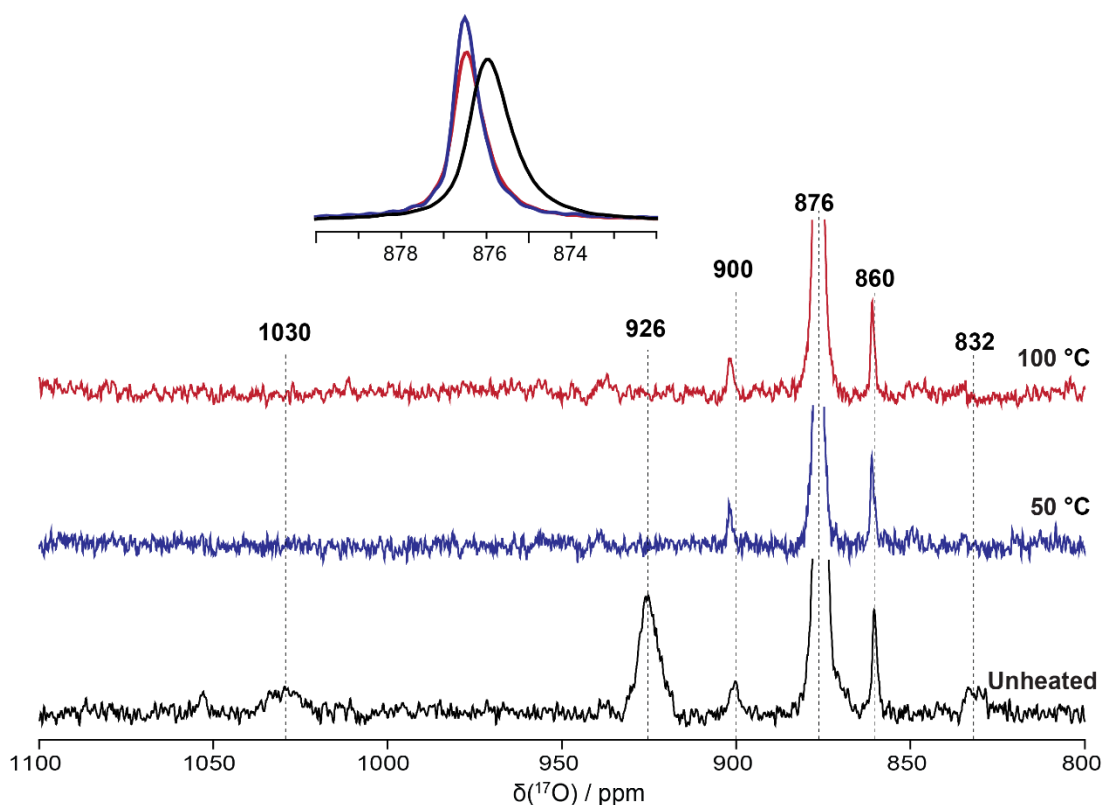


Figure 5.24: ^{17}O MAS NMR single pulse spectra of SA-700/300-Redox after heating in air at 50 and 100 °C for 30 minutes. Inset shows the bulk oxygen peak (which has been cropped in the below spectra). Acquired with 45 s recycle delay and $\nu_r = 14$ kHz.

925, 900, 875, 868 and 831 ppm. Additional, low-intensity peaks at 953, 937 ppm are also evident.

The spectra shown in (e) and (f) reveal a significant loss in signal/noise; evidently ^{17}O uptake was greatly inhibited at these lower reoxidation temperatures compared to the analogue spectra of HSA20 below them in (f) and (h). Very similar relative intensities of the peaks in (e) and (g) can be observed, with more ^{17}O incorporation in the reoxidation at 150 °C. Resonances at 1020, 953, 926, 900, 876 and 860 ppm are still apparent in (f), with those at 953, 900 and 860 ppm lost in (g). A comparison of (g) and (h) strongly suggests that the most reactive environments (likely located on the surface) of ceria are found at 1030/1020 and 926 ppm. It is important to recall that the natural abundance of ^{17}O at 0.037% is observable for oxygen with highly ionic/symmetrical bonding and therefore the bulk oxygen at 876 ppm in (f) and (g) may not be due to bulk reoxidation.

5.6.3 Heating of SA-700/300-Redox in Air

In order to probe the nature of the oxygen species seen in Figure 5.23, SA-700/300-Redox was gently heated in air in two stages, first to 50 °C for 30 mins, followed by 100 °C for a further 30 mins. The ^{17}O single pulse measurements acquired at 11.7 T are shown in Figure 5.24. It should be noted that this experiment was conducted 3 months after the initial ^{17}O redox preparative procedure. The bottom spectrum in Figure 5.24 depicts the as-of-yet unpacked (from the rotor) SA-700/300-Redox sample. It is evident, when comparing to Figure 5.23(c), acquired 3 months before, that ^{17}O has been lost. In fact, the signal located at 1030/1020 ppm has almost disappeared. This suggests that the oxygen adsorbed in the ^{17}O redox experiments is highly mobile, reactive and readily exchanges with air, with some species showing greater reactivity than others; behaviour that was observed for HSA20.

It is apparent from Figure 5.24 that the signals at 1030, 926, and 832 ppm are completely lost upon heating at 50 °C. Furthermore, there is a slight (0.5 ppm), downfield shift of the bulk oxygen position (see inset), accompanied by a peak-narrowing and some loss in overall peak intensity, indicative of an increase in order of the bulk oxygen environment. At 100 °C heating however, whilst there are no changes of the remaining oxygen environments, there is now a decrease in intensity of the bulk oxygen.

The effects of heating SA-700/300-Redox on the bulk environment ($\delta_{\text{CG}} \sim 876$ ppm) is shown more clearly by a peak devolution in Figure 5.25. It is apparent that the known bulk position is characterised by two peaks; a more-shielded broad component and a less-shielded, narrower component. This model is in-keeping with previous data (see Figure 5.6(b)), where oxygen species from the surface with O-Ce-O bonds are located upfield of bulk-like O-Ce-O bonds, due to an average shorter bond length at the surface. Before heating, these environments are more shielded and there is a greater distribution, implying ^{17}O resides in positions closer to the surface. After heating at 100 °C, both peaks shift to higher ppm, and narrow, indicating that ^{17}O is diffusing to more bulk-like positions.

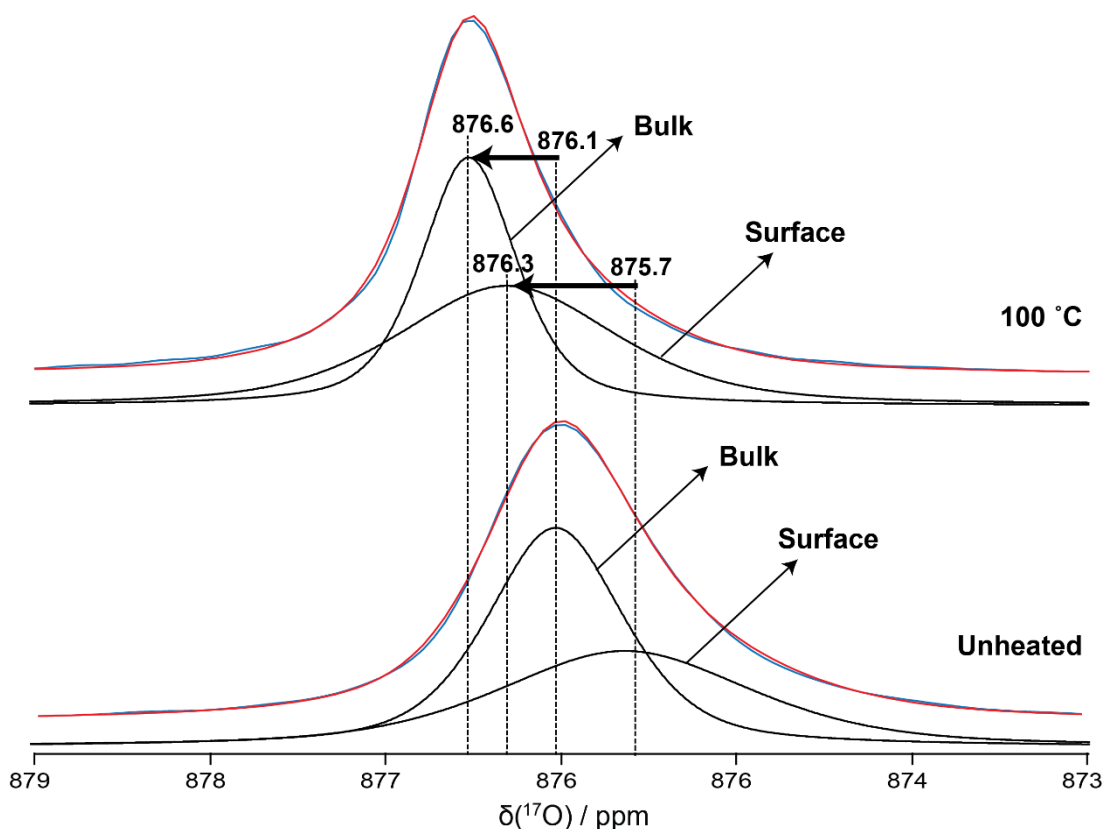


Figure 5.25: Deconvolutions of SA-700/300-Redox after heating in air at 100 °C for 30 minutes (top) and before heating (bottom). A greater spectral width of the experimental data was shown in Figure 5.24.

5.7 Morphology Comparison: Cubes and Rods

Ceria rods and cubes were discussed in Chapter 1; they preferentially expose the {110} and {100} facets in the former, and the {100} series of surfaces in the latter. Rods and cubes were sourced from Professor Edman Tsang's group from the University of Oxford. They have previously characterised the size of the particles by TEM as 8×80 nm for rods and 17.1 nm for cubes.¹⁰¹ It was revealed that when heated at 500 °C, these morphologies were maintained, i.e. the unstable {100} and {110} facets did not experience a rearrangement to the more stable {111}, but a particle sintering was observed; 8×127 nm and 30 nm measurements were confirmed for the rods and cubes after heating, respectively. Interestingly, no growth was observed in the rod width, growth was only observed along the rod length.

In order to compare the results of Sections 5.5 and 5.6, the same Redox experiments were implemented. Appendix E shows the TPR-H₂ measurements for the rods and cubes, in which the surface reduction intensity is greater than that of the bulk reduction for the rods, reflecting their much greater surface area; a result of

their small width. Furthermore, the surface and bulk reduction peak positions of the rods (475 and 750 °C) are lower than that of the cubes (525 and 800 °C).

Limited amounts of these ceria morphologies were attained, and so only $^{17}\text{O}_2$ Redox experiments were implemented to ^{17}O enrich these systems: reduction under H_2 at 700 °C, reoxidation at 300 and 150 °C, defined as, Cubes-700/300-Redox, Rods-700/300-Redox, Cubes-700/150-Redox and Rods-700/150-Redox.

5.7.1 Raman Spectroscopy

Figure 5.26 presents Raman spectra acquired of (a) Cubes-700/300-Redox, (b) Rods-700/300-Redox, (c) Cubes-700/150-Redox and (d) Rods-700/150-Redox (Raman spectra of the as-prepared samples were unfortunately not acquired). The positions and widths of the $\text{F}_{2\text{G}}$ band shown in the inset reveal similar bulk properties between

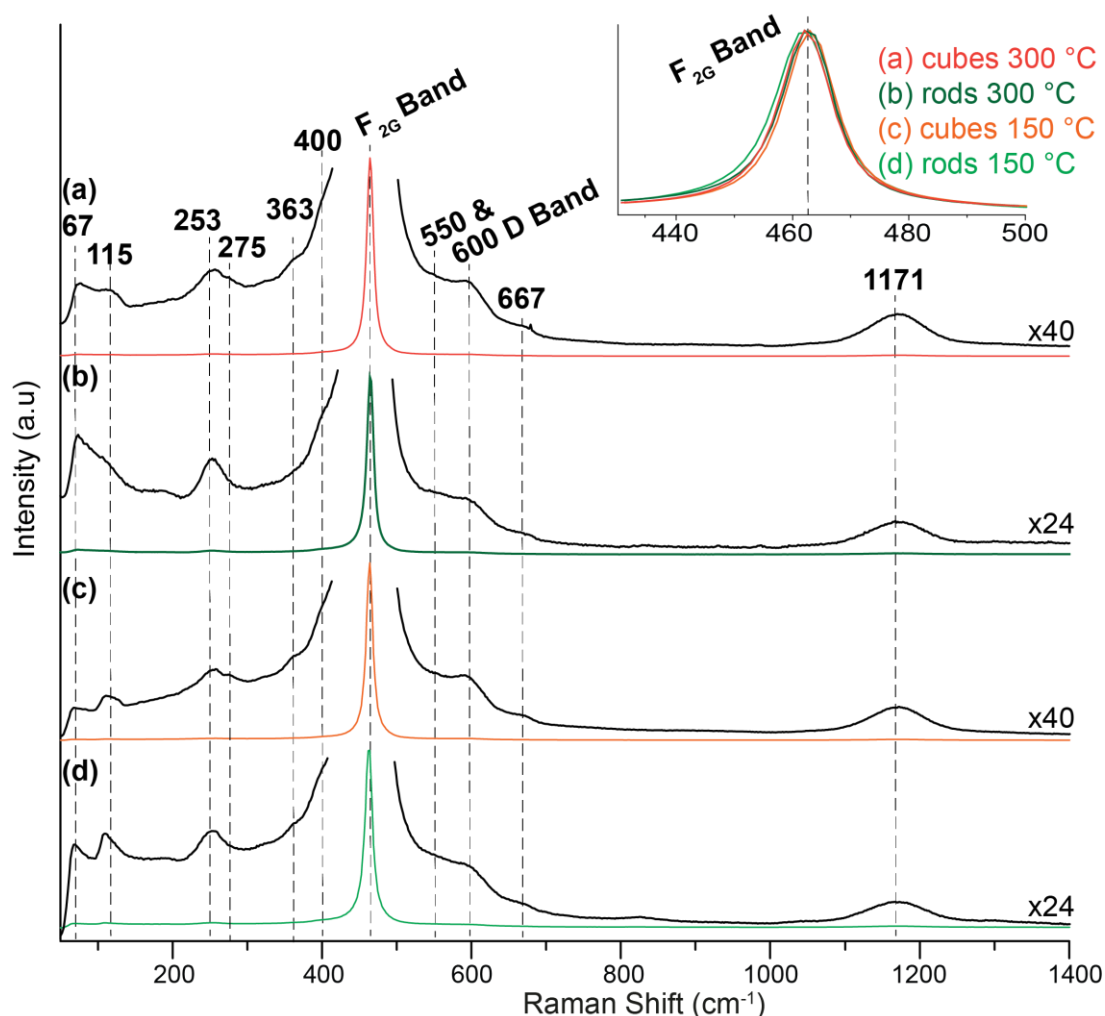


Figure 5.26: Raman spectra between 50 and 1600 cm^{-1} of (a) Cubes-700/300-Redox, (b) Rods-700/300-Redox, (c) Cubes-700/150-Redox, and (d) Rods-700/150-Redox. $\lambda_{\text{ex}}=532 \text{ nm}$.

the samples, with the exception of (d) Rods-700/150-Redox, which appears more red shifted at 462.1 cm^{-1} , and broader with $\Gamma = 10.2\text{ cm}^{-1}$ (compared to (a)-(c) where $F_{2G} = 463.2\text{--}463.8\text{ cm}^{-1}$ and $\Gamma = 8.5\text{--}8.8\text{ cm}^{-1}$). Alongside a greater defect band where $I_D/I_{F_{2G}}$ is 0.016 (smaller values of (0.09-0.012) for (a)-(c)), it is determined that Rods-700/150-Redox is in a more reduced state. Moreover, considerably less ^{17}O label (this will be shown by ^{17}O NMR data in Section 5.7.2) is present compared to Rods-700/300-Redox, confirming a non-isotopic shift of the F_{2G} mode.

From the Raman spectra of the rod particles, it is clear that the reoxidation temperature for the ~20 hour heating in $^{17}\text{O}_2$ after a H_2 -reduction has a great influence on the reoxidation process (i.e. greater reoxidation is seen at the greater temperature of $300\text{ }^\circ\text{C}$), as was seen for HSA20 and $>25\text{ nm}$ SA Ceria, for which surface reorganisation was established as the rate-limiting effect.

5.7.2 ^{17}O Solid-state MAS NMR

Figure 5.27 presents ^{17}O MAS NMR single pulse spectra acquired at 9.4 T of (a) Cubes-700/300-Redox, (b) Rods-700/300-Redox, (c) SA-700/300-Redox (d) Cubes-700/150-Redox, (e) Rods-700/150-Redox, and (f) SA-700/150-Redox. The SA Ceria from Section 5.6 have an octahedral morphology, exposing the $\{111\}$ surface series, and so they are shown again here in order to represent all three low index planes. Under the consideration that all recycle delays (128 s) and number of scans (1024) are the same for all spectra shown in Figure 5.27, results are possibly quantitative (see Section 5.7.3). It is again clear from the S/N that the difference in temperature of reoxidation, $300\text{ }^\circ\text{C}$ for the spectra on the left and $150\text{ }^\circ\text{C}$ for the spectra on the right, plays an important role in reoxidation, i.e. surface reorganisation is still a rate-limiting process for these less-stable surfaces.

Up until this point, the ^{17}O spectra of the ceria systems HSA20 and $>25\text{ nm}$ SA Ceria that have undergone the $^{17}\text{O}_2$ Redox enrichment process, have all revealed more than the one crystallographic oxygen site expected for the CeO_2 structure. Figure 5.27 (a) and (d) depicting the cubes however, are dominated by this species at 876 ppm, with a small peak at 832 ppm and almost negligible contributions of signals at 929 and 897 ppm. Spectra in (b) and (e) however, (the rods) show similar spectral

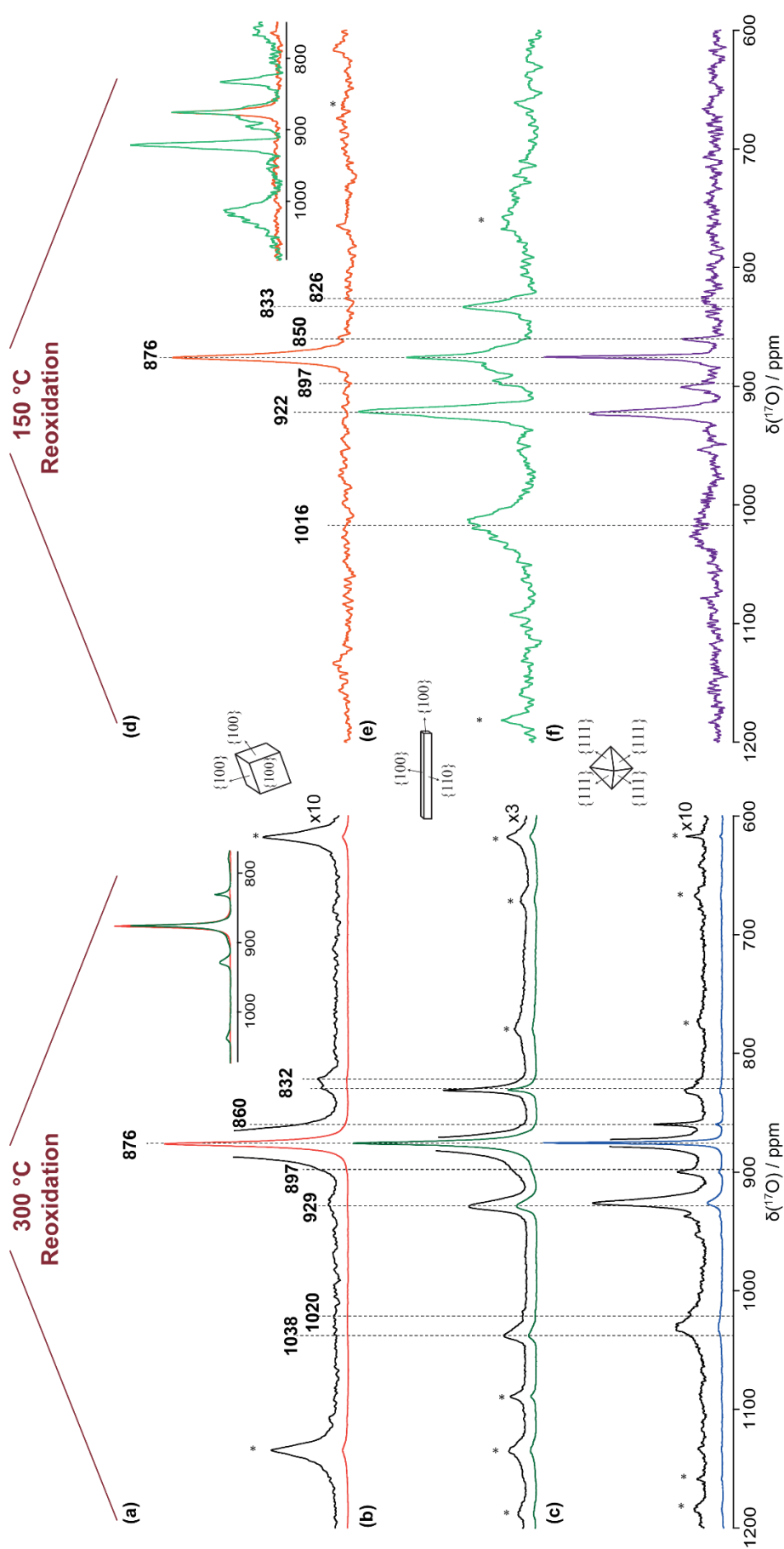


Figure 5.28: ^{17}O single pulse spectra of (a) Cubes-700/300-Redox, (b) Rods-700/300-Redox, (c) SA-700/300-Redox (d) Cubes-700/150-Redox, (e) Rods-700/150-Redox, and (f) SA-700/150-Redox. All spectra acquired at 9.4 T with a 128 s recycle delay and $\nu_r = 14$ kHz.

characteristics to those of the ceria octahedra in (e) and (f).

Theoretical studies conducted by Sayle *et al.* have found that the CeO_2 {100} surface is catalytically more active due to its dipole moment,¹³⁶ whilst OSC measurements conducted by Mai *et al.* conclude that the lattice oxygen migration from bulk to the surface of the {100} and {110} planes have a considerably lower energy barrier than that of the {111}.⁵⁷ This greater surface-bulk oxygen migration rationalises the bulk-dominated spectra of the cube systems.

The insets in Figure 5.27 overlay the expanded regions for the rods and cubes, and demonstrate that, at 300 °C (left), similar uptake of ^{17}O is observed. In this temperature range, based on their considerably smaller surface area, the cubes (<30 nm) adsorb more oxygen, demonstrating a greater OSC. At 150 °C however (right), the rods reveal a greater integrated area shared between four signals and so in this low temperature range, the rods are able to store greater amounts of oxygen.

As the Raman spectrum of Rods-700/150-Redox (Figure 5.26) indicated a greater defect density (via a greater I value), a simple correlation can be made with the so far unassigned peaks at 1016, 922 and 833 ppm, with oxygen near defects.

5.7.3 T_1 Relaxation of Cubes-700/300-Redox and Rods-700/300-Redox

T_1 measurements obtained from saturation recovery experiments, implementing 10 τ delays up to 128 s, are shown in Figure 5.28. (a) reveals fits for three peaks of the Cubes-700/300-Redox system, with two components underneath the bulk-position at 876 ppm, depicting the bulk and surface resonances. The inner bulk signal, labelled 2 in the figure, has a greater T_1 value of > 31 s (the conditions of the experiment were insufficient- longer τ delays are necessary to measure a precise value), a value that is in keeping with its position of greater symmetry in the lattice. The surface component, with its lower point symmetry, has a shorter T_1 of 18 ± 1 s and the third peak at 825 ppm has a T_1 of 14 ± 4 s; similar to the oxygen in the lattice surface.

T_1 values obtained for Rods-700/300-Redox expose a more complex structure, with many unresolved sites (more errors are likely to be associated with the fits), as shown in Figure 5.28 (b). As with Cubes-700/300-Redox, the bulk environment (labelled 7) has the longest T_1 of 20 ± 2 s. Relative to the bulk oxygen T_1

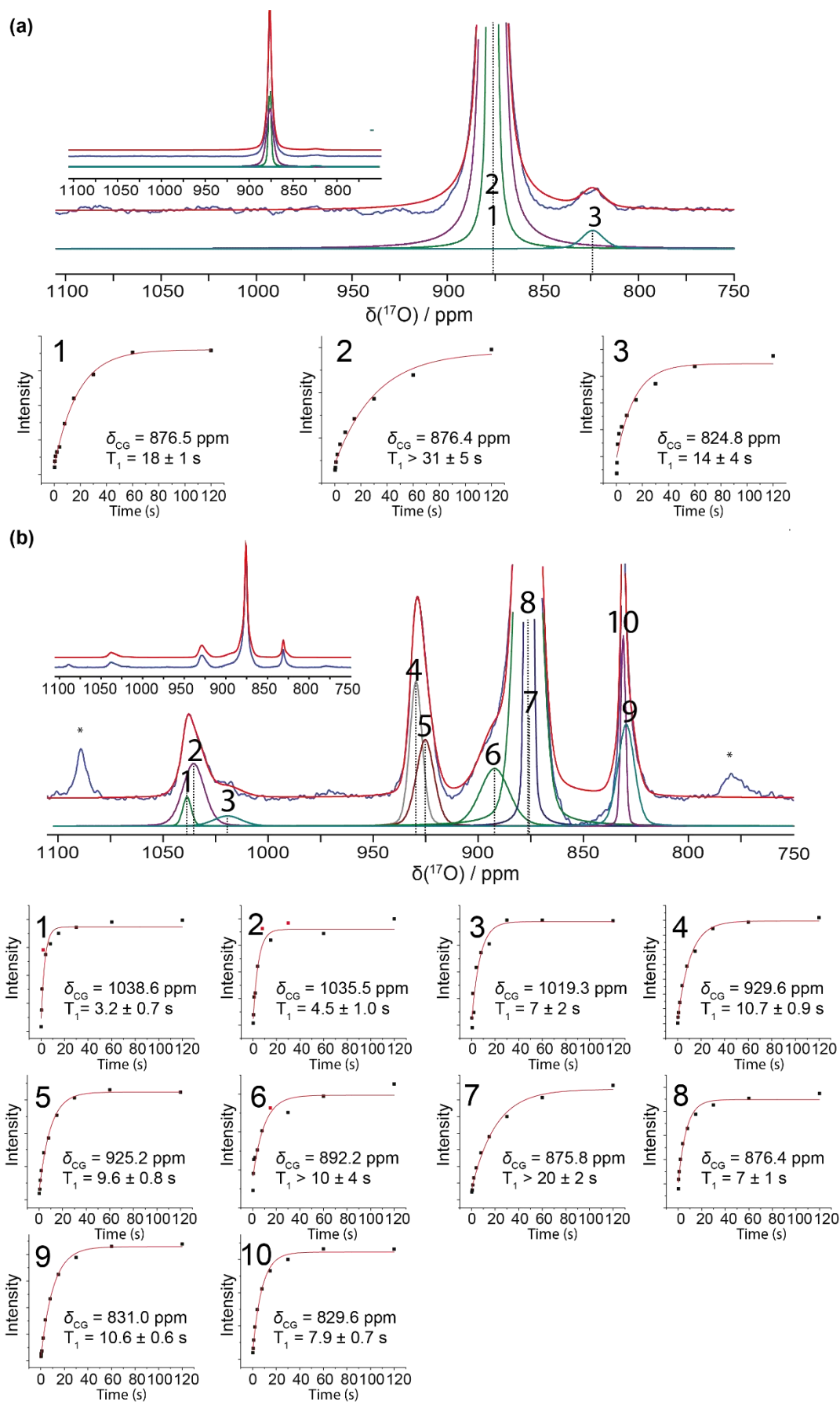


Figure 5.29: Diagram of the T_1 fits and corresponding peak positions for (a) Cubes-700/300-Redox, and (b) Rods-700/300-Redox. Experiments times were ~ 2.5 days.

for the cubes system, the bulk environment is possibly closer to points of distortion and/or paramagnetic defects that enhance relaxation times.

The data presented in Sections 5.1 to 5.6 has demonstrated that ceria has a vast range of structural-perturbing species that are intrinsic to its operation as an 'oxygen reservoir'. The rest of this chapter is dedicated to identifying these oxygen environments and observing the impact that perturbations cause to oxygen species within their sphere of influence.

5.8 Peroxides on Ceria

Via Raman spectroscopy, this chapter has seen evidence of peroxide species at 832 cm^{-1} residing on the surface of ceria. As described in Chapter 1, peroxide (O_2^{2-}) and superoxide (O_2^-) species are intermediaries in the reoxidation process of ceria by O_2 , where O_2 interacts with the one and two electron defects created during reduction. Pushkarev *et al.* investigated reduction and O_2 -reoxidation of cubes, rods and octahedra and observed (facet-dependent) vibrational bands between 832 and 862 cm^{-1} , which were stable up to $200\text{ }^\circ\text{C}$. The species observed at the lower energy range (832 cm^{-1}) are well documented as an O_2 molecule adsorbed to an isolated two electron defect, (with higher Raman shift indicating a greater degree of defect aggregation).

At the end of Section 5.5.2, observations of Raman measurements conducted by Wu *et al.* were described, in which they noted an unanticipated result. After reoxidation, the amount of peroxide species on the surface were seen to decrease in intensity when the reduction temperature was increased. They proposed that surface-reorganisation was responsible for filling the surface adsorption sites; the conclusion made for ceria systems that have undergone a $^{17}\text{O}_2$ reoxidation process in this chapter.

These studies, along with the confirmed presence of peroxide species by Raman spectroscopy, prompted a literature search of ^{17}O NMR shifts of O-O bonds; which can be categorised into two different classes of structure-type.¹³⁷ The first is related to hydrogen peroxide (H_2O_2), which has a free chemical shift of 174 ppm ¹³⁸ and the second to ozone (O_3) with free chemical shifts of 1032 and 1598 for the central and terminal oxygen, respectively, according to Solomon *et al.*¹³⁹

Recall that the as-of-yet unassigned oxygen resonances at circa 1035 ppm (an average across samples), which comprise a narrow and underlying broader component are observed in the ^{17}O NMR data of ceria having undergone a reduction-reoxidation process. Whilst Huang & Beck certainly revealed the presence of O_3 architectures on the surface of ceria nanoparticles by FTIR spectroscopy after a reoxidation process by O_2 at 650°C ,¹⁴⁰ there is no evidence of O_3 vibrations (between 1000 and 1100 cm^{-1})¹⁴¹ in the collected Raman spectra of the ^{17}O redox samples.

The pursuit of peroxidic ^{17}O NMR measurements has resulted in several failed investigations over the years^{170,171}, attributed to slow molecular tumbling however, Reynolds & Butler were successful in acquiring ^{17}O spectra of coordinated peroxocomplexes on transition metals (V, Mo and W).¹⁴² They noted a correlation of vibration frequency with ^{17}O chemical shift where vibration frequencies under 900 cm^{-1} corresponded to chemical shifts below 600 ppm. Furthermore, Bastow *et al.* assigned ^{17}O peaks located at 198 and 161 ppm (spectra acquired at 9.4 T) to interstitial peroxide in barium fluorobromide and fluorochloride materials.⁸²

In order to ascertain whether peroxide- or ozone-like species are manifesting in the ^{17}O NMR data, a method was conceived to synthesize nanoceria saturated with ^{17}O -labelled peroxo/hydroperoxo species, which are stable on the nanoparticle surface (at room temperature). Last year, Damantov and Mayer¹⁰³ published a method of reacting anhydrous H_2O_2 with organic colloidal ceria nanoparticle solutions and through FTIR observation, found that H_2O_2 reacts with the nanoparticles to form these peroxo/hydroperoxo species, located at a Raman shift of 840 cm^{-1} . In order to selectively enrich these peroxo-like species with ^{17}O , the ^{17}O label was introduced into the system via labelling of the H_2O_2 , using a direct combination process of H_2 and O_2 . Synthesis details of the ^{17}O -enriched H_2O_2 solution and the consequent ^{17}O labelled peroxo-ceria sample (defined ^{17}O peroxo-ceria) are given in Chapter 4. In summary, the ^{17}O enriched H_2O_2 dissociates on Ce^{3+} surface sites to produce a brown precipitate, indicting the presence of peroxide species coordinated to Ce^{4+} .

100% natural abundance (^{16}O) oxygen was initially used in the $\text{H}_2\text{-O}_2$ combination procedure to first ensure a viable synthesis of peroxo ceria (defined ^{16}O peroxo-ceria), which was confirmed by Raman spectroscopy, after which synthesis

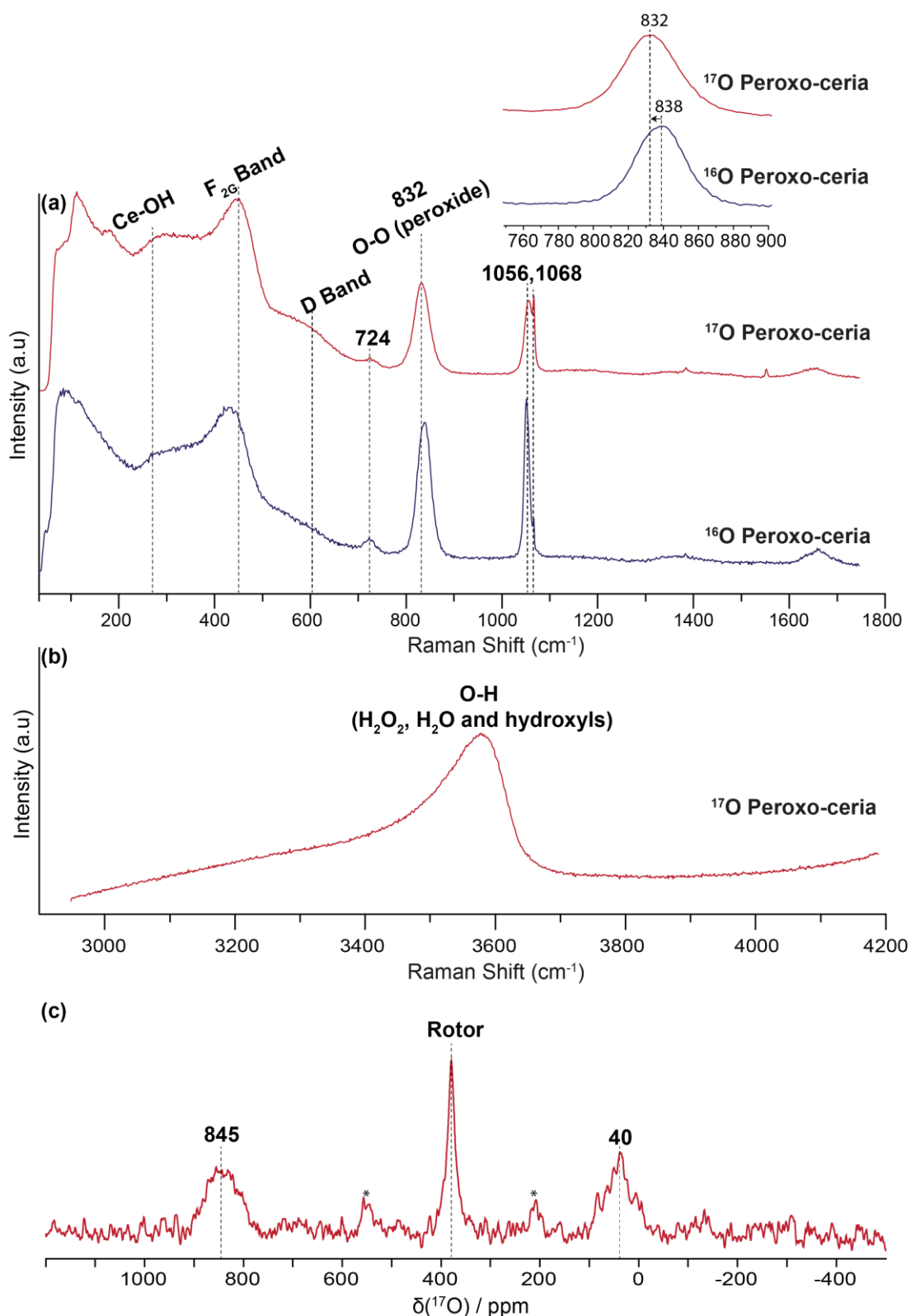


Figure 5.30: (a) The Raman spectra of ^{17}O peroxo-ceria (top) and ^{16}O peroxo-ceria (bottom) between 50 and 1750 cm^{-1} . (b) Raman spectrum of ^{17}O peroxo-ceria in the O-H region. $\lambda_{\text{ex}}=532 \text{ nm}$. (c) ^{17}O MAS NMR of ^{17}O peroxo-ceria acquired at 14.1 T, with a 30 s recycle delay and $\nu_r = 14 \text{ kHz}$.

Table 5.3: Parameters extracted from Raman data presented in Figure 5.30 (a).

	O-O position (cm ⁻¹) ± 0.3	Γ of O-O (cm ⁻¹) ± 0.8	F _{2G} (cm ⁻¹) ± 0.4	I _D /I _{F2G}
¹⁶ O Peroxo Ceria	837.7	29.1	441.6	0.202
¹⁷ O Peroxo Ceria	832.6	36.0	449.0	0.242

via ¹⁷O was undertaken. Data spanning the 50-1800 cm⁻¹ spectral range of these two preparations are seen in Figure 5.29 (a). The spectra are very similar to that seen for sample H₂¹⁷O Ceria in Section 5.1.2, in which it was determined that the nature of the sub 2 nm particle resulted in substantial broadening of the F_{2G} band, shifted to lower wavenumber. Based on the shift difference of the F_{2G} band between ¹⁷O peroxo-ceria and ¹⁶O peroxo-ceria, it is apparent that there are some differences in the amount of bulk defects present, highlighting the subtleties of ceria preparation conditions, e.g. minor variations in pH level, and changes in oxygen deficiency.

Of greatest significance however, is the intensity of the peroxide band (indicating successful synthesis), the 6 cm⁻¹ difference between ¹⁷O peroxo-ceria and ¹⁶O peroxo-ceria and a 7 cm⁻¹ increased broadening of this band for ¹⁷O peroxo-ceria, apparent in the inset and detailed in Table 5.3. This could be due to incorporation of ¹⁷O, resulting in the formation of ¹⁷O-¹⁶O vibrational bands (in addition to ¹⁶O-¹⁶O). ¹⁷O-¹⁷O bands would be almost negligible from the low amount of ¹⁷O incorporation (~5 %). However, it is possible that this shift and broadening is the caused by differences in the nature of the peroxides present instead/in addition to isotope shifts. As already stated, greater defect aggregation of peroxides on ceria results in this band at 832 ppm moving to higher Raman shift, behaviour that would correlate with a more defective sample, which was indicated by the F_{2G} position of ¹⁶O peroxo-ceria. The Raman O-H region of ¹⁷O peroxo-ceria depicted in Figure 5.29 (b) isn't able to distinguish the O-H vibrational band of the peroxide, depicting a broad range of environments that also encompass water and hydroxyls.

The single pulse ¹⁷O NMR measurement of ¹⁷O peroxo-ceria acquired at 14.1 T is shown in Figure 5.29 (c). As seen from the intensity of the natural abundance

signal of the ZrO_2 rotor, very little ^{17}O enrichment has been achieved. A broad peak arising from ceria is observed at 845 ppm, a considerably more shielded average position (9 ppm) than that seen for the 2 nm H_2^{17}O ceria sample in Section 5.1.3, perhaps implying an even smaller particle size, and a resonance at 40 ppm is apparent. As discussed in Chapter 3, Wang *et al.* observed a signal at 32 ppm after water was adsorbed to the nanoceria surface, and observed its disappearance after the sample was dried under vacuum, thus they assigned it to adsorbed water. Considering this previous assignment, and that the synthesis of ^{17}O peroxo-ceria was via H_2O conditions (the precipitate was not dried), this peak at 40 ppm can be assigned to H_2O physisorbed to the ceria surface. No other resonance is observed, which could indicate that the ^{17}O label is insufficient to observe the peroxide, implying that it is broader than the ceria peak, a result of a large C_Q or slow molecular tumbling on the timescale of the experiment (acquired at 14.1 T and under the conditions of room temperature).

As a highly experimental procedure, there were many unknowns associated with this attempt at observing peroxides by ^{17}O NMR. It is interesting to note that under the conditions of MAS at 14 kHz, i.e. heating to 35 °C, upon removing the rotor from the probe, sufficient pressure had built up to (forcibly) eject the cap from the rotor, revealing that the previous brown sample which is characteristic of peroxide, had transformed to the characteristic orange of defective ceria. Evidently the peroxide was unstable at this elevated temperature and peroxide was released from the surface as O_2 gas.

5.9 A DFT Investigation of the Frenkel Pair Defect

In addition to peroxides, the Raman spectra of ceria systems shown in this chapter has seen consistent evidence of Frenkel type defects, formed when an oxygen ion moves from its regular sublattice position to occupy an octahedral site, depicted in Figure 5.30 (a). Chapter 3 emphasized the difficulties in observing these species by experimental means, and described how in the case of Raman spectroscopy, assignment was determined on experimental deductions. However, with the recent progress of computing power and quantum chemistry, previously unknown

spectroscopic signals are increasingly identified by theory and computational simulation techniques.

Herein follows a description of how ^{17}O NMR parameters of the Frenkel-type defect in ceria have been calculated by DFT via the CASTEP 16.0 code. As outlined by Profeta *et al.* in a DFT study of ^{17}O NMR chemical shifts of systems including CaO ,¹⁴³ the default ultrasoft pseudopotentials within the PBE approximation (CASTEP) overestimate the covalency of the Ca-O bond due to the over-hybridisation of the Ca 3d and O 2p orbitals. However, the authors show that the hybridisation of the Ca 3d unoccupied states with the O 2p states can be avoided by introducing an energy penalty for the Ca 3d orbital. This empirical adjustment is applied by modifying the Ca pseudopotential string until the ^{17}O chemical shift value coincides with the experimental value.¹⁴³ Similarly in CeO_2 , the calculation of ^{17}O NMR chemical shift parameters at the GGA-DFT level of theory will have a systematic error due to the hybridisation of the Ce 4f unoccupied state with the O 2p states. In order to avoid the over-occupation of the Ce 4f orbital, an energy shift for Ce has been calibrated, analogous to the solution of Profeta *et al.*'s solution for Ca. The modification to the Ce pseudopotential string was calibrated by comparing the ^{17}O absolute shielding values of CeO_2 against four purely diamagnetic systems: ZnO , SiO_2 , Na_2WO_4 and Na_2MoO_4 , where the structures were attained from the ICSD with entry codes 157724, 173227, 2133, and 151970, respectively. At each sampling point, a geometry optimisation on the training set of experimental structures was undertaken using the PBEsol exchange-correlation functional in conjunction with the CASTEP code, before completing an NMR calculation on the relaxed structures. For all the training set calculations, the default Vanderbilt ultrasoft pseudopotentials were used as generated on-the-fly (OTF) in the CASTEP code.

The resultant ^{17}O magnetic shielding parameters (σ_{iso}) from the GIPAW NMR calculations are plotted against their known experimental δ_{iso} values taken from the literature^{144,145} and my own measurements (see Appendix G), to produce the linear calibration line seen in Figure 5.30(b). The shielding-shift correlation line ($\delta_{\text{iso}} = -1.026(\sigma_{\text{iso}} - 250.29)$) is consistent with the ideal formula that converts σ_{iso} values to δ_{iso} values via a reference shielding value (σ_{ref}), from $\delta_{\text{iso}} = -(\sigma_{\text{iso}} - \sigma_{\text{ref}})$. The corresponding ^{17}O GIPAW-NMR calculation for CeO_2 ($\sigma_{\text{iso}} = -985.10$ ppm) deviates

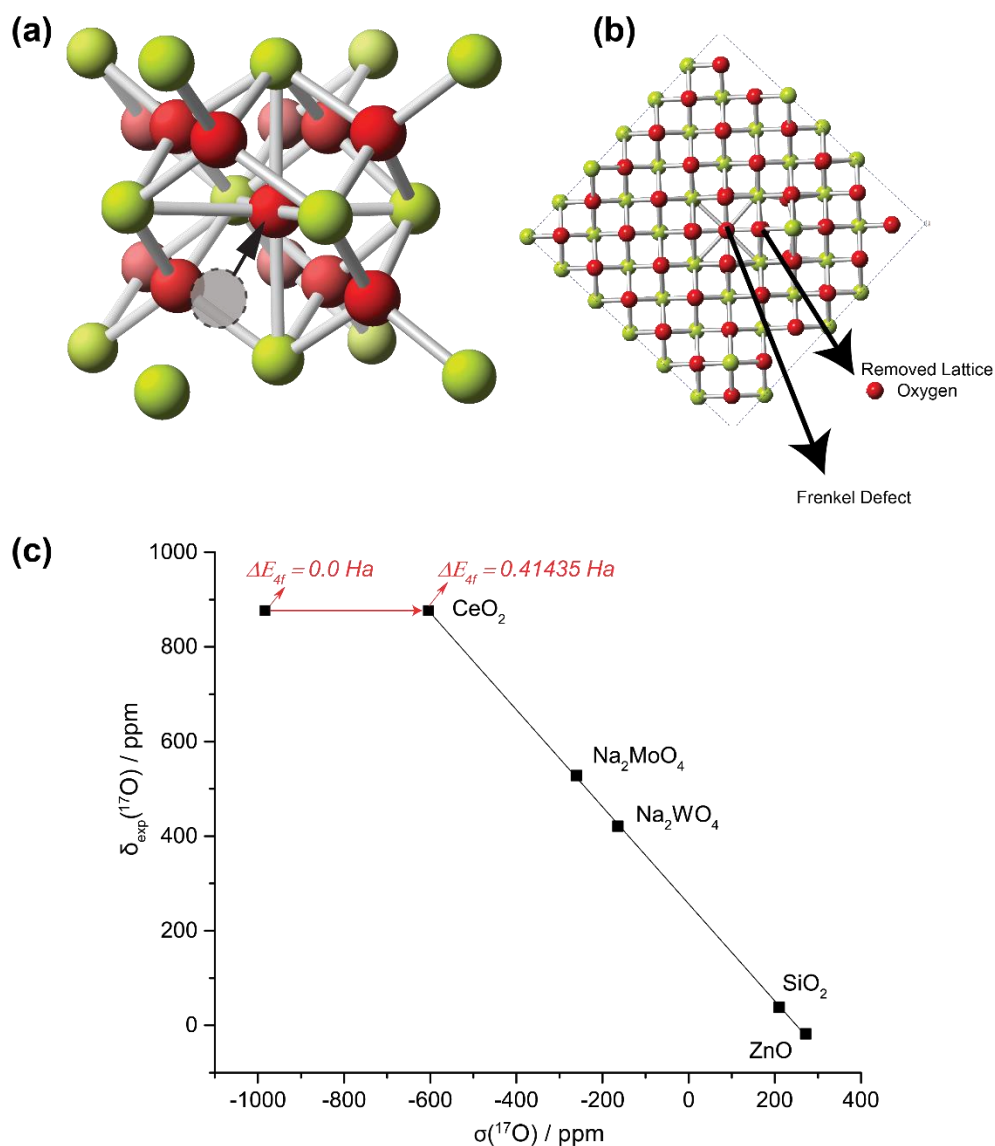


Figure 5.31: (a) The unit cell of CeO_2 showing the Frenkel defect occupying the central octahedral site, creating a vacancy in the sublattice, (b) a $3 \times 3 \times 3$ CeO_2 supercell showing the Frenkel defect in the centre (two cerium cations have been removed from in front of it) and the adjacent vacant site, and (c) a $\delta_{\text{iso}} = -(\sigma_{\text{iso}} - \sigma_{\text{ref}})$ calibration curve for ^{17}O calculated shifts, showing the energy shift of the Ce 4f site necessary to conform the calculated σ_{iso} value with the experimental δ_{iso} value.

strongly from this interpolated linear trend ($\sigma_{\text{iso}} = -604.58 \text{ ppm}$). Introducing a $+0.41435 \text{ Ha}$ shift in the Ce 4f orbital makes the CeO_2 σ_{iso} value commensurate with the proposed linear fit. The Ce OTF-generated pseudopotential strings are as follows:

```
Ce 2|2.1|9|10|11|50U:60:51:43:52L(qc=6)
```

```
Ce 2|2.1|9|10|11|50U:60:51:43U@0.41435U@0.41435:52L(qc=6),
```

with the unmodified on top and the modified below.

For the calculation of the Frenkel defect, a $3 \times 3 \times 3$ supercell with composition $\text{Ce}_{108}\text{O}_{216}$ was generated from a CeO_2 crystal structure taken from the ICSD with entry code 9009008. The Frenkel defect was created by displacing a single oxygen atom from its standard sublattice site to occupy the octahedral Frenkel position at the centre of the supercell, with fractional coordinates $(1/2, 1/2, 1/2)$ as shown in Figure 5.30 (b). For the geometry optimisation a random displacement of 0.2 \AA was applied to all the atomic positions to mimic strain effects within the lattice, and the defective Frenkel site was constrained. The resulting configuration was used to calculate ^{17}O chemical shift NMR parameters using the modified Ce pseudopotential and quadrupolar parameters using the default ultrasoft OTF pseudopotential.

The corresponding lineshape for the defective structure was calculated in SIMPSON¹⁴⁶ by considering each nucleus independently, at field strengths of 14.1 and 9.4 T. Given that the calculated ^{17}O quadrupolar parameters for CeO_2 are comparatively small ($\sim 0\text{--}1.02 \text{ MHz}$), the CSA contribution $\Delta\delta \sim 163\text{--}416 \text{ ppm}$ (in the Haeberlen convention) to the lineshape was also considered. A spinning sideband manifold based on these $\Delta\delta$ values were simulated for a spinning speed of 14 kHz.

A distribution in the NMR parameters present in a real system is manifested as a broadening to the spectral features of its corresponding NMR spectrum. This is not accounted for explicitly in the SIMPSON simulation, and so an apodization of 100 Hz was applied to the FIDs to mimic this effect. The total convoluted lineshapes were created from a summation of the 216 individual simulated lineshapes in GSIM¹⁷⁵, and can be seen in Figure 5.31.

It is evident from the simulated lineshapes presented in Figure 5.31 that the introduction of the Frenkel defect and vacancy into the CeO_2 structure has a profound effect on the distribution of oxygen environments. The Frenkel oxygen appears as the most upfield species at $\delta_{\text{iso}} = 822 \text{ ppm}$ (the smaller component of the two overlapping lines), consistent with the reported trend for increasingly shielded ^{17}O chemical environments with increasing O coordination;¹⁴⁷ bulk and Frenkel O are four and six coordinated, respectively. The formation of the Frenkel defect leaves an O vacancy in the sublattice. It is the response of the surrounding O environments to this local distortion that gives rise to the additional resonances observed in the spectral simulation. The sweep width used in Figure 5.31 (a) reveals

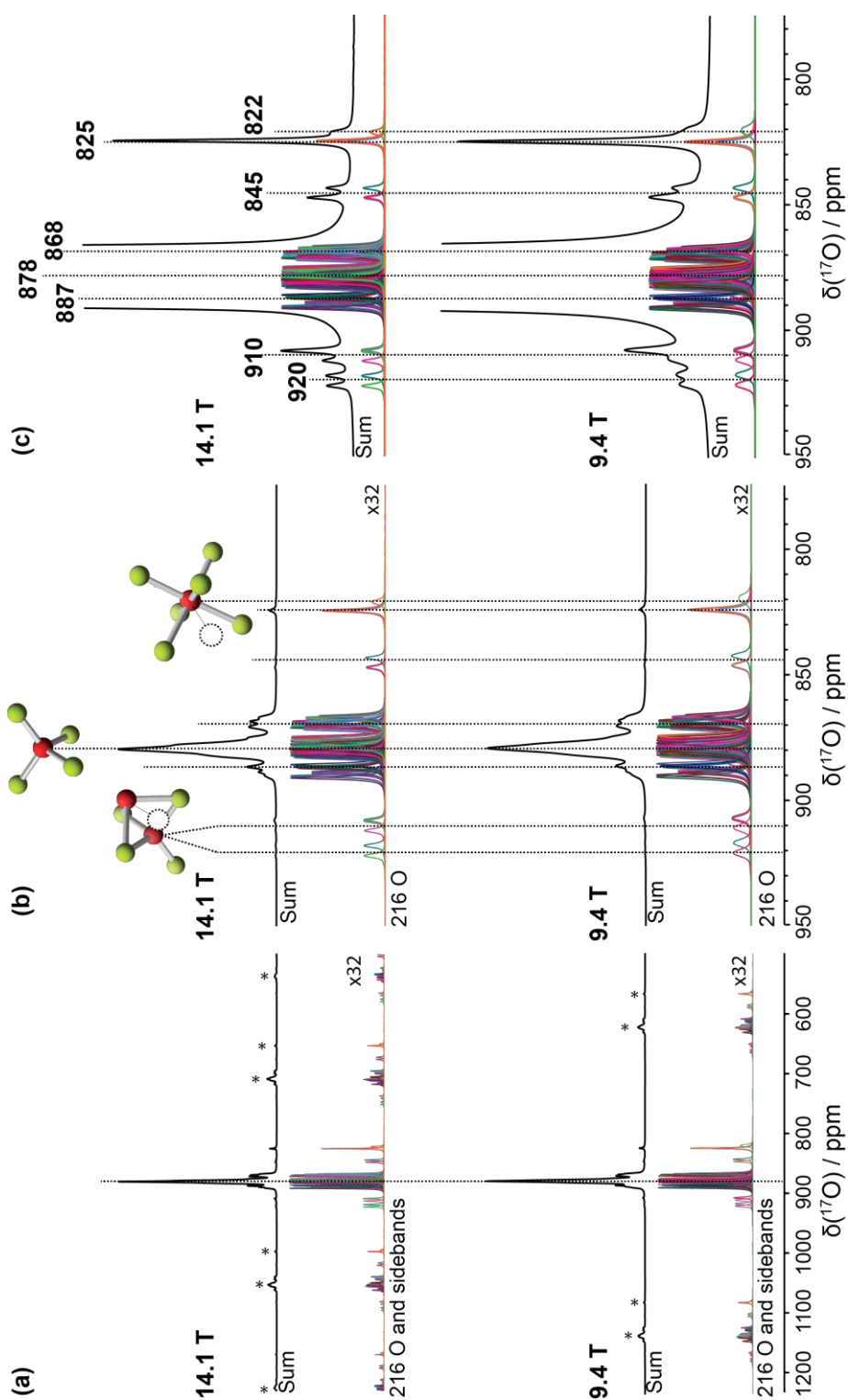


Figure 5.32: SIMPSON simulations of the DFT-calculated ^{17}O parameters of a $\text{Ce}_{108}\text{O}_{216}$ ($3 \times 3 \times 3$) supercell with an oxygen inserted into the central (previously vacant) site, charge balanced by the removal of an oxygen from an adjacent site in the sublattice, at 14.1 and 9.4 T. The convoluted lineshapes are shown in black. (a) A spectral width that includes the $1^{\text{st}}/2^{\text{nd}}$ order sidebands, (b) a horizontal expansion that shows the centre bands of the 216 O spectra only, and (c) a horizontal and vertical expansion.

the 1st/2nd order sidebands, and highlights that whilst ~ 200 oxygen residing in ‘bulk’ positions give rise to visible sidebands, the single oxygen representing the Frenkel defect has CSA large enough that its corresponding sidebands are also apparent. Figure 5.31 (c) also effectively illustrates that negligible shifts between 14.1 and 9.4 T are observed; even for the Frenkel defect which has the largest C_Q of ~1 MHz, this shift is almost undetectable. The dashed lines in the figure fall through the centre of gravity of the distinct chemical shift areas that would give rise to a resolved peak. An important observation is made regarding the perturbations induced by the Frenkel oxygen and vacancy; in addition to small shifts from the bulk resonance frequency (causing a distribution and hence broadening of the bulk peak), there are distinct oxygen environments further downfield (from the bulk) at 910 and 920 ppm, and upfield at 845 and 830 ppm. These positions shall be referred to as the Frenkel-pair associated oxygens.

Figure 5.32 overlays the DFT calculated ^{17}O NMR spectrum of $\text{Ce}_{108}\text{O}_{216}$ with the inserted Frenkel defect; simulated at 9.4 T and spinning at 14 kHz, with experimental spectra of systems taken from earlier sections: SA-600Ex, Rods-700/300-Redox and HSA20-300/300-Redox, which were acquired at $B_0 = 9.4$ T with $\nu_r = 14$ kHz. The particle sizes as determined by SAXS are also included. It is immediately evident that the calculated spectral profile matches that of the experimental ceria systems exceptionally well. Figure 5.32 (a) shows a larger sweep width of 500-1200 ppm, with full peak intensities. Several, important observations can be made. Firstly, the notable absence of the most deshielded oxygen environment at ~ 1025-1038 ppm implies that this oxygen environment is external to the simulated system. Secondly, it is evident that as the particle size decreases, not only do the resonances broaden as expected, but the Frenkel oxygen and Frenkel-pair associated oxygen resonances increase in intensity (the Frenkel manifesting as a shoulder at 822 ppm). This indicates that for a smaller particle size, more Frenkel defects and vacancies reside in the lattice, also anticipated behaviour. Additionally, Figure 5.32 (a) clearly demonstrates that there is an increased shielding of the bulk O environment with a decrease in particle size.

Figure 5.32 (b) shows an expanded region (horizontal and vertical) about the centre bands of the simulated spectrum. Unlike the trend for the bulk oxygen

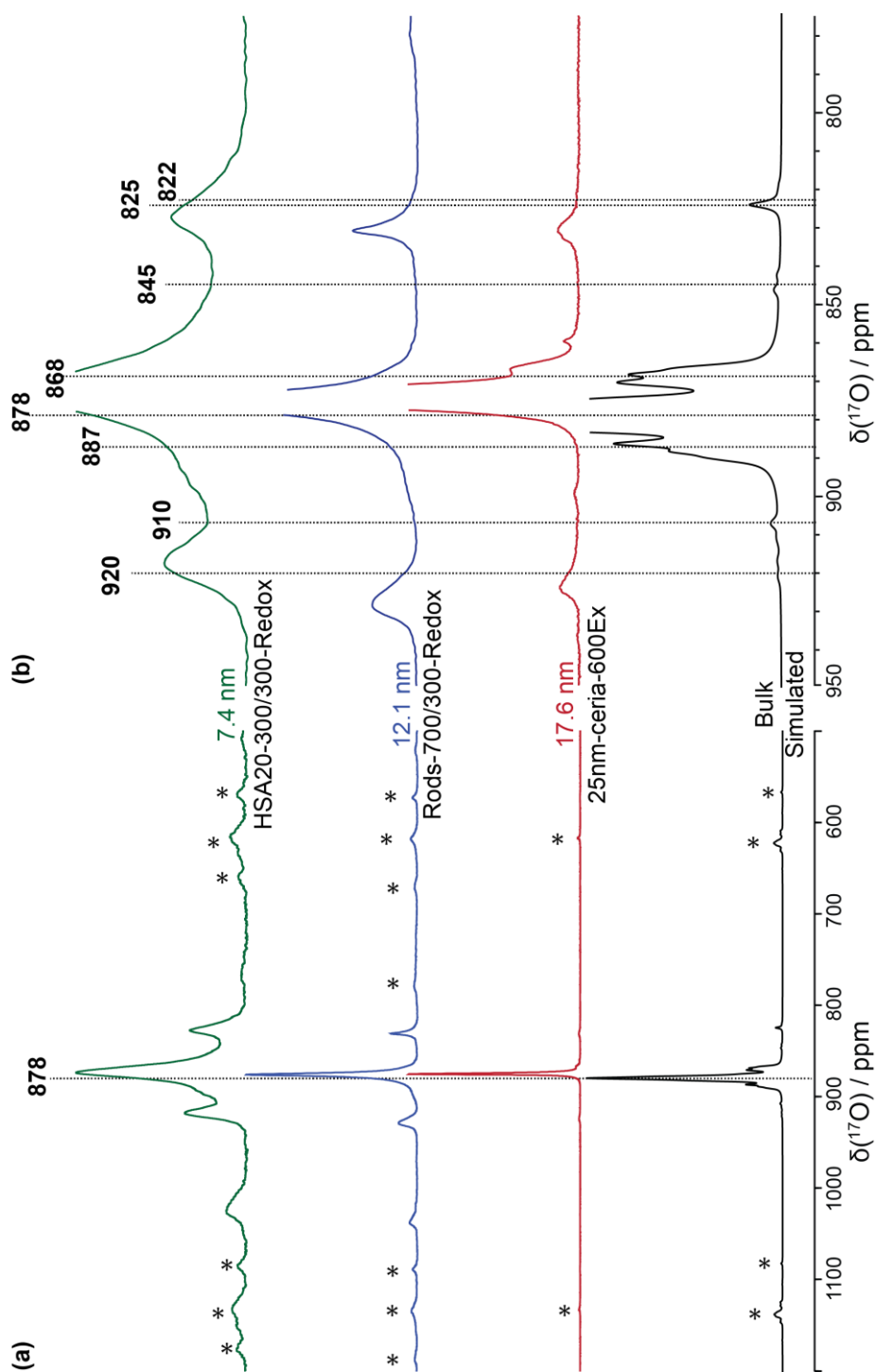


Figure 5.33: Diagram showing the DFT calculated ^{17}O NMR spectrum of $\text{Ce}_{108}\text{O}_{216}$, simulated in Simpson at 9.4 T, spinning at 14 kHz (as presented in Figure 5.32), overlaid with ^{17}O spectra from samples HSA20-300/300-Redox, Rods-700/300-Redox and SA-600Ex. (a) emphasizes the chemical shielding dependence of the bulk on particle size (determined by SAXS), and (b) validates the presence of Frenkel defects in the ceria systems reported here.

position, there appears no correlation with the peak positions of the Frenkel and vacancy associated oxygen with particle size. However, it should be recalled that these experimental positions are not stable, i.e. over an extended time, they are mobile and external influences can change their chemical environment.

5.10 An Investigation of Ce^{3+} in Ceria

Under the H_2 reducing conditions of the $^{17}\text{O}_2$ redox experiments, ceria is able to release oxygen from the surface by changing the oxidation state of two Ce^{4+} cations to paramagnetic Ce^{3+} , where the two excess electrons can become localised on cerium's 4f state. Furthermore, the $^{17}\text{O}_2$ reoxidation process is limited by the conditions of sub-ambient pressure, at a range of low temperatures. As described previously, a surface reorganisation mechanism inhibits full reoxidation and therefore leaves the samples in a partially reduced state. In fact, just heating of ceria in oxygen deficient conditions (the conditions of the exchange experiments at 600 °C) can cause some degree of reduction. Furthermore, intrinsic Ce^{3+} is known to stabilise on the surface of ceria, with Ce^{3+} concentrations experimentally detected at 180 times that of the bulk, under oxidising conditions.¹⁴⁸ Ultimately, Ce^{3+} should be present in varying abundance in all systems (which are all on the nanoscale) seen in this Chapter.

Where these Ce^{3+} cations are likely to reside is dependent on the morphology and surface detail. Sayle & Sayle investigated a reduced ($\text{CeO}_{1.95}$) ceria particle of nanopolyhedral morphology (as adopted by HSA20) via the simulation tool Amorphization and Recrystallation.¹⁴⁹ It was proposed that 46% of Ce^{3+} decorates edges, steps and terraces of the {111} surface, with just 11 % on the {100} and the remaining 43% in the bulk, but only within the first two atomic planes from the surface¹²⁸. Therefore, in all oxygen deficient ceria systems, unpaired electron spins of Ce^{3+} will be in close proximity to the oxygen nuclear environments. The resultant paramagnetic interaction should be detectable by ^{17}O solid-state MAS NMR.

5.10.1 Magnetic Measurements of HSA20

Whilst the presence of oxygen vacancies has been evidenced from the Raman measurements shown in Sections 5.1 to 5.7, it was firstly considered necessary to

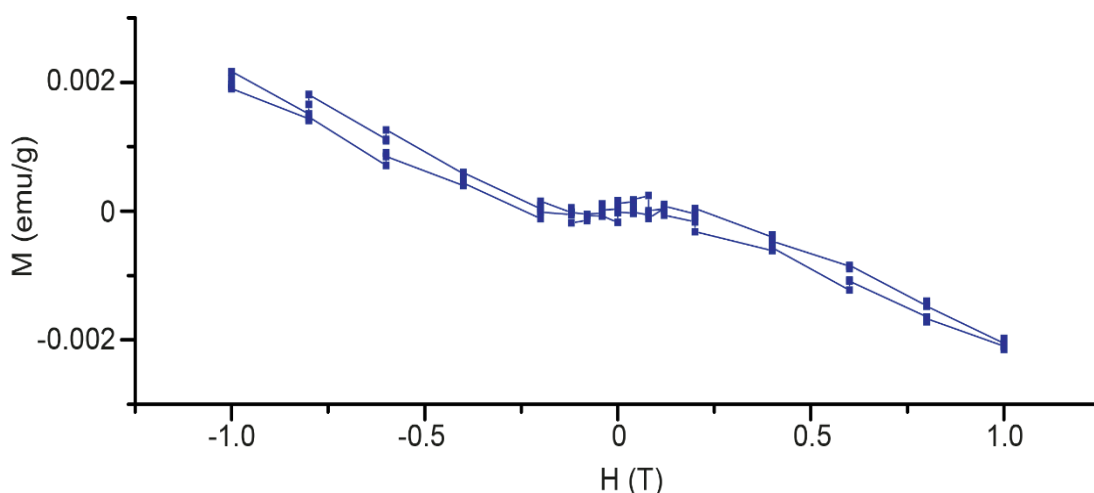


Figure 5.34: Magnetic (M vs H) measurement of HSA20-700/300-Redox.

validate the presence of Ce^{3+} by a direct route. Therefore, a magnetisation (M) vs applied field (H) measurement was carried out on HSA20-700/300-Redox using a SQUID magnetometer, the result of which is shown in Figure 5.33. The symmetric hysteresis loop confirms the absence of purely diamagnetic CeO_2 , revealing a magnetisation of 0.0021 emu/g at 1 T. In fact, the curve appears to be the additive result of a small ferromagnetic response with a larger diamagnetic response superimposed, i.e. it appears rotated about the $M=0$ axis.

Weak room temperature ferromagnetism (RTFM) of nanoceria has been observed in many studies, with the cause still deliberated in the literature¹⁵⁰. The strength of the ferromagnetic behaviour however, has been correlated with preparation conditions, with a larger magnetisation measured after a reductive treatment;¹⁵¹ suggesting that the consequent defects are responsible. Kumar *et al.* attribute RTFM in ceria to the interaction between the spin moments of Ce^{3+} and oxygen vacancies,¹⁵² where the vacancy must have a +1 charge state rather than its stable +2 state, and is thought to only be stabilised on the surface. However, excess electrons become located in vacancies only when oxygen deficiency becomes large⁵² (i.e. it becomes energetically more favourable for the electron to localise in a vacancy rather than on a Ce 4f state). If this is the case, then this complex behaviour alludes to the presence of Ce^{3+} in HSA20-700/300-Redox

Wen *et al.* also used SQUID measurements to observe RTFM (magnetisation of 0.0045 emu g⁻¹) in an untreated, ground CeO_2 crystal. After heating of the sample in oxidative conditions at 500 °C however, the powder demonstrated a weak,

paramagnetic behaviour instead. They concluded that the vacancies attract the d and f orbitals of Ce closer to the Fermi level, and so the filling of oxygen vacancies was responsible for removing the ferromagnetic ordering of the system.¹⁵³

Moreover, Phokha *et al.* observe an almost identical magnetisation result (as that shown in Figure 5.33) at room temperature of a 20 nm ceria particle, achieving a similar magnetisation of 0.0026 emu/g at 1 T, after heating the sample under vacuum overnight at 80 °C.^{106,154} They used x-ray absorption near edge spectroscopy (XANES) to elucidate a 9.7% Ce³⁺ concentration. As the SQUID measurement reported in Figure 5.33 achieved a magnetisation of 0.0021 emu/g at 1 T, it is determined that Ce³⁺ is indeed present in the sample HSA20-700/300-Redox.

5.10.2 VT Experiments of HSA20

In solid-state NMR, in order to verify the influence of paramagnetism on a nuclear environment, it is common practice to acquire NMR measurements at a range of temperatures. Peak positions of resonances associated with a paramagnetic centre will reveal an inverse temperature dependence, which is practically observed as a shift (and possible broadening) in peak position.

Figure 5.34 depicts variable temperature ¹⁷O MAS NMR data of HSA20-500/300-Redox, taken between -10 and 58 °C, acquired with a Hahn echo sequence at 14.1 T. HSA20-500/300-Redox was chosen for this experiment for its high ¹⁷O enrichment and considerable intensity in the additional resonances (relative to the bulk). Figure 5.34 (a) presents the 1200 to 600 ppm region in which the three unassigned and bulk peaks can be seen at 1030, 920, 828 ppm, and 874 ppm, respectively. Unfortunately at this field and spinning speed, sidebands from the central three resonances fall on top of the peak at 1030 ppm (time constraints, signal to noise, etc. did not allow for faster spinning). It should also be noted that a sideband from 1030 ppm also underlies the signal region between resonances 874 and 828 ppm (shown by the asterisk).

Figure 5.34 (b) shows the expanded region of the central three peaks and reveals very definite peak shifts of increased shielding, with a decrease in temperature. Figure 5.34 (c) plots these shifts against the inverse temperature and reveals a linear dependence. Over the 60 °C temperature range, resonances at centre

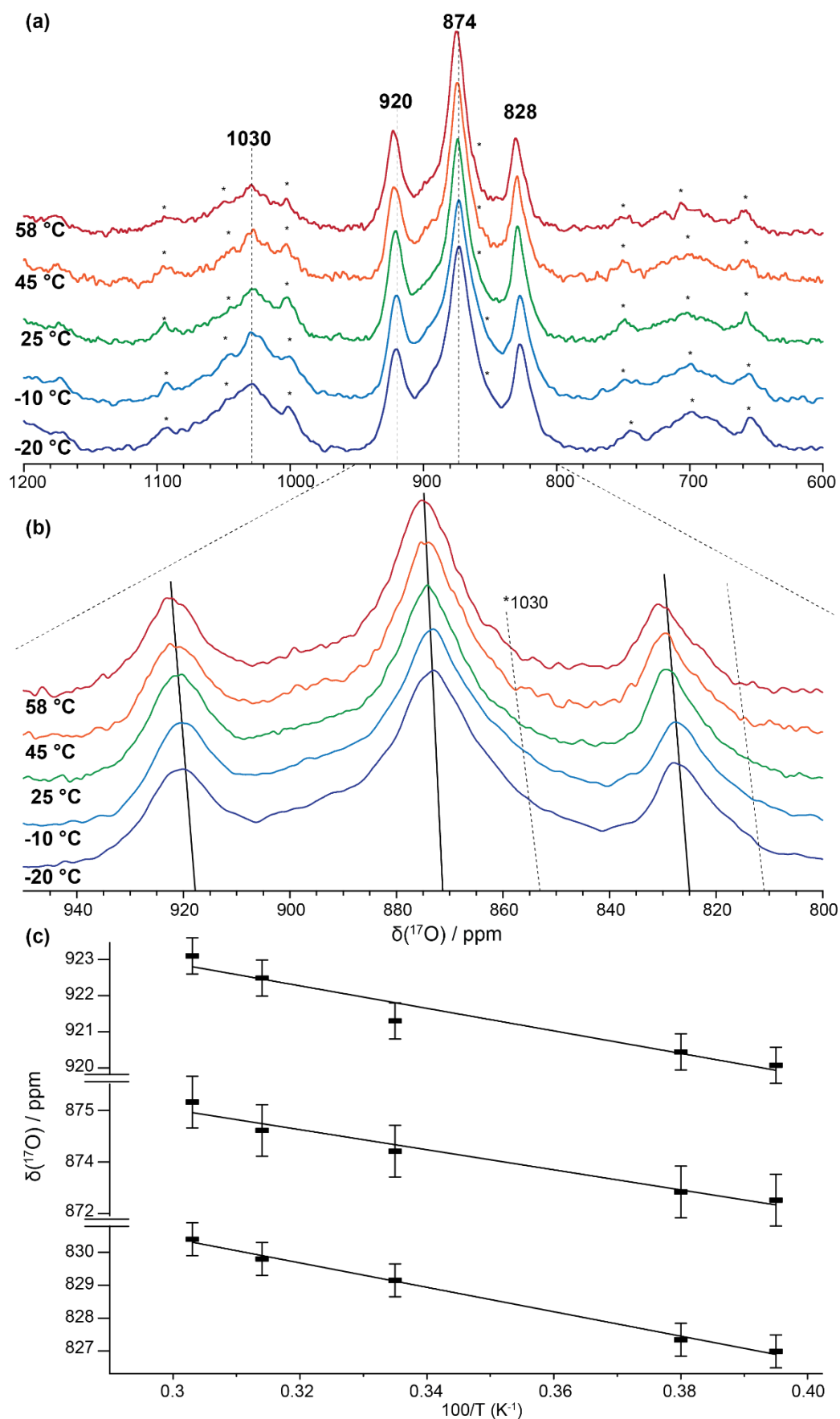


Figure 5.35: VT ^{17}O MAS NMR data of HSA20-500/300-Redox (a) 600-1200 ppm spectral region, (b) zoomed in on central 3 resonances with solid and dashed lines used to guide the eye and (c) δ_{CG} plots of peaks following solid lines drawn in (b).

of gravity positions $\delta_{\text{CG}} \sim 829, 874$ and 921 ppm experiences a 3.5, 2.7 and a 3 ppm change in shielding (± 0.4 ppm), respectively. These linear effects can be the consequence of either a lattice expansion, or a Curie dependence. When a lattice is heated, thermal vibrations of the constituent atoms can cause lattice expansion/contraction. In the ^{17}O NMR spectrum of ceria, a lattice expansion would manifest as deshielding of the oxygen peaks, shifting them to higher ppm (as is the case here). In order to ascertain the chemical shift changes induced by a lattice expansion, crystallographic information files for ceria heated to temperatures 313, 558, 656.6, and 976 K, were taken from the ICSD with respective entry codes: 155604, 155605, 182989, and 155607. ^{17}O NMR DFT calculations of the structures were collected (referenced against the calibration curve in Figure 5.30(c)), and can be seen in Figure 5.35. Evidently, the chemical shift increases linearly with temperature (and with lattice expansion), with a maximum 2 ppm shift difference projected between -20 and +58 °C. This is close to the observed increase in δ_{CG} of the bulk at 2.7 ppm, but does not account for the larger observed shifts of the sites associated with the Frenkel pair/vacancy perturbation (920 and 828 ppm) of 3.5 and 3 ppm.

This linear behaviour therefore could be attributed to a Curie dependence as governed by Equation 2.63, suggesting that all peaks shown in (b) are influenced by

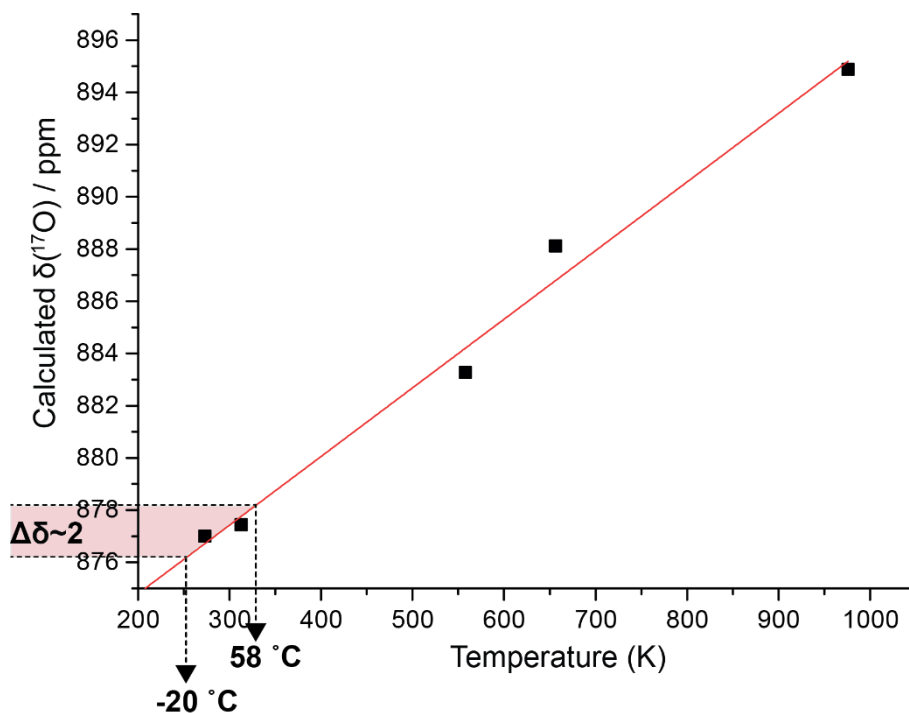


Figure 5.36: Theoretical ^{17}O chemical shifts calculated from ceria unit cells having undergone lattice expansion due to increases in temperature (closed system).

paramagnetic centres to varying degree. Whilst the more deshielded signal at 1030 ppm is obscured by sidebands (impeding the determination of shifts of the centre band), its first order sideband at ~ 858 ppm, appearing as a broad shoulder of the bulk peak at 874 ppm (which is emphasised by the dashed line in the figure), also appears to show this inverse temperature dependence, suggesting that this resonance is also paramagnetically shifted.

Whilst there are many NMR studies of different nuclei showing this behaviour for paramagnetic dopant systems (many of which can be found in a review paper by Stebbins, McCarty and Palke¹⁵⁵), there are three key studies that demonstrate this behaviour in Ce^{3+} doped systems, with McCarty and Stebbins publishing one of these just last year. They conducted a ^{27}Al and ^{89}Y MAS NMR investigation on the cubic structure of YAG ($\text{Y}_3\text{AlO}_5\text{O}_{12}$) with 0.3% Ce^{3+} dopant (replacing Y^{3+} cations). YAG has two aluminium environments: AlO_4 and AlO_6 and upon doping, they observe the appearance of several, temperature-dependent signals (confirmed by varying spinning speed) either side of the unshifted AlO_6 and AlO_4 peaks. For the AlO_6 peak for example, which has a previously determined $\delta_{\text{iso}} = 2.1$ ppm (and C_Q value of 0.6 MHz),¹⁵⁶ they show that one of these new resonances is considerably shifted to a more shielded position at ~ -16 ppm. Three others are unresolved from the unshifted position at 2.1 ppm, one of which is to a lower frequency, and two to a higher frequency. Using a model that distributes the paramagnetic cation randomly, they are able to assign these paramagnetically shifted peaks to the possible configurations that the observed ^{27}Al nucleus forms with Ce^{3+} .

George *et al.* originally observed this phenomenon¹⁷², also in Ce:YAG systems and attributed the observed ^{27}Al shifts to neighbouring Ce^{3+} through its through-bond, short-range Fermi contact shift and longer-range, through-space pseudo contact shift (PCS). The PCS shows a dependence on the proximity of the paramagnetic cation with other magnetic moments, the crystal field splitting (CFS) of Ce^{3+} and importantly, the vector between Ce^{3+} and the observed nucleus. They calculate the PCS of ^{27}Al with a Ce^{3+} cation in the first, second and third coordination spheres for a random distribution of Ce^{3+} in YAG systems, and show these calculated shifts to correspond perfectly with the experimental data. Furthermore, they show a T_1 dependence where ^{27}Al relaxes faster for closer Ce^{3+} proximities.

Finally, Fusaro and Luhmer investigated [Ln-DOTA] complexes¹⁷³ (lanthanum metal 3+ cation) in aqueous solution in which they reveal a 170 ppm chemical shift difference between oxygen directly bonded to Ce^{3+} and oxygen in the third coordination sphere. This is a similar shift difference (~162 ppm) between the bulk at 877 ppm and the most shielded position of 1038 ppm.

On account of the aforementioned studies, it is proposed that the as-of-yet unassigned resonances in the ceria spectra seen between 1030-1040 ppm, are oxygen species within three bonds lengths of Ce^{3+} , i.e. $\text{O}-\text{Ce}^{4+}-\text{O}-\text{Ce}^{3+}$.

Having already drawn some parallels with the ionic MgO structure, it is also relevant to mention another study by McCarty and Stebbins¹⁰⁶ in which they investigate paramagnetic ^{17}O shifts in CaO and MgO doped with paramagnetic cations Ni^{2+} and Co^{2+} . MgO and CaO have single magnetically equivalent sites, but for the doped systems, additional peaks are apparent with positions either side of the pure phase locations. These additional signals are confirmed as products of paramagnetic shifts by correlating changes in spinning speed (which changes the temperature) with shift position. Due to the cubic symmetry of the system, they assume that paramagnetic shifts are dependent on the Fermi contact interaction. Based on a random model, they calculate the amount of through bond pathways between ^{17}O and the paramagnetic cation up to five bonds away. They compare these with integrations of the paramagnetically shifted peaks and show a close correlation.

Sections 5.9 and 5.10 contribute significant and unique insights into the oxygen environments of ceria via ^{17}O solid-state NMR. The two current ^{17}O solid-state NMR studies of ceria that reveal this multiple-peak behaviour ascribe these shifts (away from the bulk oxygen position) as a result of surface coordination effects. Whilst it is probable that these oxygen environments are positioned on surface or subsurface sites, from the data shown in Figure 5.32 and Figure 5.34, and other solid-state NMR studies of Ce^{3+} doped systems, it is apparent that these resonances are governed by more complex behaviour, such as the proximity of paramagnetic centres (Ce^{3+} cations) seen in this section and other defects that cause lattice distortion as seen in the previous section.

Chapter 6

An Investigation of Loaded and/or Mixed Ceria

Following the investigation of pure ceria in Chapter 5, this chapter investigates systems that are more representative of a real catalyst for TWC applications, i.e. loaded with a platinum group metal (PGM) and/or mixed with zirconia. These modifications not only result in significant enhancements of ceria's properties, but (zirconia) further stabilises the surface area of ceria at the elevated temperatures experienced during typical catalyst operation. The promotional effects of PGM loaded ceria are widely applied to catalytic applications on account of their unique synergy when they come into contact with one another. This behaviour includes lowering of the reduction temperature and an increase in OSC, as compared to the non-loaded support. Whilst these effects have been known to exist since the 80s¹, the working mechanism has advanced from the theory of just H₂ spillover, to one of electronic modification of the ceria surface by the PGM metal. This was explained in Chapter 1, along with descriptions of zirconium's ability to inhibit particle sintering, and moreover its capacity to facilitate greater bulk oxygen mobility due to its distortion of the lattice.

Following on from Chapter 5, this chapter presents further evidence of paramagnetic effects via solid-state ¹⁷O NMR techniques. Compared to the unloaded support; as PGM loaded ceria systems favour a greater surface reduction, more Ce³⁺ should be evident. In the case of ceria zirconia oxides that facilitate a bulk reduction at lower temperatures, Ce³⁺ is expected to occupy bulk-like positions as well as surface positions, and ¹⁷O NMR should be sensitive to this structural perturbation.

6.1 Investigation of Pd Loaded Ceria

Preparations of the samples defined as HSA20 ceria, and ceria rods and cubes that were investigated in Chapter 5, were acquired with a 1 wt % Pd loading, herein labelled as HSA20-1%Pd, rods-1%Pd and cubes-1%Pd, respectively. As with HSA20, the former was bought in from Rhodia by Johnson Matthey, and the latter two obtained from Professor Edman Tsang (synthesis details¹⁰¹). These samples have undergone similar ^{17}O preparations as seen in Chapter 5: a H_2 -reduction at 700 °C, followed by ^{17}O reoxidations at 300 and 150 °C. They are referred to as HSA20-1%Pd-700/300-Redox, Rods-1%Pd-700/300-Redox and Cubes-1%Pd-700/300-Redox and HSA20-1%Pd-700/150-Redox, Rods-1%Pd-700/150-Redox and Cubes-1%Pd-700/150-Redox, respectively.

For a <10 wt % loading, whilst PXRD analysis can elucidate the phases of ceria, it cannot provide information about the Pd position in the structure.¹⁵⁷

6.1.1 TPR

H_2 -TPR measurements were carried out on HSA20-1%Pd up to 900 °C as seen in Figure 6.1. The results appear similar to the TPR profile of HSA20 which was shown in Figure 5.7, in that three reduction peaks are evident. However the dominant signal is instead at the low temperature of 90 °C, attributed to the reduction of PdO to Pd metal (anticipated behaviour of Pd-loaded samples that have undergone calcination in oxidative conditions). Of importance here is the shift of the peak corresponding to the ceria surface oxygen removal, down from 425 °C for the bare support, to 320 °C. The presence of 1% Pd on HSA20 has unquestionably decreased the temperature

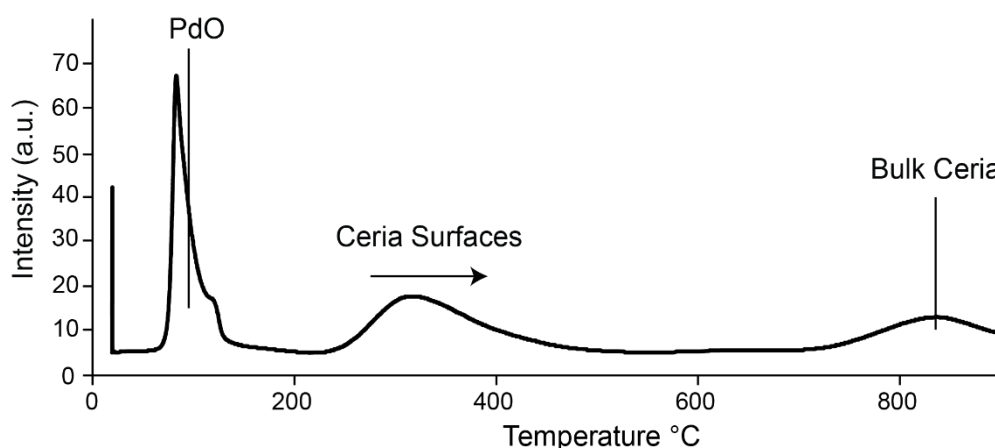


Figure 6.1: TPR- H_2 of HSA20-1%Pd to 900°C.

necessary for vacancy formation (as described in Chapter 1). Furthermore, the bulk oxygen removal occurs at 830 °C, which is a 20 °C decrease from the bare support, suggesting that Pd loading also influences vacancy formation of the bulk, contrary to the literature reports mentioned in Chapter 1. This could be due to the nano nature of the systems studied here. These enhanced-reduction effects are due to the previously mentioned properties of electronic reduction of the ceria support by the Pd metal and/or H₂ spillover to the ceria support from the Pd metal.

The H₂-TPR profiles for samples rods-1%Pd and cubes-1%Pd are shown in Appendix E (top two traces). The negative intensities at 70 °C are a result of the release of hydrogen residing in interstitial points of the Pd metal. As with HSA20, the reduction temperature of the surface oxygen species reduced considerably to 302 °C and 391 °C, from 525 °C and 475 °C for the cubes and rods, respectively.

Comparing the three morphologies (polyhedra, cubes, and rods), it is evident that there is a facet-dependent fall in temperature of surface oxygen removal when Pd is deposited on to the surface, i.e. the {100}-dominated surfaces show a greater modification when reducing at lower temperatures. This can be explained by reverse oxygen-spillage; where oxygen from the ceria surface spills on to the Pd surface from where it is more easily desorbed from,¹⁵⁸ favouring the lower index surface.

6.1.2 Raman Spectroscopy

The Raman spectra of HSA20-1%Pd are shown in Figure 6.2, where the as prepared sample is shown in (a), HSA20-1%Pd-700/300-Redox in (b) and HSA20-1%Pd-700/150-Redox in (c).

Given that the width and position of the F_{2g} band are representative of bulk defect concentration and lattice expansion/contraction effects, respectively, its behaviour is highly insightful regarding the state of reduction of the system. The data seen in the inset of Figure 6.2 (a) can therefore be rationalised as follows. HSA20-1%Pd-700/300-Redox appears (slightly) narrower than the as prepared sample; and shifted to higher energy by 0.8 cm⁻¹. These are small changes in contrast to those seen for HSA20 in Chapter 5 where, under the same ¹⁷O treatment conditions, peak width was almost halved and a 2.8 cm⁻¹ shift observed to higher frequency (compare

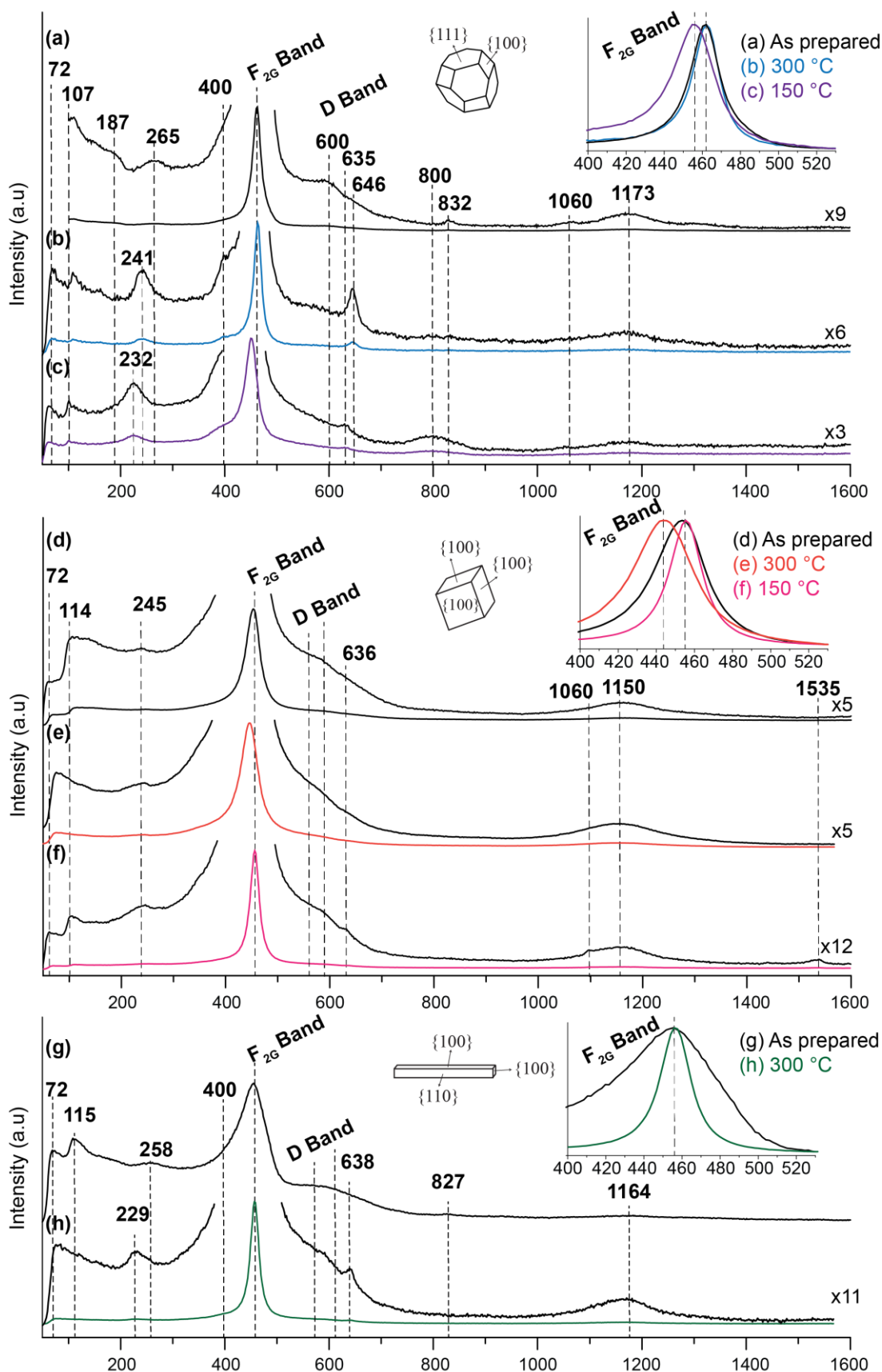


Figure 6.2: Raman spectra of as-prepared samples of (a) HSA20-1%Pd, (d) Cubes-1%Pd and (g) Rods-1%Pd. Treated samples are shown in (b) HSA20-1%Pd-700/300-Redox, (c) HSA20-1%Pd-700/150-Redox, (e) Cubes-1%Pd-700/300-Redox, (f) Cubes-1%Pd-700/150-Redox and (h) Rods-1%Pd-700/300-Redox.

HSA20 as-prepared and HSA20-700/300-Redox in Appendix A). Considering that HSA20-1%Pd and HSA20 are similar sizes after treatment under these conditions (SAXS data in Appendix B reveals a particle size and distribution of 8.3 nm and 5.1 nm for HSA20-700/300-Redox, and 10.2 nm and 6.8 nm for HSA20-1%Pd-700/300-Redox), it can be inferred that HSA20-1%Pd-700/300-Redox is still in a more reduced state, as compared to the unloaded HSA20-700/300-Redox material. This is further supported by an almost-negligible I_D/I_{F2G} ratio decrease from 0.040 to 0.039 for HSA20-1%Pd-700/300-Redox from its as-prepared state, even after particle sintering has taken place (and thus a loss in surface area). Moreover, this interpretation is strengthened when comparing (b) HSA20-1%Pd-700/300-Redox and (c) HSA20-1%Pd-700/150-Redox where the sizeable broadening ($\Gamma = 27.9 \text{ cm}^{-1}$) and low energy shift of 454.8 cm^{-1} exhibited by HSA20-1%Pd-700/150-Redox, along with the substantial increase in defects and less coordinated species ($I_D/I_{F2G}=0.065$, $I_{Ce-Ox}/I_{F2G}=0.348$), categorically confirms incomplete reoxidation.

Palladium's influence on the reoxidation of ceria can be deduced from the greater differences in the F_{2G} widths and positions of the loaded and unloaded samples. The more reduced state of HSA20-1%Pd-700/150-Redox with respect to its unloaded counterpart highlights the stabilising role palladium plays on ceria's defective state. These observations allude to two conclusions for the results shown here. When supporting HSA20 with 1% Pd, an increase in oxygen removal by the H_2 reduction process renders the 30 mL ^{17}O reoxidation insufficient, and/or there exists a greater energy barrier in the reoxidation process. So whilst the addition of Pd to these materials lowers the reduction temperature, it also stabilises this reduced state, increasing the temperature at which reoxidation occurs.

The as-of-yet unseen bands at 646 and 635 cm^{-1} in Figure 6.2 (b) and (c), respectively, are attributed to the B_{1g} modes of the square planar PdO_4 subunit in palladium oxide¹⁵⁹ (PdO). A Raman laser wavelength of 532 nm (as used in this work) is optimal for enhancing the Raman active modes of PdO, necessary to observe the small loadings used here. Pd metal is characterised by a considerably weaker band (orders of magnitude) at 316 cm^{-1} and so would not be detected for these systems.¹⁶⁰ As PdO bands are absent from the as prepared sample in (a), it could be surmised that Pd is not present as a secondary, PdO phase. However, this is not supported by

the TPR result which demonstrated a reduction of PdO to Pd metal of the as-prepared material at 90 °C. Figure 6.2 (a) however does reveal a small, broad feature at 187 cm^{-1} , which has been assigned by Gulyaev *et al.* to palladium cations in the ceria structure in a near square planar environment.³⁷ It is tentatively proposed therefore that the synthesis and/or calcination treatment of this system either allowed a Pd-ceria solid solution to form¹⁵⁹ or a Ce-Pd-O ionic surface interaction. After the treatments for measurements in (b) and (c), however, Pd extrusion from the solid solution occurs during the elevated temperatures of reduction at 700 °C (Gulyaev *et al.* observe this phenomenon from 500 °C), or there is a segregation of PdO. Regardless, bulk PdO species are formed under the ensuing oxidising conditions. This Pd-extrusion or segregation model is strengthened by the observation that a greater PdO intensity is seen for a greater reoxidation temperature in (b), as the oxidation temperature of Pd metal, whilst size dependent, begins at about 300 °C³⁸.

Raman signals between 230 and 265 cm^{-1} attributed to Ce-OH units are substantially increased after ^{17}O redox treatments (compare (a) to (b) and (c)), which can be rationalised by the decomposition of adsorbed water under the ^{17}O redox conditions, resulting in hydroxyl species. Moreover, they demonstrate a trend of increasing band frequency with increasing reoxidation temperature. These shift differences for the Ce-OH species may pertain to transformations into more stable forms when varying the reoxidation conditions or could be associated with the reduced surface and the reoxidised surface respectively. For example, as discussed in Chapter 5, Badri *et al.* exposed reduced ceria to oxidative conditions and observed a band assigned to doubly bridging hydroxyls located near vacancies at room temperature. Only after heating the system at 400 °C did this band shift to lower frequency, attributed to hydroxyls on the reoxidised surface;¹¹⁸ thus they concluded the mechanism of surface reorganisation. This behaviour correlates well with the observed red shift and broadening of the $\text{F}_{2\text{g}}$ band, revealing (b) to be in a highly reduced state, and (c) in a relatively more reoxidised state. On the other hand, the shift direction from 232 to 241 cm^{-1} and shift ratio (1.039) of the Ce-OH species is highly characteristic of an isotopic ^{17}O to ^{16}O shift ratio (1.0308). If the shift difference is due to isotope effects, this would still be indicative of a surface reorganisation mechanism, where ^{16}O from the subsurface is exchanged at the higher temperature

of 300 °C with ^{17}O at the surface. The observed redshift of the PdO signal from 635 to 646 cm^{-1} may indicate a larger PdO particle size is present in HSA20-1%Pd-700/300-Redox (small PdO particles with shorter Pd-O bonds would appear at lower Raman shift than larger particles with longer bonds).

Raman data acquired for Cubes-1%Pd is shown in Figure 6.2, showing (d) the as prepared sample, (e) Cubes-1%Pd-700/300-Redox, and (f) Cubes-1%Pd-700/150-Redox. Initially, Cubes-1%Pd appears to be a simple system to interpret, however the behaviour of the $\text{F}_{2\text{G}}$ band is contrary to that of the HSA20-1%Pd systems. The $\text{F}_{2\text{G}}$ band of Cubes-1%Pd-700/150-Redox is narrower ($\Gamma = 19.5 \text{ cm}^{-1}$) than that of the as-prepared sample ($\Gamma = 24.9 \text{ cm}^{-1}$), which appear at 455.6 and 456.3 cm^{-1} , respectively, whilst Cubes-1%Pd-700/300-Redox is broader ($\Gamma = 37.2 \text{ cm}^{-1}$) and is positioned at the exceptionally low frequency band of 444.1 cm^{-1} . $I_{\text{D}}/I_{\text{F}_{2\text{G}}}$ ratios also follow this trend so that defect concentrations are in the order: Cubes-1%Pd-700/150-Redox < Cubes-1%Pd (as prepared) < Cubes-1%Pd-700/300-Redox, reinforcing the relative states of reduction. Furthermore, there is no evidence of Pd in (d), (e) or (f), firstly suggesting that it is present in its metallic state (unobservable at these loadings) and secondly that it is more stable to the ^{17}O redox conditions.

This seemingly incongruent result can be explained by the scrutiny of two assumptions. (1) If the Pd in the Cubes-1%Pd system is stable at 700 °C, its TPR profile will not change post the redox process. (2) The TPR profile of Cubes-1%Pd in Appendix E suggests that surface reduction begins at ~ 280 °C and reaches a peak at 300 °C. Therefore, under the oxygen deficient conditions of the ^{17}O reoxidation process at 300 °C, the sample is reduced again. To summarise, HSA20-1%Pd shows less stability than Cubes-1%Pd during the 700 °C H_2 treatment, with Pd removed from the structure/ exhibiting a less active PdO phase. The consequence of the loss of Pd coordination/dispersion is an increased surface reduction temperature compared to that seen in Figure 6.1 (which was 320 °C). Further investigation of HSA20-1%Pd by H_2 -TPR cycling experiments could clarify this.

Only small amounts of the 250 cm^{-1} Ce-OH features are observed in (d) to (f), reflecting the smaller surface area of the Cubes-1%Pd (<17 nm), however as with HSA20-1%Pd, there is an increase in these bands after reoxidation, suggesting hydroxyl formation from the removal of surface water.

Figure 6.2 (g) and (h) presents Raman spectra for the as-prepared Rods-1%Pd and Rods-1%Pd-700/300-Redox, respectively (unfortunately the data for the 150 °C reoxidation temperature is missing). In their untreated state, the rods prove to be a significantly defective system with $I_D/I_{F2G} = 0.246$ and peak width $\Gamma = 52.4 \text{ cm}^{-1}$. As the rods are $8 \times 120 \text{ nm}$ in size, these Raman parameters validate the conclusions made by Filtschew *et al.*, for which they determined that Γ was not representative of particle size, but of defect density.¹⁰⁹ This is clear by comparison of the as-prepared HSA20 which has a particle size of 5.8 nm, but a peak width $\Gamma = 23 \text{ cm}^{-1}$.

The spectrum in (h) considerably narrows to 19.5 cm^{-1} (see inset), and I_D/I_{F2G} decreases to 0.04, indicating a loss in defects of nearly two orders of magnitude. A feature at 638 cm^{-1} appears, suggesting some Pd metal has oxidised to PdO. Compared to the cubes treated under the same conditions, the sample is considerably more oxidised. This is in accordance with its greater TPR surface reduction temperature of 391 °C, i.e. no reduction occurs under the ^{17}O reoxidation process at 300 °C.

The Ce-OH band at 229 cm^{-1} appears after the ^{17}O redox process in (h), and as with Cubes-1%Pd, this is at lower frequency compared to that of the as-prepared sample in (g) at 258 cm^{-1} .

6.1.3 ^{17}O Solid-State MAS NMR

Figure 6.3 depicts single pulse ^{17}O NMR spectra between 1200 and 600 ppm of (a) HSA20-1%Pd-700/300-Redox and (b) HSA20-1%Pd-700/150-Redox. Full spectral widths are shown below in order to observe two notable features. Firstly, a resonance at -400 ppm , which is outside of the normally observed ^{17}O range, is apparent for both preparations. To my knowledge, there is no evidence of this chemical shift in the literature, but based on the presence of PdO bands in the Raman spectra seen in Figure 6.2 (b) and (c), this is cautiously assigned to PdO. Furthermore, in 1983, Schramm and Oldfield proposed an empirical relationship between ^{17}O chemical shifts and cation ionic radius for a series of transition metal oxides from groups 5B, 6B, 7B and 8. A linear correlation of $\delta(\text{ppm}) = -4394r(\text{\AA}) + 3205$ was attained (with a 0.92 correlation coefficient).¹¹⁹ Depending on the geometry/coordination of the Pd cation, the ionic radius of Pd ranges between 0.64

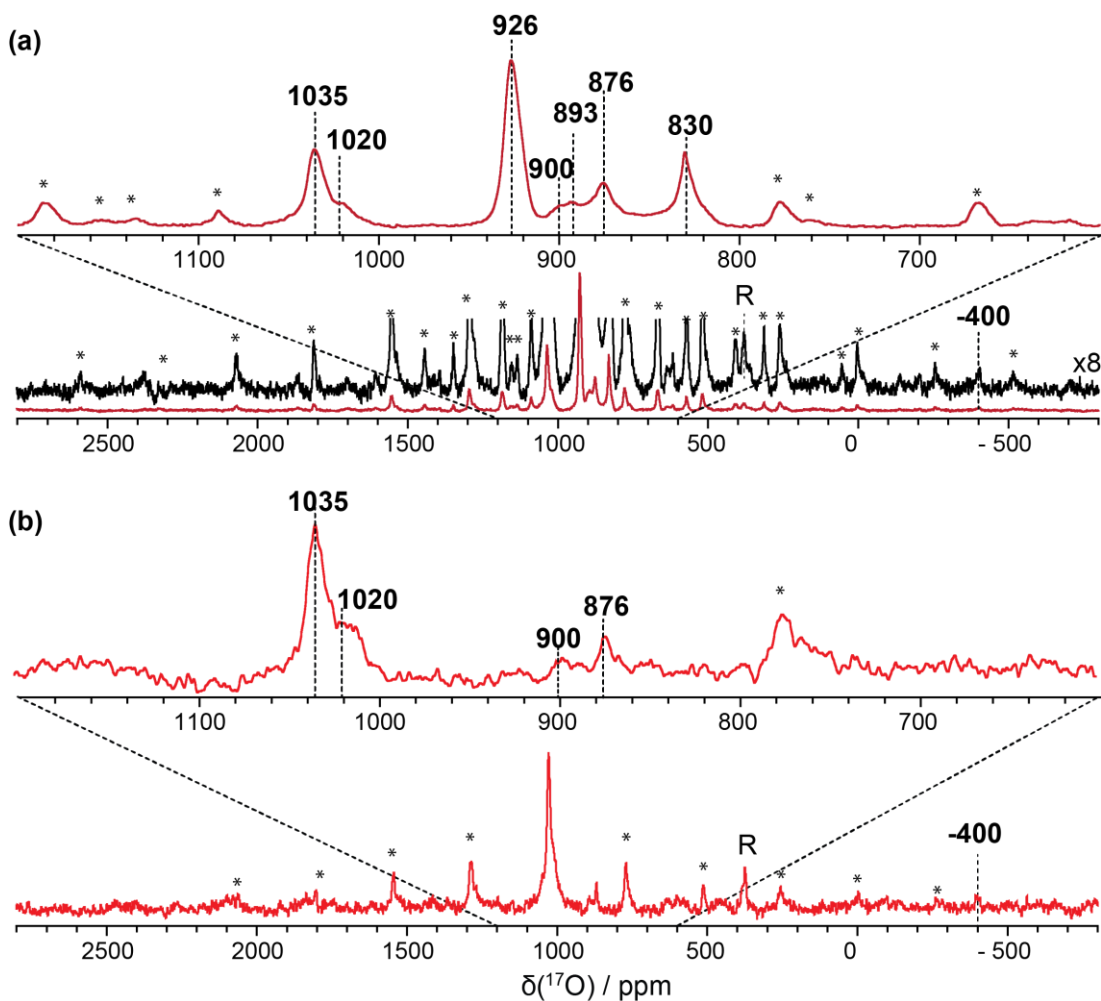


Figure 6.3: ^{17}O MAS single pulse spectra acquired at 9.4 T of (a) HSA20-1%Pd-700/300-Redox and (b) HSA20-1%Pd-700/150-Redox. $\nu_r = 14$ kHz, asterisks denote spinning sidebands, R is the rotor.

and 0.86 \AA .¹⁶¹ Applying this experimentally derived line of best fit to these cation values yields a chemical shift range between 393 and -574 ppm. Whilst a rough calculation, this supports the exceptionally shielded assignment.

The second point to note from the extended spectra are the spinning sideband manifolds, where for HSA20-1%Pd-700/300Redox, a span of >3000 ppm (200 kHz) is observed. This is extraordinarily large, (even for the sensitive ^{17}O nucleus). It was determined in Chapter 5 that negligible shifts with magnetic field are observed, implying small quadrupolar couplings. This is in a regime where the applied RF pulse becomes non selective, i.e. in addition to the CT, the STs fall within the excitation bandwidth. If the sidebands were a result of the STs of the quadrupolar interaction, then C_Q would be approximately 333 kHz ($3C_Q/5 = 200$ kHz). Between 9.4 and 14.1 T, using Equation 2.74 this would manifest as a shift difference of 0.125

ppm, which is beyond the resolution of this peak ($\delta_{FWHM} \sim 11$ ppm). Whilst excitation of the STs cannot be definitively disregarded as the occurrence of these sidebands, neither can the experimental deduction of paramagnetic shift anisotropy seen in Section 5.4.4. The increase in signal intensity of the oxygen environment at 1037 ppm was correlated with an increase of reduction temperature, and thus an increase in the Ce^{4+} to Ce^{3+} conversion via the redox process. It is therefore proposed that the sidebands here are the result of paramagnetic shift anisotropy as governed by the second term in Equation 2.63.¹⁶²

The differences of ^{17}O uptake between the two reoxidation temperatures is the overriding observation, with more ^{17}O uptake seen at the higher reoxidation temperature. This trend also corresponds nicely with the Raman spectra from Figure 6.2 (b) and (c), where HSA20-1%Pd-700/150-Redox was shown to be in a more reduced state. As seen in Chapter 5 with HSA20, this suggests that a surface reorganisation mechanism exists for HSA20-1%Pd, irrespective of the palladium loading, i.e. the reduction temperature was sufficient to initiate bulk reduction, (a)

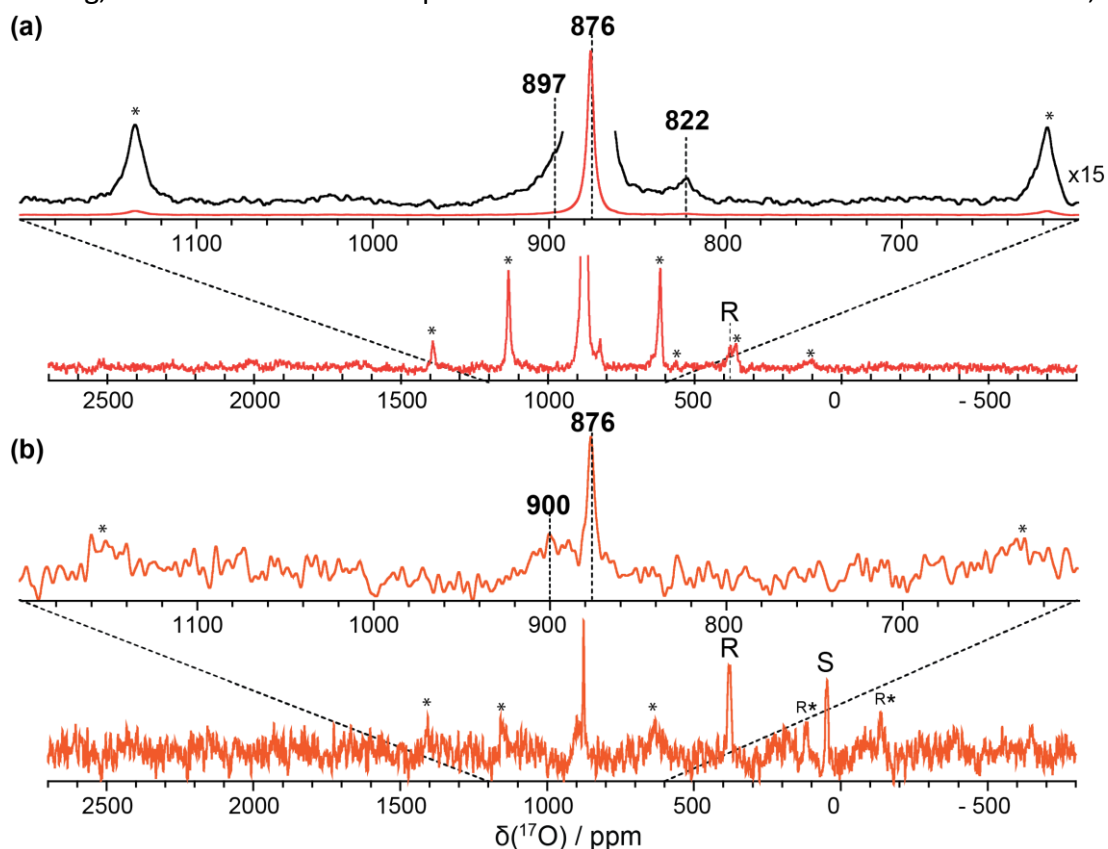


Figure 6.4: ^{17}O MAS single pulse spectra acquired at 9.4 T of (a) Cubes-1%Pd-700/300-Redox and (b) Cubes-1%Pd-700/150-Redox. $\nu_r = 14$ kHz, asterisks denote spinning sidebands, R is the rotor and S the stator.

exchanging vacancies on the surface with subsurface oxygen creating a stable buffer. Therefore to facilitate re-oxidation, there exists a minimum temperature to reverse this exchange. This description can be used to rationalise the spectral profiles in Figure 6.3 (a) and (b). As the signals at 1035 and 1020 ppm belong to the most reactive oxygen species, and as described in Chapter 5, they most likely experience a greater influence from the paramagnetic interaction, the ^{17}O that was able to adsorb in HSA20-1%Pd-700/150-Redox should be dominated by Ce^{3+} neighbours (compared to HSA20-1%Pd-700/300-Redox), for its relatively greater reduced state.

^{17}O MAS NMR measurements acquired for Cubes-1%Pd-700/300-Redox and Cubes-1%Pd-700/150-Redox are shown in Figure 6.4 (a) and (b), respectively. As with the unloaded support, the ^{17}O spectral profiles are considerably more simple than that of the other morphologies, i.e. only small signals closer to the unshifted environment (at 822 and 900 ppm) are evident, suggesting very little influence from defects such as vacancies and the paramagnetic Ce^{3+} cation. However, the Raman spectrum of Cubes-1%Pd-700/300-Redox seen in Figure 6.2 (e) indicates that this system is in a highly reduced state. To rationalise this, it is important to appreciate that the ^{17}O spectrum reveals the ^{17}O that is put into the system during the ^{17}O reoxidation, whereas the Raman spectrum detects all oxygen isotopes present. Due to their intrinsic dipole moment, the {100} surfaces adopted by the cubes are inclined to reconstruct/form defects in order to stabilise charge. Therefore, it is proposed that the highly mobile oxygen that reoxidise ceria cube systems diffuse to stable positions that are further from defect sites in the bulk.

Comparing the signal/noise of Figure 6.4 (a) and (b), as with HSA20, it is evident that a surface reorganisation mechanism takes place between the two reoxidation temperatures, effectively blocking ^{17}O reoxidation until sufficient temperature exchanges the subsurface vacancies with surface oxygen. This conclusion is supported by the TPR measurement of Cubes-1%Pd in Appendix E for which a bulk reduction is apparent from 650 °C (recall that the reduction temperature used is 700 °C). The absence of the peak attributed to PdO at -400 ppm; is in agreement with the Raman data (as was HSA20-1%Pd) for which almost negligible PdO bands were seen.

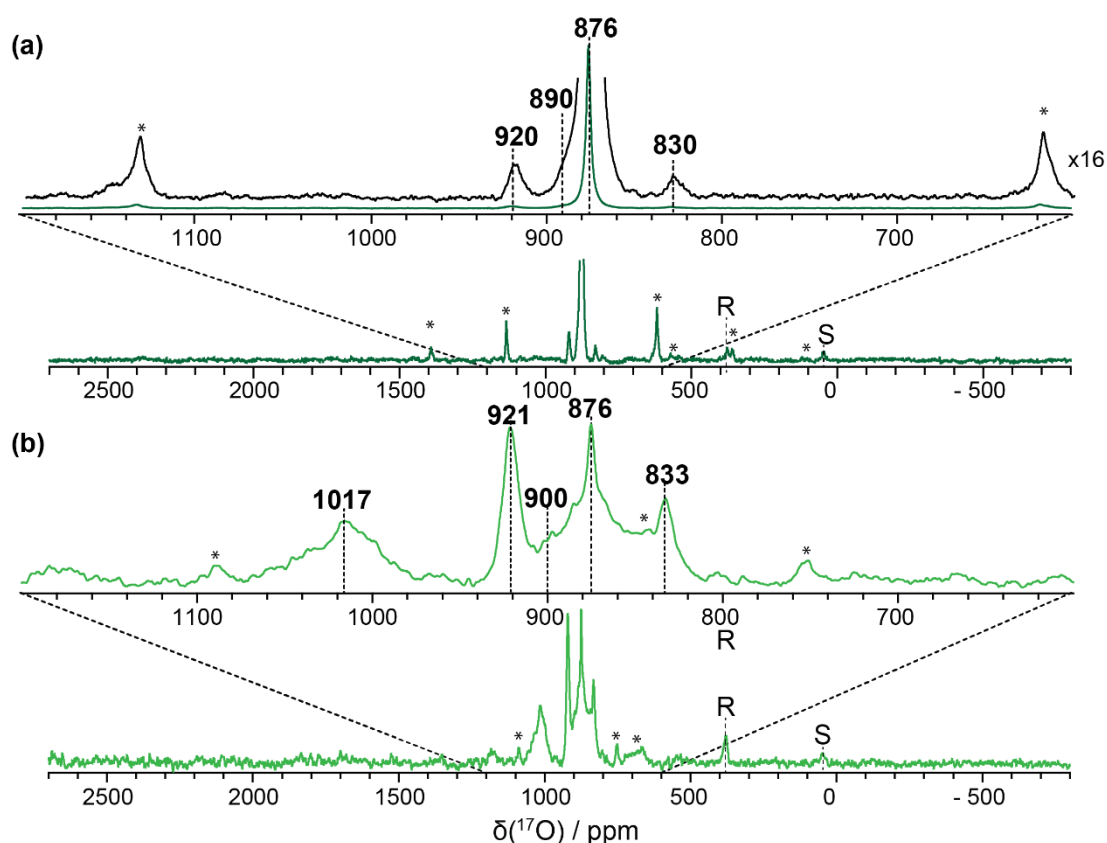


Figure 6.5: ^{17}O MAS single pulse spectra of (a) Rods-1%Pd-700/300-Redox acquired at 9.4 T and (b) Rods-1%Pd-700/150-Redox acquired at 14.1 T. $\nu_r = 14$ kHz, asterisks denote spinning sidebands, R is the rotor and S the stator.

Finally ^{17}O MAS NMR data for Rods-1%Pd-700/300-Redox and Rods-1%Pd-700/150-Redox can be found in Figure 6.5 (a) and (b), respectively, both characterised by the familiar peak positions of ~ 920 , 900 , and 830 ppm, in addition to the unshifted bulk position at 876 ppm. Furthermore, (b) exhibits a more shifted resonance at 1017 ppm, in keeping with the surface reorganisation model that implies a more reduced system at a 150°C reoxidation temperature, and therefore a greater Ce^{3+} concentration. It is interesting to note the significant differences between the sideband manifolds of the spectra shown in Figure 6.3 and Figure 6.5 in which similarly located resonances occur. Closer inspection and measurements of the sidebands in Figure 6.3 reveal that they originate from the narrow component at 1035 ppm, which is absent in the other two morphologies.

In order to compare these loaded supports with that of the bare ceria systems discussed in Chapter 5, overlaid spectra are shown in Figure 6.6. Placed in

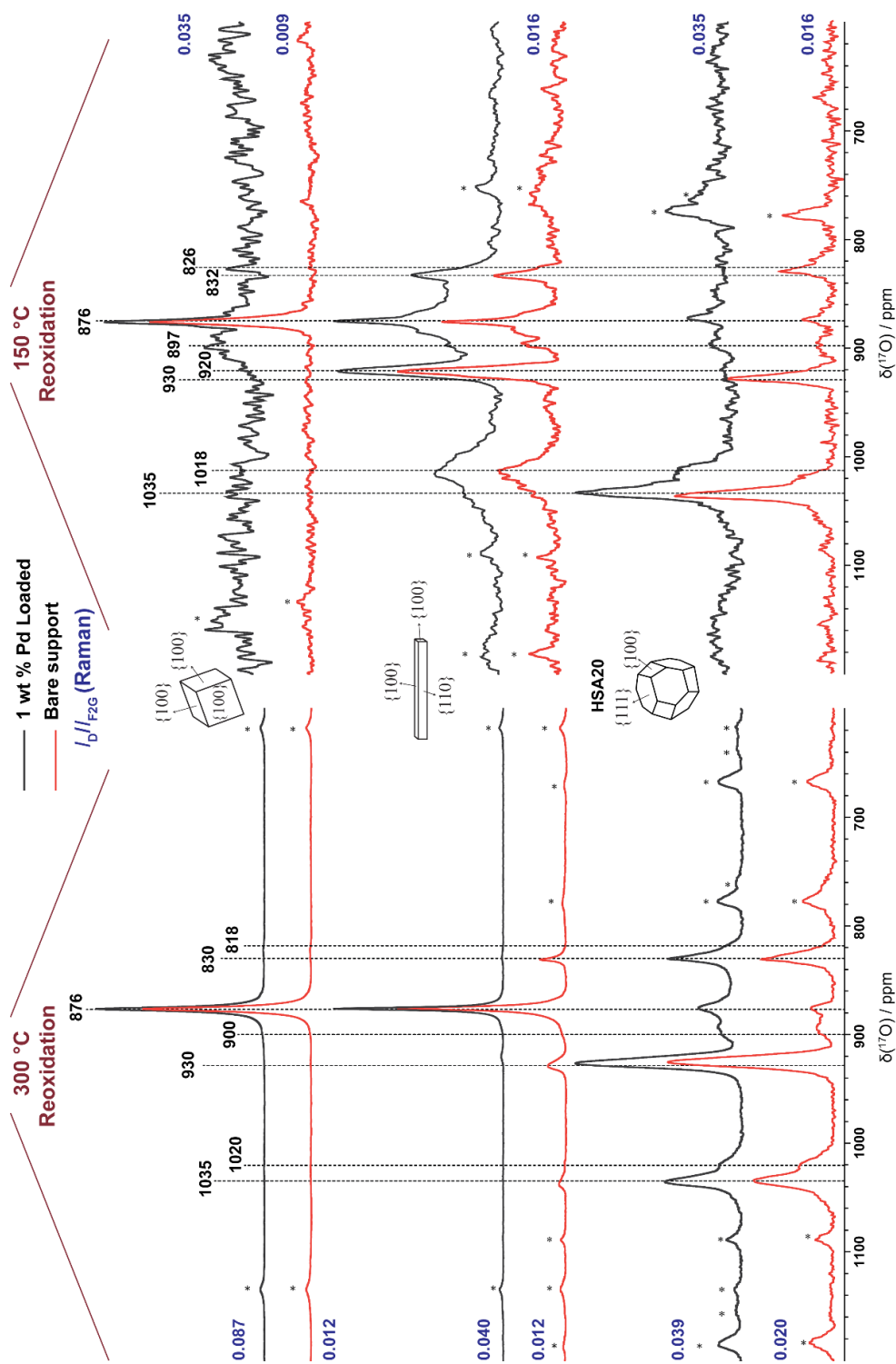


Figure 6.6: ^{17}O MAS NMR spectra of the bare supports studied in Sections 5.5 and 5.7 of Chapter 5 (red) overlaid with the corresponding Pd-loaded catalyst (black) investigated in Section 6.1 of Chapter 6. I_D / I_{F2G} ratios calculated from the Raman data representing relative defect concentration are given in blue.

descending order of surface reactivity, it is apparent that ^{17}O experiences a decreasing influence from the paramagnetic Ce^{3+} cation/vacancies, inferred from the decreasing intensity found in the perturbed (non-bulk) resonances. However, the defect concentration values taken from the Raman data of these respective samples (shown in blue in Figure 6.6) do not correlate with these results, perhaps indicating how stable the releasable oxygen (that are removed and replaced in the reoxidation process) are to locations near defects.

If the loaded and unloaded samples are directly compared within each system, it can be seen that the spectral profiles of peak positions and relative intensities are almost identical, with some small differences. In the 150 °C preparations along the right hand side, it can be perceived that the Pd-loaded systems have impeded ^{17}O reoxidation as compared to the bare support. A possible cause of this could be reverse oxygen spillover (as was briefly discussed in Chapter 1), where an electronic interaction between the Pd metal and ceria support maintains ceria's reduced state under the implemented conditions. Effectively, vacancies in the ceria support are stabilised by oxidation of the Pd metal, forming PdO at the interface between metal and support. Until the oxygen on the Pd is desorbed, $^{17}\text{O}_2$ cannot overcome the energy barrier to adsorb into a ceria vacancy near the interface. Interestingly, this observation is less significant for the rods in which very similar spectra are observed with and without the Pd-loading (note that the Pd-loaded spectrum has a sideband underneath the central peaks on account of its acquisition at 14.1 T). In fact, the Pd has facilitated greater ^{17}O incorporation, perhaps indicating that reverse oxygen spillover occurs at a lower temperature for the {110} facet.

6.2 CeZr Oxides (As-Prepared)

The X-ray diffraction patterns of three mixtures of CeO_2 - ZrO_2 mixed oxides with single phases are shown in Appendix C, with compositions $\text{Ce}_{0.75}\text{Zr}_{0.25}\text{O}_2$, $\text{Ce}_{0.5}\text{Zr}_{0.5}\text{O}_2$ and $\text{Ce}_{0.25}\text{Zr}_{0.75}\text{O}_2$. As with HSA20 in the previous Chapter, the first two exhibit peaks consistent with that of cubic ($Fm3m$) CeO_2 but they have smaller lattice parameters a of 5.345 and 5.281 Å for $\text{Ce}_{0.75}\text{Zr}_{0.25}\text{O}_2$ and $\text{Ce}_{0.5}\text{Zr}_{0.5}\text{O}_2$, respectively (recall that for CeO_2 , $a=5.411$ Å). This contraction of the lattice cell parameter is caused by the

smaller Zr^{4+} cationic radius, which is 0.84 Å compared to Ce^{4+} at 0.97 Å. However, as discussed in Chapter 1, the characteristic broadening of the XRD patterns can inhibit differentiation between the true cubic c and tetragonal t'' phases as the lattice parameter ratio a/c is 1. The diffractogram of $\text{Ce}_{0.25}\text{Zr}_{0.75}\text{O}_2$ reveals the tetragonal t $P4_2/nmc$ phase and the Scherer equation approximates crystallite sizes of 5.3, 5.2 and 6.7 nm for $\text{Ce}_{0.75}\text{Zr}_{0.25}\text{O}_2$, $\text{Ce}_{0.5}\text{Zr}_{0.5}\text{O}_2$ and $\text{Ce}_{0.25}\text{Zr}_{0.75}\text{O}_2$, respectively.

6.2.1 TPR

Figure 6.7 presents H_2 -TPR measurements between 0 and 975 °C of $\text{Ce}_{0.75}\text{Zr}_{0.25}\text{O}_2$, $\text{Ce}_{0.5}\text{Zr}_{0.5}\text{O}_2$ and $\text{Ce}_{0.25}\text{Zr}_{0.75}\text{O}_2$, showing the well-documented,^{125,163-166} characteristic overlapping signals of the surface and bulk reduction peaks. This significant decrease in bulk reduction temperature from that of pure ceria (see Figure 5.7) is valuable behaviour to TWCs that operate in this temperature region, for which more oxygen is available, providing enhanced catalysis output. However, the amount of releasable

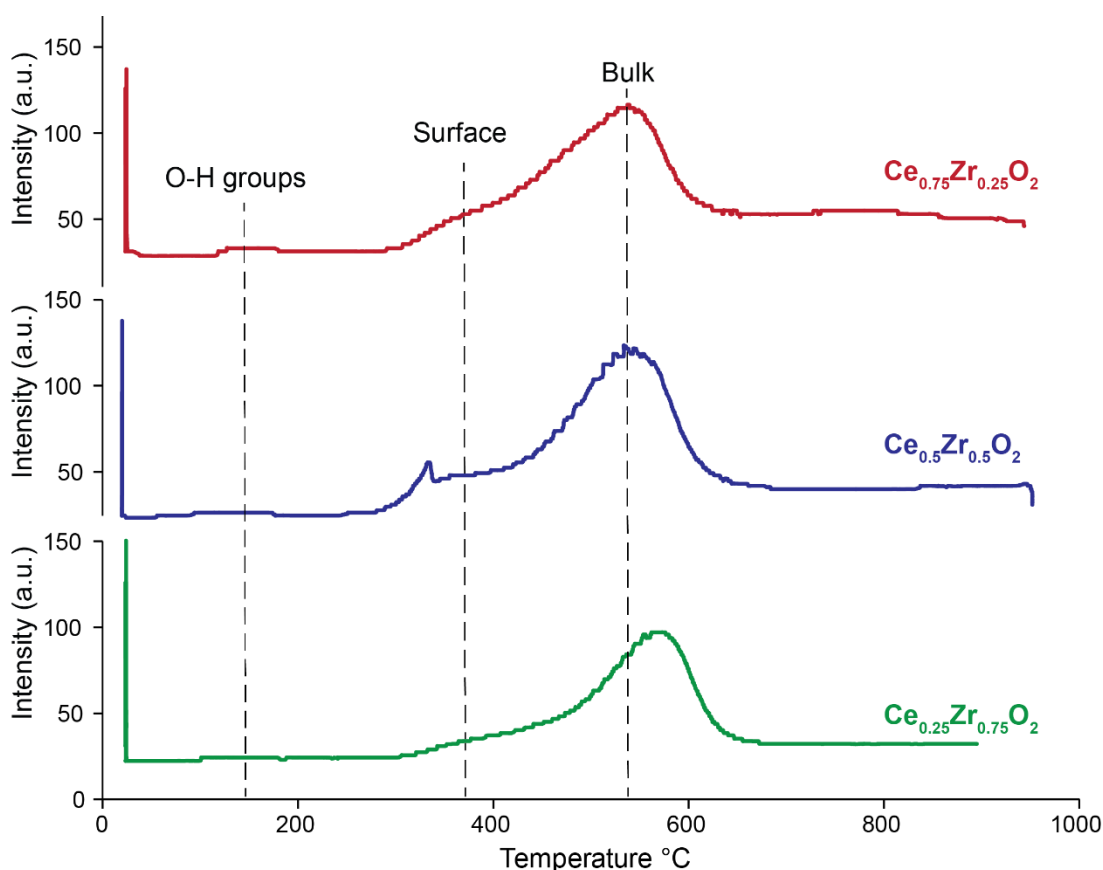


Figure 6.7: TPR- H_2 of $\text{Ce}_{0.75}\text{O}_{0.25}\text{O}_2$, $\text{Ce}_{0.5}\text{O}_{0.2}\text{O}_2$ and $\text{Ce}_{0.25}\text{O}_{0.75}\text{O}_2$ to 975°C.

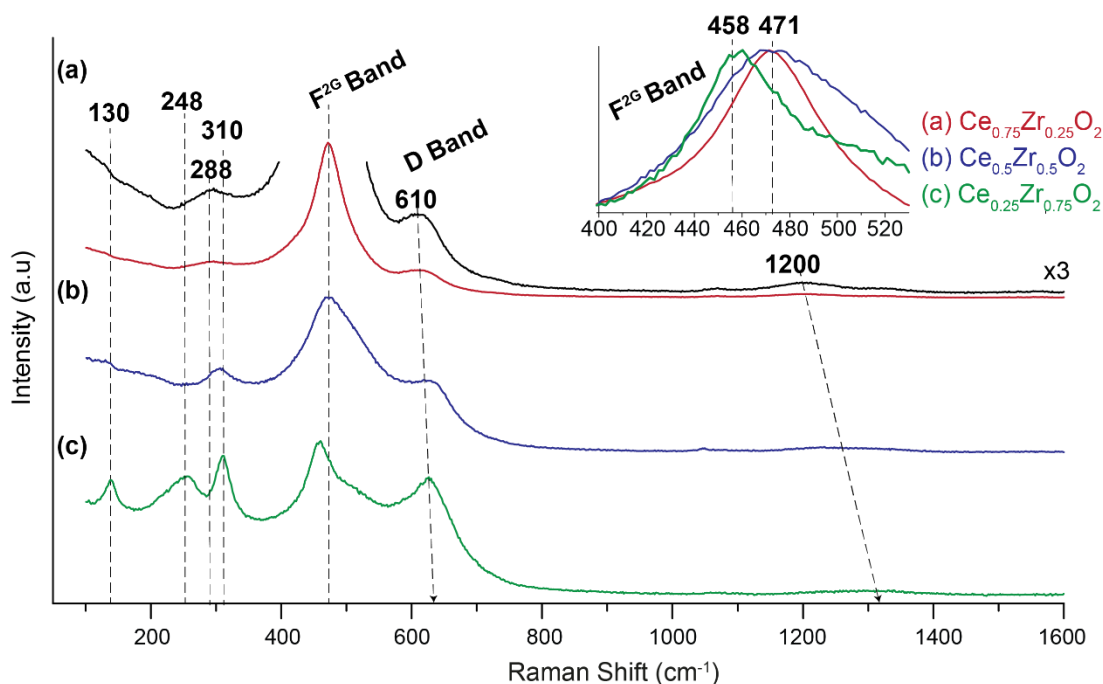


Figure 6.8: Raman spectra of as-prepared samples of (a) $\text{Ce}_{0.75}\text{Zr}_{0.25}\text{O}_2$, (b) $\text{Ce}_{0.5}\text{Zr}_{0.5}\text{O}_2$ and (c) $\text{Ce}_{0.25}\text{Zr}_{0.75}\text{O}_2$. Inset shows expanded region of the $\text{F}_{2\text{G}}$ mode.

surface oxygen available significantly decreases (indicating that at lower temperatures, catalyst output will be reduced from ceria zirconia oxides).

$\text{Ce}_{0.75}\text{Zr}_{0.25}\text{O}_2$ and $\text{Ce}_{0.5}\text{Zr}_{0.5}\text{O}_2$ depict very similar OSC properties in terms of surface and bulk reduction temperatures, centred at 370 °C and 540 °C degrees, respectively. However, more oxygen is released for $\text{Ce}_{0.5}\text{Zr}_{0.5}\text{O}_2$, with its greater reducibility in agreement with the literature.¹⁶⁴ For the highest zirconia concentration $\text{Ce}_{0.25}\text{Zr}_{0.75}\text{O}_2$, oxygen is removed at increased temperatures from the surface/bulk at 420 °C/560 °C, and overall, a lower OSC is demonstrated.

6.2.2 Raman Spectroscopy

The ambiguity of phase differentiation via PXRD techniques between the cubic and tetragonal phases was mentioned above. These phases are readily discriminated by Raman spectroscopy however, with the data presented in Figure 6.8 (a) $\text{Ce}_{0.75}\text{Zr}_{0.25}\text{O}_2$, (b) $\text{Ce}_{0.5}\text{Zr}_{0.5}\text{O}_2$ and (c) $\text{Ce}_{0.25}\text{Zr}_{0.75}\text{O}_2$. It is clear that a greater zirconia incorporation results in an increasingly altered Raman spectrum to that seen for pure ceria. There are six peaks in (c) at 130, 248, 310, 457 and 623 cm^{-1} (two are unresolved in this last signal) which correspond to the six active modes ($\text{A}_{1\text{G}}+3\text{E}_{\text{G}}+2\text{B}_{1\text{G}}$) of the less symmetric tetragonal t phase compared to the one Raman active $\text{F}_{2\text{G}}$ mode of the cubic fluorite lattice with perfect symmetry. The third band at 310 cm^{-1} is considered

validation of the tetragonal phase.⁶² Inspection of (b) reveals the presence of this characteristic tetragonal band, which indicates a displacement of oxygen atoms from their ideal lattice position and not a deformation of the lattice,¹⁶⁷ and thus $\text{Ce}_{0.5}\text{Zr}_{0.5}\text{O}_2$ is characterised with the presence of the t'' phase. Evidence of this band is less apparent for $\text{Ce}_{0.75}\text{Zr}_{0.25}\text{O}_2$ however due to a low intensity broad band at 288 cm^{-1} and so a c or t'' phase cannot be determined with confidence. The broadening and shift to higher wavenumber of the $\text{F}_{2\text{G}}$ band in (a) and (b) at 471 cm^{-1} (see inset) is ascribed to zirconium doping of the ceria lattice¹⁶⁸ resulting from lattice distortion and shortening of the Ce-O bond, respectively. This is a consistent observation with the increased lattice parameters obtained from the PXRD data.

The progressive increase of the D band with increasing Zr concentration emphasizes the increase of lattice distortion caused from vacancies/the movement of the tetrahedral, sublattice oxygen to the octahedral site, i.e. Frenkel defects.

6.3 $^{17}\text{O}_2$ Direct Exchange of CeZr Oxides at 600 °C

As carried out in Chapter 5, the following subsection shall explore the properties exhibited by $\text{Ce}_{0.75}\text{Zr}_{0.25}\text{O}_2$ and $\text{Ce}_{0.5}\text{Zr}_{0.5}\text{O}_2$ after undergoing a direct exchange with $^{17}\text{O}_2$ at 600 °C; defined as $\text{Ce}_{0.75}\text{Zr}_{0.25}\text{O}_2\text{-600Ex}$ and $\text{Ce}_{0.5}\text{Zr}_{0.5}\text{O}_2\text{-600Ex}$, respectively, firstly via Raman spectroscopy and more importantly by ^{17}O MAS NMR. As of yet, ^{17}O NMR studies on CeZr systems have not been published. Particle size measurements of these systems exposed to higher temperatures (preparations which will be seen in Section 6.4) indicated little/no particle sintering and therefore this is likely to be the case here.

6.3.1 Raman Spectroscopy

The Raman spectra of $\text{Ce}_{0.75}\text{Zr}_{0.25}\text{O}_2\text{-600Ex}$ and $\text{Ce}_{0.5}\text{Zr}_{0.5}\text{O}_2\text{-600Ex}$ can be seen in Figure 6.9 (a) and (b), respectively. Both materials exhibit a red-shift of the $\text{F}_{2\text{G}}$ band (see the insets) after the $^{17}\text{O}_2$ exchange at 600 °C under oxygen deficient conditions. In the literature, this is usually the result of a lattice expansion due to conversion of the smaller (0.97 Å) Ce^{4+} cation to larger (1.14 Å) Ce^{3+} cation, (however isotopic incorporation of ^{17}O could contribute to this shift).

Greater spectral changes are evident for $\text{Ce}_{0.75}\text{Zr}_{0.25}\text{O}_2$ from the as-prepared state, emphasized by the difference spectra shown beneath. The bands at 410 and

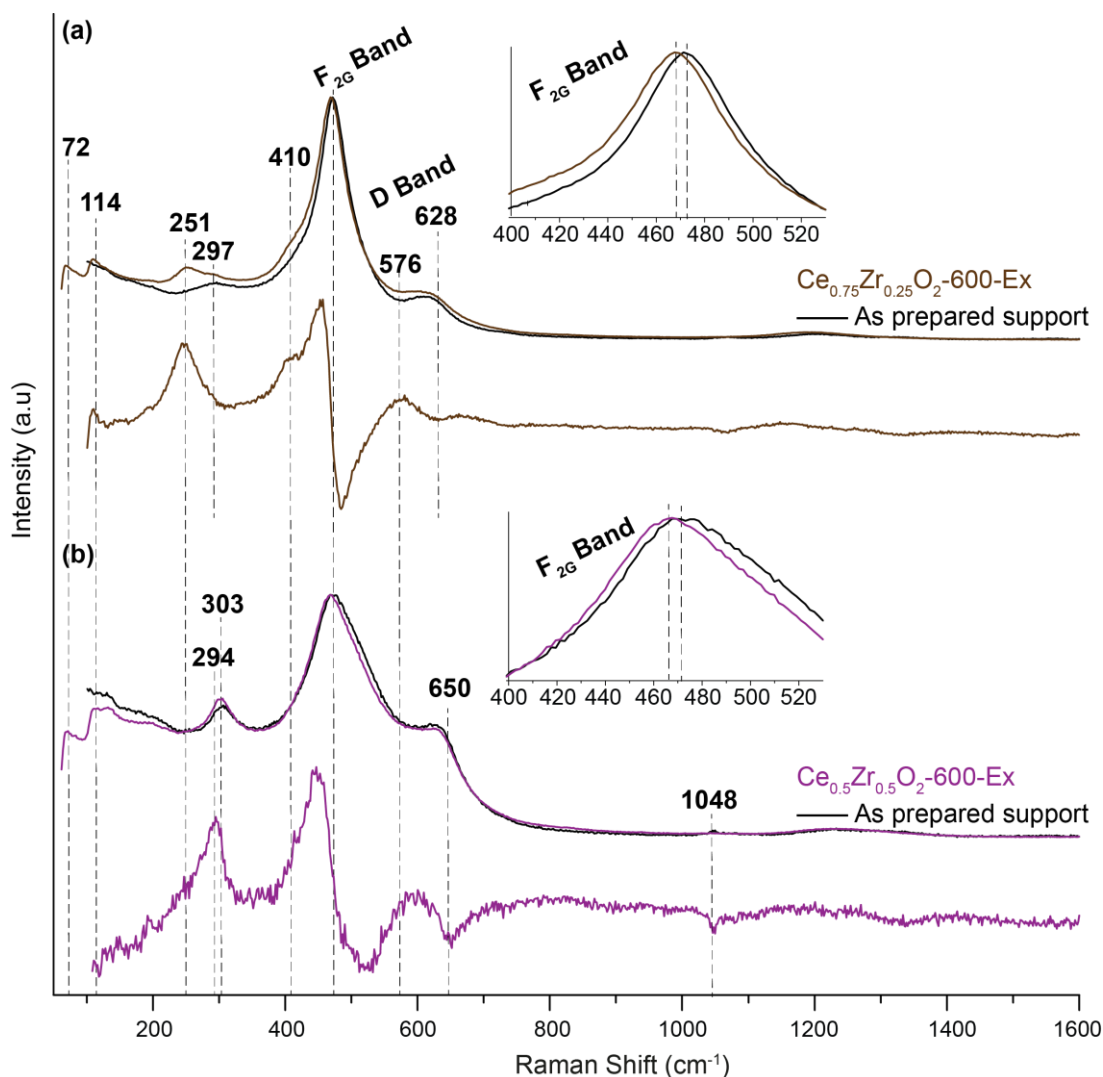


Figure 6.9: Raman spectra of (a) $\text{Ce}_{0.75}\text{Zr}_{0.25}\text{O}_2\text{-600Ex}$ (b) $\text{Ce}_{0.5}\text{Zr}_{0.5}\text{O}_2\text{-600Ex}$ (bottom), layered on top of the as-prepared material (for which the Raman spectra were presented and described in Section 6.2) and difference spectra beneath.

576 cm^{-1} , both of which indicate oxygen deficiency of the sample through the presence of CeZr-O_x ($5 < x < 8$) subunits and oxygen vacancies, respectively, are increased, in addition to the formation of a 251 cm^{-1} feature ascribed to hydroxyls on the surface. The oxygen deficiency corroborates the $\text{F}_{2\text{G}}$ band shifts as a result of lattice expansion. $\text{Ce}_{0.5}\text{Zr}_{0.5}\text{O}_2\text{-600Ex}$ in (b) demonstrates a strengthening of the 303 cm^{-1} band attributed to the displacement of oxygen from the lattice positions, although from the difference spectrum, it can be seen that this new species occurs at a Raman shift of 294 cm^{-1} .

Phonon frequencies are dependent on the mass of the constituents of the vibration produced in a Raman spectrum. This shift to 294 from 303 cm^{-1} has a ratio

of 1.0304 and whilst this could be coincidence, as this value is nearly the isotopic ratio of $^{17}\text{O}/^{16}\text{O}$, i.e. $(17/16)^{1/2} = 1.0308$, it is possible that ^{17}O from the reoxidation process has allowed more oxygen to occupy this environment of displaced oxygen ions. An analogous result may be manifesting in the spectrum of $\text{Ce}_{0.75}\text{Zr}_{0.25}\text{O}_2\text{-600Ex}$ but this is difficult to determine due to the 251 cm^{-1} feature overlap.

As discussed, $\text{Ce}_{0.75}\text{Zr}_{0.25}\text{O}_2\text{-600Ex}$ experiences an increase in bands characterising oxygen vacancies (576 cm^{-1}), however for $\text{Ce}_{0.5}\text{Zr}_{0.5}\text{O}_2\text{-600Ex}$ in (b), the D-band region is attenuated. The difference spectrum below chiefly reveals a greater loss of intensity from the feature at 650 cm^{-1} . Recall that the D band envelopes two bands attributed to vacancies at the lower frequency and interstitial defects at the higher frequency. It is apparent that both of these species are shifted to higher frequency with increased zirconia content as with the $\text{F}_{2\text{G}}$ band, indicating increased Zr incorporation. In an in situ Raman study of $\text{Ce}_{0.5}\text{Zr}_{0.5}\text{O}_2$, Andriopoulou *et al.* observed the Frenkel interstitial leave the structure after a H_2 reduction at 450°C and reappear after undergoing O_2 oxidising conditions at the same temperature.¹⁶⁹ It is therefore proposed that $^{17}\text{O}_2$ heating under oxygen deficient conditions of $\text{Ce}_{0.75}\text{Zr}_{0.25}\text{O}_2\text{-600Ex}$ and $\text{Ce}_{0.5}\text{Zr}_{0.5}\text{O}_2$ has removed some of the Frenkel interstitial oxygen to result in the concomitant reduced system. These interstitial oxygen are exposed by the difference spectra in (a) and (b) at Raman shifts of 628 and 650 cm^{-1} , respectively.

6.3.2 ^{17}O Solid State MAS NMR

Figure 6.10 (a) and (b) depicts ^{17}O MAS NMR spectra of $\text{Ce}_{0.75}\text{Zr}_{0.25}\text{O}_2\text{-600Ex}$ and $\text{Ce}_{0.5}\text{Zr}_{0.5}\text{O}_2\text{-600Ex}$, respectively, acquired at 14.1 T . Hahn-echo experiments were employed and consequently the broad components (between 0 and 1500 ppm) observed are real features. Broad components on this scale were also observed in Chapter 5 (under the conditions of Hahn echo experiments- see Figure 5.11) and are the result of oxygen directly bonding with Ce^{3+} . Incorporation of ^{17}O into $\text{Ce}_{0.75}\text{Zr}_{0.25}\text{O}_2\text{-600Ex}$ is considerably greater than that of $\text{Ce}_{0.5}\text{Zr}_{0.5}\text{O}_2\text{-600Ex}$, facilitating the use of a faster spinning probe (a 3.2 mm) which allowed greater

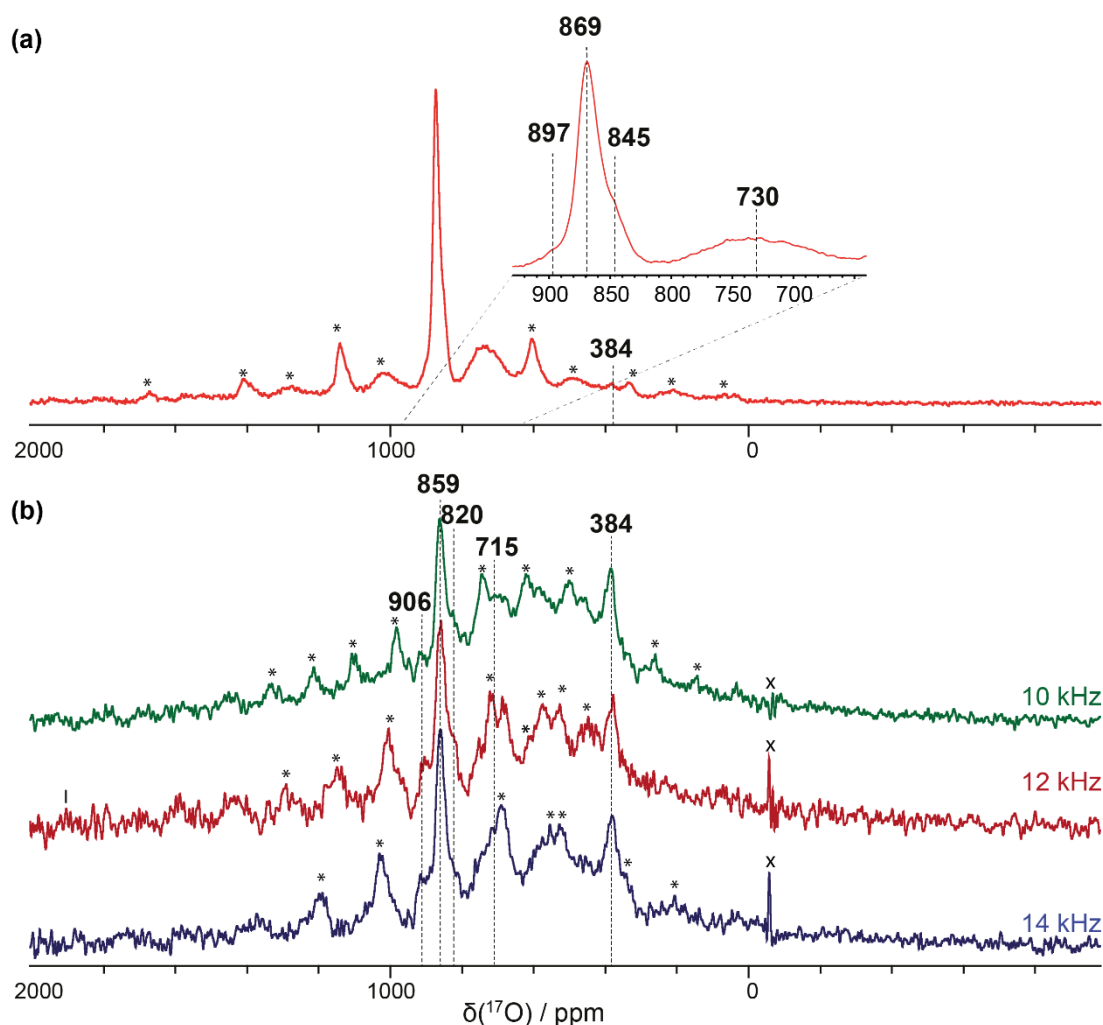


Figure 6.10: ^{17}O MAS Hahn-echo spectra acquired at 14.1 T of (a) $\text{Ce}_{0.75}\text{Zr}_{0.25}\text{O}_2\text{-600Ex}$ spinning at $\nu_r = 22$ kHz and (b) $\text{Ce}_{0.5}\text{Zr}_{0.5}\text{O}_2\text{-600Ex}$ where spinning speed is indicated on the figure. Recycle delays of 45 s were implemented. Asterisks denote spinning sidebands, X is a spurious signal.

spectral resolution than that of $\text{Ce}_{0.5}\text{Zr}_{0.5}\text{O}_2\text{-600Ex}$ (4 mm probe). In order to distinguish sidebands from centrebands, three spinning speeds were implemented in (b), with the dashed lines implying shared signal present in each spectrum, and therefore a resonance portraying an oxygen environment.

$\text{Ce}_{0.75}\text{Zr}_{0.25}\text{O}_2\text{-600Ex}$ in (a) demonstrates a dominating peak at 869 ppm, which is attributed to the bulk tetrahedral oxygen OCe_4^{4+} in the cubic fluorite lattice. The 7 ppm increased shielding observed from ceria's bulk oxygen shift at 876 ppm cannot be caused by nano effects of the 5 nm particles alone, as in chapter 5, a sub 2 nm particle was characterised with a bulk oxygen chemical shift of 873 ppm. Moreover, $\text{Ce}_{0.5}\text{Zr}_{0.5}\text{O}_2\text{-600Ex}$ in (b) reveals a further shifted bulk OCe_4^{4+} oxygen signal at 859 ppm. This increased shielding from both systems can therefore be ascribed to the

shortening of the Ce-O bond length, a result of the smaller Zr^{4+} cation entering the lattice, causing lattice contraction. This was demonstrated by Raman spectroscopy in Section 6.2.2 where the $\text{F}_{2\text{G}}$ band was shifted to higher wavenumber as compared to pure ceria. This shielding appears almost additive as; for a further 25% zirconia doping into the ceria lattice, the chemical shift moves another 10 ppm up field. Peak widths of the OCe_4^{4+} moiety furthermore reveal a trend with $\text{Ce}_{0.75}\text{Zr}_{0.25}\text{O}_2\text{-600Ex}$ (1600 Hz) < $\text{Ce}_{0.5}\text{Zr}_{0.5}\text{O}_2\text{-600Ex}$ (2900 Hz) and recall that for pure ceria, δ_{FWHM} of HSA20-600Ex is 550 Hz. This increasing trend for increasing Zr content is in-keeping with the enhanced distortion that Zr doping into the ceria lattice causes.

Additional features are observed either side of the OCe_4^{4+} peaks for both systems, seen at 897 and 845 ppm for $\text{Ce}_{0.75}\text{Zr}_{0.25}\text{O}_2\text{-600Ex}$, and 907 and 820 ppm for $\text{Ce}_{0.5}\text{Zr}_{0.5}\text{O}_2\text{-600Ex}$, appearing similar in nature to the shifted signals that were seen in Chapter 5 and attributed to oxygen near defects in the lattice. The tetragonal phase of zirconia is clear in (b) at 384 ppm (intensity is too strong for the rotor signal alone) whereas this is almost negligible in (a). The relative intensities of the bulk OCe_4 and OZr_4 oxygen species in (a) and (b) do not correlate with the respective zirconia mol %, suggesting that ^{17}O exchanges more readily with OCe_4 species.

Also, shared by both materials is a broad, lower-intensity feature centred at 730 ppm in (a) and 715 ppm in (b) for $\text{Ce}_{0.75}\text{Zr}_{0.25}\text{O}_2\text{-600Ex}$ and $\text{Ce}_{0.5}\text{Zr}_{0.5}\text{O}_2\text{-600Ex}$ respectively, (although this may be inaccurate in the latter case due to overlap with sidebands). The ^{17}O spectral profiles of the three systems HSA20-600Ex, $\text{Ce}_{0.5}\text{Zr}_{0.5}\text{O}_2\text{-600Ex}$ and $\text{Ce}_{0.75}\text{Zr}_{0.25}\text{O}_2\text{-600Ex}$ are similar to those of YDC systems (also exchanged with $^{17}\text{O}_2$ at 600 °C for 12 hours) in a study by Kim and Stebbins⁹¹ that was examined in Chapter 3 (see Figure 3.2). They assign increasingly shielded resonances with the increasingly coordinated yttrium environments, whilst observing a gradually broadened OCe_4 peak, depicting greater lattice distortion with Y concentration. Based on these conclusions, the signals seen at 730/715 ppm are assigned to oxygen species coordinated to both Ce and Zr cations.

6.4 $^{17}\text{O}_2$ Redox Experiments of CeZr Oxides

Following on from the straight $^{17}\text{O}_2$ exchange experiments, this section shall investigate the effects of firstly removing oxygen from materials $\text{Ce}_{0.75}\text{Zr}_{0.25}\text{O}_2$,

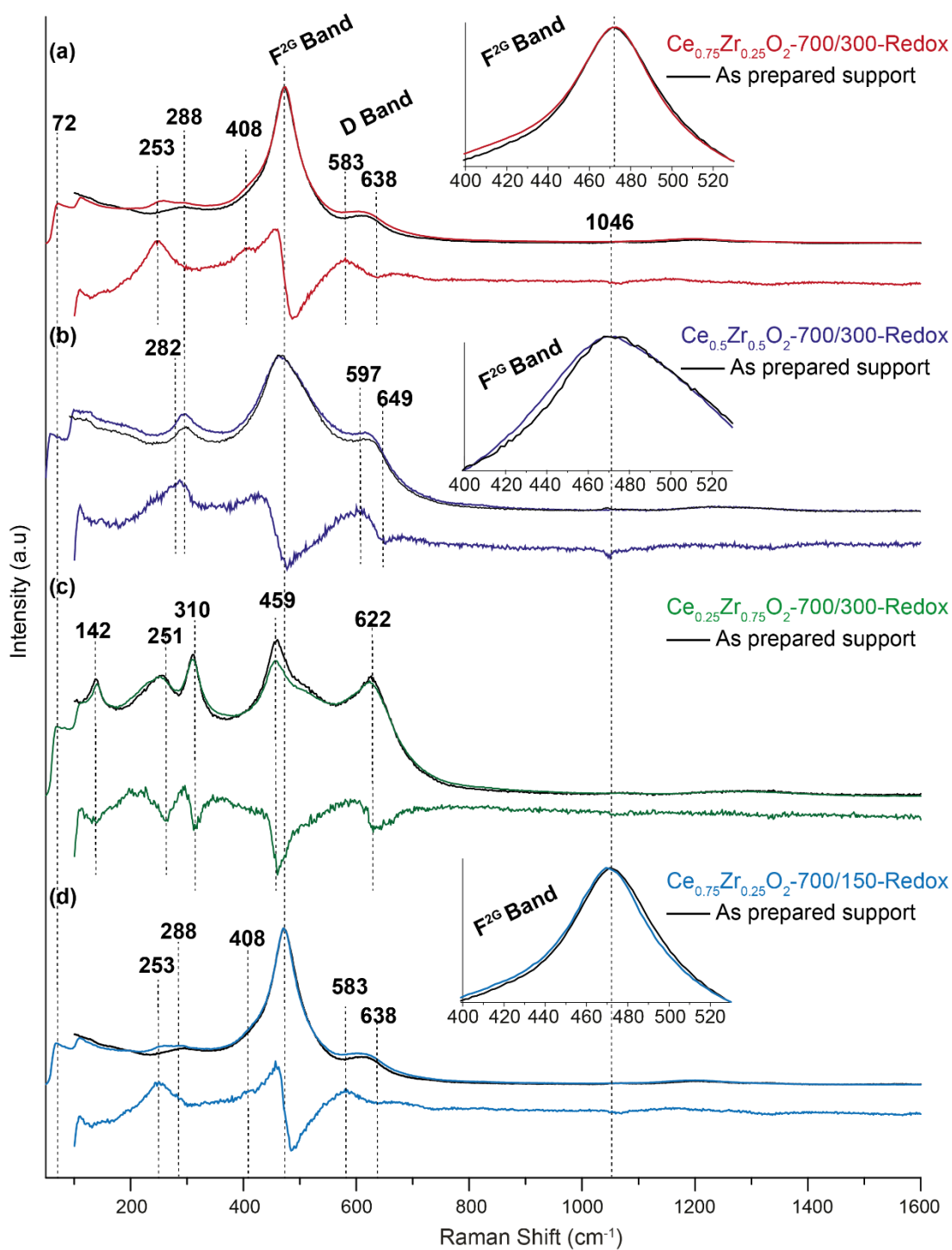


Figure 6.11: Raman spectra of (a) $\text{Ce}_{0.75}\text{Zr}_{0.25}\text{O}_2\text{-700/300-Redox}$, (b) $\text{Ce}_{0.5}\text{Zr}_{0.5}\text{O}_2\text{-700/300-Redox}$, (c) $\text{Ce}_{0.25}\text{Zr}_{0.75}\text{O}_2\text{-700/300-Redox}$ and (d) $\text{Ce}_{0.75}\text{Zr}_{0.25}\text{O}_2\text{-700/150-Redox}$. The as-prepared samples are layered underneath (black) and the difference spectra are shown below the corresponding spectra.

$\text{Ce}_{0.5}\text{Zr}_{0.5}\text{O}_2$ and $\text{Ce}_{0.25}\text{Zr}_{0.75}\text{O}_2$ by H_2 reduction at 700 °C, and reoxidising them with $^{17}\text{O}_2$ at elevated temperatures of 300 and 150 °C for the former, and only 300 °C for the latter two. At 700 °C under reducing conditions, bulk reduction has occurred as was demonstrated by the TPR measurements in Section 6.2.1. They are defined as $\text{Ce}_{0.75}\text{Zr}_{0.25}\text{O}_2$ -700/300-Redox, $\text{Ce}_{0.75}\text{Zr}_{0.25}\text{O}_2$ -700/150-Redox, $\text{Ce}_{0.5}\text{Zr}_{0.5}\text{O}_2$ -700/300-Redox and $\text{Ce}_{0.25}\text{Zr}_{0.75}\text{O}_2$ -700/300-Redox.

6.4.1 Raman Spectroscopy

Raman spectra obtained for $\text{Ce}_{0.75}\text{Zr}_{0.25}\text{O}_2$ -700/300-Redox, $\text{Ce}_{0.5}\text{Zr}_{0.5}\text{O}_2$ -700/300-Redox, $\text{Ce}_{0.25}\text{Zr}_{0.75}\text{O}_2$ -700/300-Redox and $\text{Ce}_{0.75}\text{Zr}_{0.25}\text{O}_2$ -700/150-Redox are shown in Figure 6.11 (a), (b), (c) and (d), respectively. Interestingly, the spectral profiles after the $^{17}\text{O}_2$ redox process reveal more subtle changes than the materials exchanged at 600 °C from Section 6.3. The F_{2g} bands (inset) of $\text{Ce}_{0.75}\text{Zr}_{0.25}\text{O}_2$ -700/300-Redox, $\text{Ce}_{0.5}\text{Zr}_{0.5}\text{O}_2$ -700/300-Redox and $\text{Ce}_{0.75}\text{Zr}_{0.25}\text{O}_2$ -700/150-Redox (the systems with the cubic fluorite structure) all show almost negligible changes to lower wavenumber implying less lattice expansion and/or less ^{17}O enrichment compared to materials in Section 6.3.

The D bands in (a) and (d) depicting $\text{Ce}_{0.75}\text{Zr}_{0.25}\text{O}_2$ exhibit greater intensity increases compared to the $^{17}\text{O}_2$ direct exchange of this system. This is emphasised in Figure 6.12, which shows all three difference spectra overlayed. This result implies more vacancies are retained under the conditions of the ^{17}O Redox experiments. This is rationalised if the 30 mL $^{17}\text{O}_2$ injection below ambient pressure is insufficient to refill these vacant sites. It is also clear that the lower frequency feature of the D-band of $\text{Ce}_{0.75}\text{Zr}_{0.25}\text{O}_2$ -600Ex is both red shifted (from 583 to 576 cm^{-1}) and broadened compared to $\text{Ce}_{0.75}\text{Zr}_{0.25}\text{O}_2$ -700/300-Redox and $\text{Ce}_{0.75}\text{Zr}_{0.25}\text{O}_2$ -700/150-Redox, and a similar observation can be made for the trough that represents the decrease of the interstitial at 628 cm^{-1} ; it is broader and red shifted from 638 cm^{-1} .

Small increases in the features at 408 cm^{-1} and 253 cm^{-1} are also apparent from the difference spectra of Figure 6.12, with a greater increase seen for a greater

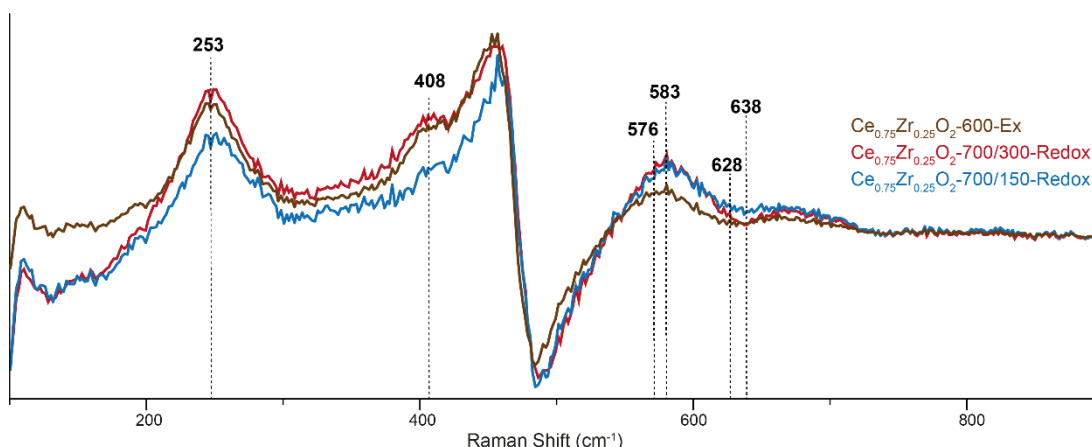


Figure 6.12: The difference Raman spectra of $\text{Ce}_{0.75}\text{Zr}_{0.25}\text{O}_2$ -700/300-Redox, $\text{Ce}_{0.75}\text{Zr}_{0.25}\text{O}_2$ -700/150-Redox and $\text{Ce}_{0.75}\text{Zr}_{0.25}\text{O}_2$ -600Ex (difference between after treatment and the as prepared sample).

temperature under oxidative conditions, indicating an increase in the less coordinated Ce/Zr- O_x ($5 < x < 8$) units and Ce-OH species.

Figure 6.11 (c) depicting the $t\text{-Ce}_{0.25}\text{Zr}_{0.75}\text{O}_2$ -700/300-Redox system (with the aid of the difference spectrum underneath) reveals that the band at 142 cm^{-1} shows the smallest intensity decrease and a narrowing relative to the other modes, whilst that at 459 cm^{-1} shows the greatest mode softening. According to the literature, these observations indicate an increase in the ‘tetragonality’^{165,166} of the structure, i.e. an increase in the c/a ratio.

6.4.2 ^{17}O Solid-State MAS NMR

Figure 6.13 depicts ^{17}O MAS NMR spectra of (a) $\text{Ce}_{0.75}\text{Zr}_{0.25}\text{O}_2$ -700/300-Redox, $\text{Ce}_{0.5}\text{Zr}_{0.5}\text{O}_2$ -700/300-Redox and $\text{Ce}_{0.25}\text{Zr}_{0.75}\text{O}_2$ -700/300-Redox, acquired with Hahn echo pulse sequences and (b) $\text{Ce}_{0.75}\text{Zr}_{0.25}\text{O}_2$ -700/150-Redox, collected with a single pulse sequence due to the very low signal/noise observed for this sample. They exhibit substantial differences to one another as well as the ^{17}O spectra of the $^{17}\text{O}_2$ exchanged systems, demonstrating the sensitive and unique spectroscopic power of ^{17}O NMR in revealing oxygen pathways during the OSC process.

$\text{Ce}_{0.75}\text{Zr}_{0.25}\text{O}_2$ -700/300-Redox and $\text{Ce}_{0.5}\text{Zr}_{0.5}\text{O}_2$ -700/300-Redox in (a) reveal significantly intense and broad O- Ce^{3+} bonded contributions, indicating that: (1) the systems is in a reduced state and, (2) a considerable amount of ^{17}O adsorbed in the reoxidation process preferentially adsorbs close to the paramagnetic centres. The

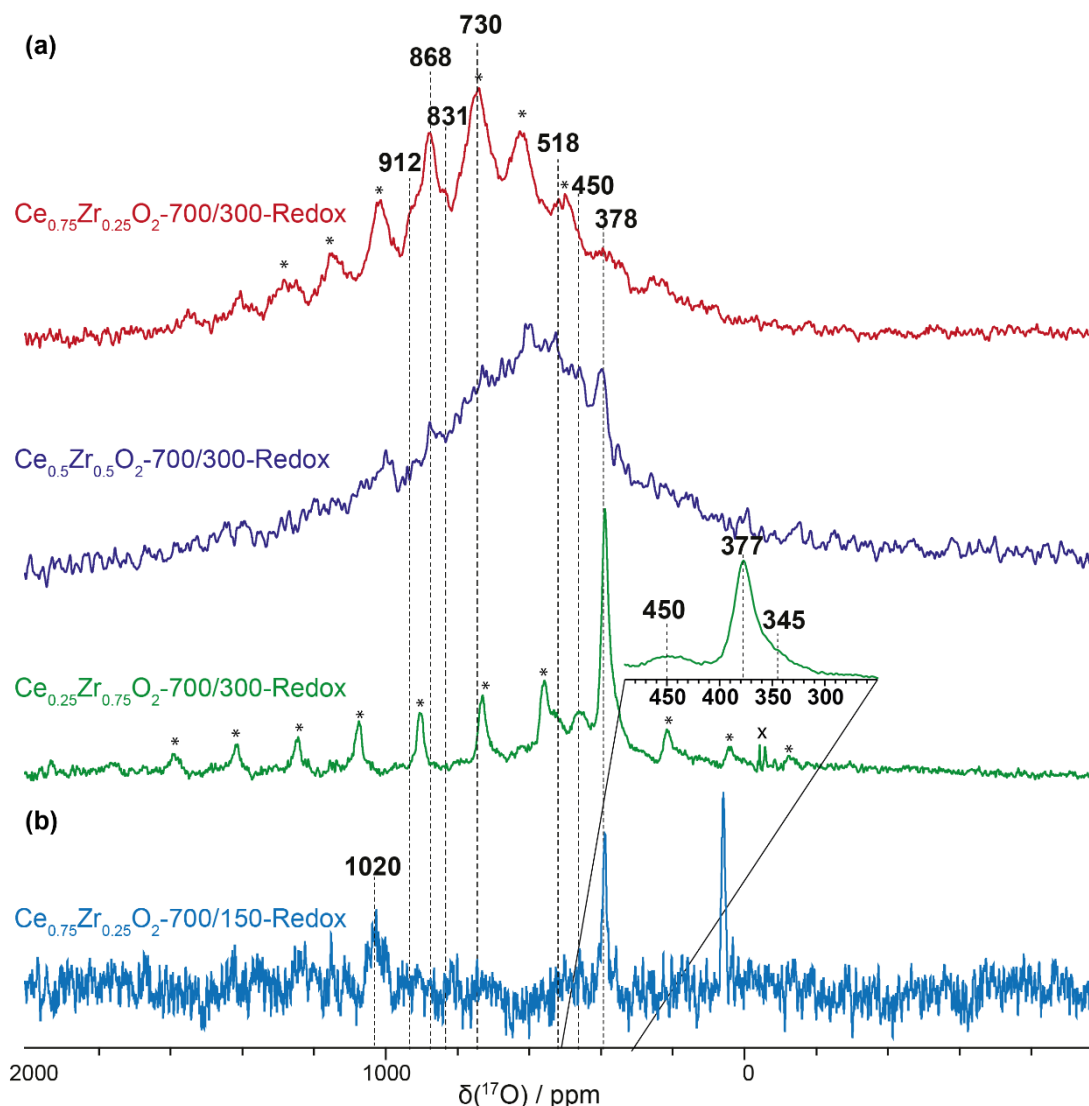


Figure 6.13: ^{17}O MAS NMR data. (a) Hahn-echo spectra acquired at 14.1 T of $\text{Ce}_{0.75}\text{Zr}_{0.25}\text{O}_2\text{-700/300-Redox}$; $\nu_r=12$ kHz, $\text{Ce}_{0.5}\text{Zr}_{0.5}\text{O}_2\text{-700/300-Redox}$; $\nu_r=12$ kHz and $\text{Ce}_{0.25}\text{Zr}_{0.75}\text{O}_2\text{-700/300-Redox}$; $\nu_r = 14$ kHz and (b) single pulse spectrum of $\text{Ce}_{0.75}\text{Zr}_{0.25}\text{O}_2\text{-700/150-Redox}$ acquired at 9.4 T; $\nu_r = 14$ kHz. Recycle delays of 45 s were implemented. Asterisks denote spinning sidebands, X is a spurious signal.

data also portrays a shift between these components where it is centred at ~ 785 ppm for $\text{Ce}_{0.75}\text{Zr}_{0.25}\text{O}_2\text{-700/300-Redox}$ and ~ 575 ppm for $\text{Ce}_{0.5}\text{Zr}_{0.5}\text{O}_2\text{-700/300-Redox}$, alluding to an increased shielding with zirconia content. Both of these chemical shift positions are between the bulk OCe_4 and OZr_4 chemical shifts at 876 and 378 ppm, respectively. Due to their weighted/incremental chemical shifts with increase in Zr content and the significant breadth, they are cautiously ascribed to a distribution of oxygen in different coordinations with Ce^{3+} , i.e. $\text{OCe}_3^{4+}\text{Ce}^{3+}$, $\text{OCe}_2^{4+}\text{ZrCe}^{3+}$, $\text{OCe}^{4+}\text{Zr}_2\text{Ce}^{3+}$ and $\text{OZr}_3\text{Ce}^{3+}$. For $\text{Ce}_{0.75}\text{Zr}_{0.25}\text{O}_2\text{-700/300-Redox}$, narrower features are

also present, in particular that of bulk ceria at 868 ppm, defect associated shifted features at 912 and 831 ppm and a relatively broader signal at 730 ppm, previously assigned to Ce-O-Zr linkages (without direct Ce^{3+} bonding). Sidebands caused by paramagnetic anisotropy otherwise obscure the spectrum. Interestingly, these narrow resonances are mostly absent for $\text{Ce}_{0.5}\text{Zr}_{0.5}\text{O}_2$ -700/300-Redox, with the exception of tetragonal zirconia apparent at 378 ppm. This result corresponds with the Raman spectrum of this system in Figure 6.11(b), where it was determined that a t'' phase is present.

6.5 Investigation of Palladium Loaded $\text{Ce}_{0.5}\text{Zr}_{0.5}\text{O}_2$

$\text{Ce}_{0.5}\text{Zr}_{0.5}\text{O}_2$ which was investigated in Sections 6.3 and 6.4 and loaded with 1 wt % Pd is probed in the following section. This system is more representative in composition of a typical TWC. The same preparations and techniques as those of previous Sections are used: a 600 °C direct exchange with $^{17}\text{O}_2$ and a H_2 reduction at 700 °C followed by a 300 °C oxidation, defined as $\text{Ce}_{0.5}\text{Zr}_{0.5}\text{O}_2$ -1%Pd-600Ex and $\text{Ce}_{0.5}\text{Zr}_{0.5}\text{O}_2$ -1%Pd-700/300-Redox, respectively.

6.5.1 Raman Spectroscopy

Figure 6.14 shows the Raman spectra obtained for (a) the as-prepared $\text{Ce}_{0.5}\text{Zr}_{0.5}\text{O}_2$ -1%Pd, (b) $\text{Ce}_{0.5}\text{Zr}_{0.5}\text{O}_2$ -1%Pd-600Ex and (c) $\text{Ce}_{0.5}\text{Zr}_{0.5}\text{O}_2$ -1%Pd-700/300-Redox. It is apparent that the as prepared state shows very little difference in spectral profile to that seen for the unloaded material seen in Figure 6.8. However, as seen from Appendix A, the $I_D/I_{F_{2G}}$ ratio and peak width Γ of the F_{2G} band are considerably increased from 0.46 to 0.56, and from 162 to 186 cm^{-1} , respectively, both of which imply a more defective system, i.e. the Pd is keeping this system in a more reduced state as expected. Figure 6.14 (b) reveals the following differences from the as prepared state to the $^{17}\text{O}_2$ exchanged system: a reduction in values of $I_D/I_{F_{2G}}$ (0.556 to 0.528) and Γ (186 to 168 cm^{-1}), implying an overall loss in bulk defects. However, $\text{Ce}_{0.5}\text{Zr}_{0.5}\text{O}_2$ -1%Pd-700/300-Redox seen in (c) has a broadened F_{2G} band suggesting the reverse behaviour, i.e. more disorder from a more reduced system after the treatment process. A greater amount of oxygen was removed in the H_2 reduction process and/or less was adsorbed in the ^{17}O reoxidation process, resulting in a more

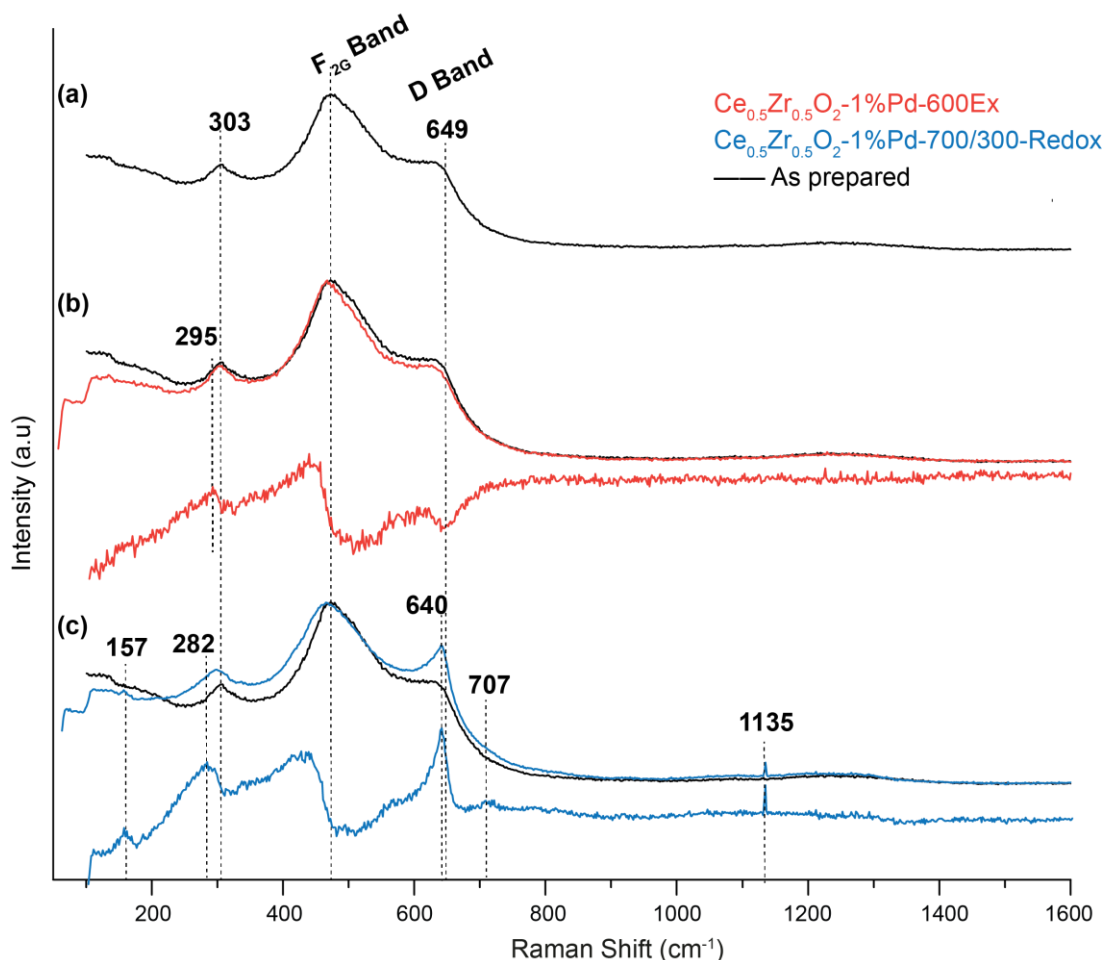


Figure 6.14: Raman spectra of (a) the as prepared $\text{Ce}_{0.5}\text{Zr}_{0.5}\text{O}_2\text{-1\%Pd}$, (b) $\text{Ce}_{0.5}\text{Zr}_{0.5}\text{O}_2\text{-1\%Pd-600Ex}$, (c) $\text{Ce}_{0.5}\text{Zr}_{0.5}\text{O}_2\text{-1\%Pd-700/300-Redox}$. The as-prepared samples are layered underneath (black) the spectra in (b) and (c) and the difference spectra are shown below the corresponding spectra.

deficient system as compared to $\text{Ce}_{0.5}\text{Zr}_{0.5}\text{O}_2\text{-1\%Pd-600Ex}$. Furthermore, $\text{Ce}_{0.5}\text{Zr}_{0.5}\text{O}_2\text{-1\%Pd-700/300-Redox}$ demonstrates a significant distinction by the appearance of a narrow feature at 649 cm^{-1} . As was seen in Figure 6.2, this is characteristic in Raman shift and breadth of a PdO species, indicating that Pd metal particles have been extruded/sintered and oxidised by the $^{17}\text{O}_2$ redox process, whilst there was no evidence of this for $\text{Ce}_{0.5}\text{Zr}_{0.5}\text{O}_2\text{-1\%Pd-600Ex}$. Unfortunately, PdO has a similar vibrational frequency to that of the Frenkel defect in ceria zirconia systems and so it is difficult to say whether there is a loss or gain of this oxygen species.

6.5.2 ^{17}O Solid-State MAS NMR

^{17}O MAS NMR spectra of $\text{Ce}_{0.5}\text{Zr}_{0.5}\text{O}_2\text{-1\%Pd-600Ex}$ acquired at 14.1 T with Hahn echo and single pulse sequences can be seen in Figure 6.15 (a), with the single pulse

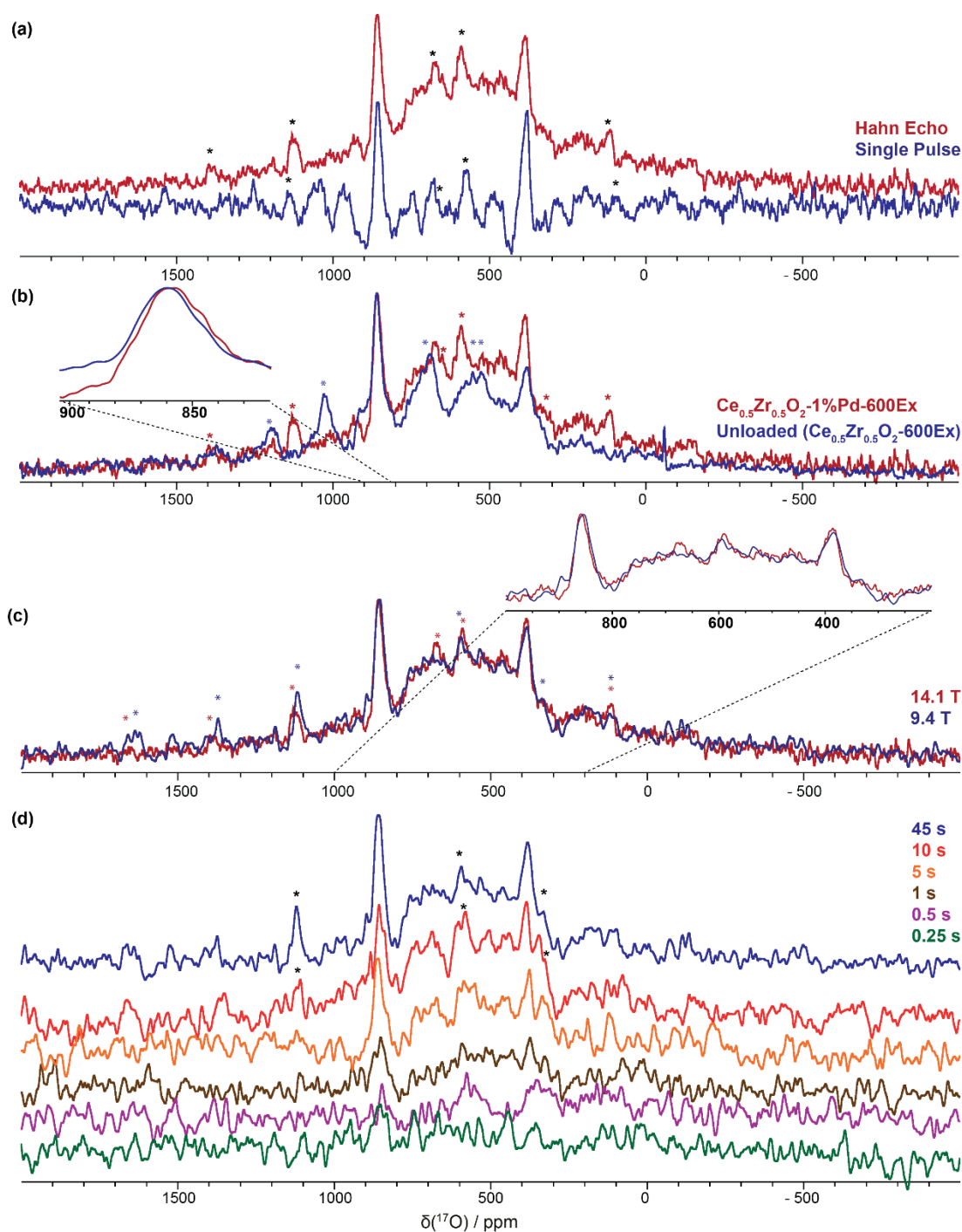


Figure 6.15: ^{17}O MAS NMR spectra of $\text{Ce}_{0.5}\text{Zr}_{0.5}\text{O}_2\text{-1\%Pd-600Ex}$ acquired with a Hahn-echo 90-180 sequence (dark red) with parameters: 45 s recycle delay, $\nu_r = 22$ kHz, 6144 acquisitions compared with (a) a single pulse $\pi/12$ sequence (bottom) with parameters: 45 s recycle delay, $\nu_r = 23$ kHz and 1024 scans, both acquired at 14.1 T, (b) a Hahn echo of the unloaded material: $\text{Ce}_{0.5}\text{Zr}_{0.5}\text{O}_2\text{-600Ex}$ (investigated in Section 6.3) with parameters: $\nu_r = 14$ kHz, 2 s recycle delay and 30,000 scans and single pulse $\pi/12$ sequence with parameters: $\nu_r = 13$ kHz, 45 s recycle delay and 1654 scans. Inset shows the OCe_4 resonance and (c) a Hahn echo acquired at 9.4 T, with parameters: $\nu_r = 14$ kHz, 45 s recycle delay and 8192 scans. (d) Implementing recycle delays of 0.25, 0.5, 1, 5, 10 and 45 s at 9.4 T with parameters $\nu_r = 14$ kHz and 8192 acquisitions. Asterisks denote spinning sidebands.

sequence effectively allowing a T_2 -edit of the spectrum, i.e. broad components for which $T_2 < \text{dead time}$ are removed, with the narrower signals surviving in the FID (as explained in Chapter 4). This is clear from the dip in the baseline for the single pulse spectrum (no baseline correction has been implemented), which is further complicated by baseline distortion manifested from the electronic ringing (sinc wiggles breaking up the broad-line intensity). The Hahn echo data allows detection of this broad (~ 120 kHz) underlying component. Both spectra are dominated by the two bulk oxygen environments pertaining to OCe_4 and OZr_4 units at 858 and 383 ppm, respectively in addition to the broad signal that has already been attributed to oxygen bonded directly to Ce^{3+} .

Figure 6.15 (b) overlays $\text{Ce}_{0.5}\text{Zr}_{0.5}\text{O}_2\text{-1\%Pd-600Ex}$ with the spectrum of the unloaded material seen in Section 6.3 (acquired under the same conditions with the exception of spinning speed). The spectral profiles are very similar but differ in relative intensity of the broad underlying component, suggesting that less $^{17}\text{O-Ce}^{3+}$ bonds exist in this system. The Raman spectral differences discussed in Section 6.4 suggested that $\text{Ce}_{0.5}\text{Zr}_{0.5}\text{O}_2\text{-1\%Pd-600Ex}$ was in a more reduced state than $\text{Ce}_{0.5}\text{Zr}_{0.5}\text{O}_2\text{-600Ex}$. The experimental observations are in agreement with the role of Pd maintaining a reduced system, and therefore the spectral differences in (b) are attributed to less Ce^{3+} concentration in the entire system. Furthermore, bulk ceria appears at 858 ppm, which is 1 ppm more shielded than the unloaded sample (apparent from the inset). This increased shielding indicates a contraction of the unit cell, implying that some Pd, has been incorporated into the lattice (due to a smaller Pd^{2+} cation size).

It has been seen that Zr acts to distort the lattice, Zr-O bonds are known to have covalency associated with their bonding, and furthermore, Pd may also be entering the structure. An EFG great enough to induce a coupling with the quadrupole moment of the ^{17}O nucleus could therefore be anticipated. In order to ascertain if quadrupolar coupling is influencing the resonances observed for $\text{Ce}_{0.5}\text{Zr}_{0.5}\text{O}_2\text{-1\%Pd}$, a Hahn echo spectrum was acquired at 9.4 T (with the same acquisition parameters), and is layered underneath the spectrum acquired at 14.1 T in Figure 6.15 (c). Recall that measurements of pure ceria (H_2^{17}O Ceria, H_2^{17}O Ceria and HSA20) in Chapter 5, demonstrated negligible shifts/broadening at lower field,

implying highly ionic systems. Whilst this appears to be the case from the full spectral width plots, the inset expanded between 200 and 1000 ppm reveals small (~ 3 ppm) shifts to lower ppm and some broadening (~ 300 Hz). Further work is needed to ascertain that these shifts are not the result of (1) Curie dependence caused by differences in temperature (due to the use of different spinning speeds) as seen in Section 5.10, or (2) an evolution in the oxygen environments with time/heating of the NMR experiments as seen in Section 5.5.

The S/N ratio of $\text{Ce}_{0.5}\text{Zr}_{0.5}\text{O}_2\text{-1\%Pd}$ is insufficient to allow the acquisition of T_1 measurements. Instead, spectra were acquired at 9.4 T with recycle delays of 0.25, 0.5, 1, 5, 10, and 45 s, as is shown in Figure 6.15 (d), in effect T_1 -editing the spectrum. Whilst S/N is still low, it is apparent that the broad component has relaxed after a 1 s delay, and the narrow signals of bulk OCe_4 and OZr_4 and corresponding sidebands show substantial intensity increases between 10 and 45 s. These differences corroborate a relaxation mechanism that is characteristic of a paramagnetic interaction. For example, in the ^{27}Al MAS NMR study of Ce^{3+} -doped YAG conducted by George *et al*, a T_1 of 0.14 s is measured for the peak attributed to Al in the first shell from Ce^{3+} , i.e. two bonds away through oxygen ($\text{Ce}^{3+}\text{-O-Al}$). The approximate T_1 here for a directly bonded Ce^{3+} appears long at first glance, however as seen in Chapter 5, bulk OCe_4 T_1 values are long (<30 s) whereas those of bulk oxygen in YAG are just 6.6 s.

The ^{17}O MAS NMR data of $\text{Ce}_{0.5}\text{Zr}_{0.5}\text{O}_2\text{1\%Pd-700/300-Redox}$ can be seen in Figure 6.16 (a), where Hahn-echo and single pulse spectra are overlayed. It is evident from the single pulse spectrum (light blue), acquired with a 45 s recycle delay, that the bulk resonance of OCe_4 , ordinarily characterised by a relatively narrow and slow-relaxing signal, is substantially reduced in intensity relative to the $\text{Ce}_{0.5}\text{Zr}_{0.5}\text{O}_2\text{1\%Pd-600-Ex}$ (investigated above and which is reprinted in Figure 6.16 (b) to assist comparison). On this basis, the Hahn-echo spectrum of $\text{Ce}_{0.5}\text{Zr}_{0.5}\text{O}_2\text{1\%Pd-700/300-Redox}$ shown in (a) was acquired with a 2 s delay to increase the number of acquisitions (and thus S/N), spectrally editing for the shorter-lived components.

With the exception of OCe_4 environments, the spectral profiles in (b) of $\text{Ce}_{0.5}\text{Zr}_{0.5}\text{O}_2\text{1\%Pd-700/300-Redox}$ and $\text{Ce}_{0.5}\text{Zr}_{0.5}\text{O}_2\text{1\%Pd-600-Ex}$ are similar, i.e.

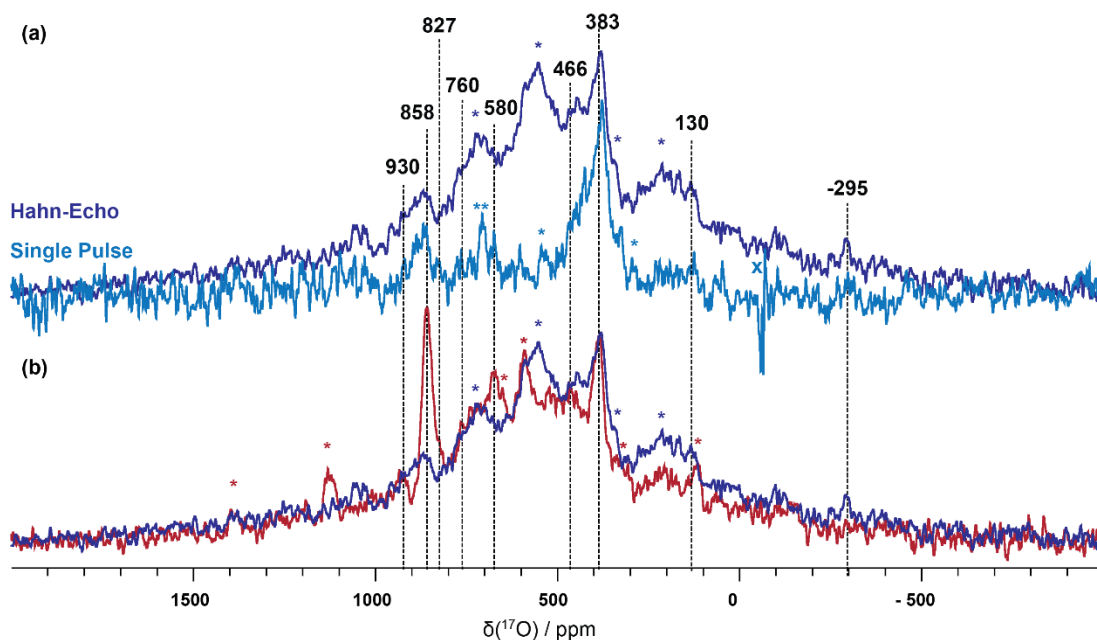


Figure 6.16: ^{17}O MAS NMR spectra acquired at 14.1 T of $\text{Ce}_{0.5}\text{Zr}_{0.5}\text{O}_2\text{-1\%Pd-700/300-Redox}$ with Hahn-Echo 90-180 sequence (dark blue) with parameters: $\nu_r=14$ kHz, 2 s recycle delay and 30,000 scans overlayed with (a) $\text{Ce}_{0.5}\text{Zr}_{0.5}\text{O}_2\text{-1\%Pd-700/300-Redox}$ acquired with a single pulse $\pi/12$ sequence (light blue) with parameters: $\nu_r=13$ kHz, 45 s recycle delay and 1654 scans and (b) $\text{Ce}_{0.5}\text{Zr}_{0.5}\text{O}_2\text{-1\%Pd-600Ex}$ from Figure 6.15 using a Hahn-echo 90-180 sequence (red) with parameters: 45 s recycle delay, $\nu_r=22$ kHz, 6144 acquisitions. Asterisks denote spinning sidebands, X is a spurious signal.

relative quantities of OZr_4 species at 383 ppm in addition to the broad component. These limited observations allow the inference of two conclusions. Firstly, in contrast to the $^{17}\text{O}_2$ direct exchange at 600 °C, the $^{17}\text{O}_2$ redox method is insufficient to exchange ^{17}O with oxygen in points of high symmetry, i.e. lattice environments far from defects. Secondly, due to the increasingly paramagnetic nature of these systems that are more representative of a TWC (greater Pd loadings and Zr incorporations promote Ce^{3+}), more sophisticated ^{17}O NMR techniques, alongside preparation procedures that allow greater ^{17}O incorporation are necessary.

Chapter 7

Conclusions

A < 2 nm ceria sample synthesized via a H_2^{17}O route (in which ^{17}O is free to occupy any site), depicted a significant lattice expansion via the (Raman observed) $\text{F}_{2\text{G}}$ position of 450 cm^{-1} , which was corroborated by its defect ratio ($I_{\text{D}} / I_{\text{F}_{2\text{G}}}$) of 0.174, a ratio normally associated with a treatment-reduced structure. The expansion is due to the presence of the larger Ce^{3+} cation in the lattice, in addition to strain effects at the surface. This analysis supported the assignment of a significant, field-dependent anisotropy, observed in the ^{17}O solid-state MAS NMR spectrum, to $^{17}\text{O}\text{-Ce}^{3+}$ bonds, or more specifically, to the dipolar interaction between ^{17}O and the free electron. Deconvolution of the ^{17}O spectrum revealed a narrow, deshielded line at $\delta_{\text{CG}} = 873\text{ ppm}$, on top of a broad, shielded component at $\delta_{\text{CG}} = 858\text{ ppm}$, which were assigned to bulk and surface OCe_4 species, respectively. When heated at $500\text{ }^\circ\text{C}$ in air (4.7 nm particle size) a significant loss of intrinsic defects (by an order of magnitude) was observed, which is likely the result of oxygen recombining with vacancies, and the annihilation of the Frenkel pair. In this latter case, oxygen can occupy the octahedral site in the sublattice until exposed to high temperatures, which provides the necessary energy to overcome the potential barrier out of the octahedral site and into the more confined, tetrahedral site. Furthermore, the ^{17}O label is lost, evident by the single narrow peak at $\delta_{\text{CG}} = 876\text{ ppm}$, most likely pertaining to the natural abundant bulk ^{17}O .

HSA20 is a ceria powder used for research purposes by Johnson Matthey, with a particle size of 5.8 nm, and a polyhedral morphology dominated by $\{111\}$ and $\{100\}$

surfaces. Chapter 3 reviewed the current literature of ^{17}O NMR measurements of ceria, where the typical ^{17}O enrichment procedure involved heating a sample with $^{17}\text{O}_2$. For comparison, HSA20 was heated at 600 °C at sub ambient pressure, and the Raman spectrum revealed a Ce^{4+} reduction, in addition to the formation of surface hydroxyls. ^{17}O NMR demonstrated a different spectral profile for HSA20 from those seen in the literature (for pure nanoceria), with observation of the surface appearing in a more shielded position, as seen for H_2^{17}O Ceria. The preparation conditions of ceria are important in determining its chemical structural state, and thus its spectroscopic profiles. To investigate this, a novel process was implemented in which ceria is reduced at elevated temperature, under H_2 conditions, followed by a $^{17}\text{O}_2$ soaking process.

Firstly, the reduction temperature is examined. In situ Raman spectroscopy of the reduction process up to 571 °C emphasizes that Raman spectroscopy is a structural probe that is sensitive to the surface and not representative of the bulk sample state (H_2 -TPR demonstrated bulk reduction for HSA20 begins above 700 °C). A rarely seen feature at 400 cm^{-1} ascribed by Agarwal¹⁴ *et al.* as a Ce-O_x unit ($5 < x < 8$), is clearly observed to gradually disappear up to 571 °C. Furthermore a recently reassigned band as a Ce-OH species at 246 cm^{-1} , made by Filtschew *et al.*¹⁰⁹ is supported by the results here; the band appears to firstly increase in intensity and disappears at 571 °C. This is rationalised by a disassociation of H_2O followed by the formation of hydroxyl groups at lower temperatures, and eventually desorption at higher temperatures. Changes to the defect band region (between 550 and 600 cm^{-1}) suggested a loss of the Frenkel defect which coincided with an increase of the vacancy band.

TPR measurements of HSA20 indicate full surface reduction by 700 °C, with different states of reduction at 500 and 300 °C. These three temperatures are used to reduce HSA20, followed by $^{17}\text{O}_2$ heating at 300 °C. Raman spectra of these reoxidised systems identify a correlation with the band at 400 cm^{-1} to particle size and reoxidation, and it is therefore cautiously assigned as a low-coordination surface environment that is released and adsorbed in the redox process. The ^{17}O NMR data for these preparations reveal exceptionally broad underlying signals, ascribed to O-Ce^{3+} direct bonding (previously seen⁹⁷), large sideband manifolds which is indicative

of paramagnetic anisotropy, in addition to three O-H species at $\delta_{\text{CG}} = 324, 277,$ and 227 ppm. The key result however, is the significant difference in spectral profiles between the higher reduction temperatures, for which full surface reduction is achieved, compared to the lower reduction temperatures that result in partial reduction only. A more quantitative spectrum is achieved by folding in the spinning sidebands for each site, from which it is apparent that the probability of ^{17}O achieving bulk positions, i.e. high symmetry, reduces as the reduction temperature increases, indicating that defects are defining the ^{17}O spectra. It appears that spectra dominated by resonances at ~ 1030 and (less so) 920 ppm distinguish oxygen deficient systems.

To explore the effects of full surface reduction (at 700°C) further, reoxidation temperatures were then varied ($300, 150$ and 25°C). The Raman spectra show almost negligible changes under these conditions, however it was inferred that the greater intensity of the Frenkel signal indicated that a higher reoxidation temperature enabled a greater incorporation of ^{17}O to enter these sites. The ^{17}O MAS NMR data corroborates this process as greater reoxidation is achieved at 300°C , with very little oxygen re-entering the structure at room temperature and 150°C . The inhibited reoxidation process (at low temperatures and pressures) has been identified as a surface reorganisation mechanism, originally proposed by Binet *et al.*¹³² Samples are therefore observed by ^{17}O NMR in an oxygen deficient state.

Sample evolutions of these systems are significant. Within the rotor, the high mobility of the adsorbed ^{17}O probes in relation to the defects can be observed overtime (months). This effect is enhanced when the sample is exposed to air, in which H_2O is seen to exchange with the surface.

To investigate the redox effects as a function of particle size, larger, octahedral >25 nm ceria particles obtained from Sigma Aldrich (SA) were studied via the same sample conditions as HSA20: by a direct $^{17}\text{O}_2$ exchange and a $^{17}\text{O}_2$ redox process (reoxidation at $300, 150$ and 25°C). ^{17}O exchange is very successful at 600°C for the SA particles, with the ^{17}O MAS NMR spectrum dominated by bulk oxygen exchange, and small contributions of defect-associated signals. A similar result is seen for the $^{17}\text{O}_2$ redox experiment (reoxidised at 300°C), with less ^{17}O uptake apparent, but the presence of the signal at 1030 ppm infers some oxygen deficiency.

To compare the $^{17}\text{O}_2$ redox (^{17}O reoxidation at 150 and 300 °C) effects of ceria with different morphologies, i.e. different exposed surface facets, the effects of the redox process on 8x80 nm nanorods and 17.1 nm nanocubes, were explored. After heating, sintering is observed in both morphologies, however, the rods maintain their 8 nm width. It is interesting that this morphology at low reoxidation temperature (150 °C) also maintains a more reduced state after the treatment, as established by the Raman and ^{17}O MAS spectra. ^{17}O MAS spectral profiles of the rods are similar to those seen for HSA20 and the SA particles, however, the cubes depict (largely) the single crystallographic site, with very small contributions from shifted positions. Nevertheless, whilst having more reactive surfaces, both morphologies still exhibit surface reorganisation, with a dramatic increase in ^{17}O reoxidation apparent at 300 °C.

Throughout the Raman spectra acquired across all samples, there is evidence of stable peroxides on the ceria surfaces. In order to ascertain whether any of the observed ^{17}O resonances were attributed to these intermediate reoxidation species, a stable-peroxo ceria sample was synthesized via H_2O_2 (enriched by a direct combination of H_2 and $^{17}\text{O}_2$). Whilst Raman spectroscopy confirmed the presence of the peroxide on the surface at 832 cm^{-1} , the peroxide was not observed with the conventional ^{17}O MAS NMR parameters used for acquisition throughout the chapter. Peroxides are therefore unrelated to the unassigned resonances present in the ^{17}O spectra of the other ceria systems. Furthermore, the peroxide was unstable under the conditions of the MAS experiment preventing further investigations to determine its resonance position.

In order to establish the presence of the Frenkel defect in the ^{17}O NMR spectra of the ceria systems, ^{17}O NMR parameters were calculated by DFT of a model $\text{Ce}_{108}\text{O}_{216}$ unit cell, in which a single oxygen was positioned in the usually vacant central site, and an oxygen adjacent to it removed from the lattice position, thus creating the Frenkel-pair. The calculated ^{17}O lineshapes for each oxygen were simulated by the software Simpson, in which spectra at 14.1 and 9.4 T were simulated. The results reveal a surprisingly profound effect on the symmetry of the structure. The oxygen pertaining to the Frenkel defect gives rise to the most shielded position at $\delta_{\text{CG}} = 822\text{ ppm}$, in keeping with its increasing coordination (OCe_6), with

additional resonances forming distinct regions at $\delta_{\text{CG}} = 825, 845, 910$, and 920 ppm, in addition to resonances either side of the bulk position (which would manifest as broadening/underlying components). These chemical shift regions can be accounted for in the ^{17}O experimental data of the ceria systems, with the exception of the resonance at $\delta_{\text{CG}} = 1030$ ppm, which has already been attributed to oxygen deficiency in the ceria samples.

An oxygen deficient system implies the presence of Ce^{3+} , and therefore HSA20 was probed for the presence of this paramagnetic centre. Magnetic measurements revealed a room temperature ferromagnetic (RTFM) response, the causes for which confirm the presence of the Ce^{3+} cation.^{152,153,154} Variable temperature ^{17}O NMR techniques were employed to verify a Curie dependence ($1/T$) of the ^{17}O resonances. Between -20 °C and $+58$ °C, peak shifts (upfield) of 2.7, 3.0 and 3.5 ppm were observed for the bulk oxygen (876 ppm), Frenkel defect (828 ppm) and the environment associated with the corresponding vacancy (921 ppm), respectively. The effects of a lattice expansion (caused by heating) were investigated by DFT calculations of the theoretical ^{17}O shifts and show a linear trend of increasing isotropic chemical shift with increasing lattice parameter. Whilst a 2 ppm shift was predicted for this temperature range for the bulk environment, this is not enough to account for the behaviour of the resonances attributed to the Frenkel-pair. Furthermore, for the case of Ce:YAG systems,^{75,106,107} the Ce^{3+} cation is seen to influence ^{27}Al resonances (from the diamagnetic positions) even at a distance of five bonds away. It is therefore determined that the ($1/T$) Curie dependence of the ^{17}O resonances is evidence of oxygen environments experiencing through-space paramagnetic Ce^{3+} cations that are near enough to the ^{17}O resonances observed to perturb their chemical environment.

The additional resonances in the ceria spectrum (additional to the single crystallographic lattice oxygen of the $Fm3m$ structure at ~ 877 ppm) seen at circa 1030/1040, 920 and 830 are thus assigned to oxygen that experience the perturbations induced by the defective ceria lattice.

Chapter 6 investigates systems that are more typical of a TWC, i.e. ceria loaded with a PGM metal and/or the incorporation of zirconia, also by ^{17}O MAS NMR, alongside

Raman spectroscopy. Due to the nature of these materials, i.e. an increased defect density, the increase in Ce^{3+} greatly complicates the ^{17}O NMR spectra.

In extension to the ceria systems probed in Chapter 5, HSA20, along with ceria rods and cubes, are studied with a 1% wt Pd loading. TPR reveals the anticipated behaviour of oxygen removal at lower temperatures for the 1% wt Pd loaded systems, with a greater modification seen for the {100} terminated cube systems, determined elsewhere¹⁰¹ as a result of reverse oxygen spillover. Analogous to Chapter 5, the materials are prepared via the $^{17}\text{O}_2$ redox experiments, with reoxidation temperatures of 300 and 150 °C implemented. The Raman spectra suggest that the low reoxidation temperature of 150 °C is insufficient to reoxidise the loaded HSA20 system, analogous to the behaviour observed for its unloaded counterpart, whereas at 300 °C, the system resembles the as-prepared state. The 1% Pd loaded cubes show the reverse behaviour. The significantly low reduction temperature of their surface oxygen (starts at 280 °C) prompts a re-reduction of the surface oxygen when the temperature of the reoxidation process reaches 300 °C, so that after the redox process, they are more oxygen deficient than the as-prepared state. The surface reduction of the 1% Pd loaded rods is not within this regime (<300 °C), revealing a less defective state after the $^{17}\text{O}_2$ redox process.

It was further proposed that the Raman measurements elucidated a Pd-extrusion from the HSA20 system after the $^{17}\text{O}_2$ treatments, indicating that the Pd was previously incorporated as a solid solution or formed a Ce-Pd-O ionic interaction with the surface (but Pd extrusion is not seen for the rods or cubes). The Ce-OH band at $\sim 250\text{ cm}^{-1}$ was evident for these Pd loaded systems, showing a clear intensity correlation with surface area.

Interestingly, a considerably broadened $\text{F}_{2\text{G}}$ band (52 cm^{-1}) was observed for the as-prepared rods with 1% Pd loading. It has been previously suggested that the breadth of the $\text{F}_{2\text{G}}$ band correlates with particle size. Given that the rods have an 8 nm width and they are larger than many of the ceria particles studied in this work, this would contradict this observation. Filtschew *et al.* have proposed that the width of the $\text{F}_{2\text{G}}$ cannot be used to accurately determine particle size, but can be used to interpret defect concentrations for a given particle size,¹⁰⁹ observations that thus validated by the current work.

The ^{17}O MAS NMR data for Pd loaded HSA20 also reveals that a surface reorganisation mechanism exists between 150 and 300 °C, with a significant incorporation of ^{17}O observed for the latter, relative to the unloaded HSA20. Moreover, a sideband manifold extending <3000 ppm is observed in the latter case, for a peak observed at 1035 ppm, again implying the proximity of Ce^{3+} with this oxygen environment. Interestingly, the nature of this oxygen environment is unique to HSA20; the interaction causing its sideband manifold is not seen for the rods or cubes. With the exception of enhanced ^{17}O uptake however, and a resonance cautiously assigned to PdO, the ^{17}O spectral profile of the loaded systems appears identical to the unloaded analogues. It can be concluded for the Pd loaded ceria materials, that whilst the addition of Pd to ceria lowers the reduction temperature, it stabilises this reduced state, increasing the temperature at which reoxidation occurs.

Ceria zirconia systems are regarded for their ability to release more bulk oxygen (implying a greater OSC is available), and inhibition of particle sintering. The investigation of $\text{Ce}_{0.75}\text{Zr}_{0.25}\text{O}_2$, $\text{Ce}_{0.5}\text{Zr}_{0.5}\text{O}_2$ and $\text{Ce}_{0.25}\text{Zr}_{0.75}\text{O}_2$ followed the methods outlined for the pure ceria systems: $^{17}\text{O}_2$ direct exchange at 600 °C and $^{17}\text{O}_2$ Redox experiments (reoxidation at 150 and 300 °C). The tetragonal $\text{Ce}_{0.25}\text{Zr}_{0.75}\text{O}_2$ structure demonstrates a lower OSC over the materials with greater Ce concentrations, and thus the cubic phases of $\text{Ce}_{0.75}\text{Zr}_{0.25}\text{O}_2$ and $\text{Ce}_{0.5}\text{Zr}_{0.5}\text{O}_2$ are favoured in this work. Raman spectroscopy is able to identify the pseudo cubic phase t' (there is a translation of oxygen along one axis) present in $\text{Ce}_{0.25}\text{Zr}_{0.75}\text{O}_2$, the ability of which eludes PXRD. Moreover, solid solutions are confirmed by the red shift of the $\text{F}_{2\text{G}}$ mode, implying incorporation of the smaller Zr^{4+} cation into the lattice.

To elucidate Raman spectral changes between the as-prepared and post-treatment sample states, difference spectra are considered. The Raman spectra of $\text{Ce}_{0.75}\text{Zr}_{0.25}\text{O}_2$ and $\text{Ce}_{0.5}\text{Zr}_{0.5}\text{O}_2$ exchanged at 600 °C reveal an increase in oxygen vacancies in the former system, and an attenuation of the defect region in the latter, indicating the loss of the Frenkel interstitial. Both of their $\text{F}_{2\text{G}}$ bands exhibit red shifts relative to the as prepared sample, characterising reduction. Surprisingly, the ^{17}O NMR profiles are markedly different, for which $\text{Ce}_{0.75}\text{Zr}_{0.25}\text{O}_2$ is dominated by a bulk-like OCe_4 signal at 869 ppm. The lower shift here (compared to ceria) is indicative of

the incorporation of Zr into the lattice, decreasing the lattice parameter. $\text{Ce}_{0.5}\text{Zr}_{0.5}\text{O}_2$ on the other hand is defined by an intense, broad signal, attributed to direct O- Ce^{3+} bonding located between the OCe_4 and OZr_4 chemical shift ranges. In comparison, the $^{17}\text{O}_2$ redox process for $\text{Ce}_{0.75}\text{Zr}_{0.25}\text{O}_2$ and $\text{Ce}_{0.5}\text{Zr}_{0.5}\text{O}_2$ revealed significantly different profiles, complicated by the presence of broad components.

As the acquisition of ^{17}O MAS NMR spectra for a 1 % wt Pd loaded $\text{Ce}_{0.5}\text{Zr}_{0.5}\text{O}_2$ system yielded similar results, it is determined that ^{17}O NMR observation for ceria zirconia systems that are prepared by these $^{17}\text{O}_2$ techniques no longer allow clear interpretation of the oxygen environments, due to the complications of increasing paramagnetic centres. As the ^{17}O incorporation achieved using the enrichment procedure detailed here (where pressure was limited to 1 atm) is relatively low, adaption of this procedure to facilitate greater exchange could ameliorate this.

The ^{17}O solid-state NMR results shown in this thesis demonstrate ceria's sensitivity to its preparation and treatment conditions. Chapter 3 emphasized the importance of these conditions to the interpretation of the NMR spectra, highlighting the need for a better understanding of ceria's operating properties. As a result of this work, ^{17}O solid-state NMR measurements via the techniques shown here have since been adopted by Johnson Matthey.

References

- 1 Harrison, B., Diwell, A. F. & Hallett, C. Promoting Platinum Metals by Ceria. *Platinum Metals Review* **32**, 73-83 (1988).
- 2 Abanades, S. & Flamant, G. Thermochemical hydrogen production from a two-step solar-driven water-splitting cycle based on cerium oxides. *Solar Energy* **80**, 1611-1623, (2006).
- 3 Kirk, T. J. & Winnick, J. A Hydrogen Sulfide Solid-Oxide Fuel Cell Using Ceria-Based Electrolytes. *Journal of The Electrochemical Society* **140**, 3494-3496, (1993).
- 4 Corma, A., Atienzar, P., Garcia, H. & Chane-Ching, J.-Y. Hierarchically mesostructured doped CeO₂ with potential for solar-cell use. *Nat Mater* **3**, 394-397 (2004).
- 5 Jasinski, P., Suzuki, T. & Anderson, H. U. Nanocrystalline undoped ceria oxygen sensor. *Sensors and Actuators B: Chemical* **95**, 73-77, (2003).
- 6 Montini, T., Melchionna, M., Monai, M. & Fornasiero, P. Fundamentals and Catalytic Applications of CeO₂-Based Materials. *Chemical Reviews* **116**, 5987-6041, (2016).
- 7 Gagnon, J. *et al.* Integrating silver compounds and nanoparticles into ceria nanocontainers for antimicrobial applications. *Journal of Materials Chemistry B* **3**, 1760-1768, (2015).
- 8 Tian, Z. *et al.* Highly sensitive and robust peroxidase-like activity of porous nanorods of ceria and their application for breast cancer detection. *Biomaterials* **59**, 116-124, (2015).
- 9 Aneggi, E., Boaro, M., Colussi, S., de Leitenburg, C. & Trovarelli, A. in *Handbook on the Physics and Chemistry of Rare Earths* Vol. Volume 50 (ed G. Bünzli and Vitalij K. Pecharsky Jean-Claude) 209-242 (Elsevier, 2016).
- 10 Spanier, J. E., Robinson, R. D., Zhang, F., Chan, S.-W. & Herman, I. P. Size-dependent properties of CeO_{2-y} nanoparticles as studied by Raman scattering. *Physical Review B* **64**, 245407 (2001).
- 11 Kosacki, I., Suzuki, T., Anderson, H. U. & Colomban, P. Raman scattering and lattice defects in nanocrystalline CeO₂ thin films. *Solid State Ionics* **149**, 99-105, (2002).
- 12 Mamontov, E., Egami, T., Brezny, R., Koranne, M. & Tyagi, S. Lattice Defects and Oxygen Storage Capacity of Nanocrystalline Ceria and Ceria-Zirconia. *The Journal of Physical Chemistry B* **104**, 11110-11116, (2000).
- 13 Mamontov, E. & Egami, T. Structural defects in a nano-scale powder of CeO₂ studied by pulsed neutron diffraction. *Journal of Physics and Chemistry of Solids* **61**, 1345-1356, (2000).
- 14 Agarwal, S., Zhu, X., Hensen, E. J. M., Lefferts, L. & Mojet, B. L. Defect Chemistry of Ceria Nanorods. *The Journal of Physical Chemistry C* **118**, 4131-4142, (2014).
- 15 Agarwal, S., Zhu, X., Hensen, E. J. M., Mojet, B. L. & Lefferts, L. Surface-Dependence of Defect Chemistry of Nanostructured Ceria. *The Journal of Physical Chemistry C* **119**, 12423-12433, (2015).
- 16 Wu, Z., Li, M., Howe, J., Meyer, H. M. & Overbury, S. H. Probing Defect Sites on CeO₂ Nanocrystals with Well-Defined Surface Planes by Raman Spectroscopy and O₂ Adsorption. *Langmuir* **26**, 16595-16606, (2010).
- 17 Sakata, M., Mori, R., Kumazawa, S., Takata, M. & Toraya, H. Electron-density distribution from X-ray powder data by use of profile fits and the maximum-entropy method. *Journal of Applied Crystallography* **23**, 526-534, (1990).
- 18 Xu, J. *et al.* Size dependent oxygen buffering capacity of ceria nanocrystals. *Chemical Communications* **46**, 1887-1889, (2010).
- 19 Liu, X., Zhou, K., Wang, L., Wang, B. & Li, Y. Oxygen Vacancy Clusters Promoting Reducibility and Activity of Ceria Nanorods. *Journal of the American Chemical Society* **131**, 3140-3141, (2009).

- 20 Namai, Y., Fukui, K.-i. & Iwasawa, Y. Atom-Resolved Noncontact Atomic Force Microscopic Observations of CeO₂(111) Surfaces with Different Oxidation States: Surface Structure and Behavior of Surface Oxygen Atoms. *The Journal of Physical Chemistry B* **107**, 11666-11673, (2003).
- 21 Sayle, T. X. T., Parker, S. C. & Catlow, C. R. A. The role of oxygen vacancies on ceria surfaces in the oxidation of carbon monoxide. *Surface Science* **316**, 329-336, (1994).
- 22 Wu, Z. & Overbury, S. H. *Catalysis by Materials with Well-Defined Structures*. (Elsevier Inc., 2015).
- 23 Yao, H. C. & Yao, Y. F. Y. Ceria in automotive exhaust catalysts. *Journal of Catalysis* **86**, 254-265, (1984).
- 24 Trovarelli, A. Catalytic Properties of Ceria and CeO₂-Containing Materials. *Catalysis Reviews* **38**, 439-520, (1996).
- 25 Johnson, M. F. L. & Mooi, J. Cerium dioxide crystallite sizes by temperature-programmed reduction. *Journal of Catalysis* **103**, 502-505, (1987).
- 26 Grau-Crespo, R., Leeuw, N., Hamad Gomez, S. & Waghmare, U. *Phase Separation and Surface Segregation in Ceria-Zirconia Solid Solutions*. (2010).
- 27 Sugiura, M. Oxygen Storage Materials for Automotive Catalysts: Ceria-Zirconia Solid Solutions. *Catalysis Surveys from Asia* **7**, 77-87, (2003).
- 28 Dole, H. A. E., Costa, A. C. G. S. A., Couillard, M. & Baranova, E. A. Quantifying metal support interaction in ceria-supported Pt, PtSn and Ru nanoparticles using electrochemical technique. *Journal of Catalysis* **333**, 40-50, (2016).
- 29 Yeung, C. M. Y. *et al.* Engineering Pt in Ceria for a Maximum Metal-Support Interaction in Catalysis. *Journal of the American Chemical Society* **127**, 18010-18011, (2005).
- 30 Kašpar, J., Fornasiero, P. & Graziani, M. Use of CeO₂-based oxides in the three-way catalysis. *Catalysis Today* **50**, 285-298, (1999).
- 31 Trovarelli, A. *et al.* Rh-CeO₂ interaction induced by high-temperature reduction. Characterization and catalytic behaviour in transient and continuous conditions. *Journal of the Chemical Society, Faraday Transactions* **88**, 1311-1319, (1992).
- 32 Acerbi, N., Tsang, S. C. E., Jones, G., Golunski, S. & Collier, P. Rationalization of Interactions in Precious Metal/Ceria Catalysts Using the d-Band Center Model. *Angewandte Chemie International Edition* **52**, 7737-7741, (2013).
- 33 Tauster, S. J., Fung, S. C. & Garten, R. L. Strong metal-support interactions. Group 8 noble metals supported on titanium dioxide. *Journal of the American Chemical Society* **100**, 170-175, (1978).
- 34 Tauster, S. J. Strong metal-support interactions. *Accounts of Chemical Research* **20**, 389-394, (1987).
- 35 Bruix, A. *et al.* Effects of deposited Pt particles on the reducibility of CeO₂(111). *Physical Chemistry Chemical Physics* **13**, 11384-11392, (2011).
- 36 Thompsett, D. & Tsang, S. C. E. Effects of Completely Encapsulating Platinum in Ceria. *Platinum Metals Review* **50**, 21-21, (2006).
- 37 Gulyaev, R. V. *et al.* The local structure of Pd_xCe_{1-x}O_{2-x-δ} solid solutions. *Physical Chemistry Chemical Physics* **16**, 13523-13539, (2014).
- 38 Baylet, A. *et al.* In situ Raman and in situ XRD analysis of PdO reduction and Pd[degree] oxidation supported on [gamma]-Al₂O₃ catalyst under different atmospheres. *Physical Chemistry Chemical Physics* **13**, 4607-4613, (2011).
- 39 Kurnatowska, M., Kepinski, L. & Mista, W. Structure evolution of nanocrystalline Ce_{1-x}Pd_xO_{2-y} mixed oxide in oxidizing and reducing atmosphere: Reduction-induced activity in low-temperature CO oxidation. *Applied Catalysis B: Environmental* **117**, 135-147, (2012).

- 40 Tsunekawa, S., Sivamohan, R., Ito, S., Kasuya, A. & Fukuda, T. Structural study on monosize CeO_{2-x} nano-particles. *Nanostructured Materials* **11**, 141-147, (1999).
- 41 Tsunekawa, S., Ito, S. & Kawazoe, Y. Surface structures of cerium oxide nanocrystalline particles from the size dependence of the lattice parameters. *Applied Physics Letters* **85**, 3845-3847, (2004).
- 42 Zhang, F. *et al.* Cerium oxide nanoparticles: Size-selective formation and structure analysis. *Applied Physics Letters* **80**, 127-129, (2002).
- 43 Wu, L. *et al.* Oxidation state and lattice expansion of CeO_{2-x} nanoparticles as a function of particle size. *Physical Review B* **69**, 125415 (2004).
- 44 Baranchikov, A. E., Polezhaeva, O. S., Ivanov, V. K. & Tretyakov, Y. D. Lattice expansion and oxygen non-stoichiometry of nanocrystalline ceria. *CrystEngComm* **12**, 3531-3533, (2010).
- 45 Kurian, M. & Kunjachan, C. Investigation of size dependency on lattice strain of nanoceria particles synthesised by wet chemical methods. *International Nano Letters* **4**, 73-80, (2014).
- 46 Sun, C., Li, H. & Chen, L. Nanostructured ceria-based materials: synthesis, properties, and applications. *Energy & Environmental Science* **5**, 8475-8505, (2012).
- 47 Sun, C. & Xue, D. Size-dependent oxygen storage ability of nano-sized ceria. *Physical Chemistry Chemical Physics* **15**, 14414-14419, (2013).
- 48 Murota, T., Hasegawa, T., Aozasa, S., Matsui, H. & Motoyama, M. Production method of cerium oxide with high storage capacity of oxygen and its mechanism. *Journal of Alloys and Compounds* **193**, 298-299, (1993).
- 49 Migani, A., Vayssilov, G. N., Bromley, S. T., Illas, F. & Neyman, K. M. Greatly facilitated oxygen vacancy formation in ceria nanocrystallites. *Chemical Communications* **46**, 5936-5938, (2010).
- 50 Nolan, M., Fearon, J. E. & Watson, G. W. Oxygen vacancy formation and migration in ceria. *Solid State Ionics* **177**, 3069-3074, (2006).
- 51 Bruix, A. *et al.* A New Type of Strong Metal–Support Interaction and the Production of H₂ through the Transformation of Water on Pt/CeO₂(111) and Pt/CeO_x/TiO₂(110) Catalysts. *Journal of the American Chemical Society* **134**, 8968-8974, (2012).
- 52 Zhou, B., Dong, S., Zhao, H. & Wu, P. Effects of electronic modification and structural distortion on ferromagnetism in sputtered CeO₂ films with isovalent Sn⁴⁺ doping. *RSC Advances* **4**, 63228-63233, (2014).
- 53 Askaric, S. *et al.* *F-centre luminescence in nanocrystalline CeO₂*. Vol. 46 (2013).
- 54 W Tasker, P. *The Stability of Ionic Crystals*. Vol. 12 (1979).
- 55 Vyas, S., Grimes, R. W., Gay, D. H. & Rohl, A. L. Structure, stability and morphology of stoichiometric ceria crystallites. *Journal of the Chemical Society, Faraday Transactions* **94**, 427-434, (1998).
- 56 Conesa, J. Computer modeling of surfaces and defects on cerium dioxide. *Surface Science* **339**, 337-352.
- 57 Mai, H.-X. *et al.* Shape-Selective Synthesis and Oxygen Storage Behavior of Ceria Nanopolyhedra, Nanorods, and Nanocubes. *The Journal of Physical Chemistry B* **109**, 24380-24385, (2005).
- 58 López, J. M. *et al.* The prevalence of surface oxygen vacancies over the mobility of bulk oxygen in nanostructured ceria for the total toluene oxidation. *Applied Catalysis B: Environmental* **174**, 403-412, (2015).
- 59 Choi, Y. M., Abernathy, H., Chen, H. T., Lin, M. C. & Liu, M. Characterization of O₂–CeO₂ Interactions Using In Situ Raman Spectroscopy and First-Principle Calculations. *ChemPhysChem* **7**, 1957-1963, (2006).

- 60 Fornasiero, P. *et al.* Rh-Loaded CeO₂-ZrO₂ Solid-Solutions as Highly Efficient Oxygen
Exchangers: Dependence of the Reduction Behavior and the Oxygen Storage
Capacity on the Structural-Properties. *Journal of Catalysis* **151**, 168-177, (1995).
- 61 Fornasiero, P., Kašpar, J. & Graziani, M. On the rate determining step in the reduction
of CeO₂-ZrO₂ mixed oxides. *Applied Catalysis B: Environmental* **22**, L11-L14, (1999).
- 62 Trovarelli, A. & Fornasiero, P. *Catalysis by Ceria and Related Materials*. 2nd edn, Vol.
12 (Imperial College Press, 2013).
- 63 Zhang, F. *et al.* Phases in Ceria-Zirconia Binary Oxide (1-x)CeO₂-xZrO₂
Nanoparticles: The Effect of Particle Size. *Journal of the American Ceramic Society*
89, 1028-1036, (2006).
- 64 Yashima, M., Arashi, H., Kakihana, M. & Yoshimura, M. Raman Scattering Study of
Cubic-Tetragonal Phase Transition in Zr_{1-x}Ce_xO₂ Solid Solution. *Journal of the
American Ceramic Society* **77**, 1067-1071, (1994).
- 65 Preda, G. *et al.* Formation of Superoxide Anions on Ceria Nanoparticles by Interaction
of Molecular Oxygen with Ce³⁺ Sites. *The Journal of Physical Chemistry C* **115**, 5817-
5822, (2011).
- 66 Pushkarev, V. V., Kovalchuk, V. I. & d'Itri, J. L. Probing Defect Sites on the CeO₂
Surface with Dioxygen. *The Journal of Physical Chemistry B* **108**, 5341-5348, (2004).
- 67 Kullgren, J., Hermansson, K. & Broqvist, P. Reactive oxygen species in stoichiometric
ceria: Bulk and low-index surfaces. *physica status solidi (RRL) – Rapid Research
Letters* **8**, 600-604, (2014).
- 68 R. Ernst, R., Bodenhausen, G. & Wokaun, A. *Principles of nuclear magnetic resonance
in one and two dimensions / Richard R. Ernst, Geoffrey Bodenhausen and Alexander
Wokaun*. (1988).
- 69 Haeberlen, U. in *High Resolution Nmr in Solids Selective Averaging* 17-35 (Academic
Press, 1976).
- 70 MacKenzie, K. J. D. & Smith, M. E. *Multinuclear Solid-State Nuclear Magnetic
Resonance of Inorganic Materials*. (Elsevier Science, 2002).
- 71 Grey, C. P., Smith, M. E., Cheetham, A. K., Dobson, C. M. & Dupree, R. Yttrium-89
magic angle spinning NMR study of rare-earth pyrochlores: paramagnetic shifts in
the solid state. *Journal of the American Chemical Society* **112**, 4670-4675, (1990).
- 72 Wang, S. *et al.* Paramagnetic Relaxation Enhancement Reveals Oligomerization
Interface of a Membrane Protein. *Journal of the American Chemical Society* **134**,
(2012).
- 73 in *Solid-State NMR in Materials Science* 191-230 (CRC Press, 2011).
- 74 McCarty, R. J. & Stebbins, J. F. Transition Metal Dopant Cation Distributions in MgO
and CaO: New Inferences from Paramagnetically Shifted Resonances in ¹⁷O, ²⁵Mg,
and ⁴³Ca NMR Spectra. *The Journal of Physical Chemistry C* **120**, 11111-11120,
(2016).
- 75 George, N. C. *et al.* Local Environments of Dilute Activator Ions in the Solid-State
Lighting Phosphor Y_{3-x}Ce_xAl₅O₁₂. *Chemistry of Materials* **25**, 3979-3995, (2013).
- 76 Smith, E. & Dent, G. in *Modern Raman Spectroscopy – A Practical Approach* 71-92
(John Wiley & Sons, Ltd, 2004).
- 77 Cowan, B. *Nuclear Magnetic Resonance and Relaxation*. (Cambridge University
Press, 1997).
- 78 Man, P. P. in *Encyclopedia of Analytical Chemistry* (John Wiley & Sons, Ltd, 2006).
- 79 L Bryce, D. *et al.* *Practical Aspects of Modern Routine Solid-State Multinuclear
Magnetic Resonance Spectroscopy: One-Dimensional Experiments*. Vol. 46 (2001).
- 80 Hore, P., Jones, J. & Wimperis, S. *NMR: The Toolkit : how Pulse Sequences Work*.
(Oxford University Press, 2015).

- 81 Oldfield, E. *et al.* 17O nuclear-magnetic-resonance spectroscopic study of high-Tc superconductors. *Physical Review B* **40**, 6832-6849 (1989).
- 82 Bastow, T. J. & Stuart, S. N. 17O NMR in simple oxides. *Chemical Physics* **143**, 459-467, (1990).
- 83 Willis, B. T. M. Positions of the Oxygen Atoms in UO₂. *Nature* **197**, 755-756 (1963).
- 84 Putna, E. S., Vohs, J. M. & Gorte, R. J. Characterization of ceria films on α -Al₂O₃(0001) and polycrystalline zirconia using O₂ TPD with labeled 18O₂. *Catalysis Letters* **45**, 143-147, (1997).
- 85 Putna, E. S., Vohs, J. M. & Gorte, R. J. Evidence for Weakly Bound Oxygen on Ceria Films. *The Journal of Physical Chemistry* **100**, 17862-17865, (1996).
- 86 Bunluesin, T., Gorte, R. J. & Graham, G. W. CO oxidation for the characterization of reducibility in oxygen storage components of three-way automotive catalysts. *Applied Catalysis B: Environmental* **14**, 105-115, (1997).
- 87 Ta, N. *et al.* Stabilized Gold Nanoparticles on Ceria Nanorods by Strong Interfacial Anchoring. *Journal of the American Chemical Society* **134**, 20585-20588, (2012).
- 88 Agarwal, S., Lefferts, L. & Mojet, B. L. Ceria Nanocatalysts: Shape Dependent Reactivity and Formation of OH. *ChemCatChem* **5**, 479-489, (2013).
- 89 O'Neill, W. M. & Morris, M. A. The defect chemistry of lanthana–ceria mixed oxides by MASNMR. *Chemical Physics Letters* **305**, 389-394, (1999).
- 90 Shackelford, J. & Doremus, R. H. *Ceramic and Glass Materials: Structure, Properties and Processing*. (Springer US, 2008).
- 91 Kim, N. & Stebbins, J. F. Vacancy and Cation Distribution in Yttria-Doped Ceria: An 89Y and 17O MAS NMR Study. *Chemistry of Materials* **19**, 5742-5747, (2007).
- 92 Ando, M. *et al.* High field O-17 NMR study of defects in doped zirconia and ceria. *Ionics* **192**, 576-579, (2011).
- 93 Florian, P., Massio, D., Humbert, G. & Counters, J. Etude par RMN de ¹⁷O et ⁸⁹Y des formes C et B de l'oxyde d'yttrium Y₂O₃ = ¹⁷O and ⁸⁹Y NMR of C and B-Y₂O₃. *Comptes rendus de l'Académie des sciences. Série II, Mécanique, physique, chimie, astronomie* **320**, 99-104 (1995).
- 94 Ando, M. *et al.* Oxygen-17 NMR Study of Defects in LnO_{1.5}-CeO₂ (Ln= La and Nd). *Chemistry Letters* **42**, 57-59 (2012).
- 95 Yashima, M. Crystal structures, structural disorders and diffusion paths of ionic conductors from diffraction experiments. *Solid State Ionics* **179**, 797-803, (2008).
- 96 Maupin, I. *et al.* Direct evidence of the role of dispersed ceria on the activation of oxygen in NaX zeolite by coupling the 17O/16O isotopic exchange and 17O solid-state NMR. *Journal of Catalysis* **300**, 136-140, (2013).
- 97 Wang, M. *et al.* Identification of different oxygen species in oxide nanostructures with ¹⁷O solid-state NMR spectroscopy. *Science Advances* **1** (2015).
- 98 Heinzmann, R. *et al.* Observing Local Oxygen Interstitial Diffusion in Donor-Doped Ceria by 17O NMR Relaxometry. *The Journal of Physical Chemistry C* **120**, 8568-8577, (2016).
- 99 Hope, M. A. *et al.* Surface-selective direct 17O DNP NMR of CeO₂ nanoparticles. *Chemical Communications* **53**, 2142-2145, (2017).
- 100 Heinmaa, I., Joon, T., Kooskora, H., Pahapill, J. & Subbi, J. Local structure and oxygen ion dynamics in La doped ceria: 17O NMR study. *Solid State Ionics* **181**, 1309-1315, (2010).
- 101 **Mahadi, A. H. Ceria morphologies as Pd nanoparticles support for heterogeneous catalysis** Doctor of Philosophy thesis, University of Oxford, (2015).
- 102 Hayles, J. & Bao, H. The reduction and oxidation of ceria: A natural abundance triple oxygen isotope perspective. *Geochimica et Cosmochimica Acta* **159**, 220-230, (2015).

- 103 Damatov, D. & Mayer, J. M. (Hydro)peroxide ligands on colloidal cerium oxide nanoparticles. *Chemical Communications* **52**, 10281-10284, (2016).
- 104 Harris, R. K., Becker, E. D., Cabral de Menezes, S. M., Goodfellow, R. & Granger, P. NMR nomenclature: nuclear spin properties and conventions for chemical shifts. IUPAC Recommendations 2001. International Union of Pure and Applied Chemistry. Physical Chemistry Division. Commission on Molecular Structure and Spectroscopy. *Magnetic Resonance in Chemistry* **40**, 489-505, (2002).
- 105 J. Clark, S. *et al.* *First principles methods using CASTEP*. Vol. 220 (2005).
- 106 McCarty, R. J. & Stebbins, J. F. Investigating lanthanide dopant distributions in Yttrium Aluminum Garnet (YAG) using solid state paramagnetic NMR. *Nuclear Magnetic Resonance* **79**, 11-22, d (2016).
- 107 He, X. *et al.* Effects of local structure of Ce³⁺ ions on luminescent properties of Y₃Al₅O₁₂:Ce nanoparticles. **6**, 22238, (2016).
- 108 Hailstone, R. K., DiFrancesco, A. G., Leong, J. G., Allston, T. D. & Reed, K. J. A Study of Lattice Expansion in CeO₂ Nanoparticles by Transmission Electron Microscopy. *The Journal of Physical Chemistry C* **113**, 15155-15159, (2009).
- 109 Filtschew, A., Hofmann, K. & Hess, C. Ceria and Its Defect Structure: New Insights from a Combined Spectroscopic Approach. *The Journal of Physical Chemistry C* **120**, 6694-6703, (2016).
- 110 Popović, Z. V., Dohčević-Mitrović, Z., Šćepanović, M., Grujić-Brojčin, M. & Aškračić, S. Raman scattering on nanomaterials and nanostructures. *Annalen der Physik* **523**, 62-74, (2011).
- 111 Kostić, R., Aškračić, S., Dohčević-Mitrović, Z. & Popović, Z. V. Low-frequency Raman scattering from CeO₂ nanoparticles. *Applied Physics A* **90**, 679-683, (2008).
- 112 Fazio, B., Spadaro, L., Trunfio, G., Negro, J. & Arena, F. Raman scattering of MnO_x/CeO_x composite catalysts: structural aspects and laser-heating effects. *Journal of Raman Spectroscopy* **42**, 1583-1588, (2011).
- 113 Grover, V. *et al.* Effect of grain size and microstructure on radiation stability of CeO₂: an extensive study. *Physical Chemistry Chemical Physics* **16**, 27065-27073, (2014).
- 114 Weber, W. H., Hass, K. C. & McBride, J. R. Raman study of $\{\mathrm{CeO}\}_2$: Second-order scattering, lattice dynamics, and particle-size effects. *Physical Review B* **48**, 178-185 (1993).
- 115 Lin, X.-M., Li, L.-P., Li, G.-S. & Su, W.-H. Transport property and Raman spectra of nanocrystalline solid solutions Ce_{0.8}Nd_{0.2}O_{2-δ} with different particle size. *Materials Chemistry and Physics* **69**, 236-240, (2001).
- 116 Alammar, T., Chow, Y.-K. & Mudring, A.-V. Energy efficient microwave synthesis of mesoporous Ce_{0.5}Mn_{0.5}O₂ (Ti, Zr, Hf) nanoparticles for low temperature CO oxidation in an ionic liquid - a comparative study. *New Journal of Chemistry* **39**, 1339-1347, (2015).
- 117 Penkala, B. *et al.* The role of lattice oxygen in CO oxidation over Ce₁₈O₂-based catalysts revealed under operando conditions. *Catalysis Science & Technology* **5**, 4839-4848, (2015).
- 118 Badri, A., Binet, C. & Lavalley, J.-C. An FTIR study of surface ceria hydroxy groups during a redox process with H₂. *Journal of the Chemical Society, Faraday Transactions* **92**, 4669-4673, (1996).
- 119 Schramm, S. & Oldfield, E. High-resolution oxygen-17 NMR of solids. *Journal of the American Chemical Society* **106**, 2502-2506, (1984).
- 120 Chadwick, A. V., Pople, I. J. F., Maitland, D. T. S. & Smith, M. E. Oxygen Speciation in Nanophase MgO from Solid-State ¹⁷O NMR. *Chemistry of Materials* **10**, 864-870, (1998).

- 121 Scolan, E., Magnenet, C., Massiot, D. & Sanchez, C. Surface and bulk characterisation of titanium-oxo clusters and nanosized titania particles through ^{17}O solid state NMR. *Journal of Materials Chemistry* **9**, 2467-2474, (1999).
- 122 Cadars, S. *et al.* Atomic Positional Versus Electronic Order in Semiconducting ZnSe Nanoparticles. *Physical Review Letters* **103**, 136802 (2009).
- 123 Berrettini, M. *Solid-State NMR Analysis of the Surfaces and Interfaces in Nanoscale Materials* Doctor of Philosophy thesis, UNIVERSITY OF CALIFORNIA, (2005).
- 124 Zabilskiy, M. *et al.* Nanoshaped CuO/CeO₂ Materials: Effect of the Exposed Ceria Surfaces on Catalytic Activity in N₂O Decomposition Reaction. *ACS Catalysis* **5**, 5357-5365, (2015).
- 125 Zhu, D. *et al.* Noble Metal-Free Ceria-Zirconia Solid Solutions Templated by Tobacco Materials for Catalytic Oxidation of CO. *Catalysts* **6**, (2016).
- 126 Taniguchi, T., Katsumata, K.-i., Omata, S., Okada, K. & Matsushita, N. Tuning Growth Modes of Ceria-Based Nanocubes by a Hydrothermal Method. *Crystal Growth & Design* **11**, 3754-3760, (2011).
- 127 Aneggi, E., Wiater, D., de Leitenburg, C., Llorca, J. & Trovarelli, A. Shape-Dependent Activity of Ceria in Soot Combustion. *ACS Catalysis* **4**, 172-181, (2014).
- 128 Sayle, D. C. & Sayle, T. X. T. in *Synthesis, Properties, and Applications of Oxide Nanomaterials* 247-286 (John Wiley & Sons, Inc., 2007).
- 129 Luo, J.-Y., Epling, W. S., Qi, G. & Li, W. Low Temperature Ceria-Based Lean NO_x Traps. *Catalysis Letters* **142**, 946-958, (2012).
- 130 Gómez, L. E., Múnera, J. F., Sollier, B. M., Miró, E. E. & Boix, A. V. Raman in situ characterization of the species present in Co/CeO₂ and Co/ZrO₂ catalysts during the COPrOx reaction. *International Journal of Hydrogen Energy* **41**, 4993-5002, (2016).
- 131 Lee, Y. *et al.* Raman Analysis of Mode Softening in Nanoparticle CeO₂- δ and Au-CeO₂- δ during CO Oxidation. *Journal of the American Chemical Society* **133**, 12952-12955, (2011).
- 132 Binet, C., Daturi, M. & Lavalley, J.-C. IR study of polycrystalline ceria properties in oxidised and reduced states. *Catalysis Today* **50**, 207-225, (1999).
- 133 Binet, C., Badri, A. & Lavalley, J.-C. A Spectroscopic Characterization of the Reduction of Ceria from Electronic Transitions of Intrinsic Point Defects. *The Journal of Physical Chemistry* **98**, 6392-6398, (1994).
- 134 Sakai, N. *et al.* Effect of water vapour on oxygen exchange kinetics of ceria and zirconia solid electrolytes. *Physical Chemistry Chemical Physics* **5**, 2253-2256, (2003).
- 135 Agarwal, S. *et al.* Exposed Surfaces on Shape-Controlled Ceria Nanoparticles Revealed through AC-TEM and Water-Gas Shift Reactivity. *ChemSusChem* **6**, 1898-1906, (2013).
- 136 Sayle, D. C., Maicananu, S. A. & Watson, G. W. Atomistic Models for CeO₂(111), (110), and (100) Nanoparticles, Supported on Yttrium-Stabilized Zirconia. *Journal of the American Chemical Society* **124**, 11429-11439, (2002).
- 137 Cerioni, G. & Mocci, F. in *PATAI'S Chemistry of Functional Groups* (John Wiley & Sons, Ltd, 2009).
- 138 Barieux, J. J. & Schirmann, J. P. ^{17}O -enriched hydrogen peroxide and t.butyl hydroperoxide: Synthesis, characterization and some applications. *Tetrahedron Letters* **28**, 6443-6446, (1987).
- 139 Solomon, I. J., Keith, J. N., Kacmarek, A. J. & Raney, J. K. Additional studies concerning the existence of "O₃F₂". *Journal of the American Chemical Society* **90**, 5408-5411, (1968).
- 140 Huang, X. & Beck, M. J. Size-Dependent Appearance of Intrinsic O_xq "Activated Oxygen" Molecules on Ceria Nanoparticles. *Chemistry of Materials* **27**, 5840-5844, (2015).

- 141 Bulanin, K. M. *et al.* Infrared Study of Ozone Adsorption on CeO₂. *The Journal of Physical Chemistry B* **102**, 6809-6816, (1998).
- 142 Reynolds, M. S. & Butler, A. Oxygen-17 NMR, Electronic, and Vibrational Spectroscopy of Transition Metal Peroxo Complexes: Correlation with Reactivity. *Inorganic Chemistry* **35**, 2378-2383, (1996).
- 143 Profeta, M., Benoit, M., Mauri, F. & J Pickard, C. *First-Principles Calculation of the 17 O NMR Parameters in Ca Oxide and Ca Aluminosilicates: the Partially Covalent Nature of the Ca–O Bond, a Challenge for Density Functional Theory*. Vol. 126 (2004).
- 144 Champouret, Y., Coppel, Y. & Kahn, M. L. Evidence for Core Oxygen Dynamics and Exchange in Metal Oxide Nanocrystals from In Situ 17O MAS NMR. *Journal of the American Chemical Society* **138**, 16322-16328, (2016).
- 145 Profeta, M., Mauri, F. & Pickard, C. J. Accurate First Principles Prediction of 17O NMR Parameters in SiO₂: Assignment of the Zeolite Ferrierite Spectrum. *Journal of the American Chemical Society* **125**, 541-548, (2003).
- 146 Bak, M., Rasmussen, J. T. & Nielsen, N. C. SIMPSON: A general simulation program for solid-state NMR spectroscopy. *Journal of Magnetic Resonance* **213**, 366-400, (2011).
- 147 Ashbrook, S. E. & Smith, M. E. Solid stateSolid-state 17O NMR-an introduction to the background principles and applications to inorganic materials. *Chemical Society Reviews* **35**, 718-735, (2006).
- 148 Chueh, W. C. *et al.* Highly Enhanced Concentration and Stability of Reactive Ce³⁺ on Doped CeO₂ Surface Revealed In Operando. *Chemistry of Materials* **24**, 1876-1882, (2012).
- 149 Sayle, T. X. T., Catlow, C. R. A., Maphanga, R. R., Ngoepe, P. E. & Sayle, D. C. Generating MnO₂ Nanoparticles Using Simulated Amorphization and Recrystallization. *Journal of the American Chemical Society* **127**, 12828-12837, (2005).
- 150 Dohčević-Mitrović, N. P. a. Z. V. P. a. Z. D. Superparamagnetism in iron-doped CeO₂–γ nanocrystals. *Journal of Physics: Condensed Matter* **24**, 456001 (2012).
- 151 Colis, S. *et al.* High-temperature ferromagnetism in Co-doped CeO₂ synthesized by the coprecipitation technique. *Physical Chemistry Chemical Physics* **14**, 7256-7263, (2012).
- 152 Kumar, R. A., Babu, K. S., Dasgupta, A. & Ramaseshan, R. Enhancing the dual magnetic and optical properties of co-doped cerium oxide nanostructures. *RSC Advances* **5**, 103465-103473, (2015).
- 153 Wen, Q.-Y. *et al.* Room-temperature ferromagnetism in pure and Co doped CeO(2) powders. Vol. 19 (2007).
- 154 Phokha, S., Pinitsoontorn, S. & Maensiri, S. Room-temperature ferromagnetism in Co-doped CeO₂ nanospheres prepared by the polyvinylpyrrolidone-assisted hydrothermal method. *Journal of Applied Physics* **112**, 113904, (2012).
- 155 Stebbins, J. F., McCarty, R. J. & Palke, A. C. Solid-state NMR and short-range order in crystalline oxides and silicates: a new tool in paramagnetic resonances. *Acta Crystallographica Section C* **73**, 128-136, (2017).
- 156 Brog, K. C., Jones, W. H. & Verber, C. M. 27Al and 89Y nuclear magnetic resonance in yttrium-aluminum garnet. *Physics Letters* **20**, 258-260, (1966).
- 157 Keating, J., Sankar, G., Hyde, T. I., Kohara, S. & Ohara, K. Elucidation of structure and nature of the PdO-Pd transformation using in situ PDF and XAS techniques. *Phys Chem Chem Phys* **15**, 8555-8565, (2013).
- 158 Vayssilov, G. N. *et al.* Support nanostructure boosts oxygen transfer to catalytically active platinum nanoparticles. *Nat Mater* **10**, 310-315, (2011).

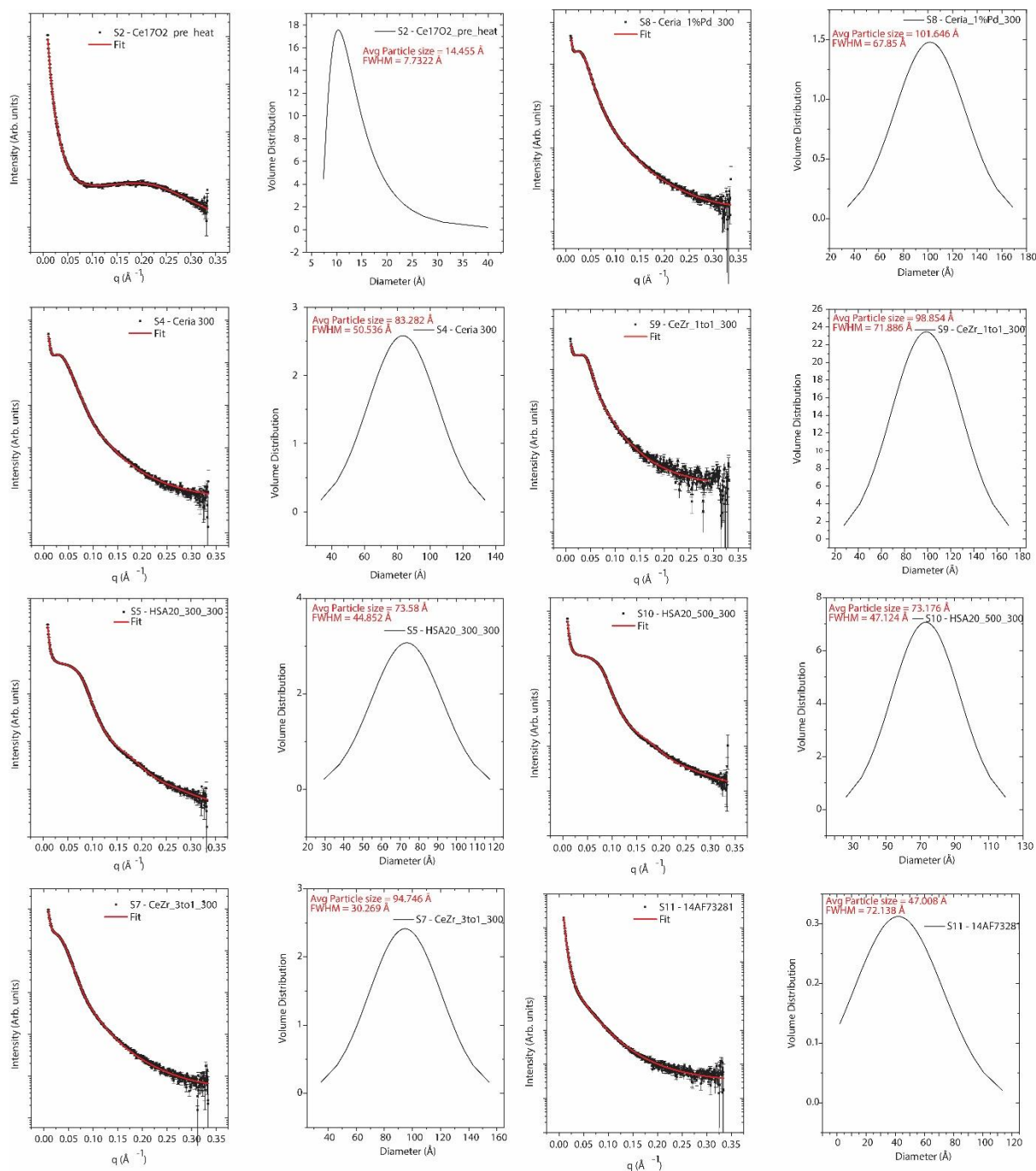
- 159 Liang, H. *et al.* Aqueous co-precipitation of Pd-doped cerium oxide nanoparticles: chemistry, structure, and particle growth. *Journal of Materials Science* **47**, 299-307, (2012).
- 160 Mamede, A. S., Leclercq, G., Payen, E., Grimblot, J. & Granger, P. Surface Raman spectroscopic study of NO transformation over Pd-based catalysts. *Physical Chemistry Chemical Physics* **5**, 4402-4406, (2003).
- 161 Hiley, C. I. *et al.* Incorporation of square-planar Pd²⁺ in fluorite CeO₂: hydrothermal preparation, local structure, redox properties and stability. *Journal of Materials Chemistry A* **3**, 13072-13079, (2015).
- 162 Kong, X. *et al.* Solid-State ¹⁷O NMR Spectroscopy of Paramagnetic Coordination Compounds. *Angewandte Chemie International Edition* **54**, 4753-4757, (2015).
- 163 Meng, L. *et al.* Preparation of ceria-zirconia solid solution with enhanced oxygen storage capacity and redox performance. *Frontiers of Environmental Science & Engineering in China* **4**, 164-171, (2010).
- 164 Das, D. *et al.* Methanol steam reforming behavior of copper impregnated over CeO₂-ZrO₂ derived from a surfactant assisted coprecipitation route. *International Journal of Hydrogen Energy* **40**, 10463-10479, (2015).
- 165 Stender, D. *et al.* Crystallization of zirconia based thin films. *Physical Chemistry Chemical Physics* **17**, 18613-18620, (2015).
- 166 Barb  ris, P. *et al.* Raman spectra of tetragonal zirconia: powder to zircaloy oxide frequency shift. *Journal of Nuclear Materials* **288**, 241-247, (2001).
- 167 Wyrwalski, F. *et al.* Bulk and surface structures of iron doped zirconium oxide systems: Influence of preparation method. *Journal of Materials Science* **40**, 933-942, (2005).
- 168 Reddy, B. M., Reddy, G. K. & Katta, L. Structural characterization and dehydration activity of CeO₂-SiO₂ and CeO₂-ZrO₂ mixed oxides prepared by a rapid microwave-assisted combustion synthesis method. *Journal of Molecular Catalysis A: Chemical* **319**, 52-57, (2010).
- 169 Andriopoulou, C. *et al.* Structural and Redox Properties of Ce_{1-x}Zr_xO_{2- } and Ce_{0.8}Zr_{0.15}RE_{0.05}O_{2- } (RE: La, Nd, Pr, Y) Solids Studied by High Temperature in Situ Raman Spectroscopy. *The Journal of Physical Chemistry C* **121**, 7931-7943, (2017).
- 170 Lapidot, A. and Irving, C. S. Oxygen-17 nuclear magnetic resonance spectroscopy and iridium and rhodium molecular oxygen complexes. *Journal of the Chemical Society, Dalton Transactions* **0**, 668-670, (1972).
- 171 Lumpkin, O., Doxon, W. T. and Poser, Oxygen-17 nuclear quadrupole resonances in molecular oxygen reversibly bonded to iridium carrier, J. *Journal of Inorganic Chemistry* **18**, 982- (1979).
- 172 George, N. C. *et al.*, Local environments of Dilute Activator Ions in the Solid-State Lighting Phosphor Y_{3-x}Ce_xAl₅O₁₂. *Chemistry of Materials*, **25**, 3979-3995, (2013).
- 173 Fusaro, L. and Luhmer, M., ¹⁷O NMR Study of Diamagnetic and Paramagnetic Lanthanide (III)-DOTA Complexes in Aqueous Solution, *Inorganic Chemistry*, **53**, 8717-8722, (2014).
- 174 Mathieu, J. and Lounsbury, M., The Raman spectra of metallic nitrates and the structure of concentrated solutions of electrolytes. *Discussions of the Faraday Society*, **9**, 196-207, (1950).
- 175 <https://sourceforge.net/p/gsim/discussion/604010/thread/aa1f1e05/>
- 176 Perdew, J. P. *et al.*, Restoring the density-gradient expansion for exchange in solids and surfaces. *Physical Review Letters*, **100**, 136406, (2007).
- 177 Bak, M., Rasmussen, J. T. and Nielsen, N. C., SIMPSON: A General Simulation Program for Solid-State NMR Spectroscopy. *Journal of Magnetic Resonance*, **147**, 296-330, (2000).

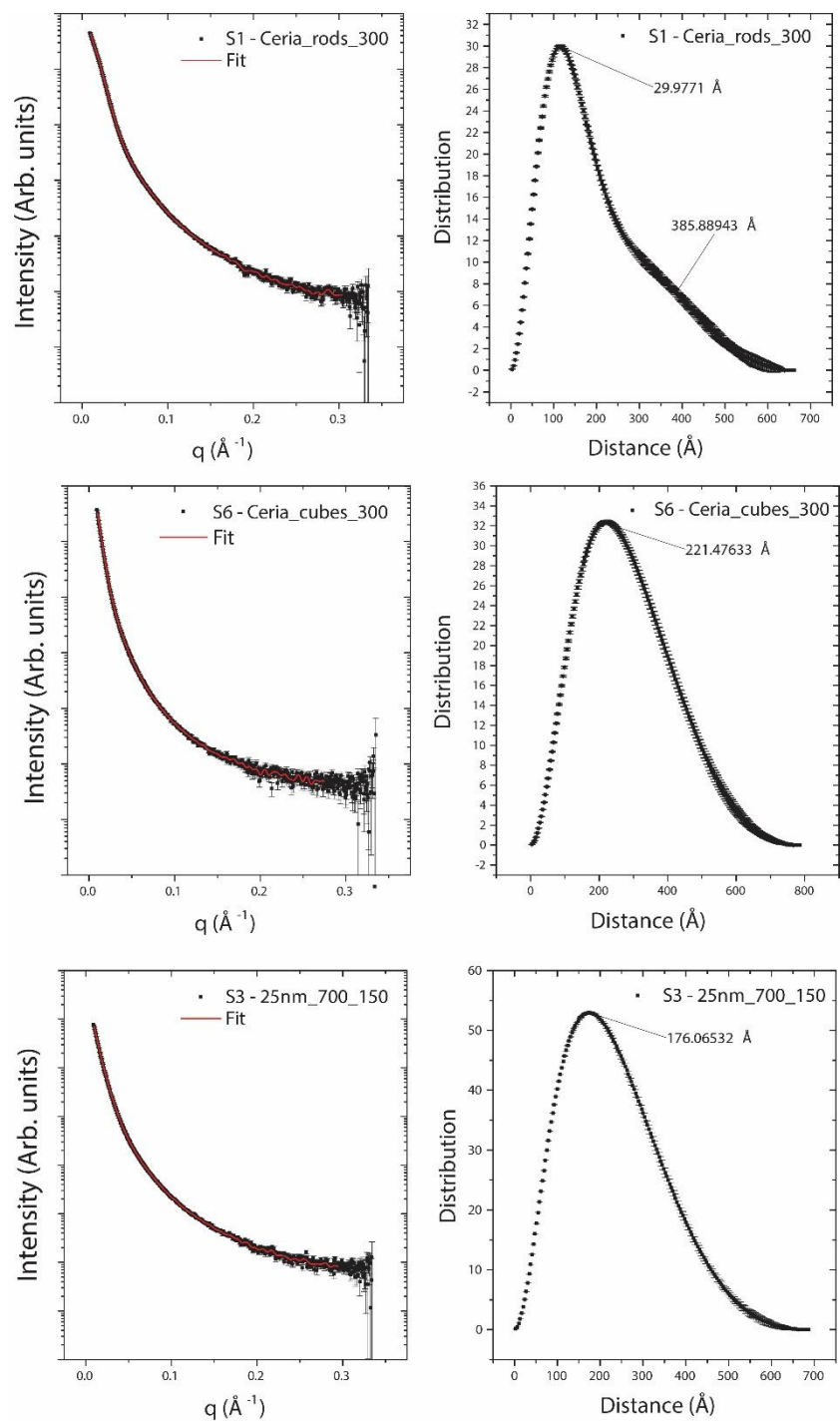
Appendix A

	Sample ID	PXRD crystallite size (nm)	SAXS particle size distributions (nm)	$F^{2G} (cm^{-1})$ ± 0.3	$D (cm^{-1})$ ± 5	I_D / I_{F2G} ± 0.002	Γ of F^{2G} (cm^{-1}) ± 0.8
5.1	H ₂ ¹⁷ O Ceria	> 2	1.5±0.8	450.0	600	0.174	77
	H ₂ ¹⁷ O Ceria 500 °C	11.0	4.7±7.2	463.8	600	0.016	12
5.2	HSA20 as-prepared	5.8		461.9	600	0.032	23.0
5.3	HSA20_600Ex	8.4	7.7±14.5	460.6	600	0.037	15.8
5.4	HSA20-700/300-Redox	12.7	8.3±5.1	464.4	600	0.019	13.9
	HSA20-500/300-Redox	8.1	7.3±4.7	461.7	600	0.037	21.7
	HSA20-300/300-Redox	8.0	7.4±4.5	461.1	600	0.042	23
5.5	HSA20-700/300-Redox (2 nd)	12.7		464.4	600	0.020	13.9
	HSA20-700/150-Redox	12.7		464.3	600	0.016	13.6
5.6	<25 nm SA Ceria (as-prepared)	-		463.4	600	0.017	11.0
	SA-600Ex	31.7		462.5	600	0.016	10.6
	SA-700/300-Redox	36.9		463.0	600	0.016	11.4
	SA-700/150-Redox	36.9	17.6, 36	464.2	600	0.013	9.35
	SA-700/25-Redox	36.9		464.3	600	0.015	9.9
5.7	Cubes-700/300-Redox	>Max	22.1, 38	463.4	600	0.009	8.6
	Rods-700/300-Redox	29.6	3, 38.6	463.8	600	0.012	8.8
	Cubes-700/150-Redox	>Max		463.2	600	0.009	8.5
	Rods-700/150-Redox	29.6		462.1	600	0.016	10.2
6.1	HSA20-1%Pd as-prepared	-		461.9	600	0.040	20.5
	HSA20-1%Pd-700/300-Redox	16	10.2±6.8	462.4	600	0.039	17.5
	HSA20-1%Pd-700/150-Redox	16		454.8	600	0.065	27.9
	Cubes-1%Pd as-prepared	-		456.3	600	0.063	24.9
	Cubes-1%Pd-700/300-Redox	-		444.1	600	0.087	37.2
	Cubes-1%Pd-700/150-Redox	-		455.6	600	0.035	19.5
	Rods-1%Pd as-prepared	-		450.3	600	0.246	52.4
	Rods-1%Pd-700/300-Redox	-		456.2	600	0.040	19.5
6.2	Ce _{0.75} Zr _{0.25} O ₂ As-prepared	5.3		472.9	610	0.172	70.7
	Ce _{0.5} Zr _{0.5} O ₂ As-prepared	5.2		473.9	623	0.464	162
	Ce _{0.25} Zr _{0.75} O ₂ As-prepared	6.7		-	-	-	-
6.3	Ce _{0.75} Zr _{0.25} O ₂ -600Ex	9.1		468.2	605	0.190	72.3
	Ce _{0.5} Zr _{0.5} O ₂ -600Ex	9.1		470.3	623	0.442	153
6.4	Ce _{0.75} Zr _{0.25} O ₂ -700/300-Redox	9.2		471.3	604	0.196	65.1
	Ce _{0.5} Zr _{0.5} O ₂ -700/300-Redox	8.3	9.9±7.2	472.8	621	0.538	171.2
	Ce _{0.75} Zr _{0.25} O ₂ -700/150-Redox	-		471.1	604	0.194	68.3
6.5	Ce _{0.5} Zr _{0.5} O ₂ -1%Pd as-prepared	-		475	632	0.556	186
	Ce _{0.5} Zr _{0.5} O ₂ -1%Pd-600Ex	-		474	627	0.528	168
	Ce _{0.5} Zr _{0.5} O ₂ -1%Pd-700/300-Redox	-		472	640	-	197

PXRD, SAXS and Raman spectra values for ceria and ceria zirconia systems investigated in Chapters 5 and 6.

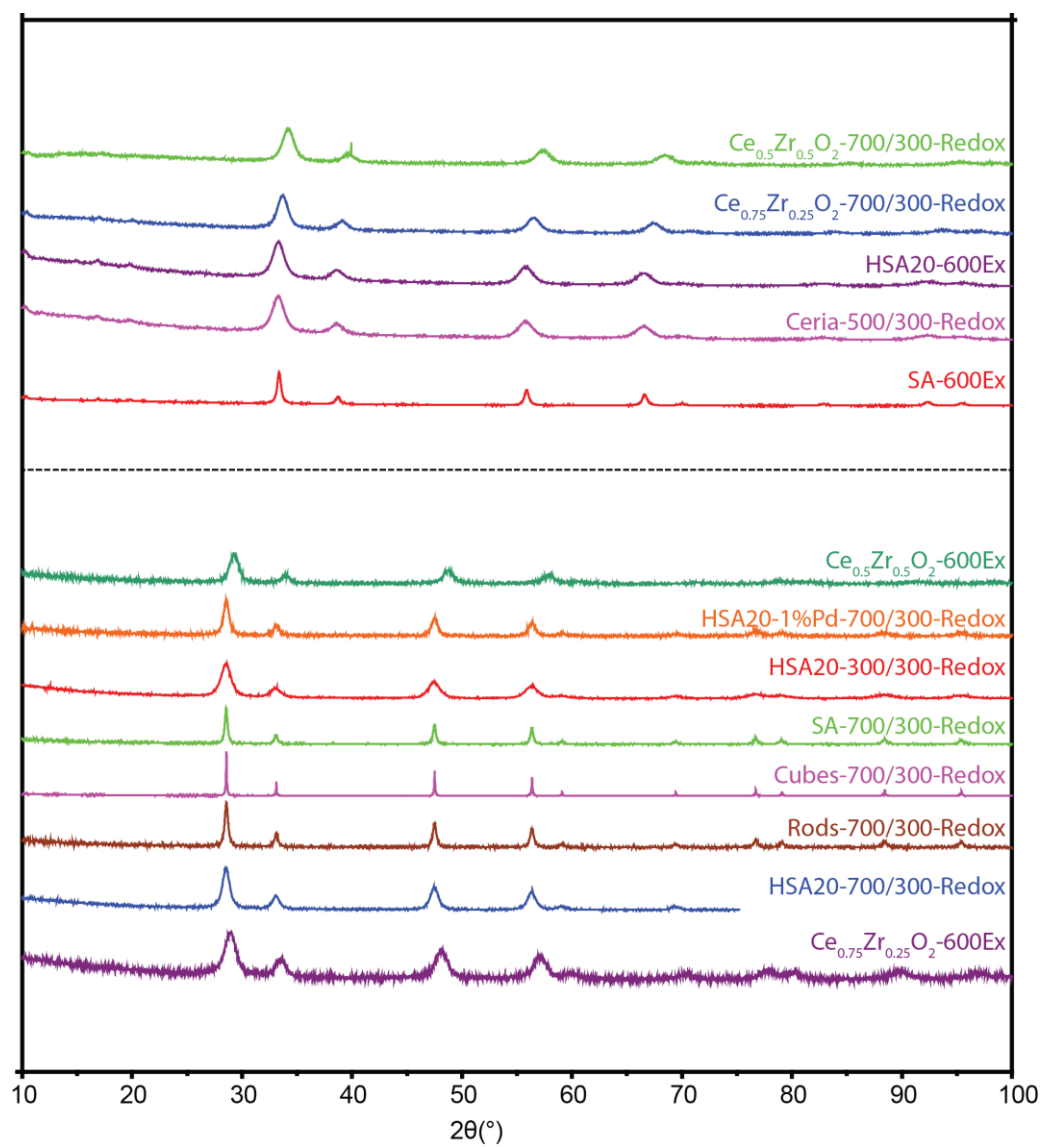
Appendix B





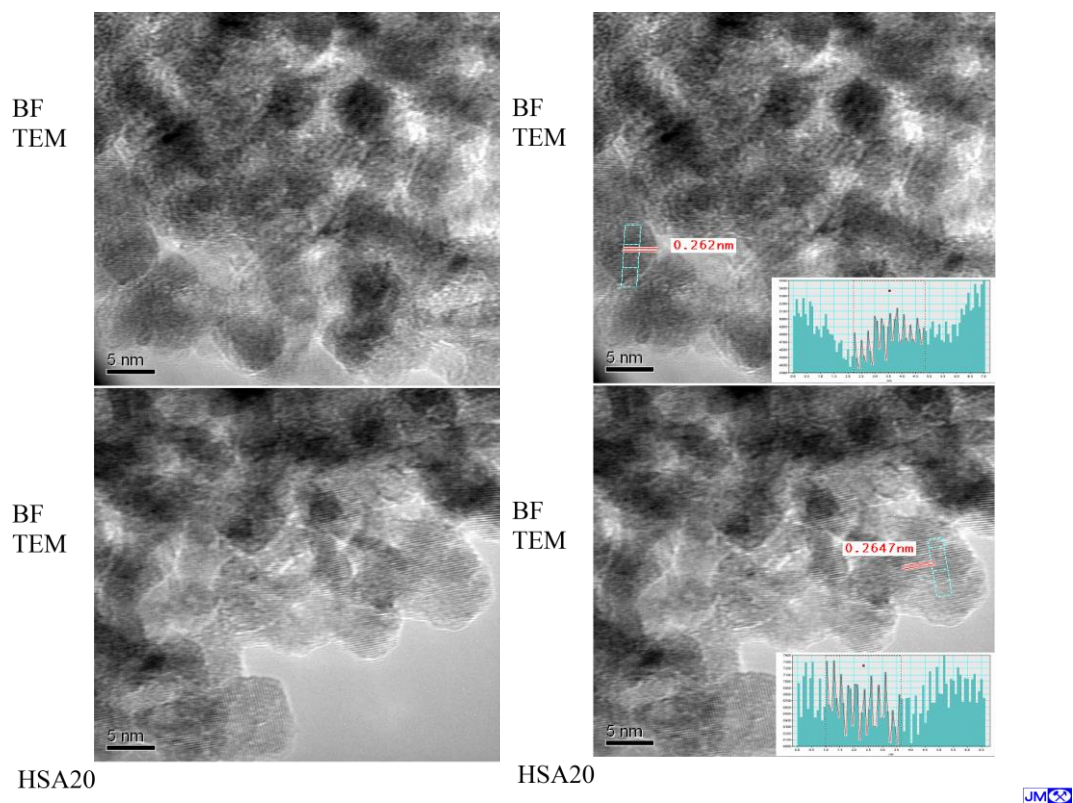
SAXS data of ceria and ceria zirconia systems, with particle sizes and distributions found in Table 1.

Appendix C



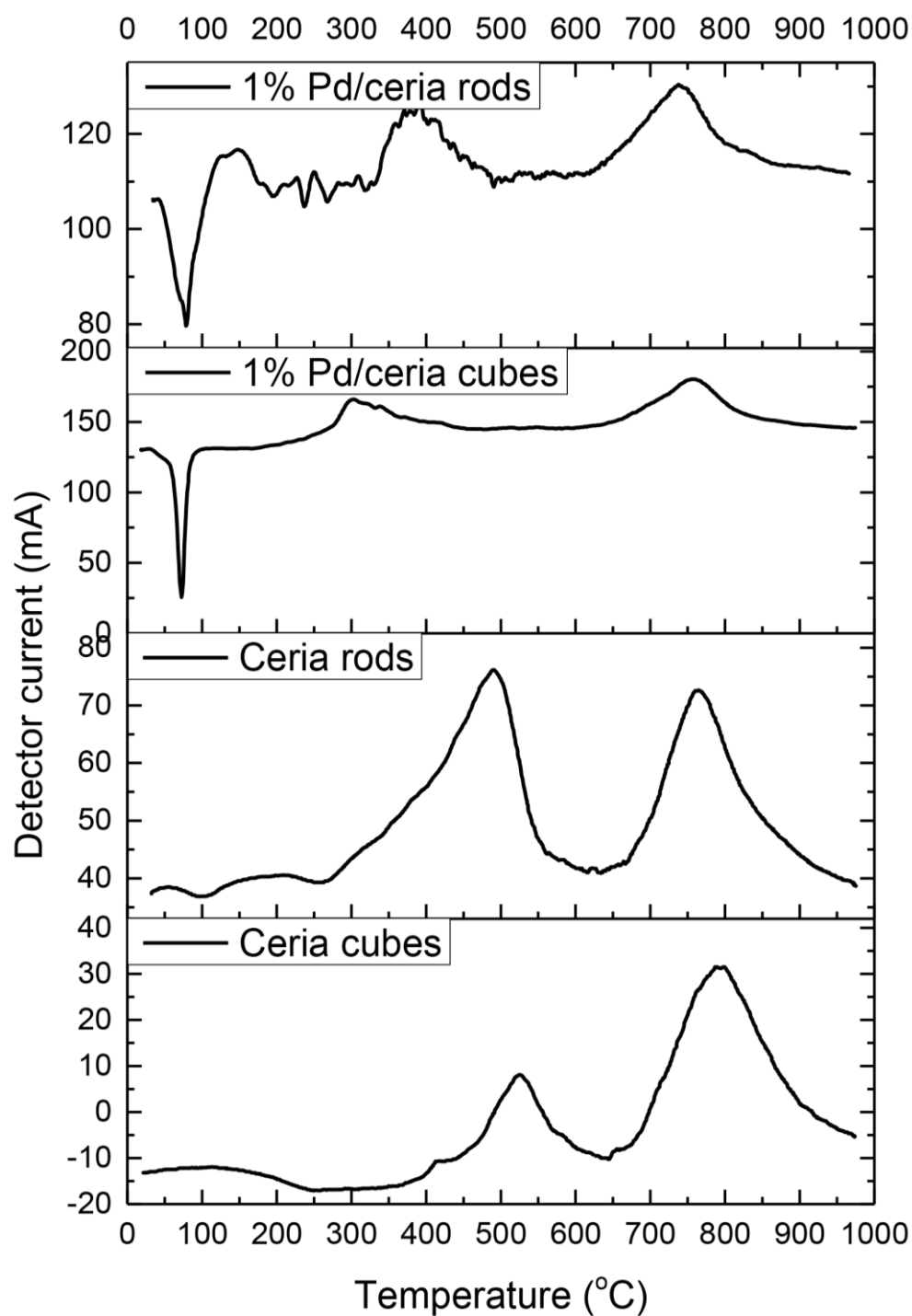
XRD diffractograms of ceria and ceria zirconia systems investigated in Chapters 5 and 6.

Appendix D



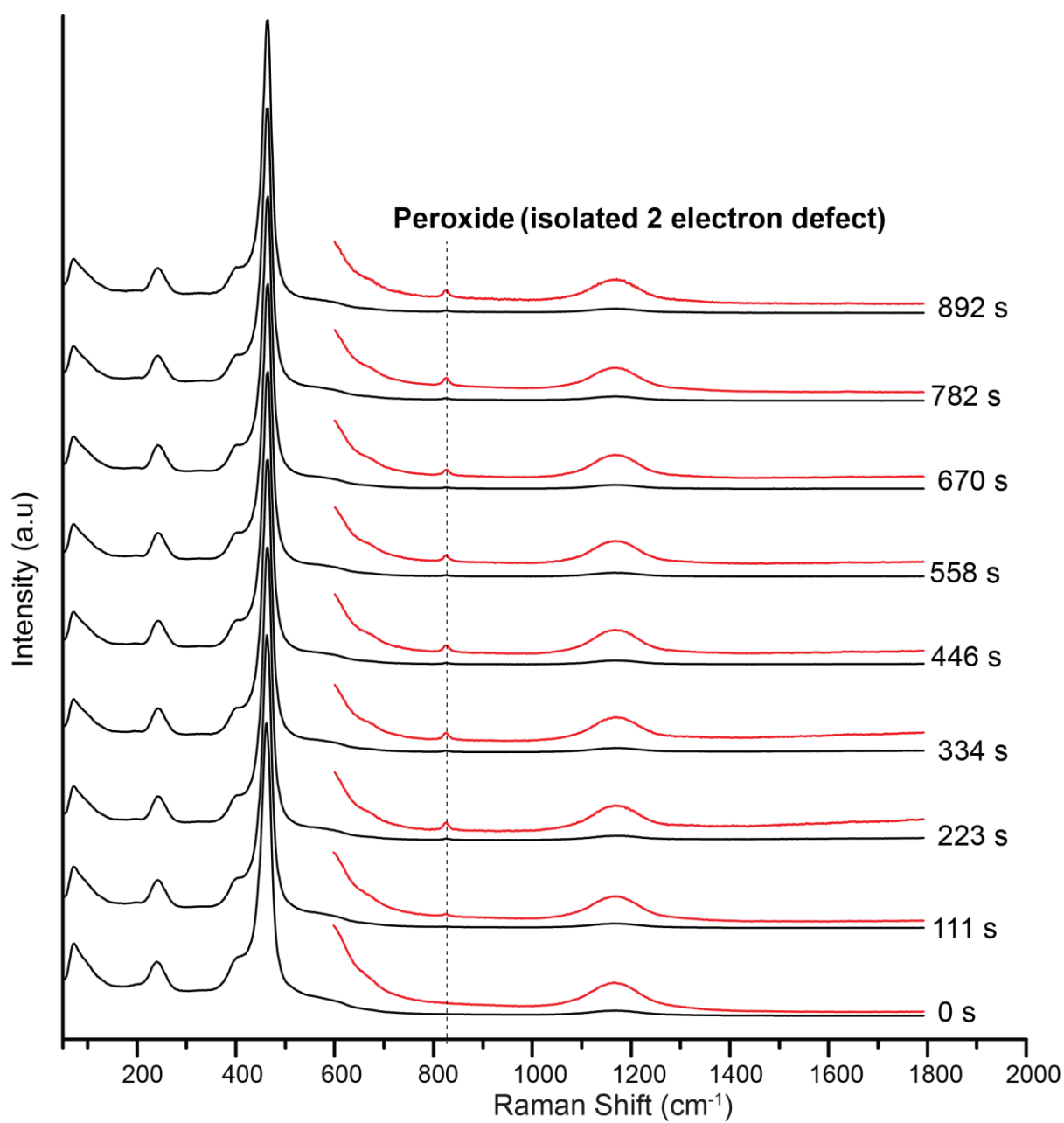
TEM images of HSA20 (as prepared), supplied by Johnson Matthey.

Appendix E



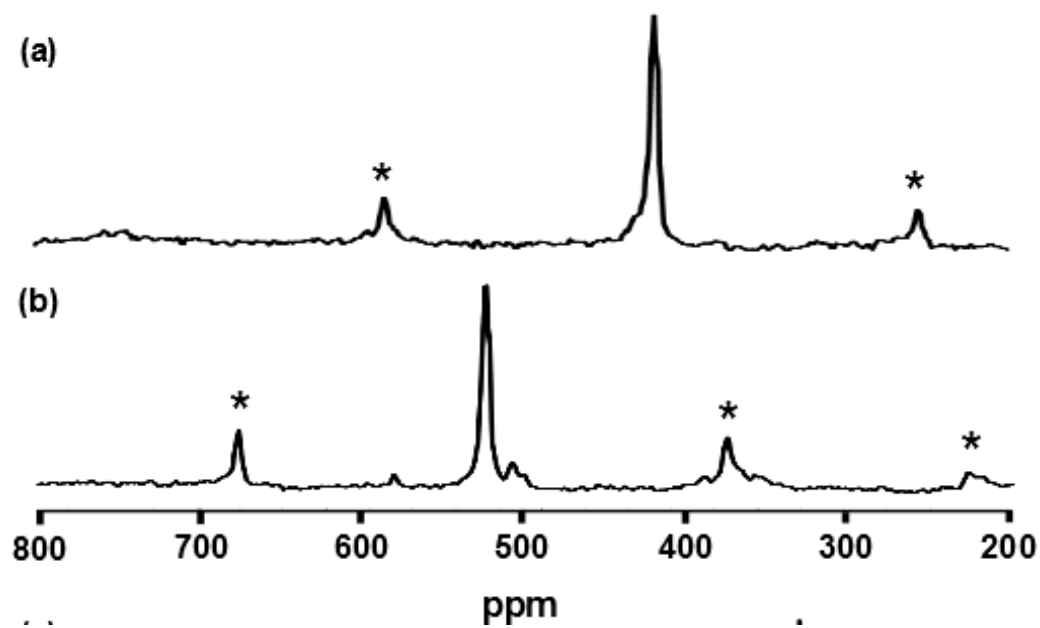
H₂-TPR data of ceria rods and cubes samples, supplied by Edman Tsang, University of Oxford. Diagram from the PhD thesis of A. H. Mahadi¹⁰¹.

Appendix F



In situ Raman spectra of HSA20 under a 5% O₂ flow sampled over 892 s. The Raman band identified is that of peroxide, which is generated (and appears stable) under oxidising conditions.

Appendix G



^{17}O solid-state MAS NMR spectra of (a) Na_2WO_4 and (b) Na_2MoO_4 acquired at 9.5 T, $\nu_r = 20$ kHz.